Inkjet Printing of Self-Healing Polymers for Enhanced Composite Interlaminar Properties

Elliot John Fleet

A Thesis Presented for the Degree of

Doctor of Philosophy

The University Of Sheffield.

Department of Materials Science and Engineering
Faculty of Engineering

University of Sheffield, UK

March 2014

Dedicated to Tala. Thank you for all the encouragement, support and most of all for believing in me.

Acknowledgements

Firstly I would like to thank my two Supervisors, Dr. Patrick Smith and Dr. Simon Hayes for their enthusiasm and support throughout the project. Simon provided much of the inspiration and shared a wealth of scientific knowledge that enabled me to give my research a solid purpose. Sadly, it was necessary for him to take absence due to illness but, nevertheless, his influence cannot be understated. Patrick kindly took over my supervision approximately halfway through my candidature in the midst of a laboratory move that caused significant practical delays. It is doubtlessly largely due to Patrick's generosity with his time, strong directional guidance, expertise and attention to detail that this thesis was possible. I owe a great debt of gratitude to both of them.

I would like to thank Dr. Simon Jones for providing invaluable organic chemistry guidance and allowing me to work as a guest in his laboratory.

I am particularly grateful for the assistance given by fellow PhD candidate Mrs. Yi Zhang with the inkjet printing of my monomers.

In addition, insightful discussions with Prof. Frank Jones, Dr. Joel Foreman, Dr. Tim Swait, Dr. Jonathon Stringer, Dr. Mohd Suzeren Md Jamil and Dr. Michael Morris have been very useful for problem solving at various different stages of the project.

And finally, I would also like to express my gratitude to the Engineering and Physical Sciences Research Council (EPSRC) for providing the funding and financial support for this project.

Abstract

This thesis reports upon a method of increasing the interlaminar fracture toughness and interlaminar shear strength of carbon-epoxy composites in order to increase the resistance to related damage propagation. In addition a thermally activated self-healing agent is introduced within the interface which has the potential to increase part lifetime and safety.

Thiele's acid (3a,4,7,7a-tetrahydro-4,7-methano-1H-indene-2,6-dicarboxylic acid) was synthesised from dicyclopentadiene with good yield (64%) and used as the main starting material for the synthesis of various monomers with interesting thermal properties. Two monomers were selected for use as composite interlaminar additives: M400 (10% yield) and M401 (18% yield).

The synthesised monomers were formulated into solutions in ethyl acetate that were used as inks for inkjet printing onto prepreg plies. The printing parameters were optimised and the printed prepreg was used to manufacture composite specimens in which the monomers are cured *in situ* with the prepreg resin. The resultant system is a thermoset composite containing polymers with thermally reversible Diels-Alder crosslinks concentrated in the interface.

Testing of the composite interlaminar properties revealed an increase in interlaminar fracture toughness; the mean initiation (NL point) mode I critical energy release rate (G_{IC}) determined by the double cantilever beam test was increased by up to 9% from 329 $\mathrm{J\,m^{-2}} \pm 6.89\ \mathrm{J\,m^{-2}}$ to 360 $\mathrm{J\,m^{-2}} \pm 22.5\ \mathrm{J\,m^{-2}}$. The mean median propagation G_{IC} was also increased by up to 27% from 331 $\mathrm{J\,m^{-2}} \pm 5.15\ \mathrm{J\,m^{-2}}$ to 420 $\mathrm{J\,m^{-2}} \pm 29.0\ \mathrm{J\,m^{-2}}$. Short beam shear testing also revealed a moderate increase

in apparent interlaminar fracture toughness of up to 11% from 105 MPa ± 2.09 MPa to 116 MPa ± 2.46 MPa.

These differences in mechanical properties are remarkable because the amount of printed material was extremely low; the volume fraction of printed material was in the range of 0.00047% to 0.014%.

In addition the short beam shear specimens showed evidence of self-healing after a thermal treatment with healing efficiencies calculated to be 48% and 53% for M401 and M400.

Publications and Presentations

- E. J. Fleet, "Self-healing polymers", *Chemistry Review (Philip Allan Updates)*, February 2011.
- E. J. Fleet, M. S. Bin Md. Jamil, S. Jones and S.A. Hayes, "Evaluation of a modified matrix and the synthesis of thermally reversible self-healing matrix polymers", *Proceedings of ICCM-18*, Jeju-do, August 2011.
- T. J. Swait, A. Rauf, R. Grainger, P. B. S. Bailey, A. D. Lafferty, E. J. Fleet, R. J. Hand and S A Hayes, "Smart composite materials for self-sensing and self-healing", *Plast., Rubber Compos.*, 2012, vol 41, **4/5**, 215-224.
- E. J. Fleet, Y. Zhang, S. A. Hayes and P. J. Smith, "Inkjet printing of self-healing polymers for enhanced composite interlaminar properties", *Manuscript in Preparation for submission to J. Mater. Chem. A.* , 2014.

Contents

Nomenclature

Care has been taken throughout this thesis to avoid duplication of symbols with different meanings. Due to the interdiciplinary nature of the work in some cases this has required a deviation from standard terminology; *e.g.* δ is commonly used for phase angle in DMA, chemical shift in NMR and to denote solubility parameters. Where possible subscripts have been added to differentiate symbols or a corresponding Roman letter has been substituted for a Greek letter or *vice versa*.

Roman Symbols

A	Arrehenius pre-exponential factor
a	Crack length
a_{r}	Nozzle radius
B	An empirical constant used in solubility parameter modelling
b	Width
C	Compliance
$\mathrm{C}_{5\%}$	Compliance +5%
d	Denotes a differential
d_c	Solute distance travelled (thin layer chromatography)
d_s	Solvent distance travelled (thin layer chromatography)
d_{d}	Distance to a defect (from the surface)
df_{between}	Degrees of freedom between groups (statistics)
df_{within}	Degrees of freedom within groups (statistics)
E	Elastic / Young's modulus
$E^{'}$	Tensile storage modulus
E^{*}	Complex tensile modulus
$E^{''}$	Tensile loss modulus
E_c	Cohesive energy
$E_0^{'}$	Onset in storage modulus drop (turning point method).
E_{a}	Activation energy
$E_{\mathrm{max}}^{''}$	Maximum loss modulus, can be used as a measure of a transition temperature
E_p	Potential energy
F	F statistic (ANOVA)
f	Frequency in Hz
F_{L}	Large displacement correction
F_z	Molar attraction constant for a molecule fragment 'z'
G	Strain energy release rate
$G^{'}$	Shear storage modulus
G^{*}	Complex shear modulus
$G^{''}$	Shear loss modulus
G_{C}	Critical energy release rate
G_{IC}	Mode I critical energy release rate
G_{I}	Mode I energy release rate
h	Thickness
ΔH_{fus}°	The enthalpy of fusion.
$h_{0.5}$	Half thickness
H_0	Null hypothesis
${}^{2}J$	Geminal coupling (NMR)
${}^{3}J$	Vicinal coupling (NMR)
${}^{4}J$	4-bond coupling (NMR)
J	Coupling constant (NMR)
k	The number of different groups (statistics)

$K^{'}$	Bulk comression storage modulus
K^{*}	Complex bulk compression modulus
$K^{''}$	Bulk compression loss modulus
L	Span length
l	Specimen length
l_1	The distance from the loading centre to the mid plane of the specimen beam
l_2	The distance from the loading centre to the end of the end block
Max/C5%	A measure of G_{IC} initiation
MS_{between}	Mean squares between groups (statistics)
MS_{within}	Mean squares within groups (statistics)
N	Load block correction factor
n	Used to denote the number of items in a group
N_{Re}	Reynolds number
N_{We}	Weber number
n_j	The number of items in the j_{th} group (statistics)
NL	A measure of G_{IC} initiation
Oh	Ohnesorge number
P	Force / load
p	Probability value
P_{max}	Maximum force/load
pK_a	A measure of acidity; the negative log_{10} of the acid dissociation constant. $pK_a = -log_{10}K_a$
pK_{aH}	A measure of basicity; the pK_a of the conjugate acid.
PROP	A measure of G_{IC} propagation
q	Damage baseline for SBS healing efficiency
R	Molar gas constant
$\overline{R}^2$	Coefficient of determination (adjusted)
R_a	Distance in Hansen space
R_f	Retention factor (thin layer chromatography)
s	Displacement
SS_{between}	Sum of squares between groups (statistics)
SS_{within}	Sum of squares within groups (statistics)
T	Wave period
t	t statistic (t tests)
T_b	Boiling point at standard pressure
T_C	Critical temperature
$T_{\alpha}*$	Alpha star transiton a liquid-liquid or crystal slip transition in DMA
T_{β}	Beta transition temperature
T_{efg}	Glass transition temperature (by DSC extrapolated end temperature)
T_{eig}	Glass transition temperature (by DSC extrapolated onset temperature)
T_{g0}	Glass transition temperature (by DSC turing point method)
T_{g}	Glass transition temperature (method of determination not indicated)
T_{mg}	Glass transition temperature (by DSC half-step height)
T_{m}	Melting temperature
U_{ε}	Internal energy stored as strain
V_{p}	Velocity (of the P-waves)
V_z	Molar volume of a molecule fragment 'z'
VIS	A measure of G_{IC} initiation
W	Work done
$\overline{x}_j$	The mean of the J_{th} group (statistics)
$\overline{\overline{x}}$	Grand mean (statistics)
x_{ij}	The i_{th} value of the J_{th} group (statistics)
Z	Inverse Ohnesorge number

Greek Symbols

α	Variable used solubility parameter modelling, represents the chain aggravation number for polymers
δ	Chemical shift (NMR)
δ_d	Hansen dispersive solubility parameter
δ_h	Hansen hydrogen bond solubility parameter
δ_p	Hansen polars solubility parameter
δ_t	Hansen total solubility parameter
Δ	End factor correction
$\tan\delta_{\max}$	Maximum loss factor, can be used as a measure of a transition temperature
$\tan\delta$	Loss factor
δ_θ	Phase angle
Δ_T^P	Critical temperature Lyderson group constants for a polymer fragment.
η	Viscosity
γ	Surface tension
λ	Wavelength
τ_{Ma}	Apparent interlaminar shear strength (unmodified specimens, calculated)
τ_{Mh}	Apparent interlaminar shear strength (healed samples)
τ_{Mv}	Apparent interlaminar shear strength (virgin samples)
τ_{M}	Apparent interlaminar shear strength
μ	Population mean
ν	Average travel velocity (of a droplet)
ω	Angular Frequency
ρ	Density
σ	Stress
σ_{A}	Stress amplitude (dynamic measurements)
$\sigma_{\max}$	Maximum stress
$\tau_{\max}$	Maximum shear stress
ε	Strain
ε_{A}	Strain amplitude (dynamic measurements)

Abbreviations

aILSS	Apparent interlaminar shear strength
ANOVA	Analysis of variance
BHT	Butylated hydroxytoluene
BVID	Barely visible impact damage
CI	Confidence interval
CIJ	Continuous inkjet printing
CPD	Cyclopentadiene
DA	Diels-Alder
DABCO	1,4-diazabicyclo[2.2.2]octane
DCB	Double cantilver beam
DCM	Dichloromethane
DCPD	Dicyclopentadiene
DEE	Diethyl ether
DGEBA	Diglicidyl ether of bisphenol A
DMA	Dynamic mechanical analysis
DMF	Dimethyl formamide
DMSO	Dimethyl sufoxide
DoD	Drop on Demand
DPE	Diisopropyl ether
DSC	Differential scanning calorimetry
EDROP	Entropy-driven ring opening polymerisation
ENB	5-ethylidene-2-norbornene
Endo	For isomers; the substituent is located closest to the longest bridge.
Exo	For isomers; the substituent is located furthest from the longest bridge.
HCl	Hydrogen chloride (in gas phase), hydrochloric acid when encountered in aqueous solution.
HOMO	Highest occupied molecular orbital
IJP	Inkjet printing
IR	Infra-red

IUPAC	International Union of Pure and Applied Chemistry
LT	Lock-in thermography
LUMO	Lowest unoccupied molecular orbital
MBT	Modified beam theory
MCC	Modified compliance calibration
Me	Methyl group
NaCP	Sodium cyclopentadienyl
NDE	Non-destructive evalution
NMR	Nuclear magnetic resonance
PAN	Polyacrylonitrile
pBPAcoE	poly(bisphenol-A-co-epichlorohydrin)
PCM	Polymer composite material
PEEK	Poly(ether ether ketone)
PEG	poly(ethylene glycol)
PF	Phenol formaldehyde
PIJ	Piezoelectric inkjet printing
PT	In pulsed thermography
PTFE	Poly(tetrafluoroethylene)
r-DA	Retro Diels-Alder
ROMP	Ring opening metathesis polymerisation
SBS	Short beam shear
SD	Standard deviation
SEFT	Spin-echo fourier transform
SHM	Structural health monitoring
TEMPO	2,2,6,6-tetramethylpiperidine-1-oxy
THF	Tetrahydrofuran
Thiele's Acid	3a,4,7,7a-tetrahydro-4,7-methano-1H-indene-2,6-dicarboxylic acid
TIJ	Thermal inkjet printing
TLC	Thin layer chromotography
UPR	Unsaturated polyester resin
UV	Ultra-violet

Chapter 1

Introduction and Literature Review

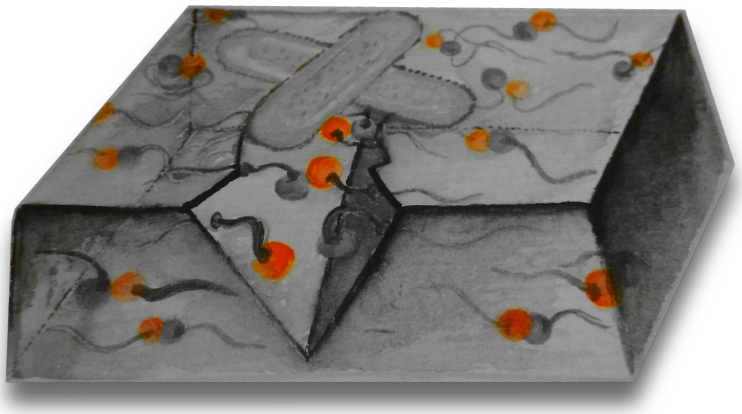

1.1 Thesis Aims and Objectives

The objective of this work is to synthesise and integrate a self-healing additive into an established epoxy resin system in order to allow for thermally activated self-healing in carbon fibre composites. This additive needs to be something that will either flow across or rebond damaged areas when activated by the application of heat. This has previously been accomplished by the addition of a compatible linear (thermoplastic) polymer into an otherwise thermoset epoxy matrix; upon the addition of heat the polymer softens and flows within the matrix free volume and has been shown to bridge and repair microcracks [1, 2].

This work aims to develop a more effective healing agent and a more efficient method of integrating it into the composite system. Polymers with thermally reversible covalent bonds were designed in order to improve the effectiveness of the healing additive. The integration of this additive could take place through a variety of different routes: an additive could be mixed into the matrix resin, it could be bonded or coated onto the reinforcing fibres or it could be applied to the surface of the resin pre-impregnated fibre intermediate materials (prepregs). Originally the modification was to be accomplished by the production of a bulk additive that could be mixed into the resin formulation. As the research progressed it became clear that a more efficient use of material was required. Inkjet printing was used as a method of prepreg modification as it is possible to use it to accurately place small amounts of material within the interface region in order to target interlaminar damage. Inkjet printing is an established and versatile technique used for controlled material deposition or patterning for a wide variety of applications but its use in the modification of composite materials is novel.

1.2 Thesis Outline

- This introductory chapter will first introduce polymer composite materials and briefly consider the current approaches towards damage detection and repair. The chapter will then focus on reviewing the literature with regards to past and current research in the field of self-healing polymers and composites in order to place this work into a suitable context.

- Chapter 2 details the development of the synthesis and the characterisation of 'Thiele's Acid', the key intermediate required for the production of the self-healing additives.
- Chapter 3 reports on the selection process and the production of the monomers for use as self-healing additives.
- Chapter 4 gives details on the formulation of inkjet printable monomer inks and the printing optimisation along with thermal characterisation of the monomers.
- Chapter 5 is concerned with the production of composite laminates and test specimens used to investigate the effect of the printed additives in an aerospace grade composite.
- Chapter 6 reports the conclusions that can be drawn from all the experiments and highlights opportunities for further work.

1.3 An Introduction to Composite Materials

Polymer composite materials (PCMs) have been produced now for over half a century with the first 'fibreglass' materials produced in the 1940s. A polymer composite material consists of reinforcements (usually fibre) within a polymer matrix (usually thermoset). The components are not dissolved, they remain separate although are bound together and so act cooperatively. The purpose of the matrix is to keep the fibres in the desired location and at the correct orientation, it also acts as a medium to transfer load between fibres. The purpose of the fibres is to act as high strength and modulus load-bearing components. The applications of PCMs are vast and range from the first radomes and aircraft fuselage in world war II through to civilian applications including boats, trucks, construction and infrastructure, sporting goods, kit cars and tanks. Over the last few decades gathering interest is leading to substantial adaptation of PCMs as aerospace materials due to their high strength; lighter weight; increased durability; high design versatility; good processability and their water, chemical and U.V. resistance.

A drawback of using PCMs as engineering materials is that during service due to cyclic stresses, impacts, or through unfavourable environmental conditions microcracks due to polymer degradations can be generated which can lower the lifetime of components. Microcracks increase the risk of structural failure but are not generated on the top plies in a composite and consequently can be difficult to detect and repair. It would therefore, be advantageous to include within a material, the ability to detect and repair small cracks or delaminations before the condition worsens; this should increase component lifetime and safety.

1.3.1 Matrices

There are many classes of polymer matrix in use today. The majority are thermosetting, however thermoplastic matrices should not be disregarded as they are growing in popularity. Some reasons for their increasing use despite their lower stiffness and fibre adhesion are their improved recycling prospects and increased toughness compared to thermosets. The focus of this section is to introduce the most common polymer thermosetting matrices as these are used in the class of high performance composites on which the work in this thesis is based.

1.3.1.1 Unsaturated Polyester and Vinyl Ester Resins

Unsaturated polyester resins (UPRs) form the matrix for the majority of polymer composites due to their low cost. They form by the condensation polymerisation reaction between an unsaturated diacid and a diol. In reality polyesters formed using a single type of unsaturated diacid leads to a very high crosslink density upon cure which causes the material to be brittle; so a saturated acid is also usually used as an additional monomer. The resins are often prepared dissolved in a reactive diluent such as styrene in order to lower the viscosity in order to increase processability. The styrene has dual purpose as it can react with the unsaturated polyester during cure to form part of the extended 3-dimensional network [3].

A typical polyester is shown in Figure 1.1. The most common curing agents are organic peroxide catalysts and a reducing agent (*e.g.* cobalt napthenate) as an accelerator in order to allow the cure to proceed at room temperature [4].

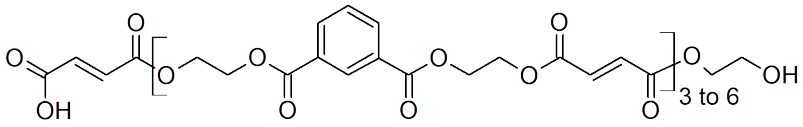

Figure 1.1: A typical isophthalic polyester formed from the condensation of saturated isophthalic acid, unsaturated fumaric acid and ethylene glycol.

Vinyl esters resins are similar to unsaturated polyester resins in that they are generally supplied in styrene and are used in similar applications. They are produced from the reaction of diepoxides and unsaturated monocarboxylic acids (*e.g* Acrylic Acid). The main difference between vinyl ester resins and UPRs is that the reactive vinyl group (double bond) is terminal; this causes an increase in toughness compared to polyesters as after cure the whole length of the polymer chains are available to absorb impact. Additionally, as there are fewer ester bonds per polymer chain, vinyl esters are more resistant to hydrolysis and therefore have better water resistance; it is for this reason that vinyl esters are often used as water tanks/pipes or barrier layers to protect polyester boat hulls.

1.3.1.2 Phenolic Resins

Phenol formaldehyde (PF) resins were one of the earliest commercial synthetic resins [5] (*e.g.* Bakelite), produced by the step-growth polymerization of phenol and formaldehyde. The cure can be either one step and require only elevated temperatures to crosslink (referred to as resoles) or require an amine catalyst and temperature (*i.e.* two step novolak resins). This cure mechanism is a condensation reaction which releases water which can cause problems for vacuum bagging processes.

The main advantage of phenolic resins are their excellent fire properties. In a fire phenolic-based composites form a thermally insulating, intumescent char layer which significantly reduces fire spread through the material. It is for this reason phenolic-glass composites are often used in aircraft interiors or mass transport interiors where the spread of fire would be considered a major hazard.

1.3.1.3 Epoxy Resins

Epoxy is a prefix referring to an oxygen atom bridge bonded to two other atoms that are already united in some way. Most often this will refer to so called 1,2-

epoxide rings consisting of an oxygen bonded to two covalently bonded carbons in a 3-membered ring [6]. This epoxide functionality allows cross-linking or curing reactions through a variety of addition reactions. Cured epoxy resins form the matrix for the majority of the high performance polymer composites incorporating glass, aramid and carbon fibres. This is due to their excellent mechanical properties, easy processing and low shrinkage with few volatiles released on cure. The most common epoxy resins are based upon the diglicidyl ether of bisphenol A (DGEBA) which is produced by the reaction between epichlorohydrin and bisphenol A as shown in Figure 1.2. Most commercial resins themselves are are mixtures of oligomers with different values of n. *P*ure DGEBA can be crystallised and isolated as a low melting point solid, in some cases it can cause a commercial resin to become cloudy by partially crystallising [7]. For most high performance composite purposes the value of n is 0 - 1 because they have a lower viscosity for processing, lower water sensitivity and have higher moduli and T_g [3].

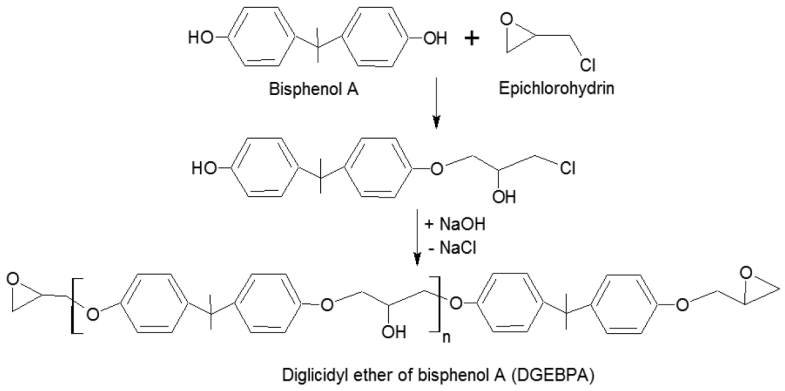

Figure 1.2: The formation of DGEBPA epoxy resin from bisphenol A and epichlorohydrin [3].

The formation of a thermoset network from epoxy resin requires some sort of crosslinking agent (also known as hardeners or curing agent). The cure can take place through the catalysed homopolymerization of the epoxy or a polyaddition reaction with a curing agent [7]. For most purposes the epoxy resins are usually cured through amine and polyamide curing agents or through acid anhydrides. The latter is often catalysed by tertiary amines as shown in Figure 1.3.

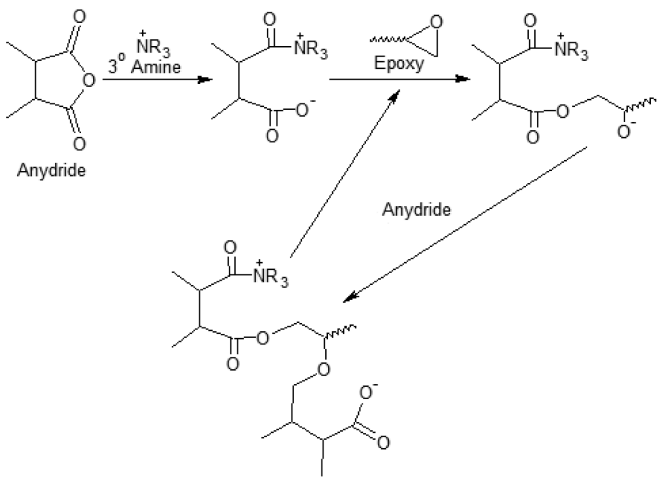

Figure 1.3: The tertiary amine catalysed curing of an epoxy with an anhydride as given in [3].

1.3.1.4 Matrix Summary

Table 1.1 gives an indication of the mechanical performance of some common resins. Please note due to the vast amount of different resin formulations and curing conditions this data is intended as a guide only. The resins are rarely used alone for any load bearing application, instead they are used along with reinforcements as part of a composite material.

Table 1.1: Properties of selected cast resins.

Resin type	Flexural strength (σ_f), MPa	Tensile strength (σ_t), MPa	Tensile modulus (E), GPa	Percentage elongation
Unsaturated Polyester (Orthophthalic) [a]	100	65-75	3.2	2.0-4.0
Unsaturated Polyester (Isophthalic) [a]	140	70-85	3.5	3.5
Phenolic resole [b]		61	3.9	1.7
Epoxy Resin, Anhydride Cured (NMA) [c]	115-146	43-80	2-3	1-6
Epoxy Resin, Amine Cured (1,2-Cyclohexane Diamine) [c]	106	71-83	2.9	4
Vinyl Ester [a]	130-140	70-80	3.3	5-6

[a] [8] ,[b] [9], [c] [10]

1.3.2 Reinforcements

This section introduces some of the most common classes of composite fibre reinforcements: glass, carbon and aramid.

1.3.2.1 Glass Fibres

Glass fibres are the most commonly used composite reinforcement (>95% by volume) and are generally used in low-mid performance applications. The most common type used is E-glass although different types are available such as R and S glass which have slightly different mechanical properties or ECR and AR glass which has improved acid and alkali resistance respectively. The glass fibres are generally coated with a silane 'sizing' which acts to protect the glass from damage and afford good adhesion to common matrix resins [3].

1.3.2.2 Carbon Fibres

Carbon fibres are produced from polyacrylonitrile (PAN), rayon or pitch [3]. They are the most important fibre family for high performance composites such as structural aerospace components or formula one. Industrially, the vast majority of carbon fibres are produced from PAN [11]. PAN is a thermoplastic fibre that decomposes before it melts (decomposition temperature: 366 °C); for this reason it has to be heat stabilised before it can be subjected to the high temperatures required for carbon fibre production (see Figure 1.4). The carbonised PAN shown in Figure 1.4 undergoes a further graphitisation step (up to 3000 °C under an inert atmosphere) in which the graphitic layers (developed during carbonisation) rearrange into structures similar to graphite (*i.e.* defects in the polyaromatic layers heal) [11].

Different grades of carbon fibre are available (such as high modulus) due to the different precursors but also due to variations in the process. As the graphitisation temperature is increased, the amount of remaining oxygen, nitrogen and hydrogen decreases. This in turn leads to a reduction in the strength of the fibres along with an increase in Young's modulus, density and thermal conductivity.

The surface of the carbon fibres is usually oxidized in order to promote adhesion to matrix resins. Industrially this is typically done in aqueous solution using anodic oxidation [11].

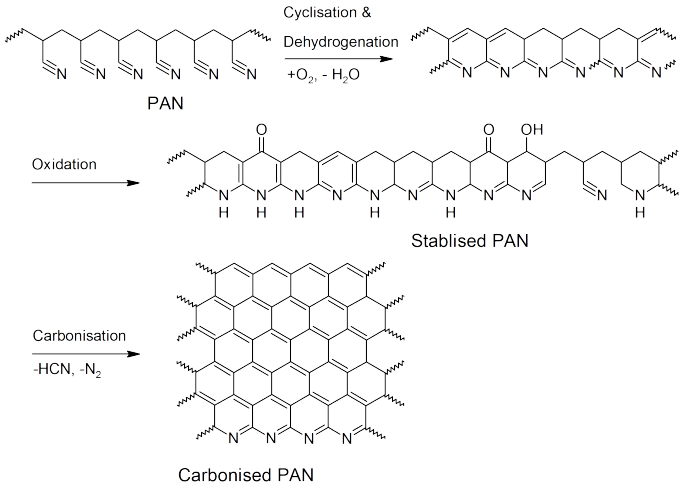

Figure 1.4: An idealised scheme showing the production of carbonised PAN from PAN fibres. The cyclisation, dehydrogenation and oxidation steps are done in an oxidising atmosphere with a residence time of 1-2 hours at 197 °C to 287 °C. The carbonisation step is done in an inert atmosphere at >527 °C [11].

1.3.2.3 Aramid Fibres

Aramid fibres are lightweight polymeric materials with good thermal stability and toughness and consists of aromatic rings and alternating amide linkages, these go by the trade names 'Kevlar', 'Nomex' and 'Twaron'. The chemical structure of a kevlar fibre is shown in Figure 1.5. The π-electrons are conjugated between the amide chain and the benzene rings which gives double bond character to all the main chain and the regular structure gives high degrees of crystallinity. Despite their excellent physical properties the aramid fibres can sometimes suffer from lack of adhesion to matrix resins despite attempts at surface coating [3]. They are generally used where impact resistance is required.

1.3.2.4 Reinforcement Summary

A summary of the properties of selected fibre reinforcements is given in Table 1.2.

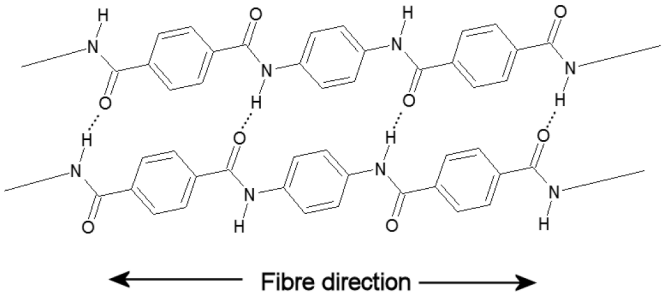

Figure 1.5: The chemical structure of a Kevlar aramid fibre [3]. In the fibre direction the polymer chain is held together with strong amide bonds, in the transverse direction the neighboring chains are held together with hydrogen bonds and van der Waals' forces which are comparatively weak.

Table 1.2: Properties of selected reinforcements.

Type of Fibre	Density (ρ)	Tensile strength ($\sigma_{\max}$)	Tensile modulus (E)	Extension (%)
	$\mathrm{g\,cm^{-3}}$	GPa	GPa	
Carbon fibre (HM) [a]	1.8	2.6 - 4.7	345 - 590	0.6 - 1.4
Carbon fibre (HS) [a]	1.8	3.3 - 3.3	230 - 300	1.5 - 2.2
Kevlar 149 [b]	1.47	3.4	186	1.9
S-glass [a]	2.49	3.1	86	4
E-glass [a]	2.56	2.4	70	3.5

[a] [12] ,[b] [3]

1.3.3 Typical Composite Mechanical Properties

A summary of the mechanical properties of several composites is given in Table 1.3 compared to mild steel. The specific properties show how much stronger and stiffer most composites are by weight; this is particularly important in transport or aerospace applications where additional weight leads to additional fuel consumption.

Table 1.3: Example properties of selected polymer composites.

Material	Density (ρ)	Tensile strength ($\sigma_{\max}$)	Tensile modulus (E)	Specific Strength ($\frac{\sigma_t}{\rho}$)	Specific Modulus (E/ρ)
	$\mathrm{g\,cm^{-3}}$	MPa	GPa	$\mathrm{kN\,m\,kg^{-1}}$	$\mathrm{MN\,m\,kg^{-1}}$
Orthotropic carbon + epoxy [a]	1.55	1550	137.8	1000	89
Orthotropic aramid + epoxy [a]	1.38	1378	75.8	999	55
Orthotropic e-glass + epoxy [a]	1.85	965	39.2	522	21
Quasi-isotropic carbon + epoxy [a]	1.55	579	45.5	374	29
Woven glass + phenolic [c]	1.5	300 - 400	16 - 20	200 - 266	10.6 - 13.3
Woven glass + UPR [b]	1.7	250	14	147	7.7
Random glass + epoxy [a]	1.85	100	8.5	54	5
Random glass + UPR [b]	1.5	100	7.5	66	5
Mild Steel [a]	7.85	410	210	52	27

[a] [13], [b] [12], [c] [14]

1.3.4 Non-Destructive Evaluation

Destructive material testing techniques are well established; the mechanical properties of materials can be evaluated to failure using a wide variety of different methods such as static tensile and bending along with dynamic mechanical response. Materials or structures can also be tested to using multiple load cycles to understand damage induced by fatigue. Crack surfaces can then be be analysed using optical or scanning electron microscopy.

In service these destructive tests are not reasonable and therefore the development of non-destructive evaluation techniques is justifiably a topic of great research interest.

1.3.4.1 Visual Inspection and 'Tap Test'

The simplest method of non-destructive evaluation (NDE) is a visual inspection of the composite surface. The fibres in the near-surface plies impart a texture that can give information about larger cracks, surface delaminations or any break in uniformity of the fibres. In the case of optically transparent composites damage can be quantified by taking digital photographs of the area followed by image analysis

software [15]. In addition, well consolidated composites should ring clearly if tapped gently with a metallic object. A muted response could be due to delaminations or invisible damage within the structure and so prompt further investigation.

1.3.4.2 Ultrasonic NDE

Within a solid, elastic waves can propagate as either primary (P) waves which are longitudinal waves consisting of compressions and rarefactions and secondary (S) waves with travel through shear effects, transverse to the direction of propagation. The velocity of P-waves can be expressed as follows for an isotropic solid [15]:

$$V_{\mathrm{p}} = \sqrt{E/\rho} \tag{1.1}$$

Where:

V_{p} is the velocity of the P-waves in $\mathrm{m\,s^{-1}}$,
E is Young's modulus in $\mathrm{N\,m^{-2}}$,
ρ is the density in $\mathrm{kg\,m^{-3}}$.

For a carbon fibre epoxy composite V_{p} is of the order of $10^4\,\mathrm{m\,s^{-1}}$ and using ultrasonic sound waves (frequency above 20 kHz) this gives a wavelength (λ) of around 1 cm (see Equation 1.2) assuming perfect acoustic coupling into the material of interest.

$$\lambda = \frac{V_{\mathrm{p}}}{f} = \frac{10^4\,\mathrm{m}\,s^{-1}}{10^6\,\mathrm{s}} = 10^{-2}\,\mathrm{m} = 1\,\mathrm{cm} \tag{1.2}$$

Where:

f is frequency in $Hz \equiv s^{-1}$.

Ultrasound for NDE is transmitted through an acoustic coupling material (usually water or gel) using a transducer in a pulse-echo mode which produces short bursts of ultrasound. Defects present below the surface of the material can reflect the wave back to the transducer where it is detected. The detection relies upon mechanical resonance within the thickness which occurs whenever the thickness is equal to $n(\frac{\lambda}{2})$ where n is an integer. By using broadband transducers (*i.e.* a large frequency range) these resonant frequencies will be present in the transmitted wave. The frequencies

will then undergo resonance in the transmitted spectrum and the reflected spectrum, this leads to destructive interference and consequently dips in the detected spectrum. If a defect is present this will reflect a portion of the incident wave and cause a characteristic set of interference dips in the detected spectrum superimposed upon the existing dips due to material thickness. The depth of the defect from the surface can be estimated from the period (T) (*i.e.* $\frac{1}{\nu}$) of the characteristic dip frequencies and the velocity of the sound in the material [16].

I.e. for a defect causing 3 dips (a fundamental and 2 harmonics):

$$d_{\mathrm{d}} = \frac{1}{2}\lambda_1 = \frac{1}{2}V_p\,T_1 \qquad d_{\mathrm{d}} = \lambda_2 = V_p\,T_2 \qquad d_{\mathrm{d}} = \frac{3}{2}\lambda_3 = \frac{3}{2}V_p\,T_3 \tag{1.3}$$

Where:

d_{d}	refers to the distance from the surface to the defect in m,
T	refers to the wave period in s,
Subscripts	1, 2 and 3 refer to dip 1, 2 and 3 respectively.

A drawback to the pulse-echo mode is that in thin composites multiple reflections or large defective areas can cause confusing superimposed spectra [17].

Another mode of operation is 'through-transmission' mode in which a separate detector is placed on the inside face of the material, in this case defects reduce the amount of transmission through the thickness compared to the surrounding area. By scanning methodically in both x and y planes it is possible to build up a two dimensional digital image of the material and its defects; this image, usually using shades of gray to indicate intensity is referred to as a 'C-Scan' [18].

The limitations of the through-transmission technique are the fact that access to both sides of the material is required and the transmission through the material has to be good. The thickness of the panel can significantly decrease transmission as polymeric systems have a damping effect on ultrasound [15]. Other limitations in using ultrasound as a method of NDE include difficulties examining heterogeneous materials or those with irregular shapes, and the requirement for experienced technicians to carry out manual scans.

Attempts have been made to remove the requirement for an acoustic coupling material in modern ultrasonic techniques by building devices capable of coupling

through the air-solid interface. The difficulty with this method is the high amount of acoustic impedance between air and the carbon fibre solid which leads to very low transmission and relies upon the mechanical resonance in the system [19].

1.3.4.3 Eddy-current Testing

Carbon-fibre composites with a high (typically 55%) fibre volume fraction are good electrical conductors; this property can be exploited as a means of testing. Eddy current is induced by moving magnetic field source or an oscillating field. Eddy current inducing proves are used, *i.e.* coils with an frequency variable A.C. current and are are placed over a block of composite. This induces characteristic eddy current within the the fibres which can be measured using a detector coil [17]. Electrical conduction occurs along the fibre and also transverse to the fibre direction due to fibre-to-fibre contacts. If the detector coil is set to be highly directional and is mechanically rotated a directional picture of the impedance can be built up which gives a clear picture of the stacking sequence in carbon fibre. Delaminations or broken fibres can be detected by missing lobes as shown in Figure 1.6. It is also possible to generate a simpler image using smaller detector coils and using the amplitude of the coil signal [20]. This approach will only work with conductive composites (*e.g.* carbon).

1.3.4.4 Radiography

Radiography using X-rays can be used to generate a good overview of foreign objects and inclusions but in lightweight materials such as polymer composites it is not easy to achieve contrast between fibre and matrix. X-radiography is not suitable for the detection of interlaminar defects and presumably delaminations [17].

Fast neutron radiography *i.e.* neutron energies of 14-15 MeV is reportedly more suitable [21]. This technique focuses a neutron beam on the polymer surface which causes, through elastic scattering, the displacement of protons which can be absorbed in a scintillation plate which produces blue-green light which can be recorded as an image. The technique gives images of damage within composites with a thickness up to 25 cm but requires expensive and bulky equipment. In addition radiography comes with inherent safety concerns about use of radiation in the field.

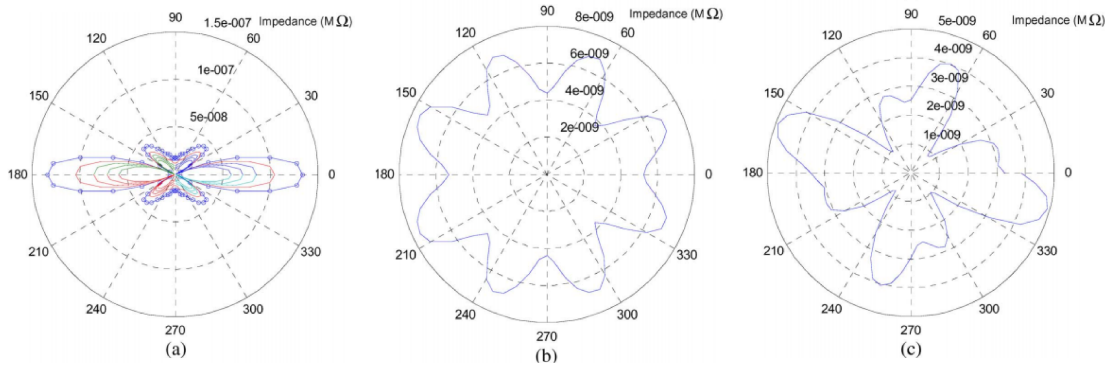

Figure 1.6: Directional measurements of impedance generated from eddy current testing on CFRP plates [20]. (a) Unidirectional layup, (b) Cross-woven laminate (0°/45°/90°/-45°), c) Sample b but impact damaged. Reprinted with kind permission © 2009 IEEE.

1.3.4.5 Infra-red Thermography

Thermography is a technique that can be applied to NDE, the concept involves the application of heat to the material surface which generates a flow of heat through the material which can be treated as a thermal wave.

This experiment has two major modes of operation. In pulsed thermography (PT) a single, rapid ($\sim$ 1 ms), pulse of heat is generated from a source such as a lamp or a heat-gun, the temperature decay is then recorded on the surface. If the material is homogeneous then the heat flow through the material should be uniform; if damage or defects are present these can interfere with heat flow and cause hot spots to develop on the surface which can be detected in the infra-red IR region [22]. Consequently a surface temperature contrast appears over time [23].

Lock-in thermography (LT) utilises a heat source, generally a tungsten-halogen flood lamp, is modulated generating sinusoidal heat waves for time periods of up to hundreds of seconds. Thermal images of the surface are continuously recorded and through post-processing the returned waves are then compared in amplitude and phase with respect to the source. Defects, due to their differing thermal properties reflect these thermal waves and so cause detectable changes in phase and amplitude [24, 25]. LT has some advantages over PT, in that the phase image generated can be used to estimate defect distance from the surface and is independent of any surface characteristics such as surface emissivity or illumination. One drawback is the need

to select suitable excitation modulation frequencies for sensitivity to defects depth [23].

1.3.4.6 Structural Health Monitoring and Self-sensing

Structural health monitoring (SHM) relates to an integrated system of sensors in an engineering structure with an aim to monitor and characterise damage. The long-term aim of SHM is to ensure a structure is serviceable after inevitable aging and degradation. In addition SHM can provide up-to-date information about damage from sources such as impacts or weather related phenomena.

SHM is a relatively mature field in civil engineering and is commonly used for long bridge spans [26, 27] but is also finding applications in areas such as aerospace [28–31] and wind turbines [32, 33].

Self-sensing is the ability of a material to sense its own damage condition using the structural material as the sensor; in this case there is no need for additional embedded or attached sensors. In composites the most common self-sensing approaches use glass fibres as optical sensors [34–36] or take advantage of the piezo-resistive nature of carbon fibres [37–41].

Self-sensing materials as part of an SHM program combined with self-healing or materials with an intrinsic repair mechanism have the potential to be a powerful combination in the next generation of smart materials. The detection and *in-situ* repair of invisible or barely visible damage will increase durability, lifetime and confidence in composite materials and consequently reduce the need for over-engineering.

1.3.5 Traditional Repair

As composites are being adopted more extensively in high value applications such as aerospace their durability, repair and maintenance is becoming a hot topic. In this section the current repair methods for polymer composites will be discussed. Currently they are time consuming and expensive repairs and are often overkill for very small areas of barely visible damage. Cole puts forward a set of basic principles that need to be followed in order to affect a successful and safe aerospace composite repair [42].

- Stiffness: Any additional material used in the repair should have a similar stiffness to the existing material. A much higher stiffness could lead to additional load transfer through the repaired region which could potentially exceed strength limits and cause failure. If the stiffness is much lower then the load can be diverted around the repair region and possibly over-stress the surrounding material.

- Strength: It is difficult to match the strength and the stiffness of the surrounding material, therefore ideally identical material and processing conditions should be used. In reality this is not always feasible, particularly if a part has been cured in an autoclave; so generally the stiffness is matched and the strength is within safety margins.

- Stability: The part must maintain its strength and stiffness under compressive loading.

- Operational Temperature: The in-service temperature of the repair has to be within the limits of the resin system used.

- Durability: A permanent repair should last the service life of the aircraft, its durability should match that of the surrounding material.

- Aerodynamic Smoothness: In order not to compromise the aircraft performance the repair must satisfy aerodynamic considerations.

Composite aerospace components in service are likely to be contaminated by a film of hydraulic fluid which is extremely hard to remove from the surface of polymers and can make repair difficult. The resin within an in-service part will have fully post-cured, possibly shrunk slightly in service and taken up some water. For this reason it is difficult to perfectly match a patch to the damaged area and the cure at high temperature may be hindered by the presence of water [15]. An ideal repair would be able to be done on site quickly and efficiently and this minimize the downtime associated with removing a part and sending it for repair.

1.3.5.1 Repair methods

Welding Welding can generally only be used with thermoplastic systems and relies upon the formation of chain entanglements between two polymer surfaces that are in intimate contact. This method of repair is only applicable to thermoset composites in the case of thermally reworkable matrices (see Section 1.4.4.1).

Injection bonding Small areas of delamination in thermoset composites are sometimes repaired by injecting liquid resin into place using a syringe but this is not suitable for more substantial areas of damage involving fibre breakage [15].

Patching and curing new resin *in-situ* Patching involves the attachment of new material via new resin, adhesives or mechanical fastenings to the damaged area. The purpose of this approach is to increase the strength by reducing the net sectional stresses [43]. In the case of mechanically fastened patches a shaped patch of cured composite or alloy is produced and literally bolted or riveted to the damaged area [15]. Mechanically fastened patches can lead to further stress concentrations around the bolt holes, therefore adhesively fastened patches are preferred.

A variation on this approach involves completely removing the damaged area first. The damaged areas are cut out using with a scarf angle as shown in Figure 1.7 and a patch is moulded which is either cured *in-situ* or hardened separately and attached using adhesive [44, 45].

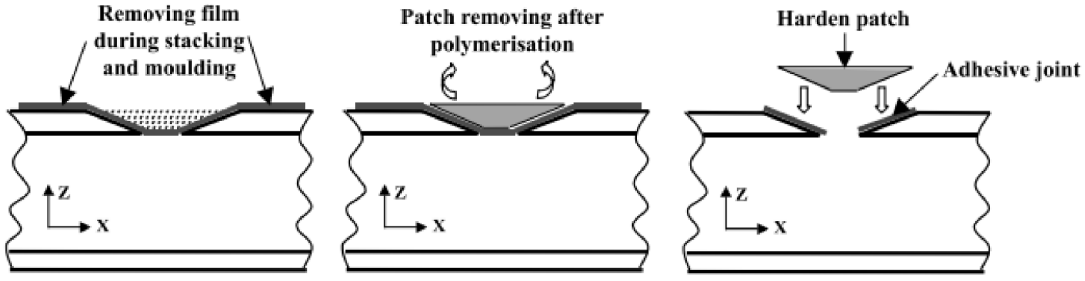

Figure 1.7: Illustration of the scarf patch procedure. Reprinted from Composite Structures [45], 53/3, T. J Chotarda, J. Pasquiet, M. L. Benzeggagh, Residual performance of scarf patch-repaired pultruded shapes initially impact damaged, 317-331, © 2001, with permission from Elsevier.

The compressive strength can be increased from 50% (unrepaired) to 80% of that of the undamaged material by using adhesively bonded patches on either side of the removed area [46].

In both adhesive bonded patches and *in-situ* resin curing techniques the interface between the old and new material is the key factor and has formed the basis of a study [47]. It was found that addition of new resin does not guarantee a good interface as the tight network structure present in the old material does not always permit adequate chain entanglements forming.

All these repair methods are moderately effective but do carry a weight penalty and can be potentially detrimental to aerodynamics as the repairs are generally heavier and bulkier than the virgin part. Improved repair methods or increases in durability are highly desirable so self-healing materials or parts with intrinsic repair functionality are exciting topics.

1.4 Self-Healing Literature Review

Self-healing in polymers and composites is a subject that has attracted a plethora of attention over the last two decades. The approaches can be split into two broad categories: those that do and do not rely upon the delivery of a liquid resin to a damage site.

1.4.1 A Note on Semantics and Comparability

It is worthwhile, before embarking on a detailed discussion of self-healing methodologies, to define exactly what is meant by a *'self-healing material'*. For the purposes of this thesis any material which has some form of built-in healing ability will be referred to as *self-healing* regardless of whether the healing requires any external intervention or activation. In the case of a material capable of self-healing without external intervention this will be referred to as *autonomic healing*. The advantages of both systems will be discussed later in Section 1.4.6 on page 46.

In most of the following discussions it is important to bare in mind that when discussing healing efficiencies most of the measurements are not standardised and are often completely different tests. When values are quoted they are intended for relative comparison within each series of studies; they can be used in order to get a feel for the healing obtained rather than an absolute value. Throughout this review section more emphasis will be put upon the underlying theory, conditions, cost and practicality of application.

1.4.2 Liquid Resin Delivery Systems

The most studied self-healing approaches rely upon the delivery of liquid resin to a damage area which is subsequently polymerised to repair the damage.

1.4.2.1 Hollow Fibres

This approach, initially applied to concrete, was first introduced to polymers by *C. Dry* in 1996 [48]. Hollow glass fibres were filled with liquid resin (a cyanoacrylate based adhesive) which upon rupture flows into damaged areas and cures *in situ*. Healing was shown to to take place over a long timescale (8-12 months). The healed

specimens were shown to impede or stop crack propagation, restore impact strength and ability to carry a load.

Motuku et al. extended the approach to S-2 glass fibre composites with epoxy and vinyl ester resin systems using a vacuum-assisted resin transfer moulding process [49]. Various parameters were varied such as the specimen thickness and the number, position and type of hollow fibres. Glass fibres were preferred over aluminium or copper tubing as they did not affect the impact characteristics of the composites. Dyed resin was used to demonstrate glass fibre fracture at small, barely visible impact damage (BVID) levels. Some problems with wetting-out of the laminates during lay-up was encountered with larger diameter fibres (1.5 to 1.6 mm) creating voids which could lead to stress-concentrations and failure; reducing the diameter (to 1.15 mm) and increasing the distance between the glass fibres was shown to reduce this effect. This work concentrated mainly on the release of resin without cure and consequently no healing results or mechanical properties are reported.

Significantly smaller glass fibres were used by *Bleay et al.* in 2001 [50] (15 μm external, 5 μm internal diameter) in a similar S-2 glass fibre composite. It was expected that the smaller fibres would also enhance rather than diminish the composite reinforcement. Some problems were encountered in the filling of the small hollow fibres due to the small diameter; a technique involving vacuum assisted capillary action helped somewhat when steps were taken to reduce resin viscosity by dilution. A one part cyanoacrylate resin system proved unsuccessful with the small diameter fibres due to the fast cure rate of the resin blocking the ends of the capillaries. A two part epoxy resin system incorporating resin into the 0° plies and hardener into the 90° plies proved successful but the authors suggested that using a slightly larger diameter fibre (40 to 50 μm) would be a necessary compromise between increasing resin flow rates and reducing voids into the composite.

Studies at the University of Bristol in 1995 by *Pang and Bond* used the hollow fibre approach with a focus on aerospace application, in particular interest is the the repair of barely visible impact damage (BVID) and delaminations [51, 52]. 60 μm glass fibres were produced in-house and integrated into epoxy composites. As with the work by *Bleay et al.* a 2 component system is used with uncured resin in the 0° layers and hardener into the 90° layers. An interesting idea presented in this work was the integration of a UV fluorescent dye into the healing agent which could assist

damage detection. In an attempt to study the shelf-life of the composites a vast decrease was noted over a 9-week period, after 9 weeks the composites proved to be incapable of self-repair. The authors argue that with optimisation the the shelf-life of the composites can be extended but in an application such as aerospace where composites are expected to have a service life of many years this would require vast improvement to be of practical use.

In 2007 this work was extended to carbon-fibre composites by the same group; hollow glass fibres were inserted within a carbon-fibre reinforced composite. A significant proportion of the virgin strength was restored (as measured using 4-point flexural testing)[53, 54].

In order for this hollow fibre approach to be successful additional research is required in several areas. Better compatibility is needed with carbon fibre reinforced composites than is available with glass fibres. The shelf-life of the healing agents when embedded within matrices needs to be improved and studied before it could be considered for use in long lifetime applications. In addition capillary filling methods need to be improved and reliable methodology established for the placing of the fibres in large scale operations.

1.4.2.2 Microencapsulation

Microencapsulation is a related approach in which hollow fibres as a liquid resin delivery system are replaced by fragile microcapsules made from, amongst other things, polyoxymethylene urea. The vast majority of the studies involve some form of cyclic diene and a ring opening metathesis polymerisation (ROMP) reaction. The most common reagents encountered are dicyclopentadiene (DCPD) and Grubbs' catalyst (benzylidene-bis(tricyclohexylphosphine)dichlororuthenium). DCPD can polymerize on contact with Grubbs' catalyst to form a dense crosslinked structure (as shown in Figure 1.8). The driving force behind this reaction is the release of the ring strain in the DCPD which is balanced against an entropic penalty associated with a more ordered system. Typical successful conditions for ROMP are high monomer concentrations at a low temperature [55]. For these reasons it is a useful reaction to employ with a liquid monomer at room temperature for autonomic self-healing.

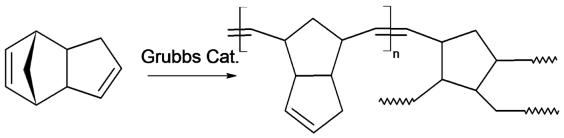

Figure 1.8: Illustration showing how DCPD can form a crosslinked structure through a ROMP reaction.

In 2002 *Kessler* argued that in order to realise microencapsulation as a strategy for self-healing four steps are required: *storage, release, transport and* rebonding [56]. The healing agent is *stored* in microcapsules that are dispersed within the matrix of the composite during manufacturing. The healing agent is *released* by the tip of a propagating crack rupturing the capsule wall. The crack is filled by healing agent, *transported* by capillary action and/or crack closure and makes contact with dispersed catalyst. The final step is the polymerisation of the healing agent and *rebonding* the crack faces back together as shown in Figure 1.9.

In the original work by a group at the University of Illinois at Urbana-Champaign, the microcapsules themselves were created *in situ* by polymerisation around an agitated oil-in-water emulsion of DCPD with an average droplet size of 200 μm [58]. The size of the microcapsules can be adjusted from 10 - 1000 μm simply by varying the agitation rate [59]. The microcapsules are removed by filtration and 10% by weight are added along with ground-up Grubbs' catalyst (2.5%) to the resin. The addition of the microcapsules and DCPD appeared to increase epoxy resin toughness [60] and showed an average healing efficiency of around 60% in fracture tests [61].

The same resin system was then used to create carbon-fibre reinforced epoxy composites using a hand lay-up technique [62]. 48 hours healing at room temperature yielded an average healing efficiency of 38% for the composites although this was shown to increase to 66% if heated to 80 °C. Testing was using width-tapered double cantilever beam fracture specimens which have a delamination introduced mid-plane and allowed to heal.

The catalyst used is available in a variety of different morphologies, which can effect the dissolution of the catalyst; as the dissolution of the catalyst determines its availability for the ROMP reaction, the morphology can also influence the healing ability of the material. Larger crystals have poor dissolution kinetics, whereas smaller crystals have lower thermal stability (as low as 90 °C) and are more likely to be

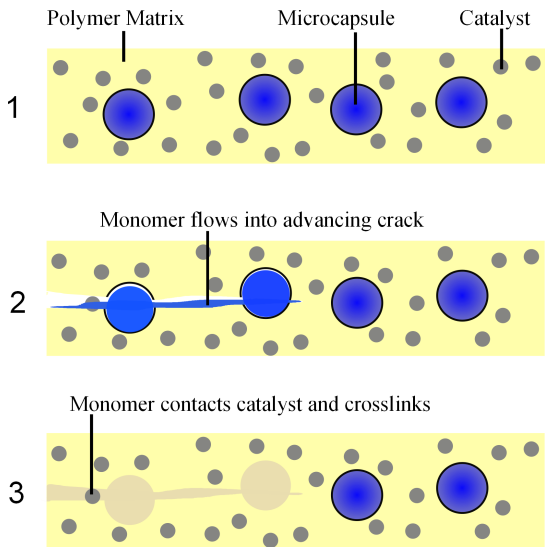

Figure 1.9: The microencapsulation self-healing concept, [57].

deactivated by amine curing agents used for epoxy composite manufacture [63]. In fact the thermal stability of the first generation Grubbs' catalyst is a considerable hindrance to the manufacturing applications of this technology because even the larger crystals are only stable to around 120 - 140 °C.

Rule et al. managed to reduce the amount of catalyst loading (0.25%) by increasing it's efficiency; deactivation of the catalyst by amine curing agents was reduced by containing it within wax microspheres that are soluble in the repair resin system used [64].

X. Liu et al. attempted to improve the system by changing or blending the monomer with 5-ethylidene-2-norbornene (ENB), see Figure 1.10, [65]. ENB when polymerised alone forms as linear polymer as the pedant unsaturation is not polymerised; as such it possesses inferior mechanical properties to that of DCPD but it has a faster rate of polymerisation. Through estimates of gelation and vitrification points using dynamic mechanical analysis (DMA) it was found that a ratio of DCPD : ENB of 3:1, yielded optimum cure rate, without significant loss of strength; presumably through the two active unsaturation sites on the DCPD allowing the entire system to form a crosslinked thermoset. The blending of ENB into the system also changed the freezing behavior of DCPD (normally around 15 °C) which would otherwise inhibit cure behaviour at low temperatures. At the time of writing no

published work has yet applied this blend to a healable resin or composite.

An alternative attempt to improved the monomer was put forward by *Mauldin et al.* who investigated the use of exo isomer of DCPD as an an alternative to the commonly used endo version [66]. It was found that exo-DCPD is has considerably faster kinetics (for steric reasons) and consequently allowed the reaction to proceed efficiently at low temperatures; the healing efficiencies 30% in these specimens, however, were lower. The authors suggested this was due to rapid polymerisation around and consequently, the immobilisation of the catalyst. A blend of 40% exo DCPD with endo DCPD showed to have the optimum healing efficiency and faster kinetics allowing the catalyst loading to be reduced to 0.25%. The faster kinetic system was shown to have significant healing ability at sub ambient temperatures.

Blaiszik et al. in 2008 produced sub-micro capsules (as small as 220 nm) using a sonification and a ultra-hydrophobe technique [67]; the microcapsules were stable up to around 150 °C (just below the boiling point of DCPD). The aim was to produce a material with more responsive healing properties that will heal the smallest of damage and to widen the application of the microencapsulation technology to thin films, coatings and adhesives where larger particles were and unsuitable.

An alternative microencapsulation approach was reported by *Cho et al.* in 2006 in which the catalyst is encapsulated and the healing agent is phase-separated in a vinyl-ester matrix [68]. The healing involves a poly condensation reaction between hydroxy end functionalised polydimethylsiloxane and polydiethoxysiloxane monomers in the presence of an organotin catalyst: di-*n*-butyltin di-laurate. The authors claim several advantages over the DCPD monomer system, in particular, the tolerance of wet or humid environments; elevated temperatures and ease of manufacture. This system, however, showed a maximum healing efficiency of 46%, lower than the reported healing efficiencies of the DCPD/Grubbs system.

Unlike the incorporation of hollow glass fibres the microcapsules do not have a structural role in the composite and the liquid resin is also not contributing to the

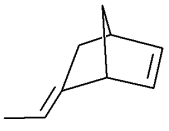

Figure 1.10: 5-ethylidene-2-norbornene (ENB) an alternative diene to DCPD.

structure. Li *et. al.* 2013 [69] showed that the inclusion of microcapsules into an epoxy resin significantly reduces the tensile strength compared to the neat resin and that smaller diameter microcapsules lead to increases in toughness but a further reduction in tensile strength. Li *et. al.* did not explicitly report the changes in tensile modulus caused by the inclusion of the microcapsules but the example stress-strain curves reported appear to show a reduction to *c.a.* 50% of the virgin modulus after inclusion of the smallest diameter microcapsules (mean diameter 36 μm). The toughness increase has already been previously noted [60]; this is analogous to the toughening observed with the inclusion of thermoplastic particles or films within thermoset matrices which is already well studied [70–74].

As with the hollow glass fibre approach, the main factor preventing this technique finding widespread application in structural parts is the fact that any liquid resin will have a limited shelf-life and there is no guarantee that the microcapsules will rupture at the right time. In addition there is a finite amount of healing resin available; therefore repeated healing in the same local area is not viable.

1.4.2.3 Microvascular Networks

Microvascular networks take the bio-inspiration of the previously discussed hollow fibre composites to the next level by connecting the channels together in a 2-dimensional or 3-dimensional structure [75] (See Figure 1.11) . This approach aims to mimic the natural vasculature in animals, plants, trees *etc.* to deliver liquid resin to a damage site. The concept behind these systems is the introduction of microchannels with a variable diameter (from 1 micron to 1 mm) [76]. The microchannels can be introduced into a polymer, composite or coating. Capillary forces can be used to distribute liquid around the network or external pumps can be used.

Some authors also propose the use of the vascular networks for a variety of tasks what are not just limited to self healing such as thermal management, electrical conductivity or electromagnetic cloaking [77].

The idea of using vascular networks for healing of polymers was suggested by Toohey *et al.* in 2007 as a method of overcoming the lack of repeated healing that was a result of the microencapsulation approach [78].

There are several methods used for introducing vasculature into a composite system. Some examples are:

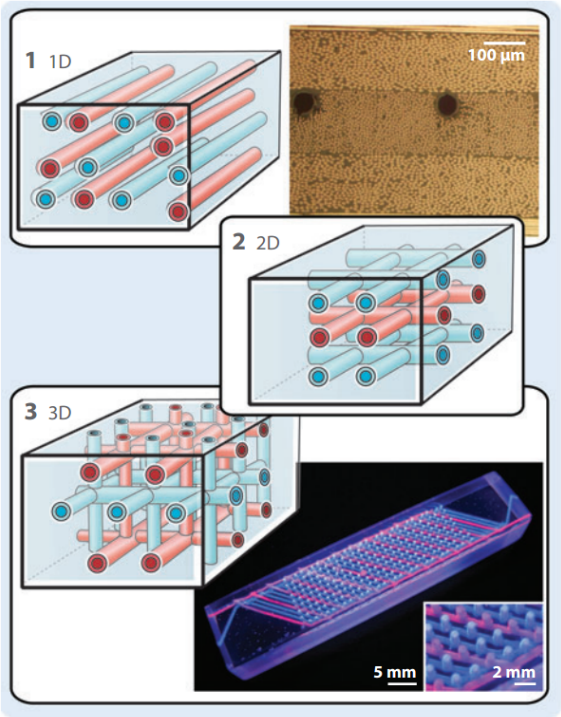

Figure 1.11: Example microvascular network architectures: 1) 1-dimensional network 2) 2-dimension network, 3) 3-dimensional network. Reprinted from Blaiszik *et al.* [75] with permission. Copyright © 2010, Annual Reviews.

- Sacrificial fibres (*e.g.* tin oxalate catalysed poly lactic acid) that can be woven amongst reinforcing fibres, manufactured into composites and then thermally decomposed into gaseous components [77].
- PTFE-coated steel wires can be placed within a composite before cure and removed mechanically [79].
- Fugitive inks (which can be later removed) can be shaped into a 3d scaffold using direct-write fabrication techniques followed by resin infusion [80, 81].

In an attempt to mimic hardwood architectures without compromising mechanical properties or adding additional mass Trask and Bond set about producing composites with vascular networks that are misaligned with the local reinforcing fibres [82]. The vascules were introduced by the inclusion of a low melting point solder which was removed from the composites by heating to 190°C and evacuating by vacuum. It was found that the inclusion of the solder wires during cure lead to resin rich

pockets around the channels and corresponding porous regions elsewhere. The results indicated that in terms of compression the inclusion of aligned channels had a negligible impact however the misaligned channels reduced the compression strength by 10%. The specimens were not tested in tension or flexture; in this case it may be that the aligned vascular channels are considerably detrimental as reinforcing fibres are effectively displaced.

The following year Huang *et al.* showed the effect of increasing vascular diameter on compressive properties; a 13% reduction was observed for an 80 μm vascular network and up to a 70% reduction for the inclusion of a vascular network with a diameter of 0.5 mm [83]. An attempt has also been made to detect damage by the loss of pressure in the vascules by the addition of low pressure sensor attached to the system [79].

Hansen *et al.* reduced the cure time in two part epoxy systems by introducing a third vasculature through which a temperature controlling fluid could be pumped [84]. This seems somewhat unnecessary as it would be more convenient (at least in carbon composites) to heat via a resistive method as this would not require further vasculature.

The methodology has also been applied to sandwich panel composites.

Williams *et al.* produced sandwich panels with vasculature within the foam core using channels down the mid-plane of the foam and drilled vertical risers [85]. Almost 100% recovery in flexural strength after impact damage was obtained when premixed epoxy and hardener were infiltrated using a syringe without any significant reduction in flexural properties compared to the control. The inclusion of the channels and risers did however produce a 25% mass penalty. Attempts to produce an autonomous version by using separate channels and risers for epoxy and hardener were partially successful as healing was observed in approximately half the samples (those that healed showed excellent property recovery).

Proposing the argument that the mid-plane of the sandwich panels is not the most efficient place for resin distribution C. Chen *et al.* [86] produced sandwich panels with a vascular interlayer between the foam core and a glass-epoxy face sheet. The vascular network contained alternating resin and hardener channels with an aim to repair damage when cracks allow the channels to mix. Good recovery in stiffness was obtained but the face sheets were not adequately re-bonded to the

core after an edgewise compression test and all the mechanical properties suffered significantly after inclusion of the epoxy interlayer.

The vascular network on the whole has the potential to allow multiple healing events with excellent recovery in properties and without shelf-life issues as fresh healing agent could be pumped into the network. If the channels are maintained in a filled state to allow for autonomic healing the same potential lifetime issues are encountered as with the other liquid resin approaches unless the vascules are periodically drained and replenished. On the other hand the inclusion of empty channels within high performance materials as a viable approach is somewhat unconvincing when considering that industries such as aerospace go through expensive steps of periodic debulking and autoclave cure in order to reduce void content. In addition over the lifetime of a material it is likely that microchannels such as these might become blocked and unusable.

1.4.3 Solid Solution Approach

The methods discussed in the previous section are all different ways of delivering a liquid healing agent to a damage area in which it can cure. In an approach pioneered by Jones and Hayes *et. al.* at the University of Sheffield [1, 2] a linear polymer healing agent is used instead of a liquid resin. The method involves dissolving a thermoplastic within a thermosetting resin (specifically selected to be compatible with each other.) The principle is that upon heating it is reported that the linear polymer is capable of diffusing via a reptation mechanism through the matrix in order to bridge cracks and small gaps. The technology has so far been applied to epoxy resin systems, specifically diglycidylethers of bisphenol A as discussed in Section 1.3.1.3. The thermoplastic selected is polybisphenol-A-co-epichlorohydrin with an M_w of 44,000 g mol^{-1}

The resin matrix (including 20% thermoplastic additive) was subjected to compact tension testing after healing over a range of temperatures (100 - 140 °C) with a recovery of between 40 - 60% of the virgin strength [2]. Using impact testing the resin matrix showed a recovery of 65% was archived with an optimum 7.5% healing agent [1]. Composites were manufactured using a hand lay-up procedure and the

healable resin system. Impact damage in glass-fibre composites was shown to visually reduce by 30% after healing; therefore this system should be suitable to repair microcracks.

Within the papers the requirements for the healing agent are stated:

1. It must be reversibly bonded to the matrix, perhaps through hydrogen bonding below the minimum healing temperature in order to limit the effect of the healing agent on the mechanical properties of the system.

2. It must become mobile above the minimum healing temperature in order to diffuse across hairline cracks.

3. The addition of the healing agent should not significant reduce the mechanical properties of the material.

The main advantages of this approach over the competing systems is its compatibility with existing manufacturing techniques and resins which would be highly preferable for aerospace in particular where approval of new resin systems is problematic. There is unlikely to be any problems with the lifetime of the healing agent as there is no liquid resin within the composites but work by Jamil and Jones suggests that the healing efficiency of the system decreases with the physical aging of the epoxy matrix [87, 88].

The disadvantages of the system include the inability to heal larger, open, fractures as in order for the thermoplastic to diffuse, the surfaces must be in contact. Another arguable disadvantage of the system is the requirement of manual intervention (in the form of heating) in order for the healing to take place means that the system is not currently autonomous. With advances in self-sensing through carbon fibre resistance measurements (discussed in Section 1.3.4.6 on page 17) an autonomous system is feasible if required as the carbon fibres could not only provide a conduit for damage detection but also a localised heating element.

1.4.4 Polymers with Reformable Covalent Bonds

For the overwhelming majority of engineering polymers the backbone and crosslinks (for a thermoset) are made up of covalent bonds therefore it is not surprising there

is a plethora of research into the disconnection and reformation of such bonds. This section will discuss some of this recent research.

In order to disconnect and reform a covalent bond typically a stimuli is needed in order to activate the healing, such as heat, light, solvent, pH, *etc* which pushes the equilibrium towards depolymerisation. Raising the temperature (perhaps locally) also has the added advantage of increasing the reaction rate simultaneously. If the material is likely to approach the healing temperatures in service this will be an application limitation as the most probable result will be undesirable deformation or certainly excessive creep. Another issue worth considering for all systems relying on a chemical equilibrium to disconnect and reform covalent bonds is the affect of solvents on the polymer [89]. Theoretically if the smaller 'disconnected' molecule is soluble then the equilibrium could be driven towards depolymerisation by the presence of a solvent. This would be a limitation if the solvent is likely to come into contact with the part in-service but if not it could be utilised to allow reprocessing of the polymer or even to initiate repair.

1.4.4.1 Diels-Alder Systems

Thermally re-workable polymers are polymeric systems that can revert back to a monomeric, oligomeric or non-crosslinked state [90]. This is useful for self-healing because the backwards reaction can result in a completely healed state at a molecular level. One of the first approaches involving breaking and re-forming of covalent bonds was pioneered by *Chen et al.* [91]. A transparent polymeric material was developed with the ability to break and reform (around 30%) chemical crosslinks upon the application of heat (120 °C). The beauty of this approach in particular is that the healing is entirely intrinsic to the matrix; no other resins, polymers or catalysts are required. A theoretical unlimited amount of healing cycles are possible as there is no material to be depleted. As the bond strength between the diene and the dieneophile will generally be weaker than the rest of the covalent bonds in the material their presence should direct crack propagation and allow later crack repair.

This first incarnation of thermally reworkable thermosets uses Diels-Alder (DA) chemistry to produce a crosslinked co-polymer between furan and maleimide based monomers as shown in Figure 1.12. During cooling the furan moiety behaves as a

diene while the maleimide moiety behaves as a dieneophile in a [4 + 2] cycloaddition; the reverse (r-DA) reaction occurs on heating.

The material produced (4M3F) contained a monomer with 4 maleimide moieties and a monomer with 3 furan moieties and was reported to have similar mechanical properties to commercial epoxy resins although displayed some yellow colouring. Healing efficiencies for fracture load recovery tests were of 41% rising to 50% at 150 °C. Healing was accomplished under a nitrogen atmosphere although it is not stated whether this is crucial.

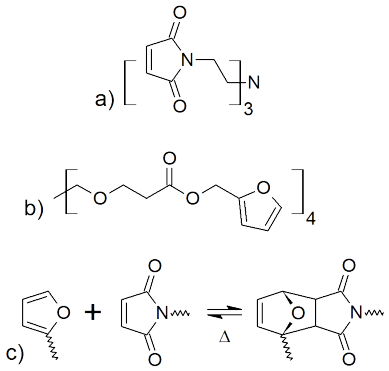

Figure 1.12: Thermally reworkable thermosets as first proposed by Chen. et al. in 2003. a) Maleimide moeity b) Furan moeity c) [4+2] Cycloaddition. Diels-Alder and rDiels-Alder reaction of polymer with pendant side chains as reported by *C*hen *et. al.* [92].

The following year the polymer was improved using different maleimide based monomers. For example using 1,8-Bis(maleimido)-1-ethylpropane (Figure 1.13) results in the transparent, harder colourless polymer (2MEP4F) [91] which was capable of a fracture healing efficiency of around 80% but not directly comparable as a different test method was used. The drawback of these system id mainly the relatively low working temperatures; the material will fail above around (120 °C) due to the depolymerisation but at low temperature the glass transition. In addition the resins are extremely costly to synthesise compared to traditional epoxy resins.

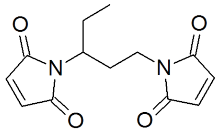

Figure 1.13: 2MEP Monomer.

The work was extended by Liu and Hsich [93] using the same principle but using more 'epoxy-like' monomers in order to utilise the thermal and electrical characteristics and the solvent and chemical resistance of epoxy resins. The healing ability was not quantified but a fissure introduced by a knife was completely visually healed after a 24h treatment cycle; this shows proof of concept. The approach was also extended to polyamides by the same group [94] and to a new class of thermally de-crosslinking polyketones by *Zhang et al.* [95, 96].

Another variation on the approach uses modified polyketones by adding pendant furan groups and crosslinking using bis-maleimide to form thermally reversible crosslinks as shown in Figure 1.14. The advantage of such a system could be that the main chain of the polymers are not self-healing, and therefore not required to have any sacrificial or weak bonds. The reported mechanical strength (40 to 100 MPa) and modulus (4 GPa) derived from the three point bending tests suggests that the mechanical performance is encouraging before and after healing [96].

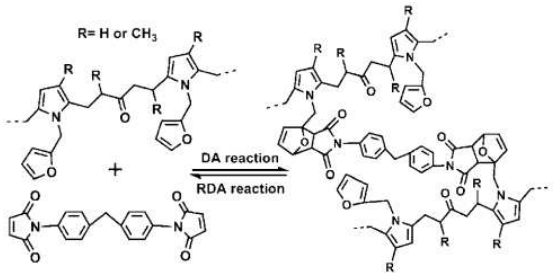

Figure 1.14: Diels-Alder and rDiels-Alder reaction of polymer with pendant side chains. Reprinted (adapted) with permission from [96] Copyright 2009 American Chemical Society.

More recently the r-DA concept has been modified further to work with a single component system based upon dicyclopentadiene (DCPD) which is a much lower cost precursor compared to the to furan and maleimide based monomers [97, 98]. The work centres on the dimerisation reaction of cyclopentadiene (acting as both diene and dienophile) to dicyclopentadiene which exists as an equilibrium. A monomer can be produced by linking opposite ends of dicyclopentadiene via an aliphatic chain. The resultant polymers were only tested in compression and fracture healing and show a lower compressive strength (85 to 95 MPa) compared to cast epoxy (>120

MPa), however, they were able to completely regain this upon healing multiple healing cycles. In terms of fracture strength the polymers were able to regain between 20 and 60 %. The healing cycles required heating to 120 °C under an argon atmosphere, it is not made clear whether the lack of an argon atmosphere would inhibit healing or simply reduce efficiency*. This is not necessarily a huge drawback as the industry is quite familiar with vacuum bagging and autoclaves.

Upon heating the monomer can undergo a r-DA reaction which causes a disconnection in the dicyclopentadiene unit (Figure 1.15). Upon slow cooling an intermolecular Diels-Alder reaction can take place in which the cyclopentadiene end groups can react to form a polymer network, an example trimer is shown in Figure 1.16.

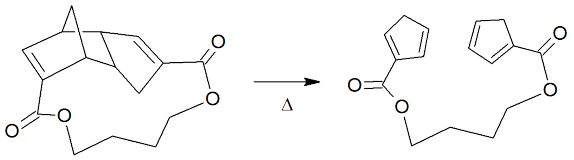

Figure 1.15: The rDA reaction of the monomer unit as proposed by Murphy *et al* [97]. Note: This has not been drawn as an equilibrium because despite the reversible nature of the Diels-Alder reaction the backwards reaction is statistically disfavoured as the intermolecular reaction dominates.

1.4.4.2 Radical Exchange Reactions

An alternative approach to Diels-Alder type chemistry was reported by *Higaki et al.* [99] using a graft polymer based upon 2,2,6,6-tetramethylpiperidine-1-oxy (TEMPO) with alcoxyamine units attached to the end and main chain. The C-O bond in the alcoxyamine junction unit is thermally unstable and can dissociate upon heating in a radical exchange reaction.

These dynamic covalent bonds will form an equilibrium which will completely reform upon cooling. The chemistry is radical in nature and can thus be applied to a variety of polymer systems [100]. In general the approach shows promise, however it requires forcing conditions for healing (anisole solution maintained at 100 °C for 24h)

*I discussed this point with Prof. Wudl on his visit to the University of Sheffield on 7th April 2011 and he maintained that the argon atmosphere is not necessary. Apparently the apparatus attached to their double manifold was the most convenient way to control the heating and this happened to be set up with argon.

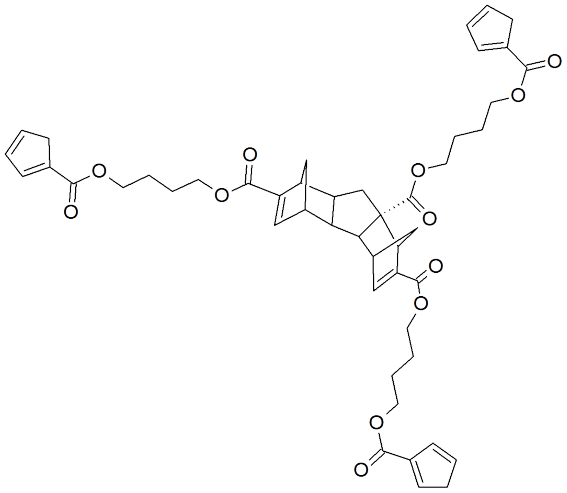

Figure 1.16: A trimer which will form part of a polymer network based on x-ray crystal structures of the same functional unit in crude Thiele's acid [97]. The cyclopentadiene end groups can react further to form the network.

so additional work is required before it is practical as an alternative to commercial resins.

Concerns have been raised about unfavourable termination reactions for radical self-healing systems that limit the long-term reversibility of the systems [89].

1.4.4.3 Transesterification

So far all the covalent bond reforming approaches rely on the manipulation of a chemical equilibrium. By using a stimulus to change the favoured thermodynamic product, *i.e.* the position of the equilibrium, bonds can be broken and reformed. A different method is design a polymer network which has cross-links that can undergo exchange reactions at a fast rate at high temperature which enables network reorganisation but leaves the topology frozen at a low temperature. This has been done using transesterification [101] by Motarnal *et al.* [89] and later the class of material is referred to as a "vitrimer" [102]. Vitrimers have a glass transition that is much broader than that encountered in the vast majority of polymer systems which in some cases will also show a classical glass transition (T_g) at lower temperatures. Capelot *et. al.* [102] liken the glass transition effect caused by the catalysed exchange reaction (referred to as T_v) to the broad glass transition displayed by silica and other strong glass formers. The main difference between T_g and T_v, other than

the latter being broader, is that above T_v the polymer follows an Arrhenius law as opposed to a Williams—Landel—Ferry law [102]. At temperatures sufficiently above T_v the vitrimers, despite possessing a cross-linked structure and undergoing no net reduction or gain in cross-links, are capable of flowing like a viscoelastic liquid [103].

One such vitrimer was prepared with its classical T_g below room temperature, *i.e.* an elastomer [89]. It has been prepared based upon the reaction of the diglycidyl ether of bisphenol A (DGEBA) and various fatty di and trifunctional carboxilic acids using a zinc acetate catalyst. The material was found to have a modulus of 4 MPa and elongation at break of 180% at 9 MPa. Swelling experiments in trichlorobenzene at 180 °C showed that the elastomer was crosslinked as it swells but does not dissolve after 16 hours.

This approach is not limited to elastomers. In the same paper Motarnal *et al.* [89] reported that hard epoxy-like materials can be produced using an extremely simple concept. Conventional epoxy resins cured with anhydrides already contain the required ester linkages and hydroxy groups required for the transesterifcation process and require only the addition of a catalyst. A depiction of this process is given in Figure 1.17. These materials have a glass transition of 50 - 80 °C, a modulus of *c.a.* 1.8 GPa, and stress at break of *c.a.* 55 MPa at room temperature. These materials have the additional (T_v) transition above the actual glass transition of the material.

Consequently, above the T_g, the vitromer materials behave like an elastomer and at higher temperatures (above T_v) they will begin to behave like a viscoelastic liquid as the exchange reaction timescale changes by orders of magnitude. The consequence of this behaviour is a thermoset material that can be reworked at high (> 200 °C) temperatures and so can be ground up and reprocessed with minimal impact on the properties. The authors note that due to the similarities with silica glasses the material may even be able to be processed by glass-blowing techniques as there is no abrupt decrease in viscosity with temperature.

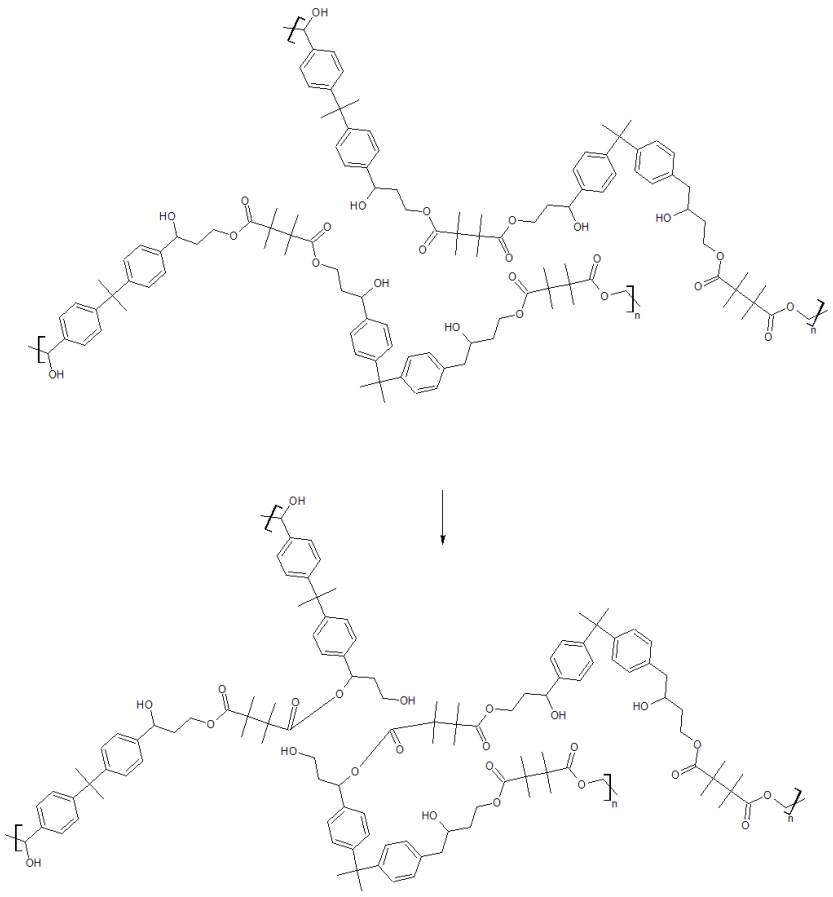

Figure 1.17: A schematic depiction of the transesterification process through which an anhydride cured epoxy can undergo network relaxation. To aid understanding some bond angles are distorted so that the other functional units can maintain their relative positions. Hydroxy groups that are present can undergo an exchange reaction with the ester groups formed. According to Motarnal *et al.* [89] with the right catalyst and temperature the timescale of this reaction can be adjusted up into a range in which the material can be reworked. It is clear that there is no net reduction in covalent bonds so solvents should not drive this process.

In terms of vitromer use as a matrix for self-healing composites no work has yet been reported, the class of materials have yet to attract much research effort outside the original research group. What is likely to be critical to the success of the vitromers is how the material perform under creep tests as it is possible that the inclusion of such a catalyst designed to speed up transesterification will cause unwanted topology rearrangements over the lifetime of a composite part at real service temperatures. One important reason for using thermoset composites in structural applications is their low creep, therefore a self-healing functionality

should not be introduced into the material at the expense of this property.

1.4.4.4 Carbonate Bond Reforming

Another covalent bond of possible interest is the carbonate bond in polycarbonates (PC). PC can suffer from deterioration of its properties due to the thermal degradation or hydrolysis of the carbonate bond. *Takeda et al.* [104, 105] found that reduction in properties and molecular weight due to hydrolysis could be repaired by drying and subsequently heating (130 °C), with sodium carbonate, under nitrogen. It was suggested that the phenoxy end groups (created by the hydrolysis) undergoes substitution with sodium carbonate which then attacks a main chain end (eliminating phenol) as in Figure 1.18.

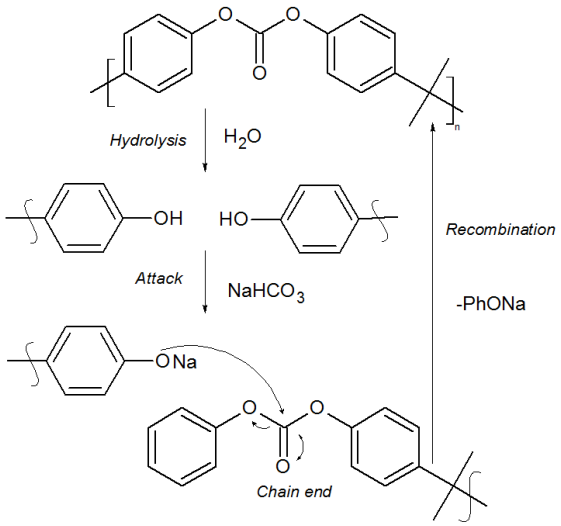

Figure 1.18: Degradation and subsequent recombination reaction of a polycarbonate polymer.

This increase in the molecular weight has a direct implication in properties due to the strong relationship between tensile strength and molecular weight in polycarbonates. After hydrolysis the tensile strength of the material reduced to 90% of the original value and improved back to around 98% after healing. Another polymer studied in the same work is poly(phenylene ether) which can be healed using a catalytic cycle involving a copper (II) catalyst.

1.4.5 Supramolecular Chemistry

Supramolecular chemistry is a branch of chemistry focussing on constructing systems from smaller subunits or components generally held together with weaker non-covalent interactions. Concepts pioneered by supramolecular chemists on small molecules can be applied to polymeric systems in order to tailor intermolecular and intramolecular forces between chain segments and gain some control over the morphology. An understanding of hydrogen bonding in particular between polymer chains is important to understand the driving force and mobility of the linear polymer in the solid solution approach (Section 1.4.3). It is also worth considering whether it is possible to construct a polymer matrix containing non-covalent bonds which could break and reform preferentially. These ideas will be discussed in the following section.

The primary structure of polymers is dominated by covalent interactions in which atoms are held together by the sharing of electron pairs. The conformation of polymer chains is often dependent upon non-covalent interactions, for example the folding of DNA into it's characteristic double helix. The energy of a typical single covalent bond is of the order 350 kJ mol^{-1} and can rise up to 942 kJ mol^{-1} for the triple bond present in dinitrogen. Non-covalent interactions usually give much weaker bonds, as low as 2 kJ mol^{-1} for dispersion forces, 20 to 40 kJ mol^{-1} for hydrogen bonding and 250 kJ mol^{-1} for ion-ion interactions [106].

The principle of the hydrogen bond was first brought into mainstream acceptance by Pauling in his 1939 book [107] and is defined as 'A chemical bond in which a hydrogen atom is attracted to an electronegative atom.' This definition could perhaps be expanded with modern examples to a hydrogen atom attracted to an area of electron density. The classical example of the hydrogen bonding is the structure of water. In water there is a bond formed between molecules through the electron poor hydrogen atom (donor) and the electronegative oxygen atom (acceptor). As outlined in Figure 1.19, there are strong and weak highly directional hydrogen bonds along with non-conventional and less directional varieties including metal centres, dihydrogen and π interactions. The latter, however can be so weak that it is difficult to distinguish from van der Waals forces [108, 109].

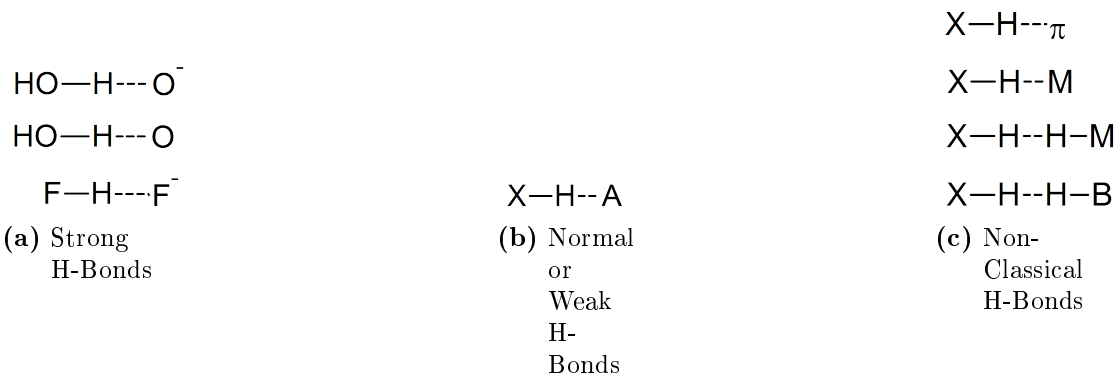

(a) Strong H-Bonds

(b) Normal or Weak H-Bonds

(c) Non-Classical H-Bonds

Figure 1.19: Different types of hydrogen bonds. Where X is usually carbon, A refers to any electronegative atom, π refers to a double bond or aromatic bond and M is a transition metal.

The hydrogen bond can occur in many different ways within polymer systems and the presence of hydrogen bonding groups within the main chain can have a large effect on ordering of the polymers which can influence crystallisation behavior and phase separation. Weak hydrogen bonding interactions can be used to enhance miscibility in two otherwise immiscible polymer systems and hence control polymer blend formation [110]. Lehn et al [111] used complementary arrays of hydrogen bonds to assemble linear 'supramolecular' polymers from small monomeric units.

1.4.5.1 Self-Healing with Hydrogen Bonds

The concept of self-assembly can apply to the formation of linear polymers and also the formation of 3d networks analogous to crosslinked structures. This could lead to self-healing matrices similar to the Diels-Alder approach discussed in Section 1.4.4.1. The hydrogen bonds would break preferentially compared to covalent bonds in the structure yet retain the ability to reform after thermal treatment.

This approach is not limited to the assembly of polymers from small molecules, the methodology can also be applied by adding complementary hydrogen bonding groups to conventional polymers which can act as pseudo cross links. Cross-linked network polymers are widely used due to their increased mechanical properties and chemical resistance compared to linear polymers. Classically the crosslinks formed are covalent bonds between different polymer chains, or different sections of the same chain, for example thermoset systems or sulphur vulcanization of natural rubber which was discovered by Charles Goodyear in 1839. Analogues of cured rubbers can now be formed by using non-covalent 'crosslinks' and heating above the glass transition temperature. Stadler [112] transformed linear polybutadinene into a thermoplastic elastomer by introducing defined hydrogen bonding donor and acceptor sites between the polymer chains.

A variation on this approach was published by Cordier [113] in which the end groups of fatty acids were modified with functional groups forming multiple hydrogen bonds. In an attempt to obtain elastomeric behaviour crystallisation is avoided by relying on mixtures of molecules with varying architectures and using fatty di and triacids that while being liquid a room temperature, form glasses on cooling. The acids are condensed with diethylene triamine and then reacted with urea to yield a mixture of oligomers which at room temperature resemble a translucent glassy plastic. This material is of particular interest because when heated to 90 °C which is above the glass transition (28 °C). At this temperature the material acts as a soft rubber with an extension at break of 350% with the ability to recover its dimensions up to 100% strain. For a conventional elastomer these properties would not be particularly inspiring; a conventional elastomer however, contains permanent covalent crosslinks that are formed in the curing process that restrict remoulding and reworking of the material. At higher temperatures (above 160 °C) Cordier's

material flows like a viscoelastic liquid and can be reworked, extruded or moulded due to the hydrogen bonding 'pseudo crosslinks' dissociating at higher temperatures. It was also found that the T_g could be lowered to sub-ambient by adding plasticisers such as dodecane or water which resulted similar properties at room temperature: large elastic deformations (up to 600%), low creep and fast relaxation times (a few seconds).

Interestingly the material also shows self-healing properties; cut strips of material placed into intimate contact would repair completely after 3 hours with the same properties as the virgin material and no visible scaring. This is only possible if the pieces are placed back together immediately after cutting. If the pieces are kept for a length of time dependent on temperature (about a week at 23 °C, 15 minutes at 90 °C) they are not able to rejoin. It is argued that the reason behind this is that the molecules reach thermal equilibrium within each side of the sample and the hydrogen bonding groups bond with each other rather than remaining free on the surface; this was confirmed using time-dependent infra-red. Water was mentioned briefly as a suitable plasticiser in that it lowers the T_g to -15 °C yet still gives 500 % elastic deformation with complete recovery, this is surprising because water might be expected to compete with hydrogen bonding and lower the physical properties.

The work by Stadler and Cordier used polymers with built-in hydrogen bonding groups attached to the main chain. An approach published by Nair *et al.* uses a simpler pendant group attached to an otherwise linear polymer. Hydrogen bonding pseudo crosslinks are obtained by adding small molecule crosslinking agents containing a pair of three or six-point complementary hydrogen bonding groups capable of bonding reversibly to the pendant groups. Dynamic mechanical measurements show the group were able to produce a both a stable elastic gel and a highly viscous liquid by adjusting the type of cross-linking agent [114].

It might be anticipated, however, that hydrogen bonded systems would be particularly susceptible to performance problems in high humidity conditions. The presence of water would most likely disrupt or interrupt the hydrogen bonding and cause similar bonding changes to that observed between nucleobases when subjected to moisture [115].

1.4.5.2 Metal Ion Mediated Systems and Ionomers

A similar approach in work by Kersey *et al.* uses a polymeric backbone as a permanent structural component and utilises metal-ligand coordination chemistry bonded to poly(ethylene glycol) (PEG) to establish reversible crosslinks [116]. This is archived by introducing pyridine pendants to the polymeric background and using bifunctional Pd(II) or Pt(II) 'pincer' compounds as illustrated in Figure 1.20.

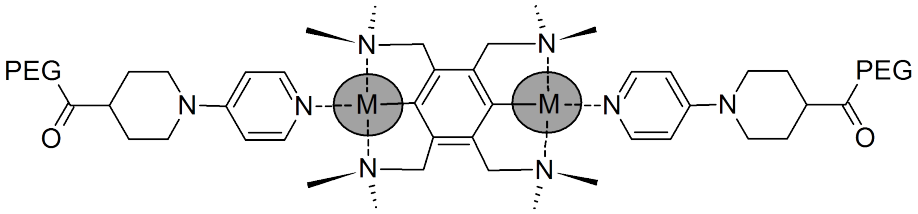

Figure 1.20: A polymeric backbone as a permanent structural component utilising metal-ligand coordination chemistry to establish reversible crosslink. M refers to the metal ion which is Pd(II) or Pt(II) and PEG refers to a polyethylene glycol chain.

A 'hybrid gel' is produced and as such this material exists with solvent rather than as a bulk material; it does, however show a proof of concept that metal ions can be used in this way. The bonding system formed is shown via single molecule force spectroscopy to bear mechanical stress, rupture and later re-associate. If it is possible to apply the same chemistry to a system in the bulk then it could be used to produce self-repairable matrices.

1.4.5.3 Self-Healing with π-π Stacking Interactions

Burattini *et al.* [117–120] reported heat activated healing in flexible polymers using supramolecular π-π stacking interactions as reversible bonding sites. The π-π stacking was shown to occur between a chain-folding electron deficient polyimide co-polymer and an electron rich pyrenyl end-capped polyamide. The pyrene based moieties were shown to form a complex within the chain folds; this interaction acts as a non-covalent thermally reversible cross-link. Perfect healing efficiency was displayed by the system as the mechanical properties of the system were repeatedly fully restored following damage and a rapid repair at 80 °C. The material was, however, not a rigid material at room temperature (elastomeric) and the stiffness was correspondingly low (tensile modulus $<$10 MPa).

In an attempt to improve the mechanical properties of the π-π system, Fox *et al.* used the same material as a matrix to produce nanocomposites reinforced with cellulose nanocrystals [121]. Fox reported that the tensile modulus was increased to 260 MPa for a 10% loading of nano-crystals while still maintaining the ability to fully heal damage (albeit at a slower rate). Loadings of above 10 wt% of cellulose nanocrystals produced phase separation and hindered the healing.

Another attempt to improve the properties of the π-π system incorporated the idea of increasing the 'supramolecular valency'. Hart *et al.* substituted the electron rich component with a trifunctional equivalent with additional pyrene moeities [122]. Hart argued based predominantly on rheological evidence that the inclusion of more π-π stacking sites reduced the distance between supramolecular crosslinks, or to put it another way, the crosslink density was increased. The mechanical properties of the material were significantly improved, however the modulus of 49 MPa and strength of c.a. 4.5 MPa are still a long way short of an engineering polymer matrix (*c.f.* >1 GPa and >40 MPa for the matrices reported in 1.1 on page 8) . Nevertheless the high healing efficiencies obtained from this line of research are very encouraging; it would be technically difficult to reach the required level of mechanical properties using non-covalent cross-links due to their relative strength but if the same concepts could be applied to produce a stiff matrix it would be a highly significant step

1.4.6 Self-Healing Summary

A wide variety of self-healing systems have been demonstrated and discussed. Capsule based systems are easily integrated into most polymer systems and hollow glass fibres are particularly suited for glass fibre composites. The microencapsulation and hollow fibre approaches both currently give the best healing efficiencies but are limited due to the local depletion of healing agent after a healing event; in addition their useful lifetime is questionable. The use of vascular networks to deliver liquid resin has has the potential for healing large damage areas repeatedly by drawing on large reservoirs of healing agent but the reduction in material performance due to the network is difficult to overcome.

Some of the intrinsic self-healing approaches such as supramolecular chemistry are highly reversible and of great academic interest but require a lot of development before they can be applied to real composite systems. The thermally reversable Diels-Alder polymers have the potential to have excellent properties and healing abilities but their cost of synthesis will limit their use as a bulk matrix.

The modification of an existing resin matrix, as outlined in Section 1.4.3 has the most potential for real world application because the healing agent is solid and load-bearing within the composite. It is for this reason that this thesis will build on the work of Hayes *et al.* [1, 2] by developing new healing agents for epoxy matrices but drawing inspiration from the Diels-Alder sytems outlined in Section 1.4.4.1 to produce a more mobile and therefore active healing agent.

1.5 References

(1) S. A. Hayes, F. R. Jones, K. Marshiya, and W. Zhang, "A self-healing thermosetting composite material", *Composites, Part A*, 2007, **38**, 1116–1120.
(Cit. on pp. 3, 30, 46.).

(2) S. A. Hayes, W. Zhang, M. Branthwaite, and F. R. Jones, "Self-healing of damage in fibre-reinforced polymer-matrix composites", *J. R. Soc., Interface*, 2007, **4**, 381–387.
(Cit. on pp. 3, 30, 46.).

(3) F. R. Jones, *Handbook of Polymer-Fibre Composites*, ed. F. R. Jones, Longman Scientific and Technical, Harlow, 1st edn., 1994.
(Cit. on pp. 5, 7–11.).

(4) H. Kramer, Polyester Resins, Unsaturated, in *Ullmann's Encyclopedia of Industrial Chemistry, Electronic Release*, Wiley-VCH, Weinheim, DE, 2012.
(Cit. on p. 5.).

(5) W. Hesse and J. Lang, Phenolic Resins, in *Ullmann's Encyclopedia of Industrial Chemistry, Electronic Release*, Wiley-VCH, Weinheim, DE, 2012.
(Cit. on p. 6.).

(6) Y. Tanaka, *Epoxy Resins Chemistry and Technology*, ed. C. A. May, Marcel Dekker, Inc., New York, 1988.
(Cit. on p. 7.).

(7) B. Ellis, *Chemistry and Technology of Epoxy Resins*, ed. B. Ellis, Blackie Academic and Professional, New York, 1993.
(Cit. on p. 7.).

(8) R. G. Weatherhead, *FRP Technologq, Fibre Reinforced Resin Systems*, Applied Science Publishers Ltd., London, 1980.
(Cit. on p. 8.).

(9) A. Bunsell and J. Renard, *Fundamentals of Fibre Reinforced Composite Materials*, Institute of Physics, London, UK, 2005.
(Cit. on p. 8.).

(10) DOW Chemical Company, *Liquid Epoxy Resins*, Published Online (Accessed 15th February 2014), 1999, `http://msdssearch.dow.com/PublishedLiteratureDOWCOM/dh_0030/0901b8038003041c.pdf`.
(Cit. on p. 8.).

(11) R. Fitzer, A. Foley, W. Frohs, T. Hauke, M. Heine, H. Jager, and S. Sitter, Fibers, 15. Carbon Fibers, in *Ullmann's Encyclopedia of Industrial Chemistry, Electronic Release*, Wiley-VCH, Weinheim, DE, 2012.
(Cit. on pp. 9, 10.).

(12) D. Kendal, *Engineering Properties, Network Group for Composites in Construction*, Available Online (Accessed 16th February 2014), `http://www.ngcc.org.uk/Information/Introduction/EngineeringProperties.aspx`.
(Cit. on pp. 11, 12.).

(13) B. Z. Jang, *Advanced Polymer Composites: Principles and Applications*, ASM International, OH, USA, 1994.
(Cit. on p. 12.).

(14) Caleb Technical Products Limited, *An Update on Phenolic Resins for use in Mass Transit, Marine, Off Shore and Construction Applications*, Available online (accessed 16th February 2014), `http://www.unitedcomposites.net/jointpages/PDFfiles/PWPaper.pdf`.
(Cit. on p. 12.).

(15) K. Ashbee, *Fundimental Principles of Fiber Reinforced Composites*, Technomic Publishing Company Inc., Lancaster, Pennsylvania, USA, 1989.
(Cit. on pp. 13, 14, 18, 19.).

(16) F. H. Chang, W. G. W. Yee, and J. C. Couchman, "Spectral analysis technique of ultrasonic ndt of advanced composite materials", *Non-Destr. Test. (Guildford, Engl.)*, 1974, **7**, 194–198.
(Cit. on p. 14.).

(17) R. Prakash, "Non-Destructive Testing of Composites", *Composites (UK)*, 1980, **11**, 217–224.
(Cit. on pp. 14, 15.).

(18) W. H. M. van Dreumel, "Ultrasonic scanning for quality control of advanced fibre composites", *NDT Int.*, 1978, **11**, 233–235.
(Cit. on p. 14.).

(19) D. K. Hsu, "Nondestructive testing using air-borne ultrasound", *Ultrasonics (Supplement)*, 2006, **44**, 1019–1024.
(Cit. on p. 15.).

(20) Y. Wuliang, P. J. Withers, U. Sharma, and A. J. Peyton, "Noncontact Characterization of Carbon-Fiber-Reinforced Plastics Using Multifrequency Eddy Current Sensors", *IEEE Trans. Instrum. Meas.*, 2009, **58**, 738–743.
(Cit. on pp. 15, 16.).

(21) K. H. Kim, R. T. Klann, and B. B. Raju, "Fast neutron radiography for composite materials evaluation and testing", *Nucl. Instrum. Methods Phys. Res., Sect. A*, 1999, **422**, 929–932.
(Cit. on p. 15.).

(22) J. R. Brown and H. R. Hamilton, "Heating methods and detection limits for infrared thermography inspection of fiber-reinforced polymer composites", *ACI Mater. J.*, 2007, **104**, 481–490.
(Cit. on p. 16.).

(23) S. Pickering and D. Almond, "Matched excitation energy comparison of the pulse and lock-in thermography NDE techniques", *NDT&E Int.*, 2008, **41**, 501–509.
(Cit. on pp. 16, 17.).

(24) W. Bai and B. S. Wong, "Evaluation of defects in composite plates under convective environments using lock-in thermography", *Meas. Sci. Technol.*, 2001, **12**, 142.
(Cit. on p. 16.).

(25) X. Maldague, F. Galmiche, and A. Ziadi, "Advances in pulsed phase thermography", *Infrared Phys. Technol.*, 2002, **43**, 175–181.
(Cit. on p. 16.).

(26) M. Modares and N. Waksmanski, "Overview of Structural Health Monitoring for Steel Bridges", *Pract. Period. Struct. Des. Constr.*, 2013, **18**, 187–191.
(Cit. on p. 17.).

(27) Roctest, *Bridge structural health monitoring*, Available Online (Accessed 16th February 2014), `http://www.roctest-group.com/applications/bridges`.
(Cit. on p. 17.).

(28) C. R. Farrar, K. Worden, N. A. J. Lieven, and G. Park, Nondestructive Evaluation of Structures, in, *Encyclopedia of Aerospace Engineering*, John Wiley & Sons, Ltd, 2010.
(Cit. on p. 17.).

(29) G. Coppotelli, P. Marzocca, and A. Behal, "Structural health monitoring techniques for aerospace applications", *Proc. - AIAA/ASME/SAE Struct., Struct. Dyn., Mater. Conf.*, 2005, **8**, 5301–5313.
(Cit. on p. 17.).

(30) T. Loutas, A. Panopoulou, D. Roulias, and V. Kostopoulos, "Intelligent health monitoring of aerospace composite structures based on dynamic strain measurements", *Expert Systems with Applications*, 2012, **39**, 8412 –8422.
(Cit. on p. 17.).

(31) K. Diamanti and C. Soutis, "Structural health monitoring techniques for aircraft composite structures", *Prog. Aeronaut. Sci.*, 2010, **46**, 342 –352.
(Cit. on p. 17.).

(32) P. Schubel, R. Crossley, E. Boateng, and J. Hutchinson, "Review of structural health and cure monitoring techniques for large wind turbine blades", *Renewable Energy*, 2013, **51**, 113 –123.
(Cit. on p. 17.).

(33) D. Adams, J. White, M. Rumsey, and C. Farrar, "Structural health monitoring of wind turbines: method and application to a HAWT", *Wind Energ.*, 2011, **14**, 603–623.
(Cit. on p. 17.).

(34) S. Hayes, D. Brooks, R. Liu, S. Vickers, and G. F. Fernando, Proc. of SPIE, 1996, vol. 2718, pp. 376–384.
(Cit. on p. 17.).

(35) S. Hayes, T. Liu, D. Brooks, S. Monteith, B. Ralph, S. Vickers, and G. F. Fernando, "In-Situ Self-Sensing Fiber-Reinforced Composites", *Smart Mater. Struct.*, 1997, **6**, 432–440.
(Cit. on p. 17.).

(36) G. Kister, B. Ralph, and G. F. Fernando, "Damage Detection in Glass Fibre-Reinforced Plastic Composites using Self-Sensing E-Glass fibres", *Smart Mater. Struct.*, 2004, **13**, 1166–1175.
(Cit. on p. 17.).

(37) L. Hou and S. A. Hayes, "A resistance-based damage location sensor for carbon-fibre composites", *Smart Mater. Struct.*, 2002, **11**, 966–969.
(Cit. on p. 17.).

(38) W. Zhang, S. A. Hayes, and F. R. Jones, Proceedings of the second international conference on self-healing materials, Chicago, IL, USA, 2009.
(Cit. on p. 17.).

(39) T. J. Swait, F. R. Jones, and S. A. Hayes, "A practical structural health monitoring system for carbon fibre reinforced composite based on electrical resistance", *Compos. Sci. Technol.*, 2012, **72**, 1515 –1523.
(Cit. on p. 17.).

(40) T. Abbasian, E. J. Fleet, T. J. Swait, and S. A. Hayes, "Development of a low-cost, light-weight damage sensor for glass-fibre reinforced composites", *Manuscript in Preparation*, 2014.
(Cit. on p. 17.).

(41) D. D. L. Chung and S. Wang, "Self-Sening of Damage and Strain in Carbon Fiber Polymer-Matrix Structural Composites by Elecrical Resistance Measurement", *Polm. & Polym. Compos.*, 2003, **11**, 515–525.
(Cit. on p. 17.).

(42) W. F. Cole, "Technical justification of repairs to composite laminates", *Int. J. Adhes. Adhes.*, 1999, **19**, 107–120.
(Cit. on p. 17.).

(43) J. Paul and R. Jones, "Repair of impact damaged composites", *Eng. Fract. Mech.*, 1992, **41**, 127–141.
(Cit. on p. 19.).

(44) H. Zhang, J. Motipalli, Y. C. Lam, and A. Baker, "Experimental and finite element analyses on the post-buckling behaviour of repaired composite panels", *Composites, Part A*, 1998, **29**, 1463–1471.
(Cit. on p. 19.).

(45) T. J. Chotard, J. Pasquiet, and M. L. Benzeggagh, "Residual performance of scarf patch-repaired pultruded shapes initially impact damaged", *Compos. Struct.*, 2001, **53**, 317–331.
(Cit. on p. 19.).

(46) C. Soutis, D. M. Duan, and P. Goutas, "Compressive behaviour of CFRP laminates repaired with adhesively bonded external patches", *Compos. Struct.*, 1999, **45**, 289–301.
(Cit. on p. 20.).

(47) J. Raghavan and R. P. Wool, "Interfaces in repair, recycling, joining and manufacturing of polymers and polymer composites", *J. Appl. Polym. Sci.*, 1999, **71**, 775–785.
(Cit. on p. 20.).

(48) C. Dry, "Procedures developed for self-repair of polymer matrix composite materials", *Compos. Struct.*, 1996, **35**, 263–269.
(Cit. on p. 21.).

(49) M. Motuku, U. K. Vaidya, and G. M. Janowski, "Parametric studies on self-repairing approaches for resin infused composites subjected to low velocity impact", *Smart Mater. Struct.*, 1999, **8**, 623–638.
(Cit. on p. 22.).

(50) S. M. Bleay, C. B. Loader, V. J. Hawyes, L. Humberstone, and P. T. Curtis, "A smart repair system for polymer matrix composites", *Composites, Part A*, 2001, **32**, 1767–1776.
(Cit. on p. 22.).

(51) J. W. C. Pang and I. P. Bond, "Bleeding composites, damage detection and self-repair using a biomimetic approach", *Composites, Part A*, 2005, **36**, 183–188.
(Cit. on p. 22.).

(52) J. W. C. Pang and I. P. Bond, "A hollow fibre reinforced polymer composite encompassing self-healing and enhanced damage visibility", *Compos. Sci. Technol.*, 2005, **65**, 1791–1799.
(Cit. on p. 22.).

(53) R. S. Trask, G. J. Williams, and I. P. Bond, "Bioinspired self-healing of advanced composite structures using hollow glass fibres", *J. R. Soc., Interface*, 2007, **4**, 363–371.
(Cit. on p. 23.).

(54) G. Williams, R. Trask, and I. Bond, "A self-healing carbon fibre reinforced polymer for aerospace applications", *Composites, Part A*, 2007, **38**, 1525–1532.
(Cit. on p. 23.).

(55) C. W. Bielawski and R. H. Grubbs, "Living ring-opening metathesis polymerization", *Prog. Polym. Sci.*, 2007, **32**, 1–29.
(Cit. on p. 23.).

(56) M. R. Kessler, Ph.D. Thesis, University of Illinois at Urbana-Champaign, 2002.
(Cit. on p. 24.).

(57) M. R. Kessler, "Self-healing: A new paradigm in materials design", *Proc. Inst. Mech. Eng., Part G*, 2007, **221**, 479–495.
(Cit. on p. 25.).

(58) S. R. White, N. R. Sottos, P. H. Geubelle, J. S. Moore, M. R. Kessler, S. R. Sriram, E. N. Brown, and S. Viswanathan, "Autonomic healing of polymer composites", *Nature*, 2001, **409**, 794–797.
(Cit. on p. 24.).

(59) E. N. Brown, M. R. Kessler, N. R. Sottos, and S. R. White, "In situ poly(urea-formaldehyde) microencapsulation of dicyclopentadiene", *J. Microencapsulation*, 2003, **20**, 719–730.
(Cit. on p. 24.).

(60) E. Brown, S. White, and N. Sottos, "Microcapsule induced toughening in a self-healing polymer composite", *J. Mater. Sci.*, 2004, **39**, 1703–1710.
(Cit. on pp. 24, 27.).

(61) E. Brown, N. R. Sottos, and S. R. White, "Fracture testing of a self-healing polymer composite", *Exp. Mech*, 2002, **42**, 372–379.
(Cit. on p. 24.).

(62) M. R. Kessler, N. R. Sottos, and S. R. White, "Self-healing structural composite materials", *Composites, Part A*, 2003, **34**, 743–753.
(Cit. on p. 24.).

(63) A. S. Jones, J. D. Rule, J. S. Moore, S. R. White, and N. R. Sottos, "Catalyst morphology and dissolution kinetics of self-healing polymers", *Chem. Mater.*, 2006, **18**, 1312–1317.
(Cit. on p. 25.).

(64) J. D. Rule, E. N. Brown, N. R. Sottos, S. R. White, and J. S. Moore, "Wax-protected catalyst microspheres for efficient self-healing materials", *Adv. Mater. (Weinheim, Ger.)*, 2005, **17**, 205–.
(Cit. on p. 25.).

(65) X. Liu, J. K. Lee, S. H. Yoon, and M. R. Kessler, "Characterization of diene monomers as healing agents for autonomic damage repair", *J. Appl. Polym. Sci.*, 2006, **101**, 1266–1272.
(Cit. on p. 25.).

(66) T. C. Mauldin, J. D. Rule, N. R. Sottos, S. R. White, and J. S. Moore, "Self-healing kinetics and the stereoisomers of dicyclopentadiene", *J. R. Soc., Interface*, 2007, **4**, 389–393.
(Cit. on p. 26.).

(67) B. J. Blaiszik, N. R. Sottos, and S. R. White, "Nanocapsules for self-healing materials", *Compos. Sci. Technol.*, 2008, **68**, 978–986.
(Cit. on p. 26.).

(68) S. H. Cho, H. M. Andersson, S. R. White, N. R. Sottos, and P. V. Braun, "Polydimethylsiloxane-based self-healing materials", *Adv. Mater. (Weinheim, Ger.)*, 2006, **18**, 997–1000.
(Cit. on p. 26.).

(69) Q. Li, A. K. Mishra, N. H. Kim, T. Kuila, K.-t. Lau, and J. H. Lee, "Effects of processing conditions of poly(methylmethacrylate) encapsulated liquid curing agent on the properties of self-healing composites", *Composites Part B: Engineering*, 2013, **49**, 6 –15.
(Cit. on p. 27.).

(70) G. D. Pasquale, O. Motto, A. Rocca, J. Carter, P. McGrail, and D. Acierno, "New high-performance thermoplastic toughened epoxy thermosets", *Polymer*, 1997, **38**, 4345 –4348.
(Cit. on p. 27.).

(71) K. Mimura, H. Ito, and H. Fujioka, "Toughening of epoxy resin modified with in situ polymerized thermoplastic polymers", *Polymer*, 2001, **42**, 9223 –9233.
(Cit. on p. 27.).

(72) P. McGrail and S. Jenkins, "Some aspects of interlaminar toughening: reactively terminated thermoplastic particles in thermoset composites", *Polymer*, 1993, **34**, 677 –683.
(Cit. on p. 27.).

(73) S. Wilkinson, T. Ward, and J. McGrath, "Effect of thermoplastic modifier variables on toughening a bismaleimide matrix resin for high-performance composite materials", *Polymer*, 1993, **34**, 870 –884.
(Cit. on p. 27.).

(74) R. A. Pearson and A. F. Yee, "Toughening mechanisms in thermoplastic-modified epoxies: 1. Modification using poly(phenylene oxide)", *Polymer*, 1993, **34**, 3658 –3670.
(Cit. on p. 27.).

(75) B. Blaiszik, S. Kramer, S. Olugebefola, J. Moore, N. Sottos, and S. White, "Self-Healing Polymers and Composites", *Annu. Rev. Mater. Res.*, 2010, **40**, 179–211.
(Cit. on pp. 27, 28.).

(76) S. Olugebefola, A. Aragón, C. Hansen, A. Hamilton, B. Kozola, W. Wu, P. Geubelle, J. Lewis, N. Sottos, and S. White, "Polymer Microvascular Network Composites", *J. Compos. Mater.*, 2010, **44**, 2587–2603.
(Cit. on p. 27.).

(77) A. P. Esser-Kahn, P. R. Thakre, H. Dong, J. F. Patrick, V. K. Vlasko-Vlasov, N. R. Sottos, J. S. Moore, and S. R. White, "Three-Dimensional Microvascular Fiber-Reinforced Composites", *Adv. Mater. (Weinheim, Ger.)*, 2011, **23**, 3654–3658.
(Cit. on pp. 27, 28.).

(78) K. S. Toohey, N. R. Sottos, J. A. Lewis, J. S. Moore, and S. R. White, "Self-healing materials with microvascular networks", *Nat. Mater.*, 2007, **6**, 581–585.
(Cit. on p. 27.).

(79) R. S. Trask, C. J. Norris, and I. P. Bond, "Stimuli-triggered self-healing functionality in advanced fibre-reinforced composites", *J. Intell. Mater. Syst. Struct.*, 2014, **25**, 87–97.
(Cit. on pp. 28, 29.).

(80) K. S. Toohey, C. J. Hansen, J. A. Lewis, S. R. White, and N. R. Sottos, "Delivery of Two-Part Self-Healing Chemistry via Microvascular Networks", *Adv. Funct. Mater.*, 2009, **19**, 1399–1405.
(Cit. on p. 28.).

(81) J. A. Lewis, "Direct ink writing of 3D functional materials", *Adv. Funct. Mater.*, 2006, **16**, 2193–2204.
(Cit. on p. 28.).

(82) R. S. Trask and I. P. Bond, "Bioinspired engineering study of Plantae vascules for self-healing composite structures", *J. R. Soc., Interface*, 2010, **7**, 921–931.
(Cit. on p. 28.).

(83) C.-Y. Huang, R. S. Trask, and I. P. Bond, "Characterization and analysis of carbon fibre-reinforced polymer composite laminates with embedded circular vasculature", *J. R. Soc., Interface*, 2010, **7**, 1229–1241.
(Cit. on p. 29.).

(84) C. J. Hansen, S. R. White, N. R. Sottos, and J. A. Lewis, "Accelerated Self-Healing Via Ternary Interpenetrating Microvascular Networks", *Adv. Funct. Mater.*, 2011, **21**, 4320–4326.
(Cit. on p. 29.).

(85) H. R. Williams, R. S. Trask, and I. P. Bond, "Self-healing composite sandwich structures", *Smart Mater. Struct.*, 2007, **16**, 1198–1207.
(Cit. on p. 29.).

(86) C. Chen, K. Peters, and Y. Li, "Self-healing sandwich structures incorporating an interfacial layer with vascular network", *Smart Mater. Struct.*, 2013, **22**, 025031.
(Cit. on p. 29.).

(87) M. S. B. M. Jamil and F. R. Jones, Proceedings of the second international conference on self-healing materials, Chicago, IL, USA, 2009.
(Cit. on p. 31.).

(88) Mohd. S. Md. Jamil, PhD Thesis, University of Sheffield, 2012.
(Cit. on p. 31.).

(89) D. Montarnal, M. Capelot, F. Tournilhac, and L. Leibler, "Silica-Like Malleable Materials from Permanent Organic Networks", English, *Science*, 2011, **334**, 965–968.
(Cit. on pp. 32, 36–38.).

(90) S. D. Bergman and F. Wudl, "Mendable polymers", *J. Mat. Chem.*, 2008, **18**, 41–62.
(Cit. on p. 32.).

(91) X. X. Chen, M. A. Dam, K. Ono, A. Mal, H. B. Shen, S. R. Nutt, K. Sheran, and F. Wudl, "A thermally re-mendable cross-linked polymeric material", *Science*, 2002, **295**, 1698–1702.
(Cit. on pp. 32, 33.).

(92) X. X. Chen, F. Wudl, A. K. Mal, H. B. Shen, and S. R. Nutt, "New Thermally Remendable Highly Cross-Linked Polymeric Materials", *Macromolecules*, 2003, **36**, 1802–1807.
(Cit. on p. 33.).

(93) Y. L. Liu and C. Y. Hsieh, "Crosslinked epoxy materials exhibiting thermal remendablility and removability from multifunctional maleimide and furan compounds", *J. Polym. Sci., Part A: Polym. Chem.*, 2006, **44**, 905–913.
(Cit. on p. 34.).

(94) Y. L. Liu and Y. W. Chen, "Thermally reversible cross-linked polyamides with high toughness and self-repairing ability from maleimide- and furan-functionalized aromatic polyamides", *Macromol. Chem. Phys.*, 2007, **208**, 224–232.
(Cit. on p. 34.).

(95) Y. Zhang, A. A. Broekhuis, and F. Picchioni, Proceedings of the second International conference on self-healing materials, Chicago, IL USA, 2009.
(Cit. on p. 34.).

(96) Y. Zhang, A. A. Broekhuis, and F. Picchioni, "Thermally Self-Healing Polymeric Materials: The Next Step to Recycling Thermoset Polymers?", *Macromolecules*, 2009, **42**, 1906–1912.
(Cit. on p. 34.).

(97) E. B. Murphy, E. Bolanos, C. Schaffner-Hamann, F. Wudl, S. R. Nutt, and M. L. Auad, "Synthesis and Characterization of a Single-Component Thermally Remendable Polymer Network: Staudinger and Stille Revisited", *Macromolecules*, 2008, **41**, 5203–5209.
(Cit. on pp. 34–36.).

(98) F. Wudl, Proceedings of the second international conference on self-healing materials, Chicago, IL USA, 2009.
(Cit. on p. 34.).

(99) Y. Higaki, H. Otsuka, and A. Takahara, "Dynamic formation of graft polymers via radical crossover reaction of alkoxyamines", *Macromolecules*, 2004, **37**, 1696–1701.
(Cit. on p. 35.).

(100) Y. Higaki, H. Otsuka, and A. Takahara, "A thermodynamic polymer crosslinking system based on radically exchangeable covalent bonds", *Macromolecules*, 2006, **39**, 2121–2125.
(Cit. on p. 35.).

(101) J. Otera, "Transesterification", *Chem. Rev. (Washington, DC, U. S.)*, 1993, **93**, 1449–1470.
(Cit. on p. 36.).

(102) M. Capelot, M. M. Unterlass, F. Tournilhac, and L. Leibler, "Catalytic Control of the Vitrimer Glass Transition", *ACS Macro Letters*, 2012, **1**, 789–792.
(Cit. on pp. 36, 37.).

(103) M. Capelot, D. Montarnal, F. Tournilhac, and L. Leibler, "Metal-Catalyzed Transesterification for Healing and Assembling of Thermosets", *J. Am. Chem. Soc.*, 2012, **134**, 7664–7667.
(Cit. on p. 37.).

(104) K. Takeda, M. Tanahashi, and H. Unno, "Self-repairing mechanism of plastics", *Sci. Technol. Adv. Mater.*, 2003, **4**, 435–444.
(Cit. on p. 39.).

(105) K. Takeda, H. Unno, and M. Zhang, "Polymer reaction in polycarbonate with Na", *J. Appl. Polym. Sci.*, 2004, **93**, 920–926.
(Cit. on p. 39.).

(106) P. D. Beer, P. A. Gale, and D. K. Smith, *Supramolecular Chemistry*, Oxford University Press, Oxford, UK, 1999, vol. 74.
(Cit. on p. 40.).

(107) L. Pauling, *The Nature of the Chemical Bond*, Cornell University Press, IIthava, NY, 1939.
(Cit. on p. 40.).

(108) M. J. Calhorda, "Weak hydrogen bonds: Theoretical studies", *Chem. Commun. (Cambridge, U. K.)*, 2000, 801–809.
(Cit. on p. 40.).

(109) N. V. Belkova, E. S. Shubina, and L. M. Epstein, "Diverse World of Unconventional Hydrogen Bonds", *Acc. Chem. Res.*, 2005, **38**, 624–631.
(Cit. on p. 40.).

(110) M. Jiang, M. Li, M. Xiang, and H. Zhou, "Interpolymer Complexation and Miscibility Enhancement by Hydrogen Bonding", *Adv. Polym. Sci.*, 1999, **146**, 121–196.
(Cit. on p. 41.).

(111) J.-M. Lehn, "Supramolecular polymer chemistry - scope and perspectives", *Polymer International*, 2002, **51**, 825–839.
(Cit. on p. 41.).

(112) R. Stadler, "Thermoplastic elastomers via supramolecular self assembling in random copolymers", *Kautsch. Gummi, Kunstst.*, 1993, **46**, 619–28.
(Cit. on p. 42.).

(113) P. Cordier, F. Tournilhac, C. Soulie-Ziakovic, and L. Leibler, "Self-healing and thermoreversible rubber from supramolecular assembly", *Nature*, 2008, **451**, 977–980.
(Cit. on p. 42.).

(114) K. P. Nair, V. Breedveld, and M. Weck, "Complementary Hydrogen-Bonded Thermoreversible Polymer Networks with Tunable Properties", *Macromolecules*, 2008, **41**, 3429–3438.
(Cit. on p. 43.).

(115) W. Doherty III, S. Sorensen, and R. Friedlein, "Selective hydrogen bond disruption in adenine monolayer films by reaction with water", *J. Electron Spectrosc.*, 2009, **174**, Advanced Spectroscopies of Molecular Materials for Electronics, 107 –109.
(Cit. on p. 43.).

(116) F. R. Kersey, D. M. Loveless, and S. L. Craig, "A hybrid polymer gel with controlled rates of cross-link rupture and self-repair", *J. R. Soc., Interface*, 2007, **4**, 373–380.
(Cit. on p. 44.).

(117) S. Burattini, H. M. Colquhoun, B. W. Greenland, and W. Hayes, "A novel self-healing supramolecular polymer system", *Faraday Discuss.*, 2009, **143**, 251–264.
(Cit. on p. 44.).

(118) S. Burattini, H. M. Colquhoun, J. D. Fox, D. Friedmann, B. W. Greenland, P. J. F. Harris, W. Hayes, M. E. Mackay, and S. J. Rowan, "A self-repairing, supramolecular polymer system: healability as a consequence of donor-acceptor π-π stacking interactions", *Chem. Commun.*, 2009, 6717–6719.
(Cit. on p. 44.).

(119) S. Burattini, B. W. Greenland, D. H. Merino, W. Weng, J. Seppala, H. M. Colquhoun, W. Hayes, M. E. Mackay, I. W. Hamley, and S. J. Rowan, "A Healable Supramolecular Polymer Blend Based on Aromatic π-π Stacking and Hydrogen-Bonding Interactions", *JACS*, 2010, **132**, 12051–12058.
(Cit. on p. 44.).

(120) S. Burattini, H. M. Colquhoun, J. Fox, D. Friedmann, B. W. Greenland, P. J. F. Harris, W. Hayes, M. E. Mackay, and S. J. Rowan, Proceedings of the second international conference on self-healing materials, Chicago, IL, USA, 2009.
(Cit. on p. 44.).

(121) J. Fox, J. J. Wie, B. W. Greenland, S. Burattini, W. Hayes, H. M. Colquhoun, M. E. Mackay, and S. J. Rowan, "High-Strength, Healable, Supramolecular Polymer Nanocomposites", *JACS*, 2012, **134**, 5362–5368.
(Cit. on p. 45.).

(122) L. R. Hart, J. H. Hunter, N. A. Nguyen, J. L. Harries, B. W. Greenland, M. E. Mackay, H. M. Colquhoun, and W. Hayes, "Multivalency in healable supramolecular polymers: the effect of supramolecular cross-link density on the mechanical properties and healing of non-covalent polymer networks", *Polym. Chem.*, 2014, **5**, 3680–3688.
(Cit. on p. 45.).

Chapter 2

Synthesis Part A: Thiele's Acid and Ester

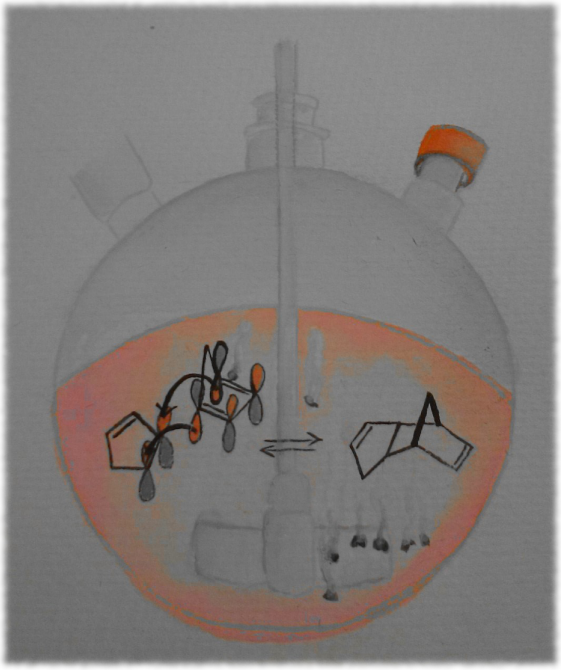

2.1 Introduction

This chapter is predominantly about the synthesis of Thiele's acid which is the main intermediate for all the self-healing monomers synthesised in this work.

Johannes Thiele produced the first carboxylic acid of cyclopentadiene (CPD) in 1900 [1] through the carbonation and acid work-up of cyclopentadienyl potassium (Figure 2.1). The cyclopentadiene carboxylic acid reversibly dimerizes as does its precursor cyclopentadiene which can also rapidly form a dimer (dicyclopentadiene, DCPD) if stored at room temperature.

The mechanism is a Diels-Alder pericyclic reaction. Essentially there is a concerted addition of a conjugated diene with a dienophile (*i.e.* 1 double bond) and can be best described using frontier molecular orbitals as shown in Figure 2.2 for cyclopentadiene. Essentially if there is a good overlap between the highest occupied molecular orbital (HOMO) and the lowest unoccupied molecular orbital (LUMO) bonding is allowed. The driving force behind the reaction is the formation of σ-bonds which are more stable than the π-bonds that they replace.

As previously discussed in Section 1.4.4.1 this reversible behaviour inspired a class of monomers capable of forming thermally reversible polymer networks [2]. As Thiele's acid will act as a precursor to many of the target self-healing polymers and matrix additives in this thesis it is important to get a thorough understanding of the molecule, its structure, isomers and synthesis and such is the purpose of this chapter. This chapter will also touch on the synthesis of the methyl ester of Thiele's acid as a prelude to chapter 3 in which the monomers will be synthesised in a similar reaction.

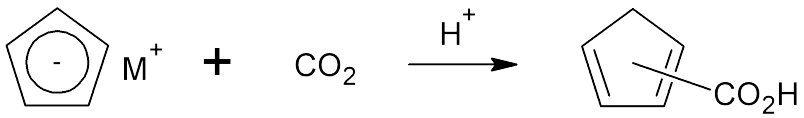

Figure 2.1: Carbonation and acid work-up of a metal cyclopentadienide ion to form cyclopentadiene carboxylic acid. The exact position of the carboxylic acid group is discussed in the following Section (2.1.1) The monomer will go on to immediately form the dimer version of the acid through a Diels-Alder reaction. M^+ represents a metal cation usually potassium or sodium.

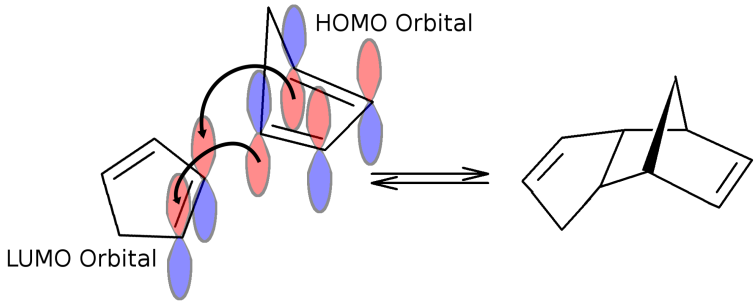

Figure 2.2: Frontier molecular orbital description of the formation of dicyclopentadiene from cyclopentadiene.

2.1.1 Cyclopentadiene Carboxylic Acid Monomer Structure and Naming

In order to properly understand the structure of the dimer it would be advantageous to understand the structure of the monomer but this is difficult because of its tendency to immediately dimerize. Nevertheless, early attempts to characterize the monomeric ester of cyclopentadiene carboxylic acid were made by Alder *et al* [3]. By mixing the dimer with fresh cyclopentadiene and allowing the forward Diels-Alder to take place mono-substituted dimers were created which could be separated and studied.

In cyclopentadiene the pair of double bonds are in the 1,3 position but this numbering is not necessarily conserved in the substituted monomers. The International Union of Pure and Applied Chemistry's (IUPAC) preferred chemical nomenclature [4] of substituted cyclic alkenes favours the ester/acid groups with a higher naming priority over the double bonds. The practical consequence of these priority rules is that the substituted carbon on the cyclopentadiene ring is always numbered in the '1' position and the relative numbering of the double bonds changes with the substitution.

Peters pointed out that three possible structures exist for the monomer depending on the substitution position of the carbonyl group [5], see Figure 2.3. The carbonyl group can be either be conjugated with the unsaturation (*i.e.* Figure 2.3b and 2.3c) or isolated (Figure 2.3a).

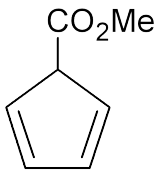

(a) methyl cyclopenta-2,4-diene-1-carboxylate

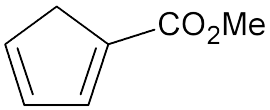

(b) methyl cyclopenta-1,3-diene-1-carboxylate

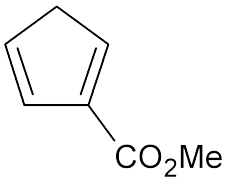

(c) methyl cyclopenta-1,4-diene-1-carboxylate

Figure 2.3: Possible structures of the monomeric 'Thiele's Ester' as proposed by Alder *et a* [3].

By studying the structure of the product it was possible to determine the structure of the monomeric ester as shown in the scheme in Figure 2.4. The compound that was isolated (Figure 2.4) can only be made from a reaction of cyclopentadiene with methyl cyclopenta-1,3-diene-1-carboxylate (Figure 2.3b) and so it was concluded that this is the structure of the monomer .

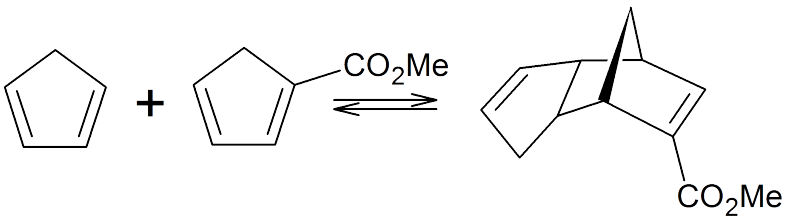

Figure 2.4: The reaction between the monomeric ester and cyclopentadiene produced the bi-cyclic structure on the right (3a,4,7,7a-tetrahydro-4,7-methano-1H-indene-6-carboxylic acid).

2.1.2 Dicyclopentadiene Dicarboxylic Acid Dimer Structure and Naming

Assigning the structure of the di-acid is not as straightforward as it might appear; even after the structure of the monomer was established. The reason for the difficulty in assigning the structure of the di-acid is that the monomeric acid could theoretically dimerize through a multitude of atoms and into both exo and endo conformations. Over the last century various different structures have been attributed to the structure of the dimeric acid and its corresponding methyl ester. In 1959, using solely the ultra-violet (UV) spectra, Peters [5] was able to determine

that the bi-cyclic ring system was of an endo conformation and that the carbonyl groups are conjugated with the unsaturated bonds on the indene ring system. Despite this information the major reaction product was still not clear as there were still another four possible locations for the carboxylic acid group.

The fact that the structure is the *endo* Diels-Alder adduct is not surprising as this would be expected due to the Alder-Stein rule [6]. The preference for the *endo* conformation is is usually the case for norbornene based structures, (such Thiele's acid and ester) due to stabilising second order orbital reactions which favour the *endo* configuration.

A decade later the structure of the major product was finally established [7] as 3a,4,7,7a-tetrahydro-4,7-methano-1H-indene-2,6-dicarboxylic acid (see Figure 2.5). This structure was more recently confirmed in 1990 using advanced nuclear magnetic resonance (NMR) techniques [8].

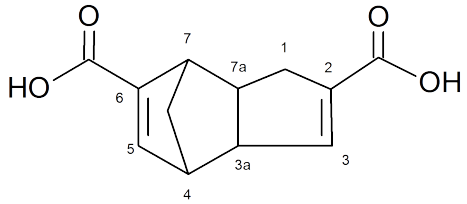

Figure 2.5: The major reaction product of the carbonation of the cyclopentadienide ion: Thiele's Acid (3a,4,7,7a-tetrahydro-4,7-methano-1H-indene-2,6-dicarboxylic acid)

The systematic name for Thiele's Acid: '3a,4,7,7a-tetrahydro-4,7-methano-1H-indene-2,6-dicarboxylic acid', is based upon the recommendations set out in IUPAC's article 'Nomenclature of fused and bridged fused ring systems' [9] in which, unless stated otherwise, the maximum number of non-cumulative double bonds is assumed. The parent compound used for the naming is indene (Figure 2.6) which is a fused ring of benzene and cyclopentene.

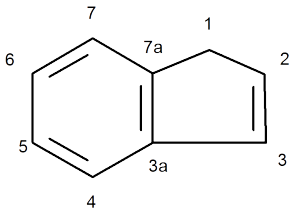

Figure 2.6: Indene, the fused ring compound used as a parent component for the systematic naming of Thiele's Acid (1H-form shown).

The numbering starts from the most counter-clockwise non-fusion carbon in the most uppermost ring to the furthest right. The atoms are numbered consecutively clockwise with the exception of the fusion carbons (3a and 7a) which are labelled with the same number as the immediately preceding position modified by the addition of a Roman character (in this case 'a'). In order to correctly number the atoms; the molecule should be drawn in an orientation that results in the lowest numbering for the fusion carbons[9]. For the remainder of this thesis the atoms will retain this numbering sequence but are drawn in an orientation designed to maximise clarity in mechanisms or reaction schemes.

The systematic name of Thiele's Acid (3a,4,7,7a-tetrahydro-4,7-methano-1H-indene-2,6-dicarboxylic acid) can be summarised as follows:

2,6-dicarboxylic acid: specifies the location of the carboxylic acid groups based upon the numbering of the parent indene ring.

1H-indene-: specifies the parent ring system and the position of the 'indicated hydrogen' which removes ambiguity about the position of the double bonds.

4,7-methano-: specifies a bridge consisting of a methylene (CH_2) atom atatched to the 4 and 7 positions of the indene ring.

3a,4,7,7a-tetrahydro: explicitly shows the hydrogenation compared to the parent indene. The position of the hydrogen atoms in the 3a, 4, 7 and 7a positions combined with the other substitutions describes by exclusion the position of the two double bonds.

2.1.3 Dimerization Mechanism

It is worth noting that the dimer structure established above and shown in Figure 2.5, does not correlate with a reaction of two instances of the monomer structure that was assigned in Section 2.1.1, *i.e.* Figure 2.3b. Peters did notice this discrepancy even before the final structure was proven and came up with a hypothesis [5] as to the dimerization mechanism which can also be used to explain the formation of the structure in Figure 2.5. Peters' explanation was that the monomer predominantly exists in the form of structure 2.3b but it is also in equilibrium with structure 2.3c via

a hydrogen shift, with the position of the equilibrium favouring the former. During dimerization the two isomers react together which in turn drives the equilibrium to the right. The proposed scheme is shown for the ester in Figure 2.7.

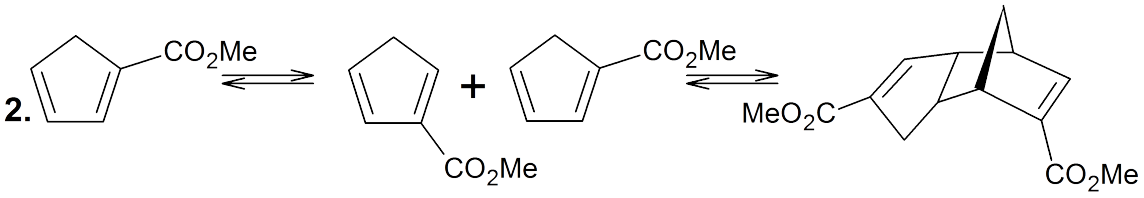

Figure 2.7: The proposed scheme in which the monomeric ester undergoes a hydrogen shift and dimerizes.

2.1.4 Thiele's Acid Synthetic Scheme

Possessing the information from the literature discussed in Sections 2.1.1 to 2.1.3 it is possible to propose a full scheme, Figure 2.8 that shows the the production of Thiele's acid that is the main topic of this chapter.

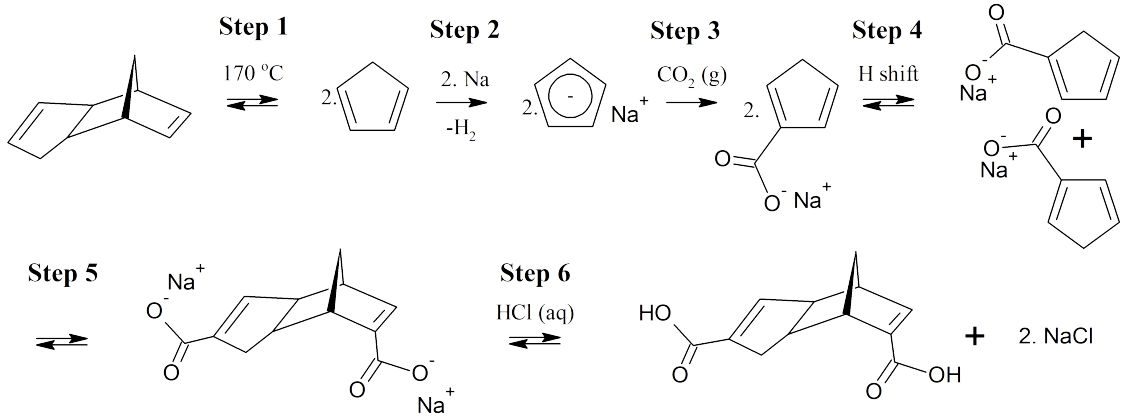

Figure 2.8: The full synthetic scheme for Thiele's acid from DCPD.

Step 1 The DCPD is cracked to the monomeric CPD using a high temperature reactive distillation which removes the lower boiling point CPD from the reaction and so forces the equilibrium to the right which enhances conversion. The CPD produced is far more reactive than DCPD with the sodium in step 2.

Step 2 The CPD is reduced using sodium metal to form a highly reactive cyclopentadienide anion.

Step 3 The cyclopentadienide anion reacts with the electrophilic carbon dioxide which forms the conjugate base of cyclopentadiene carboxylic acid: cyclopenta-1,3-diene-1-carboxylate.

Step 4 A small number of the cyclopenta-1,3-diene-1-carboxylate molecules undergo a proton shift to cyclopenta-1,4-diene-1-carboxylate (as outlined in Section 2.1.3).

Step 5 Cyclopenta-1,3-diene-1-carboxylate forms a dimer rapidly with cyclopenta-1,4-diene-1-carboxylate to form the conjugate base of Thiele's acid (3a,4,7,7a-tetrahydro-4,7-methano-1H-indene-2,6-dicarboxylate). The consumption of the cyclopenta-1,4-diene-1-carboxylate causes it to be replenished via the chemical equilibrium due to Le Chatelier's principle [10].

Step 6 3a,4,7,7a-tetrahydro-4,7-methano-1H-indene-2,6-dicarboxylate is protonated using aqueous hydrochloric acid to form Thiele's Acid (3a,4,7,7a-tetrahydro-4,7-methano-1H-indene-2,6-dicarboxylic acid) and sodium chloride salt.

2.1.5 Esterification

Thiele's acid will be used as the main precursor for the cyclic ester monomers that will be discussed in chapter 3. Esterifications are well known transformations in organic chemistry and are the reactions between carboxylic acids and alcohols to form esters. Thiele's acid, as a di-carboxylic acid can form esters. The transformation can be achieved in a variety of ways including but not limited to:

- The direct reaction between an acid and an alcohol in the presence of a suitable acid catalyst. The direct reaction is simple but can leave the reaction at the mercy of the chemical equilibrium (*i.e.* Figure 2.9). In order to get a good yield and drive the reaction to completion an excess of alcohol is needed.

- Through the acyl chloride intermediate (*i.e.* Figure 2.10) which can give much higher yields.

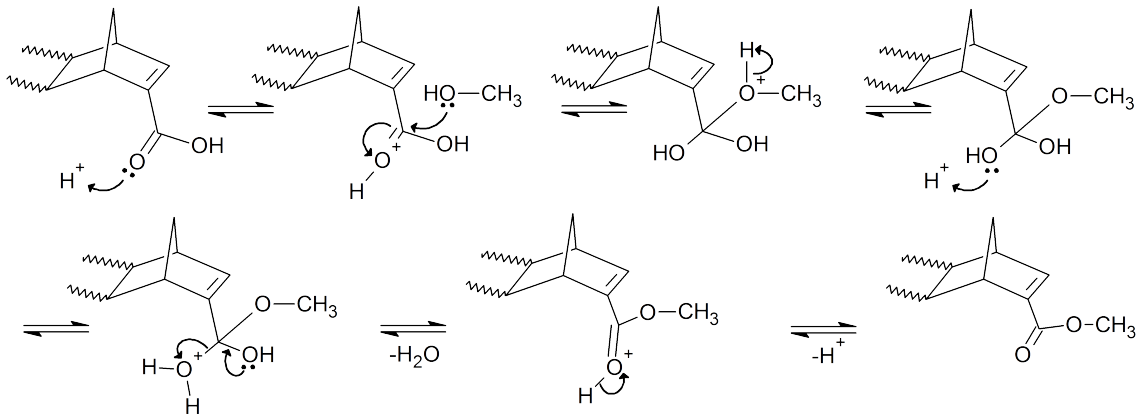

Figure 2.9: Acid catalysed (classical) esterification of Thiele's acid with methanol to form Thiele's ester [11, Chap. 12].

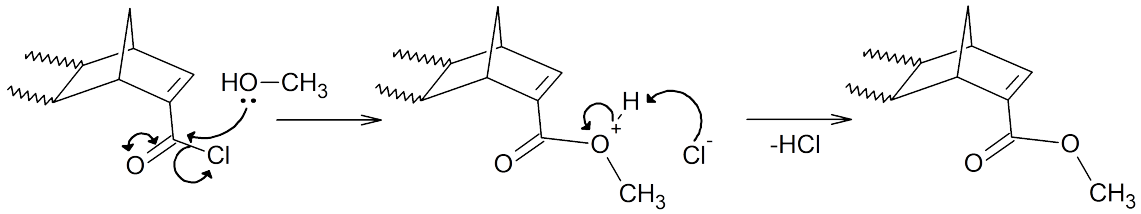

Figure 2.10: (Simplified) Route to ester via the acid chloride.

More details on the esterification mechanisms and the acyl chloride transformations are given in chapter 3. As the reactions in chapter 3 were quite difficult it was decided to first attempt to form the methyl ester of Thiele's acid (Thiele's Ester). The reason for this is that the reagent (methanol) is cheap and available and there is plenty of literature about Thiele's ester to compare against. Another reason was that the minor products are easier to separate in the ester form so it is possible analyse them independently [12].

2.2 Experimental

2.2.1 Equipment

All glassware used in this synthesis was quantitatively cleaned as detailed by A.J. Frontier in her 'Not Voodoo' chemistry resource [13] and dried overnight in a glassware oven on 'high' after a rinse with deionized water. Where glassware was needed sooner after the deionized water wash they are given a rinse with acetone followed by diethyl ether and dried under vacuum or in the oven for 30 minutes. All joints were sealed with PTFE sleeves where possible to avoid grease contamination in the final product although this was not possible for some non-PTFE taps which require a small quantity of silicone grease to avoid seizure.

2.2.2 Reagents

- Dicyclopentadiene (95%) stabilized with the antioxidant butylated hydroxytoluene (BHT) was purchased from Alfa Aesar, Heysham, UK and was used as supplied

- Sodium metal (99%) was supplied by Sigma Aldrich, Gillingham, UK in the form of large lumps (*c.a* .25 g) in kerosene. The metal was cut into smaller pieces and washed with light petroleum before use.

- All solvents were supplied by VWR, East Grinstead, UK or Fisher Scientific, Loughborough, UK and were at least 99% purity.

- Where solvents are described as 'dried' this was done using a drying column consisting of an activated alumina/copper catalyst and inert nitrogen atmosphere. The water content for the dried tetrahydrofuran was determined to be 13-14 ppm by Karl-Fischer titration. All other dried solvents had a water content of $<$10 ppm.

- All other reagents were of reagent grade and supplied by Sigma Aldrich, Gillingham, UK and used with no further purification.

2.2.3 Thiele's Acid Synthesis

Reaction Setup

A 2 litre three-necked round-bottomed flask was equipped with a 250 ml pressure equalizing dropping funnel (sealed with a septum); a Liebig condenser with a connection to a double vacuum/nitrogen manifold; a 3 way adapter with a glass tap and hose-tail for later inlet of carbon dioxide and an overhead stirrer with a PTFE paddle through a seal-able pass-through. See Figure 2.11 for a schematic of the glassware setup.

If method B (described in Section 2.2.3 on page 76) is used for the carbonation step then the overhead stirrer can be omitted and a magnetic flea can be used in its stead. The pass-through was sealed and the whole reaction setup was flamed under vacuum and refilled with dry nitrogen gas and allowed to cool. When cool the setup was further evacuated and refilled twice more to ensure complete removal of atmospheric contaminants.

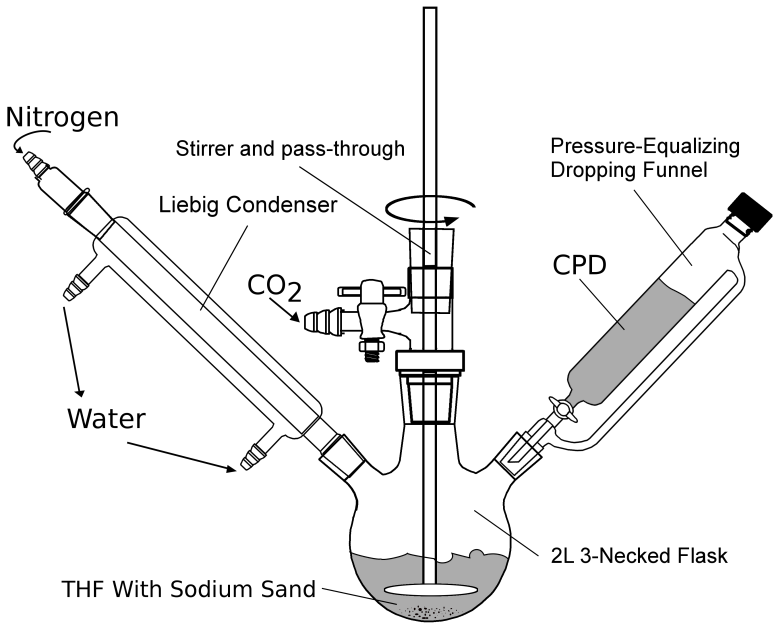

Figure 2.11: A diagram showing the reaction setup used to produce Thiele's acid in this work.

Reactive distillation, the cracking of the DCPD into CPD

Dicyclopentadiene (DCPD) (approx 150 ml) was added to a 250 ml round bottomed flask equipped with a stirrer bar. The flask was attached to a standard distillation setup integrating a 30 cm Vigreux column and a Graham's condenser. The flask was stirred and heated to the point of the DCPD reflux (170 °C) with care taken not to over-heat. The lower boiling point cyclopentadiene (CPD) distils off with the temperature at the top of the column not rising above 45 °C (see the photo in Figure 2.12).

The cyclopentadiene, which is a clear liquid, was collected in an ice cooled round-bottomed flask and generally used immediately. Alternatively it can be stored in the freezer at -18 °C for a few days before use but if it is stored at room temperature it quickly dimerizes again and yields are greatly reduced. Although the cracking step is not air-sensitive; the distillation was done under an inert nitrogen atmosphere to facilitate the air-free transfer of the CPD into the reaction apparatus used for the reduction and carbonation steps, which *are* highly air and moisture sensitive. When 100 ml of CPD was produced the distillation was stopped and allowed to cool down.

Making Sodium 'Sand'

Against a fast nitrogen counter-flow, small chunks of sodium (10 g) were added through one of the necks of the three-necked flask reactor. Dry toluene (250 ml) was added to the dropping funnel through the septum and allowed to drop into the reaction vessel via an open tap. The sodium should not bubble or evolve gas at this point otherwise the toluene is not dry enough, a slight discolouration is sometimes encountered but is tolerable. The dropping funnel was replaced and the nitrogen flow lowered. With rapid stirring via the PTFE paddle or a magnetic bar the mixture was heated to reflux. The sodium will melt and form small particles. At this point the heat was removed and the stirrer was stopped while the mixture was allowed to cool.

When cooled the sodium should be in the form of small sand-like spheres (Figure 2.13), if they have agglomerated into a mass the step should be attempted again. The toluene was removed via a syringe equipped with a long but narrow diameter needle inserted through the septum and the open tap of the dropping funnel. Wide needle

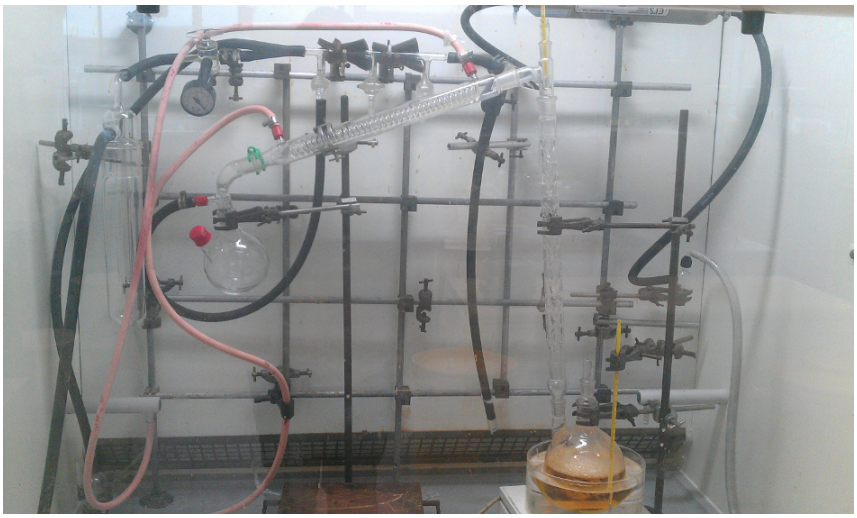

Figure 2.12: A photo showing the reactive distillation of DCPD into CPD.

diameters have the potential to remove sodium particles which can be a safety hazard and cause a yield reduction. The removed toluene should be quenched carefully by drop-wise addition of isopropyl alcohol followed by methanol and eventually water before it can be safely disposed. The sodium was washed with two portions of dry tetrahydrofuran (25 ml) which was removed, quenched and discarded.

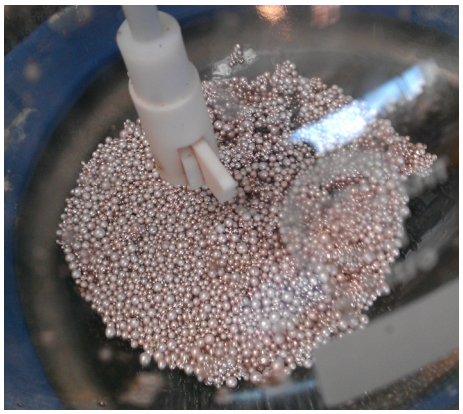

Figure 2.13: A photographic example of sodium 'sand'. In this particular example the particle size is quite large which led to a longer than optimum reaction time.

Formation of the Sodium Cyclopentadienyl Complex (NaCP)

Dry THF (500 ml) was added to the reaction vessel via the dropping funnel septum. The tap was closed and the freshly distilled CPD (50 ml) was added to the dropping

funnel again via the secured septum. Over the course of 1 hour the CPD was added drop-wise onto the sodium/THF with moderate stirring. The sodium should produce evolve hydrogen gas and the solution will start to discolour. A pale pink or red is most desirable at this stage (Figure 2.14a). A deep purple or brown colour (Figure 2.14b) suggests that the conditions are not dry/oxygen free enough and the experiment should be aborted. When all the sodium has reacted the formation of the NaCP is complete (*c.a.* 4-12 hours depending on the quality of the sodium sand).

(a) A solution of CPD in THF reacting with sodium displaying a desireable pale red colour which indicates good reaction conditions.

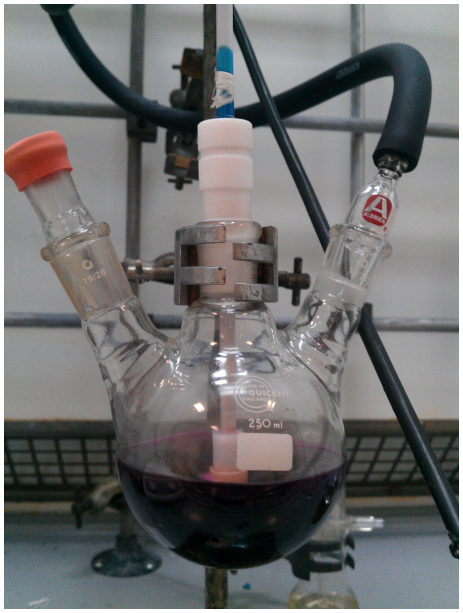

(b) A solution of CPD in THF reacting with sodium displaying a less desireable deep purple colour which indicates the presence of oxygen in the system.

Figure 2.14: Photographic examples of the different colours of NaCPD solutions.

Carbonation of the NaCP Complex: Method A

Dry ice (1 kg) was added to a very large bunged vacuum flask or any large container with a pipe-tail. The sublimation of the solid carbon dioxide generates gas which was dried through a gas washer containing concentrated sulfuric acid (50 ml) and

piped into the reaction via the tap shown in Figure 2.11 or alternatively via the nitrogen manifold if it is not shared by another user.

The mixture was stirred rapidly via the overhead motor; at this point the viscosity should increase along with the formation of white solid in suspension (see the photos in Figure 2.15). If the overhead stirrer is omitted from the equipment and an attempt is made to stir using a magnetic stirrer bar at this point it fails due to the viscosity increase. The mixture was left to react (overnight or at least 12 hours) after which the reaction mixture was concentrated via vacuum.

(a) A skin starts to form.

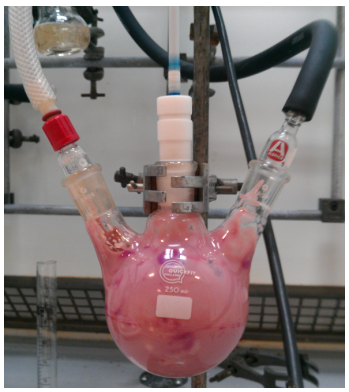

(b) A white precipitate forms and, with vigorous stirring, mixes with the red solution to form a creamy viscous pink solution.

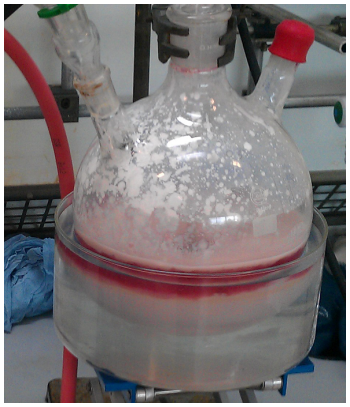

(c) The solid content increases to the point where the white precipitate is clearly visible and the solution is practically gelled.

Figure 2.15: A selection of photos showing the evolution of a white precipitate after the addition of the CO2 gas to the NaCPD solution.

Carbonation of the NaCP Complex: Method B

A slurry of dry ice (1 kg) and THF (500 ml) was added to a large Erlenmeyer flask. Portions of the NaCP solution were removed from the reaction via a syringe and injected over the solid carbon dioxide. The injections should be done rapidly otherwise the NaCP solidifies around the end of the needle causing a blockage. When all the solution was added, the flask was left until all the dry ice had sublimed.

Workup of the Carbonated NaCP / Thiele's Acid

Deionized water was added carefully drop-wise to the white solid residue produced through either method A or method B. Care should be taken at this point because any unreacted sodium can easily ignite any THF residue present. This risk can be mitigated in method A because the flask can be kept under inert atmosphere, in the case of method B if there is any suspicion that sodium particles might have been transferred, isopropanol and then methanol should first be added to quench the sodium. When it was clear that it was safe to do so the liquid was transferred to a round bottomed flask and concentrated using the rotary evaporator. Next, a larger volume of water was added (500 ml) the white solid dissolved. The solution was washed with dichloromethane (DCM) (3 x 100ml portions). Care should be taken not to shake the separating funnel too violently because the mixture is prone to forming emulsions that are difficult to clear (particularly if there is still some THF present or alcohol was used to quench the system).

The aqueous layer was decanted into a beaker (5 L) and acidified by the drop-wise addition of 10% hydrochloric acid while stirring. Crude Thiele's acid precipitates out of solution and the resulting suspension was vacuum filtered and washed with deionized water (3 x 100 ml portions). The crude di-acid was purified by re-crystallisation from methanol and dried in a vacuum oven at 50 °C. Various different yields and purities of Thiele's acid were produced with details presented in Section 2.3.1.

2.2.4 Esterification of Thiele's Acid to Thiele's Ester

Concentrated sulfuric acid (3.5 ml) was added to a solution of the Thiele's acid (4.4 g, 0.020 mol) in methanol (60 mL) and the solution was heated to reflux overnight with stirring. The reaction mixture was allowed to cool down to ambient temperature and was concentrated on the rotary evaporator down to a volume of a few mL. Water (50 mL) was added and the mixture was neutralised by the drop-wise addition of 10% aqueous sodium hydroxide solution. At this point an aqueous suspension is formed which was extracted with 3 20 ml portions of diethyl ether. The ethereal extracts were combined and washed with distilled water. The organic layer was dried with magnesium sulfate, filtered and concentrated on the rotary evaporator and finally

on the high-vacuum line. The residue was recrystallized from petrol (b.p. 60-80 °C) to yield Thiele's ester 3.25 g, 65.5% yield.

2.2.5 DSC and Melting Point

DSC was measured using a Perkin Elmer DSC 7 and 10 μL closed aluminium crucibles.

Melting points were measured using a Stuart digital melting point machine SMP20 in glass tubes with one open end. In both cases ramp rates of 10 °C were used.

2.2.6 NMR

All NMRs were measured using a Bruker Avance 400 instrument equipped with a 5mm $^{1}H/^{13}C$ probe. ^{1}H experiments were measured using a 12 ppm sweep width.^{13}C experiments were proton decoupled and measured over a 240 ppm sweep width using J modulation which uses the SEFT (Spin-Echo Fourier Transform) technique to differentiate between odd and even amounts of protons on the carbon atoms (*i.e.* CH/CH_3 from C/CH_2).

The NMR of Thiele's ester was measured in deuterated chloroform and the NMR of Thiele's Acid was measured in deuterated dimethyl sufoxide (DMSO) due to solubility issues in chloroform.

2.3 Results and Discussion

The final experimental procedure developed for this synthesis was developed over the course of many experiments with a variable yield and quality. Initially a Thiele's acid synthesis direct from DCPD [2] was attempted but this method proved to be extremely difficult without access to either a glove box or a high purity argon line due to the repeated air-free filtration steps which were very impractical using nitrogen double manifold techniques. For this reason it was decided to return to a more classical sodium cyclopentadienide synthesis that involves a DCPD pre-cracking step. On an industrial scale the direct route would most likely be more cost effective but on the sub Kg scale in the lab the author firmly believes that the indirect method is more suitable .

Two methods were used for the carbonation step of the reaction described in Section 2.2.3. The first method, A, involves the generation of gaseous carbon dioxide directly from the sublimation of dry ice. The reasoning behind this method was that by bubbling the gas through concentrated sulphuric acid it was thought possible to maintain a drier atmosphere. Method B was expected to introduce atmospheric condensation on the dry ice which would lead to high levels of water coming into contact with the reagents and consequently lower yields. This subsequently turned out not to be the case.

2.3.1 Observations and Yields

Due to the equilibrium nature of the DCPD cracking step it was required to use approximately 1.5 - 2 times the volume of DCPD compared to the necessary amount of CPD. The DCPD that remained in the boiling flask was observed to turn an orange colour over several hours of reflux. This is attributed to the onset of the thermal self-polymerisation of the DCPD. No visible thickening or gelling of the reagent was noted even after very long reaction times. The residue was not analysed because the self-polymerisation behaviour of DCPD is already well documented and understood [14–16]. If this step was to be scaled up to pilot plant scale care should be taken not to allow the self-polymerisation reaction to proliferate and consequently foul reaction vessels.

It was found that reagent grade toluene was sufficiently dry not to cause much bubbling or fouling of the sodium, upon addition. Upon reflux and heating the toluene was observed to brown slightly but this effect was also observed when dry toluene obtained from the Grubbs solvent purification system (activated alumina and copper catalyst column) was used. The THF used however had to be dried as it was found that use of reagent grade THF caused excessive bubbling when added to the sodium sand which caused considerable reductions in yield and longer reaction times due to fouling of the sodium surface.

With a stoichiometric quantity of CPD the reaction time was found to be too long $>$ 24h and sodium particles were often left unreacted. It was found that a slight excess of CPD *c.a.* 1.25:1 brought the reaction time down to around 6 hours with good quality sodium sand. The importance of adding the CPD drop-wise or in small batches can be highlighted by the tendency for the mixture to heat up dangerously and uncontrollably due to the exothermic reaction, if the CPD was added too fast. It is during this step that various colour changes can be observed dependent on the concentrations and purity of the reagents and atmosphere. With the standard lab nitrogen supply which is piped from a nitrogen generator through the building all the initial reaction attempts resulted in a dark brown CPD solution and subsequently small yields (see table 2.1). For this reason an air-free nitrogen bottle was obtained and the nitrogen was passed through a drying and oxygen scavenging column prior to use. With the dry nitrogen, dry reagents and a lot of care the mixture would turn a pale pink and later a bright red as all the sodium is consumed.

Using method A (described in Section 2.2.3) for the carbonation caused a rapid formation of a skin and with fast mechanical stirring a rapid viscosity increase, however even after $>$24 h reaction times yields were mediocre at best and lots of brown material was created during the work-up steps which suggests that the extent of reaction was rather low. It is hypothesized that unreacted CPD reagent gets trapped inside large pieces which are protected from the carbon dioxide gas by thick skins of reacted product despite attempts to break them up. Higher dilution conditions could potentially solve this problem; however this would hinder attempts to upscale the reaction due to the limits of the available glassware (2.5L flask).

Method B somewhat unexpectedly produced much more acceptable yields. It is thought that the carbon dioxide levels are so high in the slurry that the the air is

effectively displaced which does not allow high levels of moisture to build up.

Washing with dichloromethane removes residual unreacted CPD/DCPD which leaves a slightly orange coloured aqueous phase which contains the deprotonated (conjugate base) form of Thiele's acid in solution as the pH is around 12. Acidification of the phase with hydrochloric acid caused a colour change to a pale green colour and some gas evolution. The gas evolved is carbon dioxide as the carbonation step used an excess of carbon dioxide which under basic conditions can form sodium bicarbonate with the sodium cation. Upon acidification carbonic acid is formed and due to the aqueous equilibrium carbon dioxide gas is given off.

The precipitated solid was usually a cream/white solid although occasionally would appear more yellow. After recrystallisation from methanol and washing with deionised water a white crystalline solid is obtained.

Table 2.1: Some of the main Thiele's acid synthesis attempts with yields and observations grouped according to date and method. Please note that the scales used were not necessarily consistent and many small refinements in technique contributed to the improvements.

Dates	Method	Nitrogen	Toluene Grade	THF Grade	Reaction Colour	Product Colour	Yield
19/1/11	Direct (DCPD), A	Lab Supply	N/A	Dried	Brown	None	N/A
9/2/11	Indirect (CPD), A, Sodium Chunks	Lab Supply	N/A	Dried	Brown	Yellow/Brown	8.0%
19/4/11, 04/05/11	Indirect (CPD), A, Sodium Chunks	Airfree + Column	N/A	Dried	Pale Pink -> Red	Yellow	11.7%, 14.0%
20/10/11, 11/1/12, 16/2/12, 9/5/12,	Indirect (CPD), A, Sodium Chunks	Airfree + Column	N/A	Dried	Pale Pink -> Red	Yellow	7.88%., 5.48%, 7.51%, 16.9%,
17/7/12, 6/9/12, 22/11/12	Indirect (CPD), A, Sodium Sand	Airfree + Column	Dried	Dried	Pale Pink -> Red	Cream (near white)	12.4%, 20.9%, 20.1%
9/1/13	Indirect (CPD), B, Sodium Sand	Airfree + Column	Dried	Dried	Pale Pink -> Red	Cream (near white)	41.5%
16/7/13	Indirect (CPD), B, Sodium sand	Airfree + Column	Reagent	Dried	Pale Pink -> Red	Cream (near white)	63.9%

2.3.2 Thermal Data

The melting point of crude Thiele's acid was determined to be 198 - 202 °C . After recrystallisation the melting point was determined to be 210-212 °C . The literature value for the melting point can be taken from Thiele's original paper [17] as 212 °C . The increase in melting point after recrystallisation suggests that the purification step was indeed necessary. It is useful to find out which minor products are present to determine whether they are likely to cause a problem in the subsequent step,

see Section 2.3.3. The melting point of Thiele's acid was also measured using DSC (Figure 2.16) and found to be 211.7 °C with an onset at 206.1 °C and an end point of 213.0 °C . The enthalpy of fusion ΔH°_{fus}, was measured as 105.07 J g^{-1} which corresponds to 23.1 kJ mol^{-1}.

The melting point of Thiele's ester was found to be 85 °C which is an exact match with the literature [1, 5].

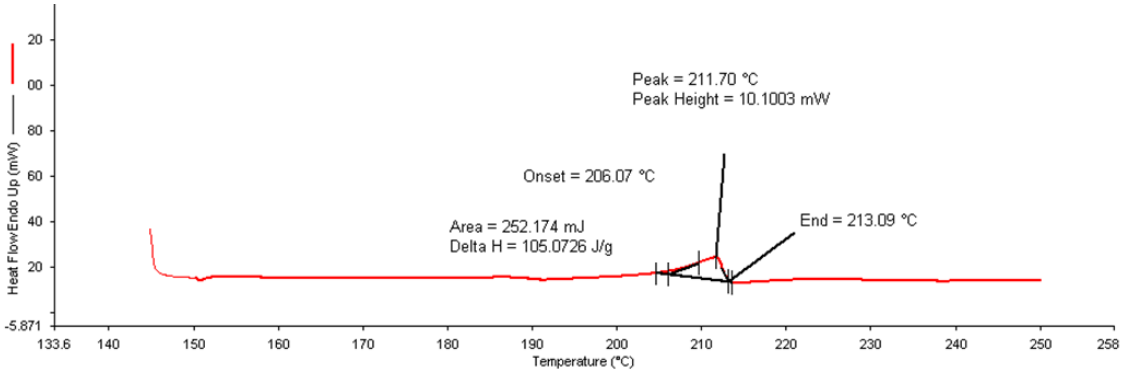

Figure 2.16: DSC of Thiele's Acid (From Batch 16/7/13)

2.3.3 NMR

The purpose of this section is to present, discus and assign the NMR spectra of the compounds synthesised in order to be confident in their identity and structure.

The NMR assignment of norbornene derivatives such as Thiele's acid is far from simple. The bi-cyclic ring system is highly strained and the electron distribution is unconventional due to an electron density redistribution towards a transition state that allows the retro-Diels-Alder reaction [18]. For example in ^{13}C NMR the bridging methylene group is moved down-field to about 50 ppm, an area of the spectrum that is normally reserved for carbons that are bonded to electronegative atoms.

In the proton NMR, due to the bi-cyclic nature of Thiele's acid, the bond angle between protons on the same carbon can be significantly reduced to less than 110° compared to 120° for their unstrained equivalents. The fixed ring system means the protons are not equivalent (*i.e.* resonate at different frequencies) and the bond angle creates unusually large geminal (^2J) couplings. Where a standard vicinal (^3J) coupling might be expected, the J value can actually be negligible if the dihedral

angle is small. In addition, enhanced long range (^4J) w-coupling interactions are often encountered where a W shaped path exists along 4 bonds and this effect is enhanced through allylic bonds [18]. The measured proton and carbon NMR spectra of Thiele's acid has a very good match to that previously reported in the literature [2] and also with that of Thiele's ester [8].

Assignment of the ^{1}H NMR of Thiele's Acid The proton NMR spectra of recrystallised Thiele's acid is presented in Appendix 1, Figure A.1 on page 276. It is of important note that the spectrum contains many complex coupling scenarios that hinders assignment however by use of NMR prediction algorithms [19, 20] and the published NMR study on Thiele's Ester [8] is is possible to assign each peak with confidence. The assignment is presented in table 2.1 using the hydrogen numbering system, shown in Figure 2.17a, along with literature shift values in brackets.

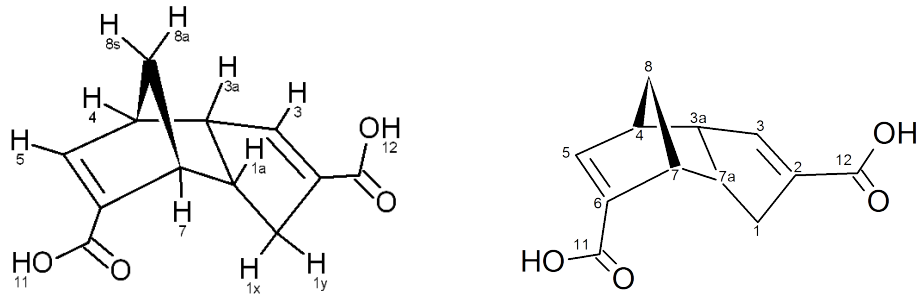

(a) Numbered Hydrogen atoms. **(b)** Numbered Carbon atoms.

Figure 2.17: Thiele's Acid Numbered for NMR Assignment

In addition to the measured J values it has been possible to make a reasonable hypothesis about the unresolved peaks (multiplets) from the literature mentioned above and their coupling. Coupling constants predicted to be about 1-3 Hz are not resolved on this NMR instrument but in some cases are clearly present. For example the resonance signatures of protons 3a and 7a are extremely complex due to multiple small interactions and are simply referred to as a multiplet (m) in the table.

For the reasons mentioned previously strong geminal coupling has been observed in two cases between individual protons in separate electronic circumstances (1x-1y) and also on the methylene bridge (*i.e.* 8x-8y). There are no examples of long range ^4J coupling that can be resolved in this case but the NMR study [8] suggests that

Table 2.2: Proton NMR Assignment of Thiele's Acid

$H_{\#}$	δ_{exp}	δ_{lit}	$\int$	Mult.	J	Comments
	2.50					Solvent Peak
11, 12	12.5	12.08	2	s		Acidic Protons
5	6.74	6.73	1	d	(5-4) $^3J = 3.4$	Vinyl Proton
3	6.40	6.39	1	s		Vinyl proton couplings with 1x, 1y and 3a too small to be resolved
3a	3.47	3.47	1	m	(3a-7a) $^3J = 8.5$	Coupled with 4 and with 1x (w-coupling)
7	3.18	3.18	1	d		Coupled with 7a
4	3.10	3.11	1	s	(4-5) $^3J = 3.4$	
7a	2.88	2.91	1	m	(7a-3a) $^3J = 8.5$ (7a-1y) $^3J = 10.4$	Also coupled with 1x (weaker than 1y) and with 7.
1y	2.30	2.31	1	dd	(1y-1x) $^2J = 18$, (1y-7a) $^3J = 10.4$	Strong geminal coupling!
1x	1.90	1.88	1	d	(1x-1y) $^2J = 18$	
8y	1.54	1.54	1	d	(8y-8x) $^2J = 8.5$	
8x	1.36	1.37	1	d	(8x-8y) $^2J = 8.5$	

$H_{\#}$ proton number from figure 2.17a.

δ_{exp} measured chemical shift from the spectrum in appendix A.1 in ppm.

δ_{lit} chemical shift from the literature [2] in ppm.

$\int$ measured integration.

Mult. multiplicity.

J coupling constant in Hz.

(3a-1x) would have a J value of about 4 Hz if it could be isolated from the multiplet. The variable intensity of the vicinal (^3J) coupling can be exemplified by the coupling of (7a-1y) which is 8.5 Hz but the coupling (7a-1x) is not observable, according to the NMR study [8] in Thiele's Ester it is 4 Hz. From this information it is possible to conclude that proton 1y is more antiperiplanar with proton 7a compared to proton 1x as would be expected in an endo configuration.

Assignment of the ^{13}C NMR of Acid The ^{13}C spectrum for Thiele's acid can be found in Appendix 1, Figure A.2 on page 277. The data and atom assignments have been compiled in table 2.3 using the atom numbering system shown in Figure 2.17b and literature values in brackets. The phase (either up or down) from the spectrum

gives information about the proton substitution on a given carbon atom. In this case due to the JMODulation experiment the carbon atoms with an odd number of protons show an UP phase whereas the carbon atoms with an even number of (or no) protons show a DOWN phase.

Table 2.3: ^{13}C NMR Assignment of Thiele's Acid

$C_{\#}$	δ_{exp}	δ_{lit}	Phase	Type	Comments
N.A.	39.35-40.68				Solvent peaks.
9	166.38	166.37	↑	C	Carbonyl carbon
10	166.12	166.12	↑	C	Carbonyl carbon
5	147.29	147.24	↓	CH	Vinyl carbon
3	142.91	142.88	↓	CH	Vinyl carbon
6	139.51	139.54	↑	C	Adjacent to carbonyl carbon
2	138.61	138.63	↑	C	Adjacent to carbonyl carbon
3a	54.26	54.27	↓	CH	
8	50.57	50.59	↑	CH_2	Methylene bridge
4	47.28	47.29	↓	CH	
7	46.54	46.56	↓	CH	
7a	40.68	40.70	↓	CH	
1	33.13	33.14	↑	CH_2	
N.A.	31.16		↓		Weak (probably just noise).

$C_{\#}$ proton number from the figure 2.17b.

δ_{exp} measured chemical shift from the spectrum in appendix A.2 in ppm.

δ_{lit} chemical shift from the literature in ppm [2].

In this particular spectrum there is a rogue signal (31.16 ppm) that does not seem to match any known impurities/solvent traces [21], however it is a fairly weak signal and can most likely be attributed to noise.

Investigation of Minor Products by the^{1}H NMR of Thiele's Ester and Crude Thiele's Acid

As a check the ^{1}H NMR was also run for Thiele's Ester. An example spectrum is shown in Appendix 1, Figure A.3. While the spectrum suffers from a poor shim, (leading to a curved baseline that inhibits proper integration) the conversion can be confirmed by the loss of the resonance associated with the acidic protons at 12.5 ppm. In addition there is a gain of the large resonance at 3.74 ppm that dominates the

other peaks due to the 2 pairs of -O-CH_3 protons in the ester. From this information (along with the melting point presented in Section 2.3.2) it is possible to conclude that Thiele's Ester has been successfully produced.

The original aim of producing the methyl ester was to replicate some of the work done by Alan Marchard in 1998 [12] and check that the minor products produced in this reaction were consistent with his findings. Unlike the acid, the different ester isomers can be separated using column chromatography. Due to time constraints and laboratory availability issues this planned work was not done. Table 2.1 shows that Thiele's acid was only produced on a reasonable scale late in 2013 (*i.e* the final year) and priorities had to shift towards optimising the monomer synthesis, resin modification, composite specimen production and testing.

One possible minor product is the trimer as reported by Murphy [2] (Figure 2.18a). Other likely minor products are the ones isolated by Marchand [12], mainly the structure shown in Figure 2.18b which was found to be 13% of the crude product. In the absence of the separated ester fractions it is possible to make some assertions based upon the proton NMR of the crude Thiele's acid (*i.e.* before recrystallisation from methanol) which is available in appendix 1 Figure A.4. The pure and the crude NMR spectra have been overlaid in Figure 2.19.

Figure 2.18: Possible minor products expected from the synthesis of Thiele's Acid [2, 12].

Running NMR prediction algorithms [19, 20] on the trimer structure showed that the major differences in the proton NMR would be mainly in the already crowded high-field 1-3 ppm area of the spectrum. The extra peaks around 1.6 ppm and 1.8 ppm could be explained by the presence of this trimer but the extra peaks in the vinyl region *i.e.* 6 and 6.2 ppm can not be explained by the trimer. The trimer

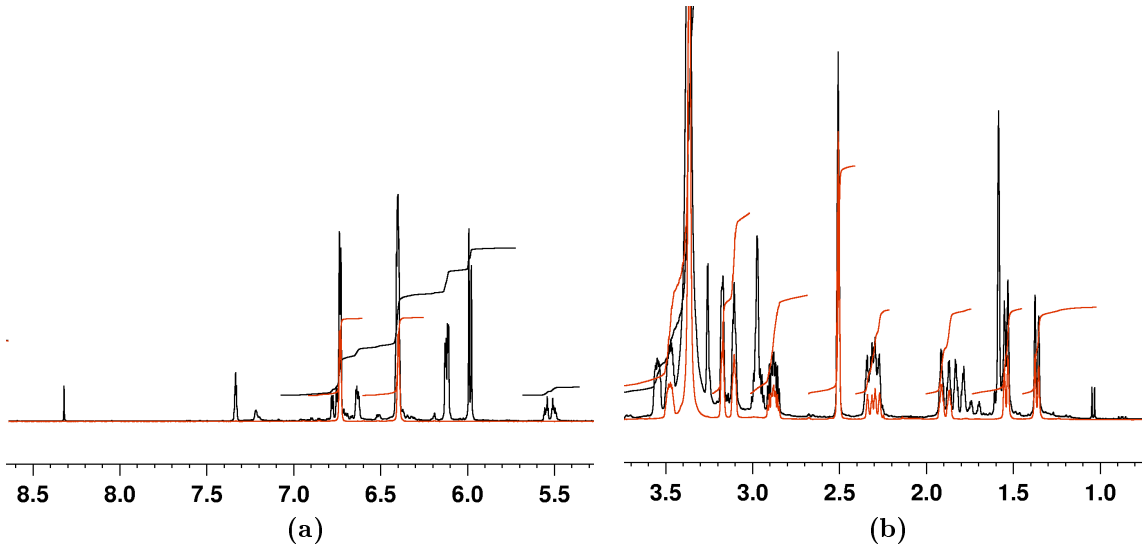

Figure 2.19: The main regions of interest in the proton NMR of crude Thiele's acid with the pure Thiele's acid overlaid in red for easy comparison (or grey in grey-scale prints).

would also give an extra acidic proton resonance in the very low-field region. The exact position of acidic protons are not easy to model with any level of accuracy (errors are 3-4 ppm) but the model did suggest that the extra acidic proton would resonate at significantly higher field 9.7 ppm (± 3.3 ppm) compared to 11.65 ppm (± 3.57 ppm) for the other acidic protons. Therefore it is possible that the small resonance at 8.3 ppm could be due to the trimer but that would be quite a leap of faith.

Running the same NMR prediction algorithms on the structure in 2.18b made the picture significantly clearer as the presence of this structure could account for all of the major additional peaks in the crude spectrum. The change in the location of the carbonyl group could cause the small changes in the high-field region and would present as additional peaks in an isomer mixture. The two peaks (6, 6.1 ppm) in the vinyl region can be explained by the presence of an unsubstituted vinyl group. This creates a new vinyl proton resonance and also due to the removal of the carbonyl group both vinyl protons now resonate at slightly higher field. It is also likely that the acidic proton resonance shifts to higher field but again this cannot be modelled with any degree of accuracy.

From this data it is possible to say with reasonable confidence that the structure

2.18b is present in the crude acid mixture. It is not possible to dismiss the possibility that the trimer is also present from the crude NMR alone. What is certain is that the recrystallisation step is efficient at removing the vast majority of these minor components.

2.4 Summary

In this chapter Thiele's Acid has been introduced as it is a constant precursor for the self-healing polymers that are synthesised and integrated into composite systems in the following chapters. As this compound underpins all subsequent work, the structure and reactivity of Thiele's acid has been discussed with reference to relevant historical literature. The synthesis of Thiele's Acid was not simple and required considerable refinement was necessary; that refinement was undertaken and presented in this chapter. The method (see Section 2.2.3) developed was a reactive distillation of DCPD into CPD which was reduced by sodium metal followed by a reaction with a slurry of tetrahydrofuran and solid carbon dioxide (all under a nitrogen inert atmosphere). An acid-base extraction followed by a recrystallisation from methanol formed the purification steps. The final process was well suited to the laboratory equipment and facilities available and did not require high purity argon or difficult air-free filtration steps.

The structure that was synthesised has been confirmed by a clear proton and carbon NMR that matches up well with literature values and does not show any significant impurities. The minor products have not been separated and identified but NMR evidence suggests that the minor products identified by Marchard [12] are present in the crude mixture.

Recrystallisation from methanol gives a product with a purity that has been demonstrated to be excellent by a close melting point match with that known in the literature. The final batch size that was synthesised is 72.32 g which corresponds to a molar yield of 63.9% which provided plenty of of material for later monomer synthesis.

2.5 References

(1) J. Thiele, "Ueber Ketonreaotionen bei dem Cyclopentadiën.", *Chem. Ber.*, 1900, **33**, 666.
(Cit. on pp. 63, 83.).

(2) E. B. Murphy, E. Bolanos, C. Schaffner-Hamann, F. Wudl, S. R. Nutt, and M. L. Auad, "Synthesis and Characterization of a Single-Component Thermally Remendable Polymer Network: Staudinger and Stille Revisited", *Macromolecules*, 2008, **41**, 5203–5209.
(Cit. on pp. 63, 79, 84–87.).

(3) K. Alder, F. H. Flock, A. Hausweiler, and R. Reeber, "Über die Konstitution der Cyclopentadien-carbonsä ure aus Cyclopentadien-kalium", *Chem. Ber.*, 1954, **87**, 1752–1759.
(Cit. on pp. 64, 65.).

(4) IUPAC, *Nomenclature of Organic Chemistry*, Pergamon Press, Oxford, 1979.
(Cit. on p. 64.).

(5) D. Peters, "Cyclopentadiene carboxylc acid: the structure of the monomer and the dimers", *J. Chem. Soc.*, 1959, 1761–1765.
(Cit. on pp. 64, 65, 67, 83.).

(6) R. B. Woodward and R. Hoffmann, "The Conservation of Orbital Symmetry", *Angew. Chem., Int. Ed. Engl.*, 1969, **8**, 781–853.
(Cit. on p. 66.).

(7) G. L. Dunn and J. K. Donohue, "The structure of thiele's ester, a dimethyl dicyclopentadienedicarboxylate", *Tetrahedron Lett.*, 1968, **31**, 3485–3487.
(Cit. on p. 66.).

(8) E. M. Minter, A. P. Marchand, and S.-p. Lu, "Structural Analysis and Complete Assignment of the 1H and 13C NMR Spectra of Thiele's Ester", *Magn. Reson. Chem.*, 1990, **28**, 623.
(Cit. on pp. 66, 84, 85.).

(9) G. P. Moss, "International Union of Pure and Applied Chemistry: Nomenclature of fused and bridged fused ring systems.", *Pure Appl. Chem.*, 1998, **70**, 143–216.
(Cit. on pp. 66, 67.).

(10) H. Chatelier-Le, "Sur un énoncé général des lois des équilibres chimiques", *Comptes rendus.*, 1884, **99**, 786 –789.
(Cit. on p. 69.).

(11) J. Clayden, N. Greeves, S. Warren, and P. Wothers, *Organic Chemistry*, Oxford University Press, 2001.
(Cit. on p. 70.).

(12) A. P. Marchand, I. Namboothiri, S. B. Lewis, W. H. Watson, and M. Krawiec, "Thiele's acid revisited: Isolation and characterization of two minor products formed by carbonation of cyclopentadienide anion", *Tetrahedron*, 1998, **54**, 12691–12698.
(Cit. on pp. 70, 87, 90.).

(13) A. Frontier, *"Not Voodoo" The Grasshopper's Guide to Cleaning Glassware*, Published Online (Accessed 2nd November 2011), `http://chem.chem.rochester.edu/~nvd/cleaningglassware.html`.
(Cit. on p. 71.).

(14) E.-S. Park, H. Park, J. Jeon, J.-U. Sung, W.-S. Hwang, and B.-Y. Lee, "Ring-opening metathesis polymerization of dicyclopentadiene and tricyclopentadiene", *Macromol. Res.*, 2013, **21**, 114–117.
(Cit. on p. 79.).

(15) M. R. Kessler and S. R. White, "Cure kinetics of the ring-opening metathesis polymerization of dicyclopentadiene", *J. Polym. Sci., Part A: Polym. Chem.*, 2002, **40**, 2373–2383.
(Cit. on p. 79.).

(16) A. Leitgeb, J. Wappel, and C. Slugovc, "The {ROMP} toolbox upgraded", *Polymer*, 2010, **51**, 2927 –2946.
(Cit. on p. 79.).

(17) J. Thiele, "Ueber Abkömmlinge des Cyclopentadiëns", *Chem. Ber.*, 1901, **34**, 68.
(Cit. on p. 82.).

(18) S. N. Steinmann, P. Vogel, Y. Mo, and C. Corminboeuf, "The norbornene mystery revealed.", *Chem. Commun. (Cambridge, U. K.)*, 2011, **47**, 227–229.
(Cit. on pp. 83, 84.).

(19) *ACD Ilabs NMR Predictor*, Online Tool (Accessed 29th September 2013), `http://ilab.acdlabs.com/iLab2/`.
(Cit. on pp. 84, 87.).

(20) A. M. Castillo, L. Patiny, and J. Wist, "Fast and Accurate Algorithm for the simulation of NMR spectra of Large Spin Systems.", *J. Magn. Reson.*, 2011, **209**, 123–130.
(Cit. on pp. 84, 87.).

(21) H. E. Gottlieb, V. Kotlyar, and A. Nudelman, "NMR Chemical Shifts of Common Laboratory Solvents as Trace Impurities", *J. Org. Chem.*, 1997, **62**, 7512–7515.
(Cit. on p. 86.).

Chapter 3

Synthesis Part B: The Monomers

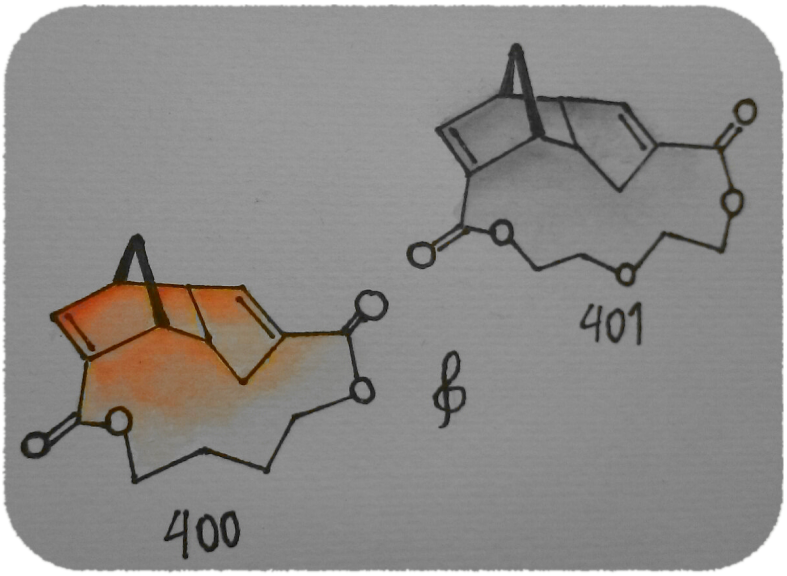

3.1 Introduction

As stated in Section 1.1 on page 3 the overall objective of this work is to synthesise and integrate a self-healing additive into an established epoxy resin system in order to allow for thermally activated self-healing in carbon fibre composites. The purpose of this chapter is to present the synthesis of monomers that have the potential to be that additive and can polymerise thermally via a Diels-Alder mechanism. The concept of reversible Diels-Alder based polymers was first introduced in Chapter 1, Section 1.4.4 on page 31 in the discussion about the work by Chen *et al.*[1]*;* Liu and Hsich [2, 3] and Murphy *et al.* [4] in which their aim was to produce self-healing bulk materials.

In this thesis the application is different; it is to investigate if this class of materials can be used as additives to established polymer composite resin systems in order to impart self-healing or other beneficial properties without requiring a complete change in resin system. Advantages of a additive system include lower costs, established performance, easier certification and acceptance in the market compared to the development of a completely new matrix system.

Thermally activated self-healing in epoxy matrices by the inclusion of additives has been established previously as a viable approach by Hayes *et al.* in 2007 [5, 6] and was discussed in Chapter 1, Section 1.4.3 on page 30. The work by Hayes *et al.* featured the inclusion of a compatible linear polymer that can bridge microcracks upon heating. The migration of the linear polymer was shown to arrest further damage propagation and restore physical properties.

Recent work by Jamil identified a limitation of this healing system in that after physical ageing of the epoxy matrix the intrinsic repair ability reduces in its effectiveness [7]. The reduction in effectiveness was shown to be due to the reduction of free volume within the matrix, which in turn reduces the ability of the linear polymer to migrate to the damage site. The migration of the healing agent occurs via a reptation mechanism through the free volume of the polymer matrix but as this reduces and contracts with age and consequently this migration is hindered. The fact that the healing agent is a high molecular weight linear polymer restricts migration still further. This is a difficult hurdle to surmount because reducing the

molecular weight increases the mobility of the healing agent but also reduces the mechanical properties of the polymer and thus the extent of property recovery.

The original aim of this work was to overcome this limitation by the synthesis of an alternative healing agent containing reversible covalent bonds that, upon heating, can disconnect and thus enable diffusion throughout the matrix. A class of compounds, based on Thiele's acid, were selected as potential healing agents. The rationale behind choosing this class of materials was that the final structure could be fine-tuned by selection of an appropriate diol or glycol and thus could be matched to the composition of the epoxy matrix.

3.1.1 Synthesis of Thiele's Acid Chloride

3a,4,7,7a-tetrahydro-1H-4,7-methanoindene-2,6-dicarbonyl dichloride, which is the acyl chloride derivative of Thiele's acid, is the subject of this section; it will be known throughout this thesis simply as Thiele's acid chloride. The formation of an ester group by the reaction of an acyl chloride (such as Thiele's acid chloride) with an alcohol is a common reaction in organic chemistry. This reaction is more efficient than the direct esterification between a carboxylic acid and an alcohol because the acyl chloride is more reactive than a carboxylic acid and has a better leaving group (the chloride). Good quantitative yields are possible because the ester is more stable than the acid chloride and so the thermodynamic equilibrium particularly favours the formation of the product. It is for this reason the synthesis of the monomers will take place via an acyl chloride path. In this section the methods of generating Thiele's acid chloride will be proposed.

Using Thionyl Chloride

The most common reagent used for forming acyl chlorides from carboxylic acids is thionyl chloride ($SOCl_2$). This thio-chloride reagent would react with Thiele's acid as shown in the scheme presented in Figure 3.1 [8].

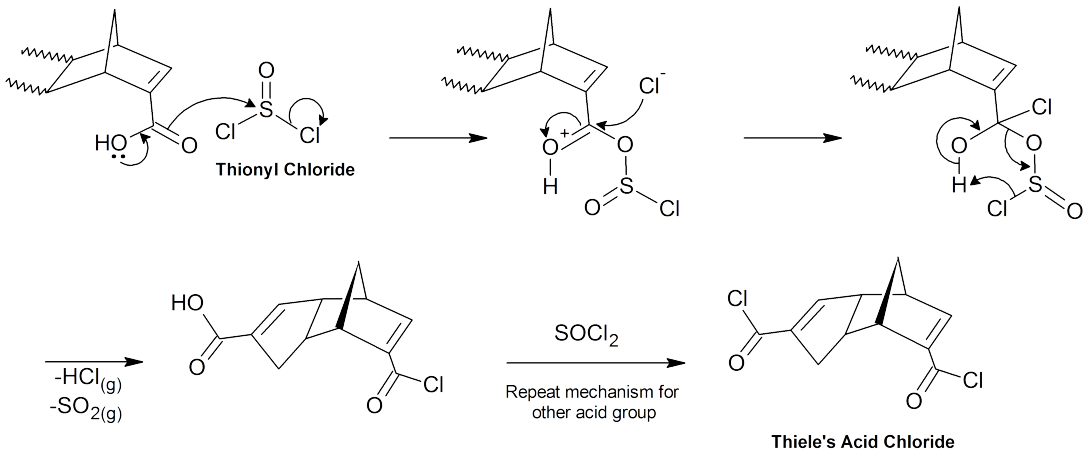

Figure 3.1: The reaction of Thiele's acid with thionyl chloride to form Thiele's acid chloride. For the first half of the mechanism half of the molecule has been omitted to aid clarity[9] [8].

The main advantage of using thionyl chloride is its high reactivity and the fact that gaseous by products (HCl and SO_2) are generated, which can be easily removed from the system and effectively ensure the reaction is not reversible. The cessation of gas generation is also useful as a marker for the end of the reaction. The high volatility of thionyl chloride allows easy removal of excess reagent from the reaction by vacuum distillation which makes it a convenient reagent to use.

Using Oxalyl Chloride

Oxalyl chloride, $(COCl)_2$, is another reagent that can be used to form acyl chloride from carboxylic acids. The reaction proceeds via a similar mechanism as that shown for thionyl chloride (Figure 3.1); but it is generally milder and more selective than thionyl chloride and so requires longer reaction times. In order to speed up the reaction, it is common to use dimethyl formamide (DMF), $(CH_3)_2NC(O)H$) as a catalyst which reacts with oxalyl chloride as shown in Figure 3.2 to form a reactive substituted chloroiminium ion, also called the Vilsmeier reagent. The Vilsmeier reagent is also commonly encountered in the Vilsmeier–Haack reaction in which an aryl ketone or aldehyde is produced from a substituted amide.

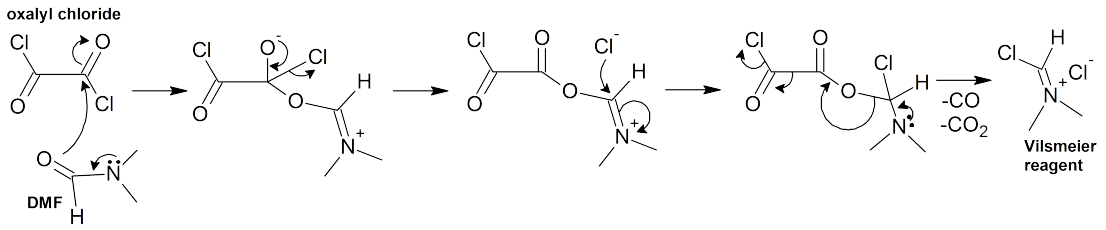

Figure 3.2: The reaction of oxalyl chloride with dimethyl formamide to form the reactive Vilsmeier reagent.

The Vilsmeier reagent goes on to react with the carboxylic acid (in this case, Thiele's acid) to form Thiele's acid chloride (see Figure 3.3). DMF is regenerated in the reaction and can therefore go on to react with another equivalent of oxalyl chloride to form more Vilsmeier reagent.

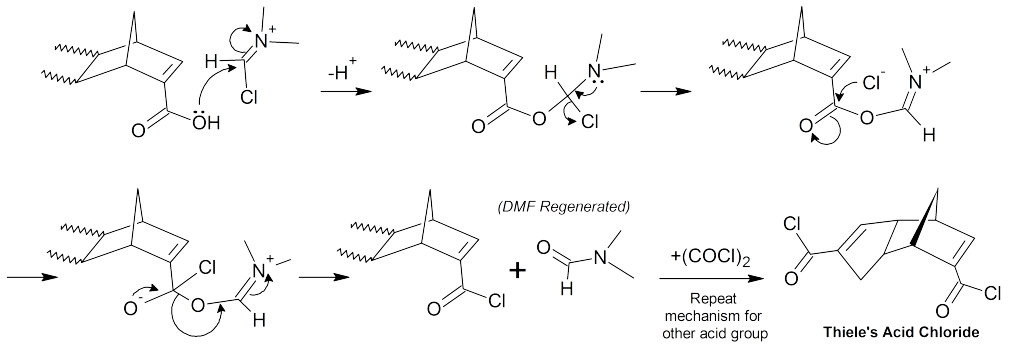

Figure 3.3: The reaction of the Vilsmeier reagent with Thiele's acid to produce Thiele's acid chloride.

The advantages of using oxalyl chloride and DMF are similar to those for thionyl chloride, in that the by products are gaseous (CO and CO_2) and the work-up is similar because excess oxalyl chloride can also be removed easily using vacuum distillation. The reaction can be done in a dry solvent such as dichloromethane which gives milder conditions for sensitive substrates; therefore oxalyl chloride only tends to be used where the milder conditions are necessary due to the fact that it costs around twice as much as thionyl chloride. It should be noted that DMF can also act as a catalyst with thionyl chloride to produce milder conditions, but this also produces a carcinogenic minor product (dimethylcarbamoyl chloride) and so its use today is not advised [10].

Using Phosphorus Pentachloride

Phosphorus pentachloride (PCl_5) is a general purpose chlorinating agent and is also an effective reagent for forming acyl chlorides from carboxylic acids as shown on Figure 3.4.

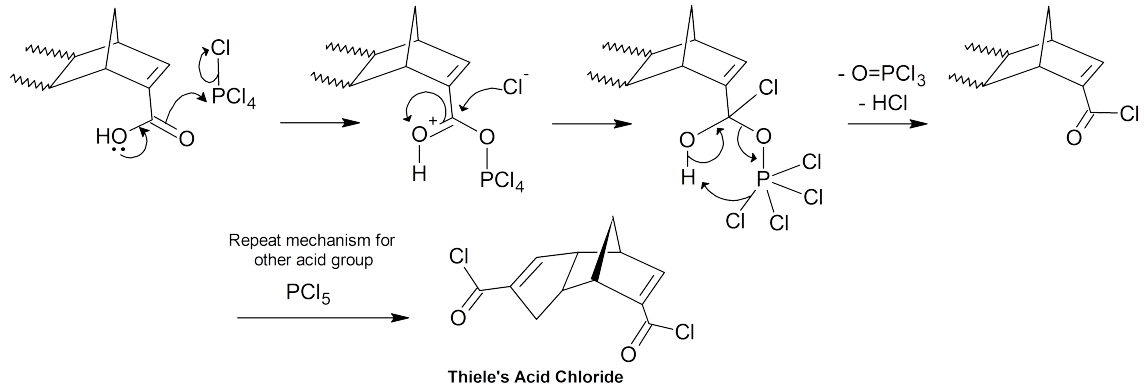

Figure 3.4: The reaction of Thiele's acid with phosphorus pentachloride to produce Thiele's acid chloride [8, 9].

As with the previous reactions this mechanism is driven by the production of gaseous HCl however unlike the previous reactions the main by-product phosphoryl chloride is liquid at room temperature (*b.p.* 106 °C) and so has to be separated by fractional distillation which makes the work-up inconvenient and expensive.

3.1.2 Nucleophilic Acyl Substitution with Pyridine Catalyst

The acyl substitution reaction is often conducted in the presence of a nucleophilic or basic catalyst; in this work that catalyst is pyridine and it will be discussed in this section.

Pyridine, C_5H_5N, (Figure 3.5) is used as a catalyst for the esterification reactions between Thiele's acid chloride and the various types of hydroxyl bearing reagents used in this chapter. Pyridine is an aromatic compound in which the nitrogen atom contributes 1π electron to the 6π electrons required for the system to be aromatic ($4n + 2$ n=1).

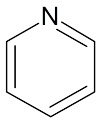

Figure 3.5: Pyridine.

Pyridine's lone pair on the nitrogen is accommodated in a hybrid sp^2 orbital which makes it available for protonation, and therefore, basic. The pK_a of pyridine's conjugate acid (pK_{aH}) is 5.21 which means pyridine is a relatively weak base compared to hydroxide, for example, which has a $pK_{aH} > 13$.

There are three main types of catalysis that may occur during a nucleophilic substitution at a carbonyl carbon such as the conversion of Thiele's acid chloride into an ester. The first and most widely accepted is nucleophilic catalysis as shown in Figure 3.6.

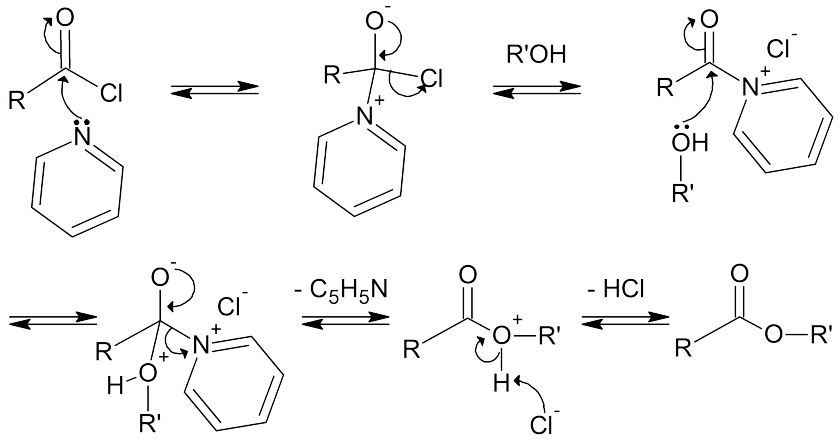

Figure 3.6: A mechanism showing pyridine acting as a nucleophilic catalyst in the generalised reaction between an acyl chloride and an alcohol [11, Chap. 3].

Pyridine is more nucleophilic than most alcohols and so reacts with the acyl chloride to form, via a tetrahedral intermediate, a positively charged and therefore highly electrophilic species. The electrophilic species reacts directly with the alcohol, again via a tetrahedral intermediate, to form an ester. The tetrahedral intermediate (N-acetylpyridinium) is an excellent leaving group and cannot form a resonance stabilised amide because its tertiary nature means it can not lose a proton [12]. The

pyridine is regenerated during the reaction but will react with the hydrogen chloride produced to form a pyridinium hydrochloride salt; this is incapable of further catalysis so a stoichiometric minimum of pyridine is required [8].

The other two types of catalysis are base catalysed and can either be specific (Figure 3.7a) or general (3.7b). In water, specific base catalysis involves the hydroxide (OH^-) ion; but in aprotic solvents (such as the reactions in this chapter) specific base catalysis would require the direct deprotonation of the alcohol by the base (pyridine) in a fast pre-equilibrium step [8]. Due to the low acidity of the alcohol groups and the weakness of the pyridine as a base, specific base catalysis can be dismissed as a viable mechanism. Attempts to use stopped flow kinetics to identify reaction orders and experiments designed to detect alcoxide intermediates also suggest that specific base catalysis is not a significant contributor to the reaction path for these kind of amine-catalysed reactions of carbonyl compounds [13].

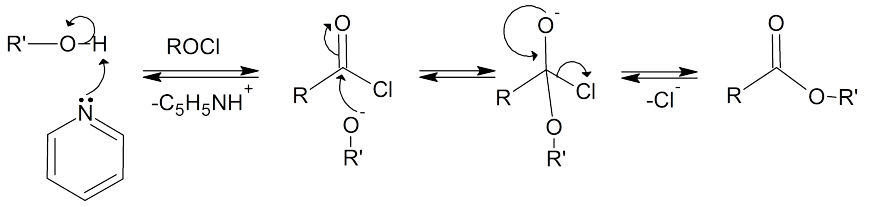

(a) Specific base catalysis.

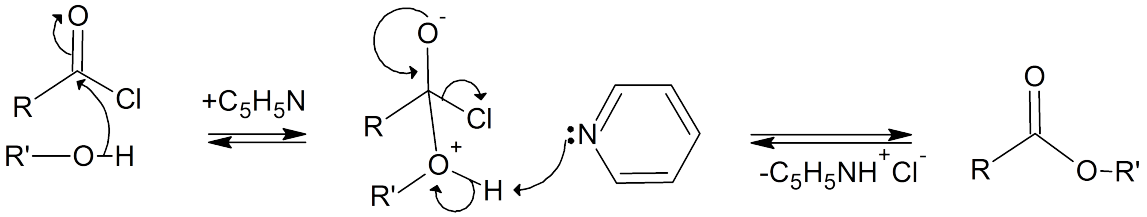

(b) General base catalysis.

Figure 3.7: Types of possible base catalysis involving pyridine as a catalyst for the formation of esters from acyl chlorides and alcohols.

General base catalysis (Figure 3.7b) operates in a similar manner to specific base catalysis, except that instead of deprotonating the alcohol, the base can be seen as removing the proton either in the tetrahedral intermediate or somewhere between the attack of the alcohol on the carbonyl and the intermediate [8]. Another way to view general base catalysis is that the base co-ordinates to the alcohol and so increases

the local negative charge on the oxygen atom and so facilitating nucleophilic attack on the carbonyl carbon.

There is limited information available in the literature about the mechanism of reaction of acyl chlorides with alcohols in aprotic solvents and what is available does not include amine catalysis [14, 15]. There is some limited evidence of general base catalysis for alcohol reactions with aromatic acid chlorides [13], but no work has been done involving large fused-ring substrates such as Thiele's acid chloride.

In the absence of detailed mechanistic information and the fact that such study is far from the scope of this thesis the catalysis mechanism will be assumed to be nucleophilic; but it is accepted that there is a possibility that general base catalysis may also have a part to play.

3.2 Experimental

3.2.1 Modelling of the Hansen Solubility Parameters

Hansen solubility parameters can be calculated by using a semi-empirical group contribution method [16].

For high molecular weight polymers the repeat unit can be used for these purposes. Throughout the calculation data from Barton [17] has been used.

The total solubility parameter (δ_t) [17] can be calculated as follows for oligomers and small molecules:

$$\delta_t = \frac{(\sum_z F_z + B)}{V_z} \tag{3.1}$$

and for polymers:

$$\delta_t = \frac{(\sum_z F_z + \frac{B}{n})}{V_z} \tag{3.2}$$

$$n = \frac{1}{2} \sum_z \Delta_T^P \tag{3.3}$$

Where:

F_z is the molar attraction constant for the fragment 'z' in $J^{\frac{1}{2}}$ $cm^{\frac{1}{2}}$ mol^{-1},

V_z is the molar volume of the fragment 'z' in mol cm^{-3},

B is a constant of value 275.3 $J^{\frac{1}{2}}$ $cm^{\frac{1}{2}}$ mol^{-1},

n is the number of monomer units estimated for a segment of chain (Equation 3.3),

Δ_T^P are critical temperature Lyderson group constants for a polymer fragment 'z' [17].

The hydrogen bond contribution δ_h is calculated from the total solubility parameter as follows:

$$\delta_h = \delta_t \sqrt{\frac{(\alpha - 1)}{\alpha}} \tag{3.4}$$

In the case of a small molecule or oligomer:

α is calculated as follows:

$$\log \alpha = 3.39006 \frac{T_b}{T_c} - 0.15848 - \log(\sum_z V_z) \tag{3.5}$$

T_b is the normal boiling point .

T_c is the critical temperature..

$\frac{T_b}{T_c}$ is calculated from the Lyderson equation as follows [17]:

$$\frac{T_b}{T_c} = 0.567 + \sum_z \Delta_T - \log(\sum_z \Delta_T)^2 \tag{3.6}$$

Δ_T is the Lyderson constant (case small molecule) for the fragment 'z'.

In the case of a polymer: α is the chain aggregation number for the polymer that can be calculated as follows [17].

$$\alpha = \frac{777.4 \sum \Delta_T^P}{\sum V_z} \tag{3.7}$$

The polar contribution (δ_p) is calculated from the total solubility parameter as follows:

$$\delta_p = \delta_t \sqrt{\frac{\sum_z F_{zp}}{a(\sum_z F_z + \frac{B}{n})}} \tag{3.8}$$

Where:

F_{zp} is the polar molar attraction parameter for the fragment 'z'.

The dispersive contribution (δ_d) is calculated by subtracting the (squared) polar and hydrogen bonding contributions from the total solubility parameter [17].

$$\delta_d = \sqrt{\delta_t^2 - \delta_h^2 - \delta_p^2} \tag{3.9}$$

3.2.2 Equipment

All glassware used in this synthesis was cleaned, dried and prepared as described in Chapter 2, Section 2.2.1 on page 71.

3.2.3 Reagents

- Thiele's acid was produced in Chapter 2 was not further purified other than the recrystallisation described in Section 2.2.3 on page 77.
- Pyridine was supplied by Sigma Aldrich, Gillingham, UK as 99.8% anhydrous grade in a sure-seal bottle and used as received.
- Thionyl chloride and oxalyl chloride were supplied by VWR, East Grinstead, UK as reagent grade >97% purity and used as received.
- 1,4-butane diol and triethylene glycol was supplied by Sigma Aldrich, Gillingham, UK as 'reagent plus' 99% and initially used as received. Later the 1,4-butane diol reagent was distilled from (and stored over) 4Å molecular sieves in an attempt to troubleshoot yield problems.
- Diethylene glycol was supplied by VWR, East Grinstead, UK as reagent grade 98% and used as received.
- Bisphenol-A was supplied by Sigma Aldrich, Gillingham, UK as a general purpose 97% grade and used as received.
- Ppoly(tetrahydrofuran) M_n = 250 g mol^{-1}, hydroxyl value = 415.6 - 487.8 mg KOH g^{-1}, was supplied by Sigma Aldrich, Gillingham, UK with no purity given .

- Where solvents are described as 'dried' this was done using a drying column consisting of an activated alumina/copper catalyst and inert nitrogen atmosphere. The water content for the dried solvents varied on a day-to-day basis but was always <14 ppm as determined by Karl-Fischer titration.
- All other reagents were of reagent grade and supplied by Sigma Aldrich, Gillingham, UK and used with no further purification.

3.2.4 Thin Layer Chromatography

Thin layer chromatography was carried with silica gel on aluminium plates with a U.V. fluorescent indicator. The UV fluorescence was not used as an indicator due to lack of convenient access to a UV light box in the laboratory. Ttherefore in order to visualise, the plates were dipped in a solution (*c.a.* 1%) of phosphomolybdic acid in methanol and developed using a heat gun.

The plates were spotted using a glass capillaries that were produced by drawing a glass pasteur pipettes in a blowtorch flame.

The retention factor R_f is the ratio of the distance travelled by the solvent front against the distance travelled by the compound. It was calculated as follows:

$$R_f = \frac{d_c}{d_s} \tag{3.10}$$

Where:
d_c is the distance travelled up the plate by the compound of interest.
d_s is the distance travelled up the plate by the solvent front (mobile phase).

3.2.5 Flash Column / Preparative Chromatography

Flash column chromatography was carried out using the technique first described by Still in 1978 [18] with the following modifications.

Two different columns were used depending on the size of the sample to load. For small quantities the small column was used and for larger quantities of material >0.5 g the larger column was used.

The small column was a 3 cm diameter, 10 cm height, addition funnel (without the pressure equalising side-arm) with cotton wool inserted above the tap and then covered with sand until the end of the taper. A second dropping funnel was connected to the top of this addition funnel to act as a solvent reservoir.

The large column was purpose made with a glass frit above the tap, 6.5 cm diameter, 46 cm height with the addition of a fixed 1L solvent reservoir bulb.

The columns were wet-packed and the full volume of solvent used was allowed to flow through the columns to allow sufficient pre-equilibrium. The mixtures were mostly wet-loaded without an upper sand layer.

The silica gel used had a pore size of 60 Å, and a mesh of 200-400 μm.

3.2.6 NMR

All NMRs were measured using a Bruker Avance 400 instrument equipped with a 5mm $^{1}H/^{13}C$ probe. ^{1}H experiments were measured using a 12 ppm sweep width.^{13}C experiments were proton decoupled and measured over a 240 ppm sweep width using J-modulation which uses the SEFT (Spin-Echo Fourier Transform) technique to differentiate between odd and even amounts of protons on the carbon atoms (*i.e.* CH/CH_3 from C/CH_2. All NMR experiments for this chapter used deuterated chloroform as the solvent.

3.2.7 Thionyl Chloride with Oxalyl Chloride Comparison

Two parallel experiments were undertaken, one with thionyl chloride, the other with oxalyl chloride. Under dry nitrogen Thiele's acid (0.1 g, 0.45 mmol) was added to a 3-necked 100 ml round bottomed flask equipped with a reflux condenser; to this was added 20 ml of thionyl chloride or oxalyl chloride. The flask was warmed to 60 °C for 4 hours and the acylating agent was removed by vacuum distillation. Dry THF was added (50 ml) along with pyridine (0.2 ml, 2.48 mmol) and methanol (0.1 ml, 2.47 mmol).

The mixture was stirred for 30 min after which the solvent was removed on the rotary evaporator. The resulting brown solid was washed with 10% aqueous hydrochloric acid (HCl) and extracted, three times, with dichloromethane (DCM). Thin layer chromatography (TLC) was done on the solution using DCM as the

mobile phase. The DCM was removed using a rotary evaporator and the products were left to dry under high vacuum for 24 hours.

3.2.8 Thiele's Acid Chloride Synthesis

Reaction Setup

A standard vacuum distillation assembly was used (see Figure 3.8) which consisted of a two-necked 500 ml distillation flask with one neck sealed with a glass stopper; a standard distillation head and thermometer; a Liebig condenser; a vacuum adaptor connected to the double manifold; and a 500 ml round-bottomed receiving flask. The distillation equipment was flamed under vacuum and refilled with dry nitrogen gas and allowed to cool. When cool, the setup was further evacuated and refilled twice more to ensure complete removal of atmospheric contaminants.

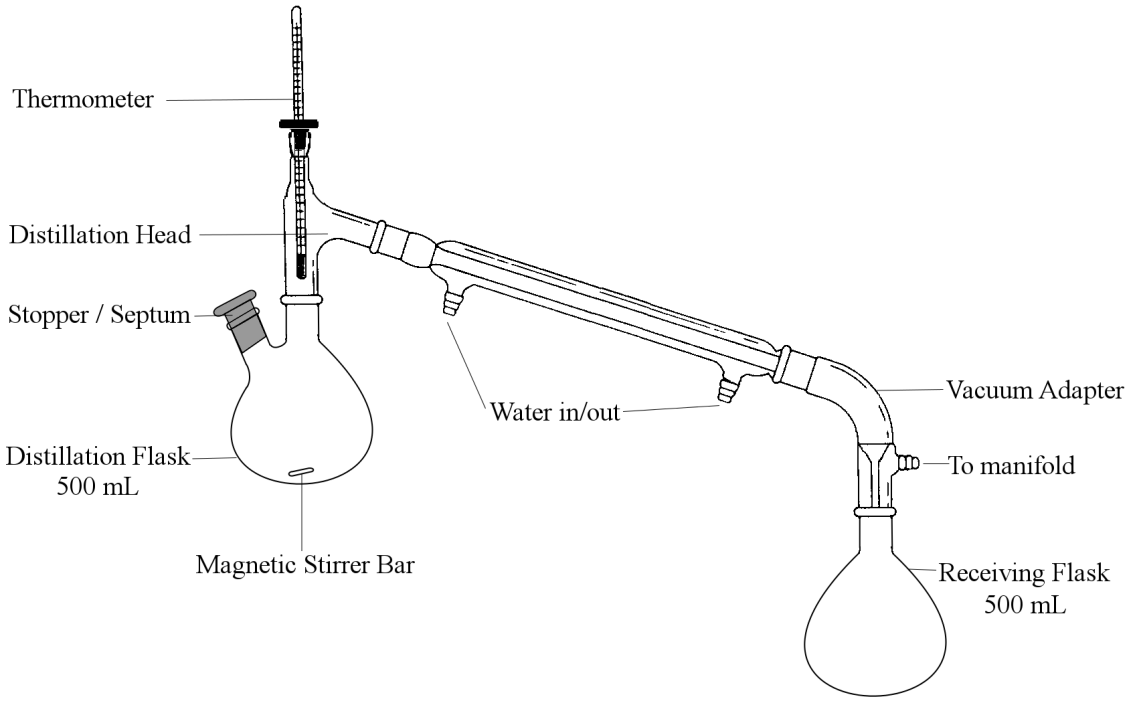

Figure 3.8: A diagram showing the reaction setup used to produce Thiele's acid chloride from Thiele's Acid.

Thionyl Chloride Acylation

Through the unstoppered neck of the two-necked distillation flask, against a dry nitrogen counterflow, was added Thiele's acid (10.04 g, 0.046 mol), followed by thionyl chloride (300 ml). The open neck was sealed using a septum and the nitrogen flow was lowered. The mixture of Thiele's acid and thionyl chloride was stirred using a magnetic stirrer at room temperature. HCl gas was produced which was captured by passing the Schlenk-line output bubbler through a beaker of water. At the point where the solution had turned transparent and there was no further gas evolution the reaction was deemed to be complete; but an extra 30 minutes was allowed to ensure full conversion. The reaction was usually complete in 2 hours. The excess thionyl chloride was recovered using vacuum distillation using gentle heat from a hot-air gun. After the vacuum distillation a viscous brown oil remained which was directly used in the lactonisation step (*i.e.* Section 3.2.9).

3.2.9 Monomer Synthesis

There were multiple monomers synthesised throughout this project with a variety of different experimental conditions. For this experimental section the most successful set of conditions have been given.

Reaction Setup

A 2.5 litre 3-necked round-bottomed flask was equipped with two septa-sealed, pressure-equalising dropping funnels (250 mL) on the outer necks; to the middle neck, was fitted a coil condenser that connected the reaction to the double manifold (see Figure 3.9). The whole reaction setup was flamed under vacuum and refilled with dry nitrogen gas and allowed to cool. When cool, the setup was further evacuated and refilled twice more to ensure complete removal of atmospheric contaminants.

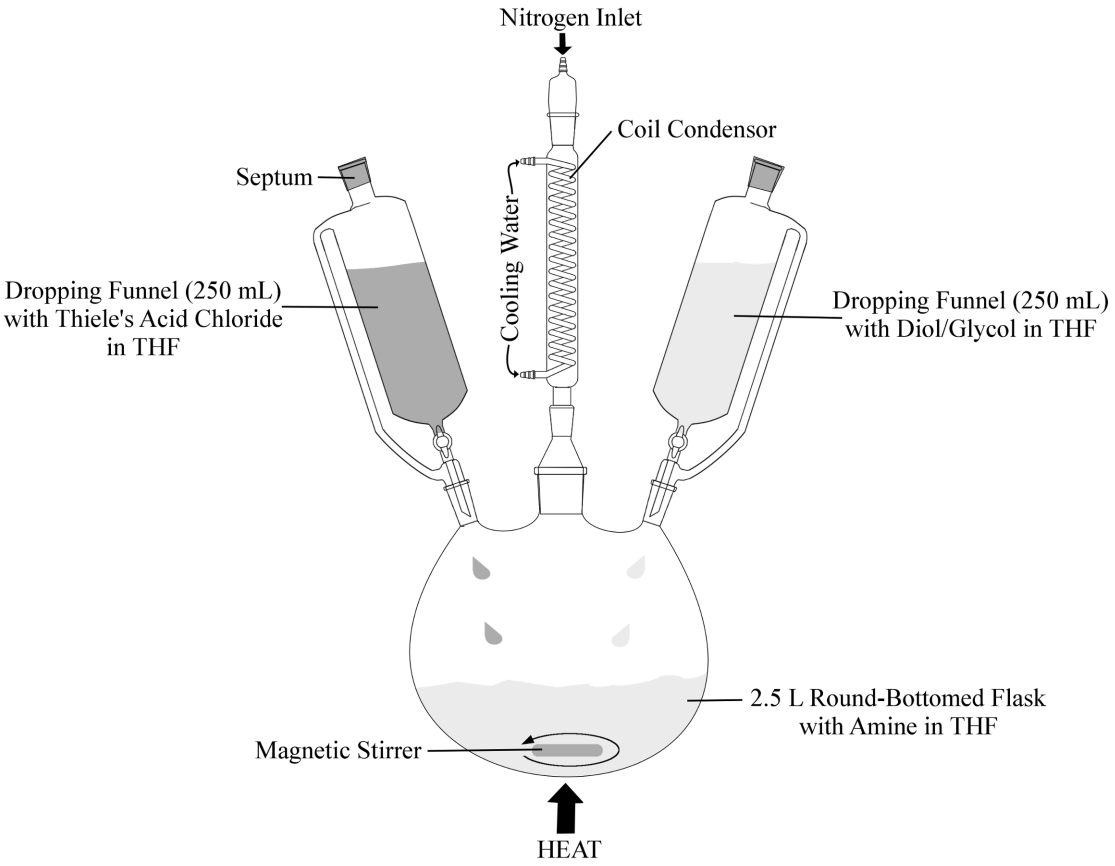

Figure 3.9: A diagram showing the reaction setup used to produce the monomers from Thiele's acid chloride.

Monomer 400

Pyridine (18 mL, 0.23 mol), followed by dry THF (500 mL) was added to the 2.5 L reaction vessel (Figure 3.9) through one of the septa in an open dropping funnel and the dropping funnel was then closed.

Dry THF (100 mL) was added via the septum to the Thiele's acid chloride (46 mmol, assuming the acylation is quantitative) produced in Section 3.2.8 and stirred using the magnetic stirrer to form a clear brown solution. The solution of Thiele's acid chloride in THF was transferred via syringe batches or a cannula through a septum into one of the closed pressure-equalising dropping funnels. To ensure a quantitative transfer; any remaining Thiele's acid chloride was washed into the dropping funnel by repeating the transfer with 2 more batches of 50 ml THF. The

dropping funnel was then filled up to 250 mL volume with dry THF.

1,4-butane diol (4.11 g, 46 mmol) in THF was added through the septum to the second closed dropping funnel and topped up to the 250 mL line with more dry THF.

The contents of the dropping funnels were stirred carefully with a long syringe needle and then added drop-wise at approximately equal rates to the rapidly stirred solution of pyridine in THF. The solution was heated to reflux over the entire addition process (*c.a.* 5 hours).

After cooling, the solution was concentrated using the rotary evaporator and the resulting oily brown solid was washed with 10% aqueous hydrochloric acid (HCl) and extracted, three times, with dichloromethane (DCM). The organic phase was dried over anhydrous magnesium sulfate, filtered, and concentrated; forming a brown viscous oil.

The higher oligomers were removed by passing a solution of the crude product in DCM through a short (*c.a.* 4 cm silica gel) pre-column which made loading the main column significantly easier. Flash column chromatography was used to purify the remaining crude product using silica gel (250 g, dry) as the stationary phase and 10% diethyl ether in dichloromethane as the mobile phase through a 6.5 cm diameter column.

Monomer 401

Using the same transfer methods described for the synthesis of Monomer 400 (on the preceding page); pyridine (3.7 ml, 45 mmol) and dry THF (500 ml) were added to the 2.5 L reaction vessel (Figure 3.9). To this was added drop-wise a solution of Thiele's acid chloride (9.3 mmol) in 250 mL THF simultaneously with a solution of diethylene glycol (0.99 g, 9.3 mmol) in 250 mL THF at approximately equal rates. After approximately 5 hours the solution was concentrated using the rotary evaporator and the resulting oily brown solid was washed with 10% aqueous HCl and extracted, three times, with DCM. The organic phase was dried over anhydrous magnesium sulfate, filtered, and concentrated; forming a brown viscous oil.

Flash column chromatography was used for purification using silica gel (100 g, dry) as the stationary phase and 20% diethyl ether in dichloromethane as the mobile phase through a 3 cm diameter column.

Monomer Based on Poly(THF)

Using the same transfer methods described for the synthesis of Monomer 400 (on page 112); pyridine (14 ml, 0.19 mol) and dry THF (500 ml) were added to the 2.5 L reaction vessel (Figure 3.9). To this was added drop-wise a solution of Thiele's acid chloride (37 mmol) in 250 mL THF simultaneously with a solution of poly(tetrahydrofuran) (M_n = 250 g mol^{-1}, 9.30 g, 37 mmol) in 250 mL THF at approximately equal rates. After *c.a.* 5 hours the solution was concentrated using the rotary evaporator and the resulting oily brown solid was washed with 10% aqueous HCl and extracted, three times, with DCM. The organic phase was dried over anhydrous magnesium sulfate, filtered, and concentrated; forming a brown viscous oil.

Flash column chromatography was used for purification using silica gel (250 g, dry) as the stationary phase and 20% diethyl ether in dichloromethane as the mobile phase through a 6.5 cm diameter column.

Monomer 15-0-0

The synthesis of Monomer 15-0-0 was attempted once and was not optimised (see Section 3.3.2.2 on page 124 for an explanation as to why this work was not continued). The following is what was done in that initial experiment.

To a dry 2-necked round bottomed flask (100 ml) was added Thiele's acid (1.00 g, 4.54 mmol) under nitrogen. To this, 50 ml of thionyl chloride was added and stirred at 55 °C until gas evolution ceased. Excess thionyl chloride was removed by a rotary evaporator equipped with an acetone/dry ice cold finger and the resultant brown oil was dissolved in 50 ml THF. To a second dry 2-necked round bottomed flask (250 ml) containing pyridine (1.80 g, 22.7 mmol) and THF (30 ml) the Thiele's acid chloride solution was transferred slowly via syringe simultaneously with a second syringe of bisphenol-A (0.98 g, 4.3 mmol) in 50 ml THF.

The addition took around 45 minutes after which the mixture was concentrated on the rotary evaporator and dissolved in 100 ml of aqueous HCL (10%) before extracting with 3 x 50 ml portions of DCM. The organic layer was dried over magnesium sulphate, filtered, and concentrated. Flash column chromatography was

used for purification using silica gel (100 g, dry) as the stationary phase and 20% ethyl acetate in 40-60 °C petrol ether as the mobile phase through a 6.5 cm diameter column.

3.3 Results and Discussion

3.3.1 Monomer Selection

The choice of target monomer to synthesize is of vital importance to the success of this research. Initially the monomer was expected to be used as a healing additive in a standard epoxy resin in order to impart some reworkability or healing functionality to the cured network. Since the healing using the linear polymer within the epoxy thermoset matrix was found to work only if the linear polymer was miscible [5, 6] it is important to target monomers that are expected to be miscible within this matrix. One method of predicting miscibility is by modelling the Hansen solubility parameters of the matrix and the healing agent.

3.3.1.1 Hansen Solubility Parameters of 828 Epoxy Resin

The cohesive energy, E_c, of a solvent is a measure of how much energy is required to break it apart into gas molecules. This can be broken down into three components arising from dispersive, polar and hydrogen-bonding forces. The Hansen solubility parameters were first presented by Hansen in his 1967 thesis [19] as a more accurate model of solubility compared to the one dimensional Hildebrand solubility parameter δ which does not work well for polar molecules or those capable of hydrogen bonding. The total solubility parameter and the three contributory parameters are derived from the square root of the cohesive energy density and are described as follows:

δ_d the energy from dispersion forces between molecules.

δ_p the energy from dipolar intermolecular forced between molecules.

δ_h the energy from hydrogen bonds between molecules.

δ_t the total solubility parameter.

The total solubility parameter is roughly equivalent to the Hildebrand solubility parameter. It is the parameter obtained from the sum of the cohesive energy densities. (*i.e.* the square root of the sum of the squares of the three other parameters).

These three parameters are often presented in units of $MPa^{\frac{1}{2}}$, but this author considers that the unit implies a relation to pressure and is thus misleading; it is

clearer to present the parameters in equivalent units of square root specific volumetric energy, $J^{\frac{1}{2}}\ cm^{-\frac{3}{2}}$.

The three parameters can be treated as co-ordinates in three dimensions (also known as the Hansen space) for a point. The closer that two molecular species are together in this three dimensional space, the more likely they are to be miscible.

In order to select a target monomer for synthesis it is sensible to first study the linear polymer which is known to be misible with the resin and is known to facilitate thermal healing. In the early work based upon the solid solution approach to self healing [5, 6] an industry standard epoxy resin (Epikote 828) was used which is a resin based upon the diglicidyl ether of bisphenol-A (*i.e.* Figure 3.10). In the case of Epikote 828 the index value of n is known to be 1.2 [20] (*i.e.* mostly monomer and a little dimer); for the purpose of the modelling this index was approximated to 1 as this reflects the majority of the resin molecules in the distribution.

By using the group interaction approach first published by Hoy in 1970 [16], it is possible to estimate the Hansen solubility parameters for the resin. The constants and data [17] required for the calculation, for a molecule of Epikote 828, are presented in Table 3.1 by group fragment.

From this data it is possible to calculate the following solubility parameters for Epikote 828 epoxy resin using the method presented in Section 3.2.1:

$\delta_t = 21.98\ J^{\frac{1}{2}}\ cm^{-\frac{3}{2}}$

$\delta_d = 18.00\ J^{\frac{1}{2}}\ cm^{-\frac{3}{2}}$

$\delta_p = 11.88\ J^{\frac{1}{2}}\ cm^{-\frac{3}{2}}$

$\delta_h = 4.25\ J^{\frac{1}{2}}\ cm^{-\frac{3}{2}}$

These parameters are used for comparative purposes in the following sections.

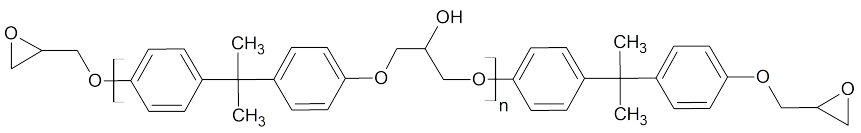

Figure 3.10: Diglicidyl ether of bisphenol A (DGEBPA)

Table 3.1: Data for epoxy resin Epikote 828.

Fragment	**Frequency**	F_z [a]	V_{zp} [b]	Δ_T	F_{zp} [a]
Phenylene, C_6H_4	4	1360.83	63.62	0.066	378.33
Ether oxygen, O	6	235.13	6.36	0.021	215.95
Methyl, CH_3	4	303.27	31.04	0.02	0
Methylene, CH_2	6	268.92	16.54	0.02	0
Trisubstituted carbon, >CH	3	175.85	2.53	0.012	0
Tetrasubstituted carbon, >C<	2	65.50	-13.33	0	0
Secondary hydroxyl, $_s$OH	1	591.41	10.42	0.082	591.41

Data from Barton [17], [a] in units of $MPa^{\frac{1}{2}}$ cm^3 mol^{-1} , [b] in units of $MPa^{\frac{1}{2}}$

3.3.1.2 Hansen Solubility Parameters for pBPAcoE.

The healing agent used in the original solid solution healing approach [5, 6] was poly(bisphenol-A-co-epichlorohydrin) (pBPAcoE), see Figure 3.11.

Effectively the healing agent (Figure 3.11) is a higher molecular weight, thermoplastic (*i.e.* linear and with no epoxy end-groups) analogue of the epoxy resin (Figure 3.10). It is a long linear polymer, therefore the contribution of the end groups is limited and so the repeat unit can be used to calculate the solubility parameters.

Since it is known that this molecule works as a healing agent, it is misible with the matrix resin and that miscibility in the matrix is of high importance for a successful healing formulation; its solubility parameters can be used as benchmark for new monomer selection.

The results, by group, of this calculation for a molecule of poly(bisphenol-A-co-epichlorohydrin) were calculated using the same method as the 828 resin (Section 3.2.1) and are presented in Table 3.2.

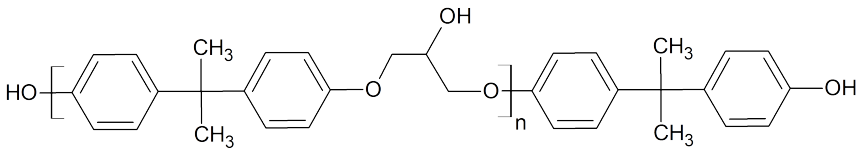

Figure 3.11: Poly(bisphenol-A-co-epichlorohydrin)

The constants and data required for the calculation, for a molecule of healing agent (Figure 3.11), are presented in Table 3.2 by group fragment.

From this data it is possible to calculate the following solubility parameters for poly(bisphenol-A-co-epichlorohydrin) using the method presented in Section 3.2.1:

$\delta_{\mathrm{t}} = 21.55\ \mathrm{J}^{\frac{1}{2}}\ \mathrm{cm}^{-\frac{3}{2}}$

$\delta_{\mathrm{d}} = 16.14\ \mathrm{J}^{\frac{1}{2}}\ \mathrm{cm}^{-\frac{3}{2}}$

$\delta_{\mathrm{p}} = 11.35\ \mathrm{J}^{\frac{1}{2}}\ \mathrm{cm}^{-\frac{3}{2}}$

$\delta_{\mathrm{h}} = 8.67\ \mathrm{J}^{\frac{1}{2}}\ \mathrm{cm}^{-\frac{3}{2}}$

The parameters can be used to compare with those calculated for the matrix resin.

3.3.1.3 Solubility Parameter Comparison in Hansen Space

In order to compare the Hansen parameters obtained for both resin and polymer; the distance (R_{a}) between parameters in Hansen space can be calculated using the following equation [17]:

$$R_a = \sqrt{4(\delta_{d2} - \delta_{d1})^2 + (\delta_{p2} - \delta_{p1})^2 + (\delta_{h2} - \delta_{h1})^2} \tag{3.11}$$

For the epoxy resin and the healing agent R_{a} is calculated:

$$R_{\mathrm{a}} = 5.80\ \mathrm{J}^{\frac{1}{2}}\ \mathrm{cm}^{-\frac{3}{2}}$$

It is known from experiment [5] that these two substances are not phase separated for formulations with up 7.5% healing agent, therefore as a benchmark it can be assumed that if an R_{a} of *c.a.* under 6 $\mathrm{J}^{\frac{1}{2}}\ \mathrm{cm}^{-\frac{3}{2}}$ can be achieved then there is a good likelihood of miscibility. This value will be used as an upper limit for the monomer selection.

Hansen solubility parameters are a useful tool for estimating miscibility but they are not without their limitations. The approach does not take into account the shape of the phase diagram; the temperature dependence of mixing is not modelled and neither are concentration effects.

Table 3.2: Fragment data for poly(bisphenol-A-co-epichlorohydrin). (Note that the values of V_{zp} and Δ_T^P are different compared to those given in Table 3.1 as these are the constants for the polymer case.)

Fragment	**Frequency**	F_z [a]	V_{zp} [b]	Δ_T^P	F_{zp} [a]
Phenylene, C_6H_4	2	1360.83	68.512	0.101	378.33
Ether oxygen, O	2	235.13	6.462	0.0175	215.95
Methyl, CH_3	2	303.27	21.548	0.02	0
Methylene, CH_2	2	268.92	15.553	0.0226	0
Trisubstituted carbon, >CH	1	175.85	9.557	0.02	0
Tetrasubstituted carbon, >C<	1	65.50	3.562	0.0131	0
Secondary hydroxyl, $_s$OH	1	591.41	12.457	0.044	591.41

Data from Barton [17], [a] in units of $MPa^{\frac{1}{2}}$ cm^3 mol^{-1} , [b] in units of $MPa^{\frac{1}{2}}$

3.3.1.4 Monomer Naming Scheme

The monomer naming scheme used in the original paper [4] named the monomers based upon the number of carbons, nitrogen and oxygen atoms in the 'X' unit, such that the monomer formed from using a 1,4-butane diol is referred to as 'Monomer 400' and that the monomer formed from diethylene glycol is referred to as 'Monomer 401'. The naming scheme is not without its limitations, but it is useful and will be preserved in this thesis where possible; any attempt to generate systematic names for these complex molecules would be unwieldy and generally not useful to the reader. Where numbers of atoms increase beyond nine hyphens will be used between the numbers (*i.e.* Monomer 1202 will be referred to as Monomer 12-0-2). In all cases, figures will be used to avoid any ambiguity.

3.3.1.5 Calculating the Hansen Solubility Parameters for the Potential Monomers

The monomers synthesised will have the generalised structure and reactivity shown in Figure 3.12. In reality there is most likely some trimer crosslinking sites but for the purpose of simplifying the modelling the linear repeat unit shown is used.

In essence, what the scheme shows is that with the first application of heat, the reverse Diels-Alder reaction occurs; this cleaves the DCPD fused ring unit and

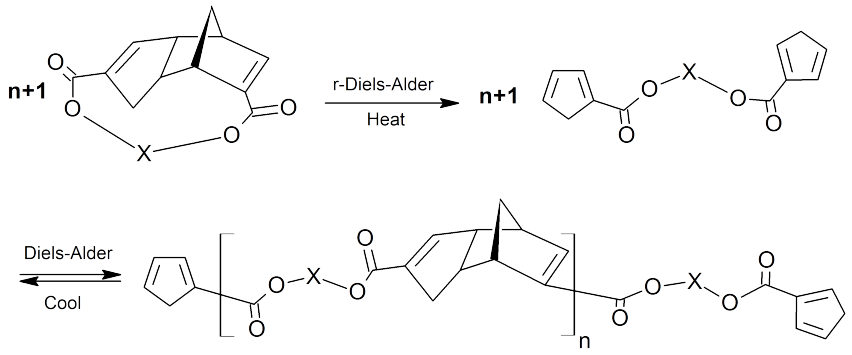

Figure 3.12: A general scheme showing the polymerisation of the class of Diels-Alder polymers synthesised in this work. The identity of X depends on the diol or glycol used in the synthesis.

forms a pair of cyclopentadiene moieties with ester groups attached. The esters are joined using a chain (marked 'X' in the figure), which varies depending on the diol used to construct the monomer. The actual structure of 'X' relates to the chain between the two terminal hydroxy groups on the diol; in the case of 1,4-butane diol HO-CH_2-CH_2-CH_2-CH_2-OH), X refers to a -CH_2-CH_2-CH_2-CH_2- fragment.

As the Diels-Alder reaction is reversible, upon cooling, the forward reaction dominates and the cyclopentadiene moieties react to reform the DCPD units; however reformation of the monomers via an intramolecular reaction is statistically unlikely and the intermolecular reaction dominates forming a polymer. It is this behaviour that allows the thermal reworkability (or self-healing) of what would otherwise be a thermoset polymer.

There is a plethora of relatively low cost diols and glycols available that could be used to synthesise monomers with custom 'X' tethers. A selection of these are presented in Figure 3.13.

The potential polymers made through the process shown in Figure 3.12, using the diols and glycols shown in Figure 3.13 as tether units (*i.e.* X) have been had their solubility parameters modelled as part of the monomer selection process. This data is presented in Table 3.3.

From this table it is possible to conclude that the best polymers as healing agent candidates are those based on triethylene glycol, bisphenol-A and diethylene glycol because their R_a values are near that or lower than pBPAcoE. Poly(THF) would also be potentially suitable as its average R_a over n=1 to n=4 is 5.00 $J^{\frac{1}{2}}$ $cm^{-\frac{3}{2}}$. In

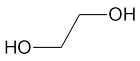

(a) ethylene glycol

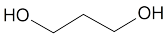

(b) 1,3-propanediol

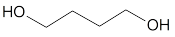

(c) 1,4-butanediol

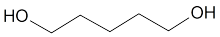

(d) 1,5-pentanediol

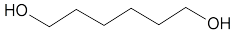

(e) 1,6-hexanediol

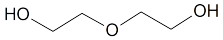

(f) diethylene glycol

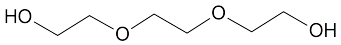

(g) triethylene glycol

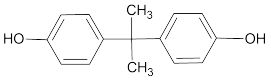

(h) bisphenol-A

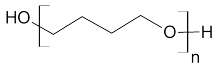

(i) poly(tetrahydrofuran)

Figure 3.13: Different diols and glycols considered for use in pre-screening monomer selection.

Table 3.3: A summary of the modelled solubility parameters showing the distance R_a (in Hansen space, see Section 3.3.1.3) between each possible polymer and the reference Epikote 828 epoxy resin matrix along with the healing agent that was previously used (pBPAcoE); sorted by the shortest distance.

Diol Name	**Figure**	**Monomer Name [4]**	**Calculated Parameter**			R_a
			δ_d	δ_p	δ_h	
Epikote 828[a]	3.10	N/A	18.00	11.88	4.25	0.00
poly(THF) n=4	3.13i	16-0-3	16.80	9.15	2.92	3.87
triethylene glycol	3.13g	602	16.21	10.91	2.15	4.26
poly(THF) n=3	3.13i	12-0-2	16.70	9.43	1.83	4.31
bisphenol-A	3.13h	15-0-0[b]	16.10	10.48	0.96	5.22
poly(THF) n=2	3.13i	801	16.45	9.76	0.00	5.67
pBPAcoE[a]	3.11	N/A	16.14	11.35	8.67	5.80
diethylene glycol	3.13f	401	16.02	10.95	0.00	5.88
1,6 hexane diol	3.13e	600	16.20	9.58	0.00	6.03
1,5 hexane diol	3.13d	500	16.09	9.87	0.00	6.06
1,4 butane diol	3.13c	400	15.95	10.19	0.00	6.14
poly(THF) n=1	3.13i	400	15.95	10.19	0.00	6.14
1,3 prop diol	3.13b	300	15.80	10.54	0.00	6.26
ethylene glycol	3.13a	200	15.62	10.92	0.00	6.45

δ values in units of $J^{\frac{1}{2}}\ cm^{-\frac{3}{2}}$.

[a] Not a diol, the data is included for comparison.

[b] This naming scheme is not very useful in the case of bisphenol-A.

the case of poly(THF), very low molecular weight material would have to be used in order to make formation of the monomers possible in the first place. The reason for this is that the chain can not be too long otherwise the chance of the opposite ends reacting to form the cyclic monomer would be statistically unlikely even using high dilution conditions.

3.3.2 Observations, Separations and Yields

3.3.2.1 Oxalyl Chloride vs. Thionyl Chloride

After a brief discussion with Prof. Fred Wudl who supervised the original research [4], it was concluded that oxalyl chloride was not really necessary for this synthesis as it has been shown (although as yet unpublished) to work equally well with thionyl chloride for the Thiele's acid substrate. Therefore a quick small scale experiment was devised in order to confirm that the lower cost thionyl chloride was equally suitable (see Section 3.2.7 on page 109). In this experiment Thiele's ester was produced using both reagents, the yields were taken and the composition of the crude product was qualitatively analysed using thin layer chromatography (TLC).

Thiele's acid was found to dissolve directly in both reagents, therefore it was not necessary to use a solvent and catalytic DMF. The dried yield of crude Thiele's ester using thionyl chloride was 105.6 mg which is 94% based on Thiele's acid; the dried yield using oxalyl chloride was 101.2 mg which is 91% based on Thiele's acid. The TLCs of the two product solutions were more or less identical with a single species eluting at $R_f = 0.7$ in 20% diethyl ether (DEE) in dichloromethane (DCM); there was a faint species present on the baseline for both samples which can perhaps be attributed to some ring opening polymerisation of the DCPD units.

From this information it was decided that the choice of acylating reagent does not make a large difference to the reaction and therefore for cost reasons thionyl chloride was used for later experiments.

3.3.2.2 Monomer 15-0-0 (Bisphenol-A Based)

The first monomer that was selected as a good candidate for a self-healing additive to epoxy was the monomer based on a reaction between Thiele's acid chloride and bisphenol-A (see Figure 3.14). The name, 'Monomer 15-0-0' only gives information

about the number of carbons in the tether unit so it is not particularly appropriate in this case. However, as there is no 15 carbon linear diol presented in this thesis and the fact that the systematic name would be far too unwieldy this name will be used.

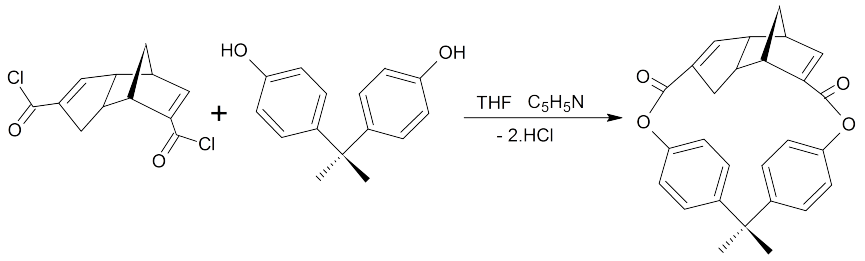

Figure 3.14: A scheme showing the proposed reaction of Thiele's acid chloride with bisphenol-A under high dilution conditions. For clarity the monomer has been drawn with the bisphenol-A unit in the plane of the page; in reality this molecule would conform into a circular unit with the bisphenol-A perpendicular to the page and the methyl groups sticking out.

The reaction was conducted on a particularly small scale (4 mmol) and produced a yield of 0.031 g, 0.075 mmol, 1.9% after purification. This yield was very small and only barely enough to produce a proton NMR but the concentration after transfer losses wasn't high enough to produce a good carbon NMR.

The compound submitted for NMR was the first compound to elute from the column ($R_f = 0.5$, 30% ethyl acetate in 40-60 petrol), the second was a large amount of unreacted bisphenol-A ($R_f = 0.3$, 30% ethyl acetate in 40-60 Petrol, identified by NMR). The large proportion of unreacted starting material present in the mixture is not ideal, therefore the conditions should be adjusted (*i.e.* a raised reaction temperature, a change of catalyst or longer addition times). In order to troubleshoot this reaction it was decided that it would be more efficient to try the reaction with a diol that had already been done and published to test the reaction conditions. In general this second synthesis step proved to be more challenging than originally anticipated even with the more reactive diols (*e.g.* 1,4-butane diol) and consequently, due to time constraints, it was not possible to continue with this route.

3.3.2.3 Monomer 400 (1,4-butane diol Based)

Monomer 400, the monomer produced from Thiele's acid chloride and 1,4-butane diol, (*i.e.* Figure 3.15 with X having the structure -CH_2-CH_2-CH_2-CH_2-) was se-

lected for synthesis in order to optimise the synthetic process. This monomer was chosen because its synthesis had already been reported and there is literature data with which to compare it [4].

Initial attempts at this reaction were undertaken on a small scale, with smaller glassware (250 ml flask, 50 ml dropping funnels) which led to very poor yields after flash chromatography of (0.09 g, 6.9%) which was only enough to run NMR. Despite months of work this yield was not improved a great deal; some improvement was achieved by heating the reaction to reflux during the addition of the two reagents.

In order to try and improve this yield new reagents were purchased, the 1,4-butane diol was purified via distillation from 4A molecular sieves, the pyridine was stored in the fridge, anhydrous solvents were used and various different flash column conditions were tried. The product was a white crystalline solid and the best yield achieved was based upon a 46 mmol reaction which gave 1.214 g of monomer (9.6% based on Thiele's acid). The compound eluted with a TLC R_f of 0.75 in 20% DCM in DEE.

The reaction produced a large quantity of brown oligomeric material which was likely to be caused by difficulties controlling equal and simultaneous slow addition of the diol and the Thiele's acid chloride solution. The problem was trying to control the simultaneous additions at the same drop-wise rate over several hours as they required constant attention. It was common for drop rates to slow down or speed up or for particulates to block the taps which made it very difficult to maintain equal addition rates.

Another problem was during the column purification stage, often the mass required to load was quite large and the target monomer appeared to be a small proportion of that mass. Wet loading of the compound to the top of the column resulted in a very wide band and consequent poor separation simply due to the volume

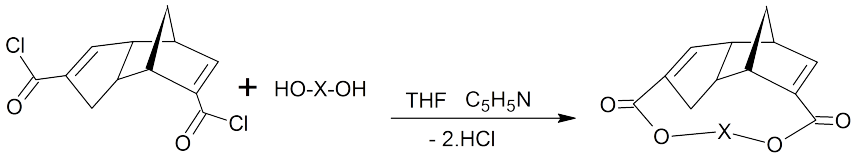

Figure 3.15: A generalised reaction scheme showing the reaction of Thiele's acid chloride with a diol represented by HO-X-OH under high dilution conditions to produce the class of monomers used in this thesis.

of solvent required to dissolve the crude material. Attempts to dry-load the sample on silica was particularly unsuccessful because the amount of silica required to adsorb the compound was far too high. The purification step was improved slightly by running a short pre-column before the main column (*c.a.* 4 cm of silica gel) which acted as a tool to remove a proportion of the baseline oligomers from the crude sample. This reduced the mass of the sample by around 50% and made running the main column much easier.

For health and safety reasons initial attempts to purify the crude product used petrol/ethyl acetate mixtures; this worked, but led to streaks on the TLC and subsequently poor separation on the main column. The situation was much improved by switching to dichloromethane (DCM) /diethyl ether (DEE) mixtures for the columns; this mixture worked much better as a mobile phase.

3.3.2.4 Monomer 401 (diethylene glycol based)

Monomer 401 is a monomer that is structurally similar to Monomer 400, the difference being diethylene glycol is used rather than 1,4-butane diol in the synthesis which produces a structure represented by Figure 3.15 (where X is -CH_2-CH_2-O-CH_2-CH_2-). This monomer was chosen because it has potential compatibility with the epoxy matrix (as discussed in Section 3.3.1.5) and also has some literature data associated with it [4].

Initially (as with Monomer 400) the reaction were attempted on a smaller scale (14 mmol) and there were difficulties producing any kind of acceptable yield; the first few attempts gave a slight smear on the side of the Schlenk flask which was not even enough to run a proton NMR. The problems with the reaction and purification were identical to those mentioned in the previous section.

A scale up to 69 mmol and the use of DCM/DEE mixtures for the column produced a yield of 3.64 g, 12.6 mmol, 18.2% of a pale yellow crystalline solid. The compound had a TLC R_f value of 0.63 in 20% DEE in DCM. This yield, although still not impressive, did provide enough material to do some NMR, DSC and to fabricate some samples for dynamic mechanical analysis (DMA) (see Chapter 4, Section 4.3.3.6 on page 191).

3.3.2.5 Monomer Based on Poly(THF)

The monomer produced from the reaction between poly(THF) and Thiele's acid chloride (see Figure 3.16) was synthesised as a candidate monomer for compatibility with an epoxy matrix. The prefix 'poly' in this case is slightly misleading because the poly(THF) had an M_n of 250 g mol^{-1} and is therefore barely classed as an oligomer and certainly not a polymer. This candidate was chosen as it is a) novel, and b) components with index number n>1 show a good potential compatibility with epoxy matrix (as discussed in Section 3.3.1.5). In addition because poly(THF) is commonly produced in large quantities for the production of polyurethanes there are a wide variety of grades available. The length of the tether chain depends on the index number of the poly(THF) and as most polymers have a non-discrete molecular weight this reaction should generate a mixture of different monomers with varying tether lengths when the M_n is used for the stoichiometry calculations. It is hypothesised that there is likely to be very little n=1 material present in most poly(THF) but the higher oligomers (n>4) are unlikely to have a good statistical chance of reacting in an intramolecular fashion with Thiele's acid chloride.

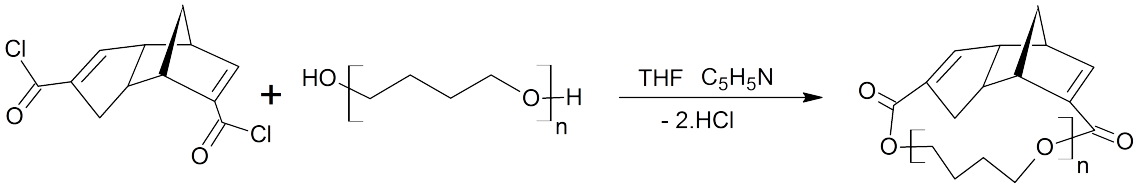

Figure 3.16: A generalised reaction scheme showing the reaction of Thiele's acid chloride with a poly(THF) under high dilution conditions to produce the monomer (or monomer mixture) based on poly(THF).

For poly(THF) with an M_n of 250 g mol^{-1} the average index number should be about n = 3.22; while there was no dispersity quoted by the material supplier it is known that poly(THF) usually has an $\frac{M_w}{M_n}$ of 1.04 to 1.08 [21] and therefore it is not expected to have too wide a distribution.

The synthesis was carried out on a medium (17.0 mmol) scale and resulted in a brown rubbery solid, (6.63 g, *c.a.* 14.2 mmol, 83% crude).

Thin layer chromatography of the crude mixture on silica gel eluting with 20% DEE in DCM gave rise to spots at retention factors, R_f = 0.71, 0.34 and 0.29 along with several pale spots and quite a dark spot on the baseline.

As with some of the other monomers it was advantageous to first filter the mixture through a short pre-column in order to remove a proportion of the higher oligomers; this made loading the main column easier and that led to better separation due to thinner bands. The aim was then to separate the compounds using flash column chromatography. A solvent gradient elution was applied starting at 20% DEE in DCM for approximately 1000 ml, followed by pure DCM for another 500 ml and finally a methanol flush. The TLC that was used to analyse the fractions is shown in Figure 3.17. For the purposes of discussion this column and its fractions will be referred to as 'column A'.

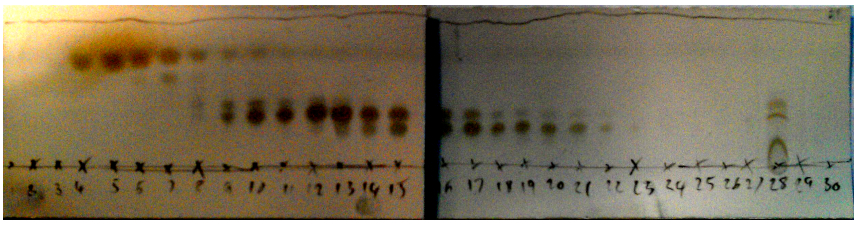

Figure 3.17: The TLC showing the main column fractions from column A run on the poly(THF) monomer mixture (TLC solvent: 20% DEE in DCM).

The TLC in Figure 3.17 gives an indication of the position of the different compounds dissolved in the 30 different separate fractions. Some of these fractions were combined and concentrated as follows:

- Fractions 2-8, a yellow waxy solid, 30 mg, containing the species with R_f = 0.74, were combined and will be referred to as compound A1. Compound A1 was submitted for NMR in $CDCl_3$. This was later identified using NMR (see Section 3.3.3.4) as the monomer arising from the fraction of poly(THF) with the index number n=1, (*i.e.* Monomer 400), identical to that produced by 1,4-butane diol.

- Fractions 9-23, 0.38 g, a yellow oil, containing the 3 closely eluting species with R_f = 0.46 (faint), 0.35 and 0.27 were combined and will be referred to as mixture A2.

As mixture A2 appeared to be a mixture of multiple compounds it was decided that a second flash column should be run using different conditions in an attempt to separate them. This second column will be referred to as 'column B'. This column

was run with a solvent system consisting of 50% DCM and 50% diisopropyl ether (DPE). This solvent mixture was chosen as it is slightly less polar than the original which should slow down the elution and allow better separation between the two compounds. The TLC of the flash column fractions using the same TLC solvent (20% DEE in DCM) is presented in Figure 3.18.

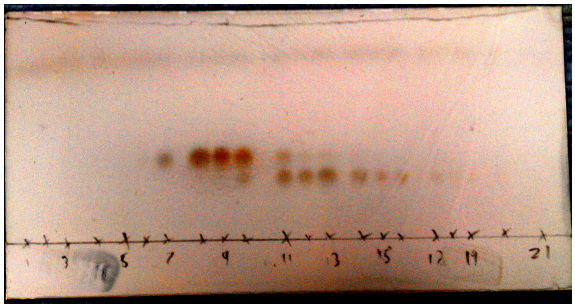

Figure 3.18: The TLC showing the main column fractions from column B run on the poly(THF) monomer mixture (TLC solvent: 20% DEE in DCM).

Analysis of the fractions by TLC revealed only two compounds of interest with an $R_f = 0.36$ and 0.27. The lack of any pale spots could be due to a more appropriate TLC loading concentration; the perceived pale spots in column A could be due to a streak of the lower spots caused by high loading concentrations. The fractions were combined and concentrated as follows:

- Fractions 7-9, a white crystalline solid, 77.2 mg, containing the species with $R_f = 0.37$, were combined and will be referred to as compound B3. Compound B3 was submitted for NMR in $CDCl_3$ and identified as the monomer made from the reaction of poly(THF), index n=2, (*i.e.* Monomer 801), see Section 3.3.3.4.

- Fractions 12-16, a white crystalline solid, 11.7 mg, containing the species with $R_f = 0.27$, were combined and will be referred to as compound B4. Compound B4 was submitted for NMR in $CDCl_3$ and identified as the monomer made from the reaction of poly(THF), index n=3, (*i.e.* Monomer 12-0-2), see Section 3.3.3.4.

Due to the fact that compounds A1, B3 and B4 were identified as variations on the same target compound, the mixture was thought to have potential without

separation. Therefore a second synthesis was done using the same conditions as the first; the second time all the compounds with an R_f of $>$0.27 (in 20% DEE in DCM) were combined to give a mass yield of 0.65 g. This mixture was combined with the material left over from the first synthesis to give 0.80 g of mixed poly(THF) monomers for sample fabrication in the following chapter. It was anticipated that it would be possible to cure the mixture concurrently and form a polymer.

3.3.3 NMR

The purpose of this section is to interpret, assign and discuss the various monomer NMR spectra of the monomers synthesised. The information gathered from these experiments can be used to gain confidence in the structure of the compounds and used to infer whether a particular synthesis has been successful. Details on the general NMR characteristics of this category of structures has been discussed previously in Chapter 2, Section 2.3.3 on page 83. In this chapter an attempt will be made to highlight the main structural motifs that manifest themselves as the differences between the measured spectra and those of Thiele's acid. Due to the highly overlapping nature of the spectra and the absence of any dedicated NMR studies in the literature on these compounds; J values will not be discussed unless they can be measured and they are directly relevant to the assignment or a particular nuclei.

3.3.3.1 Monomer 15-0-0

The ^{1}H-NMR spectrum (Appendix A.5 on page 280) of flash-column purified Monomer 15-0-0 was measured and this was initially dismissed and the experiment branded a failure due to a variety of incomprehensible peaks in the NMR that made assignment impossible.

In bisphenol-A, the para substitution on the aromatic rings gives a characteristic pair of raked doublets at about 6.8 and 7.1 ppm (Figure 3.19a) that arise because the aromatic protons are not equivalent. The same motif was sought in the NMR spectrum of Monomer 15-0-0 and was found. A pair of raked doublets were indeed present in the correct place with the addition of an unknown multiplet at lower field (see Figure 3.19b). The vinyl protons appeared to be missing from their usual position of 6.5-6.7 ppm and a multiplet appeared at around 7.2 ppm; this caused considerable confusion and it was concluded there had been an unanticipated side reaction.

Upon revisiting this NMR spectrum one thing is clear, there are lots of impurities but some of the features make a little more sense if the molecule is modelled (Figure 3.19c). The low field section of the measured monomer is presented in Figure 3.19 for comparison with the modelled spectrum and the similarity is striking. What appears to have happened, if the simulation is to be trusted, is that the raked doublet in

the ^{1}H-NMR is not the characteristic aromatic proton resonance that it was first attributed and is instead the vinyl protons that are deshielded to a greater extent. The aromatic protons in the monomer tether have also moved down field compared to bisphenol-A and are not split to such an extent that they present themselves as a multiplet rather than a pair of raked doublets.

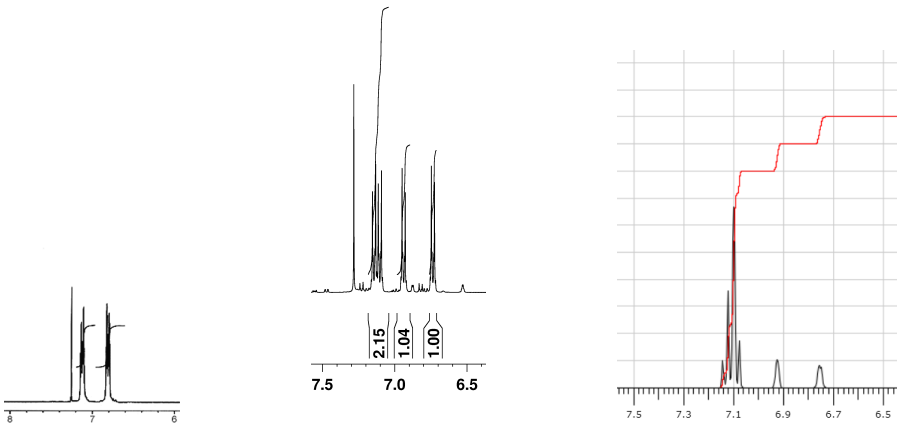

(a) Bisphenol-A **(b)** Measured **(c)** Modelled [22].

Figure 3.19: Low-field sections of the bisphenol-A, the proposed Monomer 15-0-0 and the modelled Monomer 15-0-0 ^{1}H-NMR . Note that the sharp peak at 7.26 ppm is due to the deuterated chloroform solvent.

The conclusion that can be made from this is that there was most likely some, albeit a very small amount, of Monomer 15-0-0 made in the reaction, but the purification column step was not particularly effective in this case as it had not been optimised. It would have been worthwhile if time had been available to revisit this reaction as it is likely after the later improvements in the practical steps that it would have been possible to synthesise Monomer 15-0-0.

3.3.3.2 Monomer 400

A diagram showing Monomer 400 with numbered atoms for NMR assignment is presented in Figure 3.20.

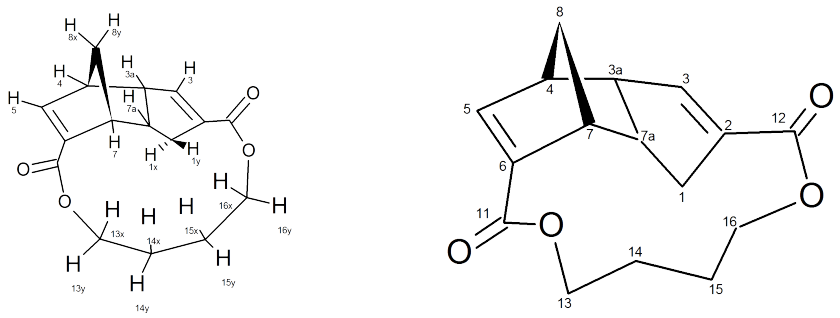

(a) Numbered Hydrogen atoms.

(b) Numbered Carbon atoms.

Figure 3.20: Monomer 400 Numbered for NMR Assignment.

Assignment of the ^{1}H-NMR of Monomer 400

The ^{1}H-NMR spectrum of flash-column purified Monomer 400 is presented in Appendix A.6 on page 281. The assignment along with literature values and modelled shifts is presented in Table 3.4 using the hydrogen numbering system shown in Figure 3.20a.

The main points to consider from this NMR spectrum are the changes compared to the spectrum of Thiele's acid discussed in Chapter 2, Section 2.3.3 on page 83. The first major change is the absence of acidic protons at 12.5 ppm which indicates that there is no acid starting material present. The second major change is the addition of overlapping proton resonances between 1.69-1.95 ppm due to the two CH_2 groups in the middle of the butane tether. Finally the third major change is the addition of overlapping proton resonances from the two CH_2 groups on the butane tether next to the ester group which resonate between 3.45 and 3.62 ppm due to the deshielding inductive effect of the ester oxygen. These two separate sets of resonances are characteristic of a butyl chain with an electron withdrawing group on either side, such as the tether in Monomer 400, because the inner two carbons are less affected by the deshielding than those adjacent to the ends.

The measured chemical shifts compare closely with the values previously published in the literature and the predicted chemical shifts are generally quite accurately modelled with the exception of protons 4 and 3a. The reason protons 4 and 3a resonate at lower field is most likely due to the deshielding caused by the electron

Table 3.4: ^{1}H-NMR Assignment of Monomer 400.

$H_{\#}$	δ_{exp}	δ_{lit}	δ_{mod}	$\int$	Mult.	Comments
	0.90					Grease
	7.26					Solvent Peak
5	6.58	6.57	6.93 ± 1.26	1H	d	Vinyl Proton
3	6.50	6.49	6.76 ± 0.41	1H	d	Vinyl proton
3a	4.92	4.91	2.95 ± 0.65	1H	m	3a and 4 more deshielded compared to Thiele's acid.
4	4.79	4.78	3.33 ± 0.65	1H	m	
13x, 13y, 16x, 13y	3.45-3.62	3.47-3.59	4.27 ± 0.17	4H	m	Overlapping region: protons from the end 2 carbons on the butyl 'tether'.
7	3.21	3.21	3.04 ± 0.65	1H	m	
7a	2.83	2.83	2.95 ± 0.69	1H	m	
1y	2.40	2.39	2.86 ± 0.65	1H	m	
1x	2.16	2.14	2.55 ± 0.65	1H	d	
14x, 14y, 15x, 15y	1.69-1.95	1.67-1.82, 1.84-1.9	1.64 ± 1.79	4H	m	Overlapping region: protons from the middle 2 carbons on the butyl 'tether'.
8y	1.54	1.54	1.63 ± 0.65	1H	d	
8x	1.31	1.31	1.40 ± 0.65	1H	d	

$H_{\#}$ proton number from Figure 3.20a.

δ_{exp} measured chemical shift from the spectrum in Appendix A.6.

δ_{lit} chemical shift from the literature [4].

δ_{mod} chemical shift modelled using the web-based tool [22].

$\int$ measured integration.

Mult. multiplicity.

withdrawing effect of the adjacent conjugated vinyl-carbonyl groups; this appears not to have been fully accounted for by the model.

In summary, the ^{1}H-NMR gives good evidence supporting the successful synthesis of Monomer 400; further evidence can be gained by examining the ^{13}C-NMR .

Assignment of the ^{13}C-NMR of Monomer 400

The ^{13}C-NMR spectrum of flash-column purified Monomer 400 is presented in Appendix A.7 on page 282. The assignment along with literature values and modelled shifts is presented in Table 3.5 using the carbon numbering system shown in Figure 3.20b.

Table 3.5: ^{13}C-NMR Assignment of Monomer 400.

$C_{\#}$	δ_{exp}	δ_{lit}	δ_{mod}	Phase	Type	Comments
N.A.	76.70-77.34			↑		Solvent peaks.
12	-	165.21	167.98 ±3.08	-	C	
11	-	-	167.64 ±2.79	-	C	
5	146.98	148.13	149.05 ±5.39	↓	CH	
3	144.75	145.11	149.05 ±5.29	↓	CH	
2	-	139.84	138.65 ±16.61	-	C	
6	-	137.10	133.80 ±5.39	-	C	
13	64.28	65.77	65.13 ±3.88	↑	CH_2	
16	63.62	63.26	65.13 ±3.88	↑	CH_2	
3a	53.37	55.25	55.36 ±4.84	↓	CH	
4	47.84	48.85	45.87 ±4.84	↓	CH	
7	47.24	48.21	45.6 ±4.84	↓	CH	
8	46.78	-	46.8 ±1.185.59	↑	CH_2	
7a	39.89	39.96	42.69 ±4.82	↓	CH	
1	33.18	33.43	35.67 ±4.26	↑	CH_2	
15	25.93	26.60	25.8 ±3.74	↑	CH_2	
14	25.20	26.15	25.8 ±3.74	↑	CH_2	

$C_{\#}$ proton number from the Figure 3.20b.

δ_{exp} measured chemical shift from the spectrum in Appendix A.7.

δ_{lit} chemical shift from the literature [4].

δ_{mod} chemical shift modelled using the web-based tool [22].

The assignment of the ^{13}C-NMR spectrum is relatively straightforward using the modelled shifts, the JMOD phase information and the previously measured Thiele's acid shifts in Chapter 2, Section 2.3.3 on page 83.

The most striking thing about Table 3.5 is the fact that in both the measured spectrum and in the literature there are carbon atom resonances missing. There are 16 carbon atoms total present in Monomer 400 which consists of 4 quaternary

carbons, 6 tertiary carbons and 6 secondary carbons. In the measured spectrum all the quaternary carbons are missing (in NMR terminology carbons with no protons attached are referred to as quaternary despite the fact that >C= would not normally be referred to as this).

Quaternary carbons, in ^{13}C-NMR experiments are notoriously weak due to their extremely long relaxation times and this is the likely explanation for the lack of these carbons from the NMR spectrum. This could be verified by running a much longer NMR experiment but it was decided that it was not ultimately necessary considering that the NMR equipment was very busy.

The most puzzling aspect of Table 3.5 is that there is a secondary carbon missing from the literature values that was successfully measured in this work and predicted in the model. It is not possible to formulate an explanation for this without viewing the original spectrum as it could simply be a transcription error; it is very unlikely that some of the quaternary carbons are measured but a secondary carbon is missing.

Despite the missing features which are easily explained, the ^{13}C-NMR results are convincing that the target structure for Monomer 400 has been synthesised.

3.3.3.3 Monomer 401

A diagram showing Monomer 401 with numbered atoms for NMR assignment is presented in Figure 3.21.

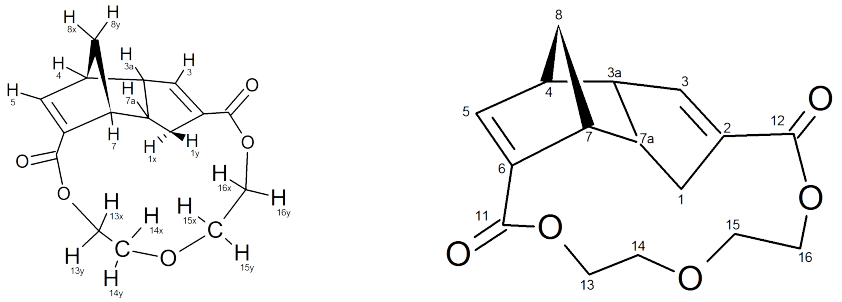

(a) Numbered Hydrogen atoms.

(b) Numbered Carbon atoms.

Figure 3.21: Monomer 401 Numbered for NMR Assignment.

Assignment of the ^{1}H-NMR of Monomer 401

The ^{1}H-NMR spectrum of flash-column purified Monomer 401 is presented in Appendix A.8 on page 283 A partial assignment along with literature values and modelled shifts is presented in Table 3.6 using the hydrogen numbering system shown in Figure 3.21a.

Table 3.6: ^{1}H-NMR Assignment of Monomer 401.

$H_\#$	δ_{exp}	δ_{lit}	δ_{mod}	Int.	Mult.	Comments
	7.26					Solvent Peak
5	6.71	6.69	6.93 ± 1.18	1H	d	Vinyl Proton
3	6.52	6.48	6.75 ± 0.43	1H	d	Vinyl proton
3a	4.95	4.86-4.94	2.93 ± 0.65	1H	m	
4	4.85	4.67-4.73	2.87 ± 0.65	1H	m	
	3.88	3.82-3.89		1H	m	
	3.75	3.68-3.70	4.43 ±	2H	m	
13-16	3.66	3.61 -3.67	0.37, 3.86	2H	m	Overlapping region prohibits exact assignment.
	3.53	3.47 -3.08*	± 0.45	2H	m	
	3.45	3.43		1H	m	
7	3.25	3.29	3.33 ± 0.65	1H	m	
7a	2.86	2.81 -2.89	2.56 ± 0.65	1H	m	
1y	2.42	2.35-2.46	2.86 ± 0.66	1H	m	
1x	2.19	2.21	2.55 ± 0.66	1H	m	
8y	1.57	1.57	1.64 ± 0.65	1H	m	
8x	1.32	1.32	1.39 ± 0.65	1H	d	

$H_\#$ proton number from Figure 3.21a.

δ_{exp} measured chemical shift from the spectrum in Appendix A.8.

δ_{lit} chemical shift from the literature [4].

δ_{mod} chemical shift modelled using the web-based tool [22].

Int. measured integration.

Mult. multiplicity.

* Suspected typo in literature value (lit. should read 3.47-3.58 instead of 3.47-3.08).

It has not been possible to fully assign the ^{1}H-NMR of Monomer 401, in particular the protons in the tether group; this can be explained as follows:

The only structural difference between Monomer 400 and Monomer 401 is the addition of an ether oxygen in the tether group. The ether oxygen deshields adjacent protons in the tether unit; the result of this is that the tether in Monomer 401 (unlike

Monomer 400) does not have two separate sets of protons with different resonances. Instead, all 8 of the tether protons in Monomer 401 resonate in a crowded region between 3.88 and 3.45. As the carbons in the tether are also prevented from rotating there is also the potential for non-equivalence between protons on the same atom which can lead to complex splitting patterns.

By comparing the Monomer 401 spectrum to the spectrum measured of Monomer 400 (*i.e.* Table 3.6 compared to Table 3.4) it can be seen that the higher field 1.69 to 1.95 resonances are not present and that there are additional peaks in the 3.88 to 3.45 ppm region; other than this the two spectra are more or less the same. This information supports the successful synthesis of Monomer 401.

Assignment of the ^{13}C-NMR of Monomer 401

The ^{13}C-NMR spectrum of flash-column purified Monomer 401 is presented in Appendix A.9 on page 284. The assignment along with literature values and modelled shifts is presented in Table 3.7 using the carbon numbering system shown in Figure 3.21b.

The assignment of the ^{13}C-NMR of Monomer 401 was relatively easy compared to the proton spectrum. It can be seen in Table 3.7 that the measured values of chemical shift match very well with the literature values and those generated by the model. In this spectrum, in contrast to the one measured for Monomer 400, all the quaternary carbons were measured albeit the carbonyls were quite weak; the reasons for this have been explained.

As mentioned during the discussion of the ^{1}H-NMR , the only structural difference between Monomer 400 and Monomer 401 is the addition of an oxygen group to the tether; the effect of this can be clearly seen in the spectrum. The carbons numbered 13 and 14 which were previously present at high field (around 26 ppm) have moved to lower field (around 62 ppm) due to the slight inductive deshielding effect of the ether; the spectra are otherwise identical.

As the phase information from the JMOD experiment also supports the assignment it is possible to conclude from the ^{13}C-NMR that Monomer 401 had been synthesised with reasonable purity.

Table 3.7: ^{13}C-NMR Assignment of Monomer 401.

$C_{\#}$	δ_{exp}	δ_{lit}	δ_{mod}	Phase	Type	Comments
N.A.	77.33-76.70			↑		Solvent peaks.
12	165.21	165.21	167.98 ± 3.08	↓	C	(Weak) Carbonyl Carbon
11	165.00	165.00	167.64 ± 2.79	↓	C	(Weak) Carbonyl Carbon
3	147.38	147.37	149.05 ± 5.39	↑	CH	Vinyl Carbon
5	143.96	143.95	149.05 ± 5.39	↑	CH	Vinyl Carbon
2	138.00	138.02	138.65 ± 16.61	↓	C	Adjacent to ester carbonyl
6	136.75	136.77	133.80 ± 5.39	↓	C	Adjacent to ester carbonyl
13	69.80	69.80	69.07 ± 3.65	↓	CH_2	Tether adjacent to ester oxygen
16	68.30	68.31	69.07 ± 3.65	↓	CH_2	Tether adjacent to ester oxygen
15	62.31	62.32	64.16 ± 2.48	↓	CH_2	Tether adjacent to ether oxygen
14	62.25	62.26	64.16 ± 2.48	↓	CH_2	Tether adjacent to ether oxygen
3a	53.61	53.61	53.36 ± 4.84	↑	CH	
8	48.00	48.00	46.80 ± 5.59	↓	CH_2	Bridge methylene
4	47.63	47.63	45.87 ± 4.84	↑	CH	Bridgehead carbon
7	46.88	46.89	45.60 ± 4.84	↑	CH	Bridgehead carbon
7a	40.27	40.28	42.69 ± 4.84	↑	CH	
1	33.33	33.34	35.67 ± 4.26	↓	CH_2	

$C_{\#}$ proton number from the Figure 3.6.

δ_{exp} measured chemical shift from the spectrum in Appendix A.9.

δ_{lit} chemical shift from the literature [4].

δ_{mod} chemical shift modelled using the web-based tool [22].

3.3.3.4 Monomer(s) Based on Poly(THF)

There were three compounds isolated by column chromatography from the mixture produced by the reactions of Thiele's acid chloride and poly(THF) as discussed in Section 2.3.1. The proton NMR of these compounds are similar to those already encountered in this section as the variation occurs in a crowded 4.13-3.44 ppm part

of the spectrum therefore ^{1}H-NMR is not the best tool to identify the different fractions. ^{13}C-NMR , however, should provide sufficient information.

Compound A1 (Monomer 400)

Compound A1 was the first to elute from the flash column and had an R_f of 0.74 when a TLC was run using 20% DEE in DCM. The ^{1}H-NMR shows the same features as the ^{1}H-NMR discussed for the first compound, Monomer 400 (in Section 3.3.3.2). The ^{13}C-NMR also showed a strong similarity, with the addition of two of the missing quaternary carbons at 139.84 and 137.10 but again no carbonyl carbons. Therefore it is reasonable to suggest that the identify of this compound is indeed Monomer 400. This would be the case where the fraction of poly(THF) with an index number n=1 reacts with Thiele's acid chloride. For this reason a separate assignment is not presented in this section as it is assumed to be the same as that presented in Section 3.3.3.2. It is likely that compounds that eluted later are molecules made from higher index number poly(THF) chains.

Assignment of the ^{13}C-NMR of Compound B3 (Monomer 801)

Compound B3 was separated from mixture A2 by use of a second flash column.

The ^{1}H-NMR of compound B3 can be found in Appendix A.10 on page 285, due to its similarity with previous spectra a separate assignment will not be made as there are not enough places that it differs. The ^{13}C-NMR (Appendix A.11 on page 286), however, shows clearly that a structure has been made that is consistent with the molecule formed from the reaction of Thiele's acid chloride with the fraction of the poly(THF) that has the index value of n=2 (*i.e.* Monomer 801 in Figure 3.22*)*.

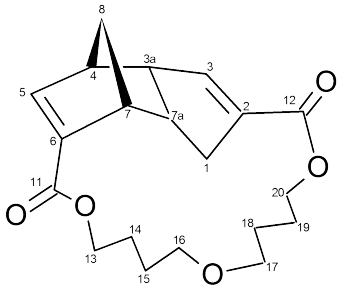

Figure 3.22: Monomer 801 Numbered for NMR Assignment.

The ^{13}C-NMR assignment along with literature values and modelled shifts is presented in Table 3.8 using the carbon numbering system shown in Figure 3.22.

Table 3.8: ^{13}C-NMR Assignment of Compound B3 (Monomer 801).

$C_{\#}$	δ_{exp}	δ_{mod}	Phase	Type	Comments
N.A.	77.33-76.70		↑		Solvent peaks.
12	165.03	167.98± 3.08	↑	C	Carbonyl Carbon
11	164.98	167.64± 2.74	↑	C	Carbonyl Carbon
3	147.23	149.05± 5.29	↓	CH	Vinyl Carbon
5	143.06	149.05 ± 5.03	↓	CH	Vinyl Carbon
2	138.81	138.65± 16.61	↑	C	Adjacent to ester carbonyl
6	138.029	133.80 ± 5.39	↑	C	Adjacent to ester carbonyl
16, 17	69.71, 70.18	69.67 ± 4.76	↑	CH_2	Tether methylene adjacent to ether group.
13, 20	63.89, 63.87	65.13 ± 3.88	↑	CH_2	Tether methylene adjacent to ester group.
3a	54.08	53.39± 7.70	↓	CH	
8	50.38	47.03 ± 5.54	↑	CH_2	Bridge methylene
4	47.34	48.35 ± 4.84	↓	CH	Bridgehead carbon
7	46.58	45.60 ± 4.84	↓	CH	Bridgehead carbon
7a	41.12	43.46 ± 8.18	↓	CH	
1	33.07	35.73± 5.89	↑	CH_2	
14, 15, 18, 19	25.45, 25.98, 26.04, 26.32	25.8 ± 3.74	↑	CH_2	Tether methylene group adjacent to other methylene.

$C_{\#}$ proton number from the Figure 3.22.

δ_{exp} measured chemical shift from the spectrum in Appendix A.11.

δ_{mod} chemical shift modelled using the web-based tool [22].

The ^{13}C-NMR spectrum of compound B3 is clearly consistent with the structure given in Figure 3.22 with the measured values close to those generated by the model. In addition, all the carbons were successfully measured including the weak quaternary carbons. The important features of this spectrum that separates it from

the others are the presence of three separate regions in which the methylene tether protons resonate. The first of these regions are the 4 discrete resonances with an 'up' phase between 25.45-26.32 ppm which can only be due to a shielded secondary carbon such as those present in the tether that are not adjacent to an electron withdrawing oxygen atom. The other carbons from the tether are much more deshielded as they resonate at *c.a.* 64 and 70 ppm due to being adjacent to the ether and ester oxygen respectively. The total number methylene carbons in the tether, eight, combined with their shift confirms that the attributed structure is correct.

Compound B4 (Monomer 12-0-2)

Compound B4 was separated from mixture A2 using the second flash column.

The ^{1}H-NMR spectrum of compound B4 can be found in Appendix A.12 on page 287 but a specific assignment will not be made here for as, like compound B3, there are not enough features to differentiate it from previous proton NMR spectra. The ^{13}C-NMR of compound B4 is more useful and can be found in Appendix A.13 on page 288; its assignment is shown in Table 3.9.

Table 3.9: ^{13}C-NMR Assignment of Compound B3 (Monomer 12-0-2).

$C_{\#}$	δ_{exp}	δ_{mod}	Phase	Type	Comments
N.A.	77.33-76.70		↑		Solvent peaks.
12	-	167.98± 3.08	↑	C	Carbonyl Carbon
11	-	167.64± 2.79	↑	C	Carbonyl Carbon
3	147.19	149.05± 5.39	↓	CH	Vinyl Carbon
5	142.71	149.05 ± 5.39	↓	CH	Vinyl Carbon
2	138.91	138.65± 16.61	↑	C	Adjacent to ester carbonyl
6	138.32	133.80 ± 5.39	↑	C	Adjacent to ester carbonyl
16, 17, 20, 24	69.53, 69.90, 70.29, 70.41	69.67 ± 4.76	↑	CH_2	Tether methylene adjacent to ether group.
13, 24	63.96, 64.20	65.13 ± 3.88	↑	CH_2	Tether methylene adjacent to ester group.
3a	54.18	53.39± 7.70	↓	CH	
8	50.3, 50. 57	47.03 ± 5.54	↑	CH_2	Bridge methylene
4	47.30	48.35 ± 4.84	↓	CH	Bridgehead carbon
7	46.59	45.60 ± 4.84	↓	CH	Bridgehead carbon
7a	41.12	43.46 ± 8.18	↓	CH	
1	32.99	35.73± 5.89	↑	CH_2	
14, 15, 17, 18, 22, 23	25.81, 25.98, 26.32,	25.8 ± 3.74	↑	CH_2	Tether methylene group adjacent to other methylene. Spectrum crowded at this point so it resembles a band, so not all carbons are identified as peaks.

$C_{\#}$ proton number from the Figure 3.23.

δ_{exp} measured chemical shift from the spectrum in Appendix A.13.

δ_{mod} chemical shift modelled using the web-based tool [22].

The spectrum of compound B4 supports the suggestion that a structure has been

made that is consistent with the molecule formed from the reaction of Thiele's acid chloride with the fraction of the poly(THF) with the index n=3 (*i.e.* Monomer 12-0-2 in Figure 3.23*)*.

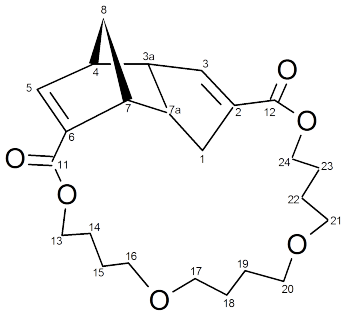

Figure 3.23: Monomer 12-0-2 Numbered for NMR Assignment.

Unlike the ^{13}C-NMR of compound B3 in this case the notoriously weak quaternary carbonyl carbons are not present in the spectrum but despite this the assignment is clear. The quaternary carbons that are adjacent to the carbonyl on the fused ring system are present although they are weak. The resonances of interest in this spectrum are again those arising from the tether. At the highest field there is a group peaks at *c.a.* 26 ppm with an 'up' phase that can only arise from the tether methylene carbons that are not adjacent to an oxygen; in Monomer 12-0-2 there are six of these carbons which resonate at similar field and are so not individually resolved in the spectrum. For this reason it is not possible to count the number of carbons in this situation. If this were the only evidence for the identity of the structure it would not be possible to tell apart this monomer from those with a longer tether (*i.e.* Monomer 16-0-3 or Monomer 20-0-4) but this is not the case. The two methylene carbons that are adjacent to the ester (13 and 24), resonate at 63.96 and 64.20 ppm, this is to be expected and a similar resonance is present in all the previous ^{13}C-NMR spectrum. The remaining carbons from the tether are those that are adjacent to the ether oxygen atoms; in Monomer 12-0-2 there are four of these carbons (16, 17, 20 and 21) and these are individually represented in the ^{13}C-NMR 70.41 to 69.53 ppm.

In summary, with this evidence it is possible to state with confidence that compound B3 has the structure of Monomer 12-0-2 (Figure 3.23)

3.3.4 Thermal Data

As these monomers polymerise upon heating the thermal analysis data has been presented and discussed in the following chapter which is about the polymers.

3.3.5 Dimer, Trimer and Oligomer Rings

The NMR data presented in this chapter provides evidence regarding the identity and structure of the monomers. There is, however, a possibility that a growing linear chain can also form cyclic species made up of multiple units (*i.e.* macrocyclic oligomers), for an example see Figure 3.24. These compounds, if present, are practically impossible differentiate from the monomer rings using NMR alone and would generally have similar solubility and polarity to the monomers and would therefore be unlikely to separate using TLC.

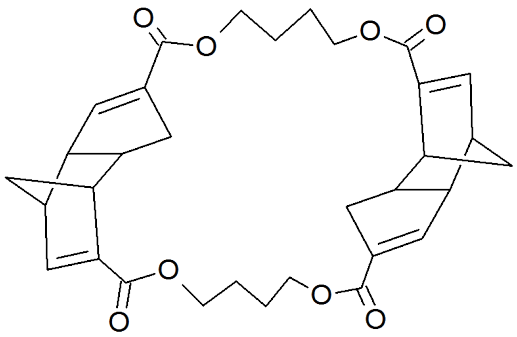

Figure 3.24: Monomer 400 Dimer Ring that would exhibit a very similar NMR to Monomer 400 due to its connectivity being almost identical except with two instances of each atom environment.

Ben-Haida, Hodge, Colquhoun and coworkers [23–28] have exploited the lower viscosity of analogous macrocyclic aromatic esters, ethers and sulfones to enable the in-situ synthesis of highly crystalline high molecular weight thermoplastics such as poly(ether ether ketone) (PEEK). The synthesis involved entropy-driven ring opening polymerisation (EDROP) which does not rely on strained ring systems. The reactive processing of PEEK from molten macrocyclic oligomers is an approach that could allow the production of high performance thermoplastic composites with good fibre wetting (compared to attempts to directly process the high melting, high viscosity, linear thermoplastics.

For the purposes of this work, the dimer, trimer and oligomer rings should perform the same function as the monomers as they contain the key DCPD unit that allows the reversible Diels-Alder reaction. Upon polymerisation it would not be expected that a network formed from the oligomer macrocycles should be substantially different from one formed by the monomers.

3.4 Summary

In this chapter a variety of different monomers have been synthesised with varying degrees of success.

The monomers were chosen as potential candidates to be used as epoxy resin additives in order to facilitate a thermal self-repair mechanism. The monomers have been successfully synthesised and this has been demonstrated by their NMR spectra. The yields of monomer have unfortunately, been quite low. Work has been undertaken to improve the yields and scale-up the reactions and improvements have been made but despite this there has not been a monomer synthesised in a large enough quantity to be used as an epoxy resin additive. The mass of monomer required to produce the compact tension specimens that were used in previous work [5, 6] would be of the order of tens of grams (including losses) to produce even a minimum quantity of specimens at a low concentration of healing agent.

The main difficulty with the lactonisation reaction that most likely leads to poor yields is the difficulty forming the cyclic product. Instead a large proportion of higher oligomers which are formed from the intermolecular rather than intramolecular esterification reaction. There may also be the presence of macrocyclic oligomers. In theory both the linear and macrocyclic oligomers should also be precursors to the reworkable polymer network but upon application of heat to the crude mixture no cure was observed; therefore the purified monomers are required. The oligomers are unsuitable for further use because it had not been possible to separate them from other reaction impurities as they do not move from the baseline on silica gel; presumably due to their molecular weight. It might be possible to purify these oligomers using preparative gel permeation chromatography rather than silica gel which could be a method to attempt in the future. The macrocyclic oligomers, however, could be present in the monomers and remain undetected by NMR.

Potential methods for improving the yields by reducing the amount of oligomers produced could include:

- Higher dilution levels.
- Slower addition of the reagents, *i.e.* better pseudo high dilution.

- Better control of reagent addition; this could be done by replacing the dropping funnels with syringe pump devices.
- A change of catalyst; a suitable catalyst as an alternative to pyridine could be 1,4-diazabicyclo[2.2.2]octane (DABCO).
- The use of polymer supported synthesis.

DABCO is a particularly good nucleophilic catalyst and has been shown in other work to increase the fraction of intramolecular lactones formed [13, 29].

Hodge *et al.* report that one method of improving the yield of cyclic products is to tether one of the reagents to an insoluble polymer support [26, 30]. This approach has the advantage that the linear products remain attached to the polymer support but the cyclics (including macrocyclics) are free in solution.

Time constraints eventually dictated that the project must progress beyond the synthesis towards work with polymers and polymer composites as this research was intended to be more applied and not purely as an exercise in organic synthesis.

The main monomers produced were Monomer 400 and Monomer 401. Monomer 400 was successfully produced (1.2 g) with a yield of 9.6%. The best monomer mass yield produced was 3.64 g (18.2%) of Monomer 401 and this was quite late in the project. Therefore an alternative method of sample fabrication was required that uses only small amounts of healing agent. A potential fabrication method is inkjet patterning onto individual pre-preg plies due to the ability to precisely position material while only requiring small quantities.

Therefore, despite lower than expected yields the monomers were successfully produced and a method of integrating them into composite materials has been identified. The next chapter will present the polymerisation of the monomers, fabrication of small DMA samples and inkjet printing of the monomers.

3.5 References

(1) X. X. Chen, M. A. Dam, K. Ono, A. Mal, H. B. Shen, S. R. Nutt, K. Sheran, and F. Wudl, "A thermally re-mendable cross-linked polymeric material", *Science*, 2002, **295**, 1698–1702.
(Cit. on p. 97.).

(2) Y. L. Liu and C. Y. Hsieh, "Crosslinked epoxy materials exhibiting thermal remendablility and removability from multifunctional maleimide and furan compounds", *J. Polym. Sci., Part A: Polym. Chem.*, 2006, **44**, 905–913.
(Cit. on p. 97.).

(3) Y. L. Liu and Y. W. Chen, "Thermally reversible cross-linked polyamides with high toughness and self-repairing ability from maleimide- and furan-functionalized aromatic polyamides", *Macromol. Chem. Phys.*, 2007, **208**, 224–232.
(Cit. on p. 97.).

(4) E. B. Murphy, E. Bolanos, C. Schaffner-Hamann, F. Wudl, S. R. Nutt, and M. L. Auad, "Synthesis and Characterization of a Single-Component Thermally Remendable Polymer Network: Staudinger and Stille Revisited", *Macromolecules*, 2008, **41**, 5203–5209.
(Cit. on pp. 97, 121, 123, 124, 126, 127, 135, 136, 138, 140.).

(5) S. A. Hayes, W. Zhang, M. Branthwaite, and F. R. Jones, "Self-healing of damage in fibre-reinforced polymer-matrix composites", *J. R. Soc., Interface*, 2007, **4**, 381–387.
(Cit. on pp. 97, 117–120, 148.).

(6) S. A. Hayes, F. R. Jones, K. Marshiya, and W. Zhang, "A self-healing thermosetting composite material", *Composites, Part A*, 2007, **38**, 1116–1120.
(Cit. on pp. 97, 117–119, 148.).

(7) Mohd. S. Md. Jamil, PhD Thesis, University of Sheffield, 2012.
(Cit. on p. 97.).

(8) J. Clayden, N. Greeves, S. Warren, and P. Wothers, *Organic Chemistry*, Oxford University Press, 2001.
(Cit. on pp. 98, 99, 101, 103.).

(9) M. Green and D. M. Thorp, "The mechanism of reaction of phosphorus pentachloride and thionyl chloride with carboxylic esters", *J. Chem. Soc. B*, 1967, 1067–1068.
(Cit. on pp. 99, 101.).

(10) D. Levin, "Potential Toxicological Concerns Associated with Carboxylic Acid Chlorination and Other Reactions", *Org. Process. Res. Dev.*, 1997, **1**, 182–.
(Cit. on p. 100.).

(11) F. A. Carey and R. J. Sundberg, *Advanced Organic Chemistry: Part B: Reaction and Synthesis: Reaction and Synthesis Pt. B*, Springer, New York, 5th Edition, 2007.
(Cit. on p. 102.).

(12) A. R. Fersht and W. P. Jencks, "Acetylpyridinium ion intermediate in pyridine-catalyzed hydrolysis and acyl transfer reactions of acetic anhydride. Observation, kinetics, structure-reactivity correlations, and effects of concentrated salt solutions", *J. Am. Chem. Soc.*, 1970, **92**, 5432–5442.
(Cit. on p. 102.).

(13) P. Hubbard and W. J. Brittain, "Mechanism of Amine-Catalyzed Ester Formation from an Acid Chloride and Alcohol", *J. Org. Chem*, 1998, **63**, 677–683.
(Cit. on pp. 103, 104, 149.).

(14) D. N. Kevill and F. D. Foss, "Acylation mechanisms in aprotic solvents. I. Methanolysis of p-nitrobenzoyl chloride in acetonitrile", *J. Am. Chem. Soc.*, 1969, **91**, 5054–5059.
(Cit. on p. 104.).

(15) M. A. J. Bayliss, R. B. Homer, and M. J. Shepherd, "Aromatic acylation of hydroxy groups via the rare S1 reaction pathway", *Chem. Commun. (Cambridge, U. K.)*, 1990, 305–306.
(Cit. on p. 104.).

(16) K. Hoy, "New values of solubility parameters from vapour pressure data", *J. Paint Technol.*, 1970, **42**, 76–118.
(Cit. on pp. 105, 118.).

(17) A. F. M. Barton, *Handbook of solubility parameters and other cohesion parameters.* CRC Press, Boca Raton, Florida, 2nd, 1991.
(Cit. on pp. 105–107, 118–121.).

(18) W. C. Still, M. Kahn, and A. Mitra, "Rapid chromatographic technique for preparative separations with moderate resolution", *J. Org. Chem.*, 1978, **43**, 2923–2925.
(Cit. on p. 108.).

(19) C. J. Hansen, PhD Thesis, Copenhagen (Danish Technical Press), 1967.
(Cit. on p. 117.).

(20) F. R. Jones, *Handbook of Polymer-Fibre Composites*, ed. F. R. Jones, Longman Scientific and Technical, Harlow, 1st edn., 1994.
(Cit. on p. 118.).

(21) T. Fujimoto, M. Kawahashi, M. Nagasawa, and A. Takahashi, "Preparation of Narrow-Molecular-Weight-Distribution Poly(tetrahydrofuran)", *Polym J*, 1979, **11**, 193–199.
(Cit. on p. 128.).

(22) *ACD Ilabs NMR Predictor*, Online Tool (Accessed 29th September 2013), `http://ilab.acdlabs.com/iLab2/`.
(Cit. on pp. 133, 135, 136, 138, 140, 142, 144.).

(23) A. Ben-Haida, P. Hodge, and H. M. Colquhoun, "Ring-Chain Interconversion in High-Performance Polymer Systems. 3. Cyclodepolymerization of Poly(m-phenylene isophthalamide) (Nomex) and Entropically Driven Ring-Opening Polymerization of the Macrocyclic Oligomers so Produced", *Macromolecules*, 2005, **38**, 722–729.
(Cit. on p. 146.).

(24) A. Ben-Haida, H. M. Colquhoun, P. Hodge, and D. J. Williams, "Synthesis of a Catechol-Based Poly(ether ether ketone) (PEEK) by Classical Step-Growth Polymerization and by Entropically Driven Ring-Opening Polymerization of Macrocyclic Oligomers", *Macromolecules*, 2006, **39**, 6467–6472.
(Cit. on p. 146.).

(25) P. Hodge, "Cyclodepolymerization as a method for the synthesis of macrocyclic oligomers", *React. Funct. Polym.*, 2014, **80**, Cyclic polymers: New developments, 21 –32.
(Cit. on p. 146.).

(26) P. Hodge, M. P. Houghton, and M. S. K. Lee, "A novel approach to the synthesis of cyclic oligo- and poly-esters", *Chem. Commun. (Cambridge, U. K.)*, 1993, 581–583.
(Cit. on pp. 146, 149.).

(27) A. Ben-Haida, H. M. Colquhoun, P. Hodge, and J. L. Stanford, "A Novel Approach to Processing High-Performance Polymers that Exploits Entropically Driven Ring-Opening Polymerization", *Macromol. Rapid Commun.*, 2005, **26**, 1377–1382.
(Cit. on p. 146.).

(28) A. Ben-Haida, H. M. Colquhoun, P. Hodge, and D. J. Williams, "Cyclic oligomers of poly(ether ketone) (PEK): synthesis, extraction from polymer, fractionation, and characterisation of the cyclic trimer, tetramer and pen-

tamer", *J. Mater. Chem.*, 2000, **10**, 2011–2016.
(Cit. on p. 146.).

(29) P. Hubbard, W. J. Brittain, W. J. Simonsick, and C. W. Ross, "Synthesis and Ring-Opening Polymerization of Poly(alkylene 2,6-naphthalenedicarboxylate) Cyclic Oligomers", *Macromolecules*, 1996, **29**, 8304–8307.
(Cit. on p. 149.).

(30) P. Hodge and P. Peng, "Polymer-supported syntheses of some cyclic oligoamides and some cyclic alternating oligo(amide-ester)s", *Polymer*, 1999, **40**, 1871 – 1879.
(Cit. on p. 149.).

Chapter 4

Inkjet Printing, Characterisation and Polymerisation of Monomers

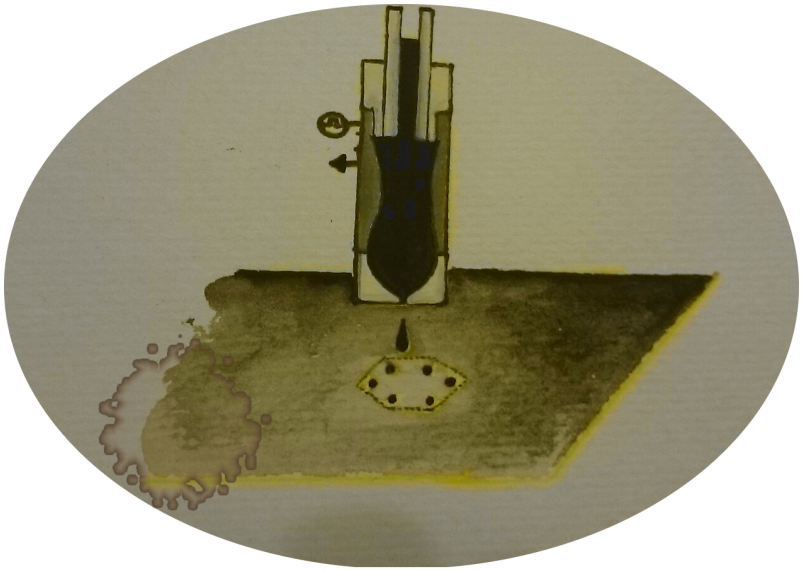

4.1 Introduction

Chapter 3 detailed the synthesis of a variety of different monomers that when thermally polymerised, through a reversible Diels-Alder reaction, are expected to show self-healing behaviour due to the same reversible chemistry used in curing. The quantities of material produced in the synthesis were insufficient to use as an additive to bulk epoxy resin; therefore an alternative method of integration into composites was proposed at the end of Chapter 3. The proposed route of integration is to deposit the monomers between individual plies of carbon-epoxy prepreg material where they can be cured *in situ* and act as a healing agent active on interlaminar damage.

This chapter introduces the principles of inkjet printing, details the formulation of inkjet printable solutions of the monomers (referred to as inks), their subsequent printing and their polymerisation behaviour. In addition the thermal mechanical properties of the polymers are investigated through the fabrication of small specimens suitable for dynamic mechanical analysis (DMA).

4.1.1 Inkjet Printing

Inkjet Printing (IJP) is a flexible, precise material deposition technique which is historically widely used for graphical printing. While graphical applications are still important; IJP is also increasingly gaining popularity as a patterning technique in a variety of technical fields . Some advantages of IJP involve the precise control of the deposition of small amounts of material with minimal waste and without the need for masks such as those used in photo lithography or screen printing. Another advantage is that additional print-heads can be added to a system making scale-up to mass production relatively simple.

The study of forced liquid ejection through a capillary has roots in some of the first experiments on electricity that were conducted by Jean-Antoine Nollet in the 18th Century [1]. Nollet studied many different aspects of electricity and was arguably the first to postulate the existence of electricity in thunderclouds. His experiments on the flow of liquids through a nozzle under the influence of an electric field allowed him to observe an influence on the speed of liquid flow and the attraction of charged droplets to a neutral substrate [2, 3].

Felix Savart was the first to observe, with the naked eye, that ejected liquid columns have a tendency to form perturbations which go on to produce near spherical droplets with associated 'satellite' drops, [4] but it was Joseph Plateau and Lord Rayleigh who recognised that the driving force for this is the reduction of surface area caused by surface tension [5–7]. These findings form the basis of inkjet science and are known as Rayleigh-Plateau instability which explains why and how a stream of fluid, falling due to gravity, breaks up into smaller droplets with the same volume but a lowered surface area after a critical length.

Streams of ink droplets such as these were used to produce a telegraph recorder galvanometer which directed the flow of droplets using a movable nozzle [8]; previous to this, transatlantic telegrams used mirror galvanometers which operated by moving a beam of light across photographic paper. This mechanism, however, could not be considered to be a true inkjet printer because the droplets were of a variable size and unevenly spaced.

Richard Sweet designed the first system that used a 100 kHz nozzle vibration to cause an ink steam to break down into droplets in a controlled manner [9]; the trajectory of the droplets were affected by an electric field which was driven by an input signal. In the absence of signal the droplets were deflected into a gutter. This allowed recording to take place at relatively high speed and forms the basis of modern continuous inkjet printers (CIJ). A problem with these continuous inkjet printers is that they are large, expensive and require inks that can be charged; so they are better suited to high throughput printing. For this reason various printers that could produce a drop on demand (DoD) were designed by a multitude of different companies in the mid to late 20th century.

Thermal inkjet printers (TIJ), also known as bubble jets, work by rapidly heating a portion of ink above its boiling point which forms a local expansion and expels a droplet. This principle was employed successfully by Canon and Hewlett Packard who commercialised the technology at around the same time [10, 11]. This method dominates the home graphical printing market due to the low cost of the thermal actuator components.

Piezoelectric inkjet printing (PIJ) is another method of forcing expulsion of a drop by squeezing, bending, pushing or shearing within a print-head by use of a piezoelectric device which changes shape upon exposure to a voltage. PIJ is well

suited to laboratory printing due to the wide tolerance of different solvents and ink types and the fact that it does not subject the ink to a rapid vaporisation. It is for these reasons that DoD PIJ printing will be used to print the monomer solutions in this work.

For the printing in this chapter a Microfab Jetlab IV system is used which is a PIJ DoD system including a squeeze mode 60 μm device comprising of a ceramic piezo tube which is polarised radially with electrodes on the inner and outer surfaces. A droplet is expelled by the application of a short rise voltage to the piezo actuator. The decrease in tube volume causes a pressure wave that ejects a droplet from the nozzle. The voltage fall time is generally longer than the rise time in which the piezo actuator returns to its original shape; because of this longer time period the rate of volume change is relatively low and cannot overcome the surface tension at the nozzle opening. The result is that liquid is drawn in from the reservoir to replace the ink that was ejected in the droplet [12]. This has been illustrated schematically in Figure 4.1 .

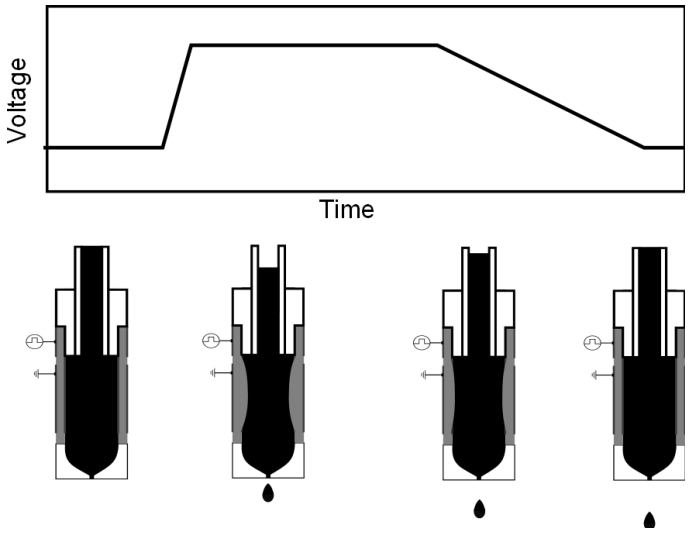

Figure 4.1: The working principle of droplet ejection from a squeeze mode print head such as the Microfab head used in this chapter. A voltage is applied to a piezo transducer (pictured grey) which expands and creates a pressure pulse that ejects a droplet.

In order to consider IJP as a viable delivery method for the monomers that were synthesised in the previous chapter the first consideration that needs to be addressed is whether the monomers can be formulated into a printable ink. Printable is defined

as an ink that can form stable, uniform droplets when ejected from a nozzle with consistent volumes and velocities [13].

The most important intrinsic physical properties that affect the printability of a given ink are its viscosity (η) , density (ρ) and surface tension (γ) which can be used with information about the print head nozzle diameter to predict the printability of a given system [14]. A modified Navier-Stokes equation which was originally proposed by Fromm for the ejection of a droplet [15] (Equation 4.1) can be used to calculate a dimensionless 'Z' number, the value of which estimates whether a stable droplet is achievable. The 'Z' number is the inverse of the Ohnesorge number which is the ratio of the square root of the Weber number (Equation 4.2) to the Reynolds number (Equation 4.2) and relates viscous forces to surface tension and inertial forces.

$$Z = \frac{1}{O\mathrm{h}} = \frac{N_{\mathrm{Re}}}{(N_{\mathrm{We}})^{1/2}} = \frac{(a_{\mathrm{r}}\rho\gamma)^{1/2}}{\eta} \tag{4.1}$$

Where:

a_{r} is the nozzle radius.

N_{Re} is the Reynolds number.

N_{We} is the Weber number.

$O\mathrm{h}$ is the Ohnesorge number.

$$N_{\mathrm{We}} = \frac{\nu^2 a_r \rho}{\gamma} \tag{4.2}$$

Where:

ν is the average travel velocity.

$$\mathrm{N}_{Re} = \frac{\nu a_{\mathrm{r}} \rho}{\eta} \tag{4.3}$$

A printable range of Z values was determined to be between 1 and 10 by Reis and Derby in 2000 [16] using computational fluid dynamics and an experimental study in parallel. Reis and Derby state that the upper limit of Z exists because of the tendency for satellite droplets to form instead of a single stable droplet and that the lower limit of Z exists because the fluid viscosity dissipates the applied pressure pulse. This is not an absolute range as it has been shown that inks outside this

range can be perfectly printable [17, 18], however as a broad tool it is useful. In practice the viscosity is the main limiting factor; if it is too high the fluid is too viscous to be printed by inkjet.

4.1.2 Dynamic Mechanical Analysis (DMA)

Dynamic mechanical analysis (DMA), sometimes referred to as dynamic mechanical thermal analysis (DMTA) is a technique in which a small sinusoidal force is applied to a sample as a function of time, temperature or frequency [19]. The applied force brings about a corresponding strain with its own amplitude and phase angle (relative to the applied force) as illustrated in Figure 4.2.

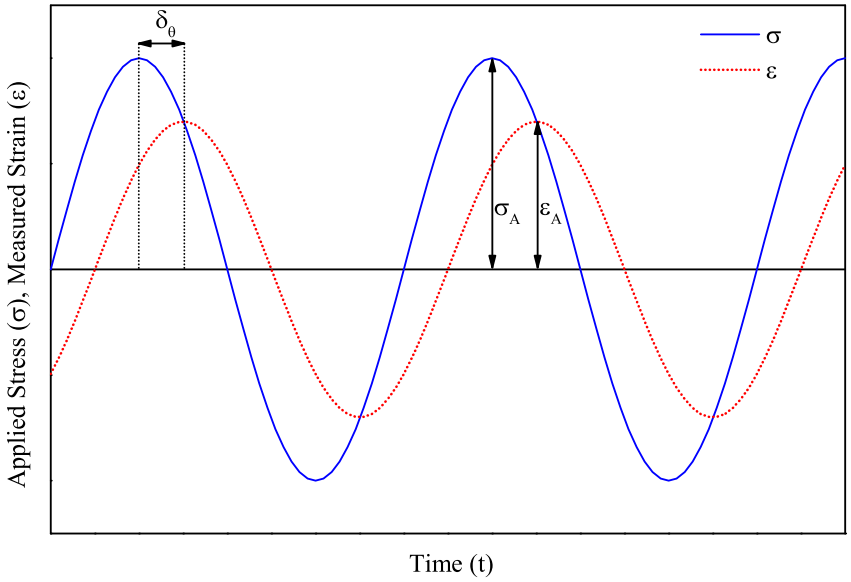

Figure 4.2: The principles of DMA illustrated by the application of a sinusoidal stress (σ) to a linear viscoelastic material yielding a sinusoidal strain (ε) with a phase angle δ_θ, stress amplitude σ_A, and a strain amplitude ε_A .

The mode of deformation depends upon the clamp assembly used. Common assemblies include single and dual cantilever bending; 3-point bending, tension, shear and compression; the use of which are generally dictated by the type of specimen and the capabilities of the equipment. Tension, for example, is usually used for thin films and fibres whereas 3-point bending would usually be used for stiff materials such as carbon-fibre composites where the amount of force the equipment can generate is small. The phase angle (δ_θ*) is the difference (usually measured in Radians) between a the applied stress and measured strain waves.

*The symbol for phase angle is usually δ, the subscript theta has been added to differentiate it from the other common uses of δ in this thesis (NMR chemical shift and solubility parameters)

The complex modulus (tension: E^*, shear: G^* or bulk compression: K^*) represents the stiffness of the material and can be measured directly by taking the ratio of the amplitudes of the applied stress and the measured strain. It is made up of the storage modulus E', G' or K') which is the real part and the loss modulus (E'', G''or K'') which is the imaginary part. This relationship is shown in Equation 4.4 [20].

$$|E^*| = \frac{\sigma_A}{\varepsilon_A} = \sqrt{[E'(\omega)]^2 + [E''(\omega)]^2} \tag{4.4}$$

Where:

ω is the applied frequency in $\mathrm{rad\,s^{-1}}$

The storage component of the complex modulus is proportional to the energy stored by elastic deformations within the material and is roughly equivalent to Young's modulus for a single small stress, rapidly applied, within the elastic region of a given material. The loss component of the complex modulus is proportional to the energy lost as heat by the viscous behaviour of the material. For a specific frequency (ω) the storage modulus (E') and loss modulus (E'') can be calculated from the measured DMA parameters as follows:

$$E' = \cos\delta_\theta(\frac{\sigma_A}{\varepsilon_A}) \tag{4.5}$$

$$E'' = \sin\delta_\theta(\frac{\sigma_A}{\varepsilon_A}) \tag{4.6}$$

A perfectly elastic material such as steel shows no difference in phase ($\delta = 0$) between the applied stress and measured strain and therefore shows no loss modulus as $\sin 0 = 0$ and $\cos 0 = 1$. A perfectly viscous material such as a liquid has a phase angle of $90°(\frac{1}{2}\pi$ rad) and therefore there is no storage contribution to the complex modulus as $\sin 90 = 1$ and $\cos 90 = 0$ [20].

Another important parameter is the dimensionless loss factor ($\tan\delta_\theta$[†]) which is a measure of mechanical damping or internal friction within the viscoelastic system. The loss factor can be also expressed as the ratio of loss modulus to storage modulus

[†]The subscript theta will be omitted from the loss factor for the remainder of this thesis as it is no longer ambiguous.

as shown in Equation 4.7 (as a result of the definition of the tan function $\tan\theta = {}^{\sin\theta}/_{\cos\theta}$).

$$\tan\delta_\theta = {}^{\sin\delta_\theta(\frac{\sigma_A}{\varepsilon_A})}/_{\cos\delta_\theta(\frac{\sigma_A}{\varepsilon_A})} = \frac{E''}{E'} \tag{4.7}$$

As the loss factor is the ratio of the loss to the storage modulus a low loss factor indicates that a material is behaving elastically while a high loss factor indicates that the material is presenting viscous behaviour. This is particularly useful for polymers which most commonly show viscous and elastic behaviour. A plot of the loss factor against a change in temperature gives characteristic peaks that can be attributed to a wide range of physical transitions such as gamma transitions, beta transitions, glass transitions (also known as alpha transitions) or melting and small scale crystal slippage; some of which are frequency dependent. By running the same experiment at a range of different frequencies it is possible to differentiate between these different types of transitions. Gamma and beta transitions show some small frequency dependence; alpha transitions such as the glass transition show a pronounced frequency dependence (5 to 7 °C for every decade change in frequency [21]) and melting is frequency independent.

The frequency dependence can be used to calculate the activation energy for the transition by using the Arrhenius activation energy equation (Equation 4.8)[22–24].

$$f = Ae^{-E_a/RT} \tag{4.8}$$

Where:

A is the Arrhenius pre-exponential factor,

E_a is the activation energy,

R is the molar gas constant,

T is temperature (K).

By taking the natural logarithm of both sides of the equation this can be expressed as Equation 4.9.

$$\ln(f) = \ln(A) - \frac{E_a}{RT} \tag{4.9}$$

The activation energy can be calculated using either loss factor or loss modulus by plotting the (natural log) frequency of the applied oscillation against the inverse of the temperature of the peak position. This should yield a straight line in which the slope is equal to the negative activation energy $-E_a$ in $J\,mol^{-1}$ divided by the gas constant R in $J\,K^{-1}\,mol^{-1}$. Alpha transitions such as the glass transition have activation energies of around 300 to 611 $kJ\,mol^{-1}$ whereas beta transitions have an activation energy of around 40 to 80 $kJ\,mol^{-1}$[25].

The measurement of the glass transition (T_g) by DMA is particularly industry or background dependent and can be a matter for disagreement. Multiple factors will effect the value of the glass transition such as the heating rate, frequency and applied strain. Values for the T_g can be calculated from the storage modulus, the loss modulus and the loss factor traces with various different methods. The most popular methods are:

The step in the storage modulus can be analysed using the same methodology employed for DSC.

- As described in ISO ISO 11357-1 and ISO 6721-11:2012 [26, 27] Tangents are applied to the linear portion above and below the step and at the point halfway between the two. The intersections of the linear tangents with the halfway point tangent gives the extrapolated onset temperature (T_{eig}) and the extrapolated end temperature (T_{efg}). The midpoint temperature (T_{mg}) is determined from the half-step height.

  - An alternative onset point uses the turning point method. In this method a tangent is applied to the linear portion above the step and a tangent is applied at the point of inflexion which is determined by the local maximum in the first derivative curve. The intersection point gives the onset (T_{g0}) [20].

- The peak of the loss factor curve can be used ($\tan\delta_{max}$) [27].

- The peak of the loss modulus curve can be used (E''_{max})[27, 28].

The advantage of the turning point method is that a linear portion is not needed after the glass transition. Therefore, for this thesis the turning point method will be used for the onset of drop in storage modulus and will be given the symbol (E_0') presented alongside the peak of the loss factor and the loss modulus curves where transitions are to be analysed from the DMA.

4.2 Experimental

4.2.1 Preparation of Monomer Solutions for Inkjet Printing

All solvents were supplied by Fisher Scientific, Loughborough, UK and were at least 99% purity.

Monomer 401, 5% (w/v) and 1% (w/v) Solution in Chloroform

Monomer 401, 1.00 g was added to 20 mL of chloroform in a 25 mL vial. The vial was stoppered and the vessel was shaken gently for *c.a.* 10 minutes after which time the material was fully dissolved.

To make the 1% solution: 10 mL of the 5% solution prepared above was removed using a volumetric pipette and transferred into a 50 mL volumetric flask. The volumetric flask was filled to the mark using fresh chloroform and gently shaken. Both solutions were filtered through cotton-wool in a Pasteur pipette into 10 mL vials ready for printing.

Monomer 401, 4.5% (w/v) Solution in 90% Chloroform, 10% Acetophenone

To 9 mL of the 5% solution of Monomer 401 in chloroform (measured using a graduated pipette) was added 1 mL of acetophenone. This created an effective concentration of 4.5% monomer in 90% chloroform, 10% acetophenone.

Monomer 401, 5% (w/v) in Ethyl Acetate

Monomer 401, 0.20 g was added to 4 mL of in a 10 mL vial. The vial was stoppered and the vessel was shaken gently for *c.a.* 10 minutes after which time the material was fully dissolved.

The solutions was filtered through cotton-wool in a Pasteur pipette into a 10 mL vial ready for printing.

Monomer 400, 5% (w/v) and 1% (w/v) Solution in Ethyl Acetate

Monomer 400, 2.00 g was added to 40 mL of chloroform in a 50 mL vial. The vial was stoppered and the vessel was shaken gently for *c.a.* 10 minutes after which time

the material was fully dissolved.

To make the 1% solution: 10 mL of the 5% solution prepared above was removed using a volumetric pipette and transferred into a 50 mL volumetric flask. The volumetric flask was filled to the mark using fresh chloroform and gently shaken. Both solutions were filtered through cotton-wool in a Pasteur pipette into 10 mL vials ready for printing.

4.2.2 Inkjet Printing of the Monomer Solutions

For both glass microscope slide substrates and carbon fibre epoxy prepreg substrates (977-2) the monomer inks were printed at room temperature using a drop-on-demand (DOD) JetLab 4xl printer setup with the standard 60 μm printheads. All printing devices were purchased from MicroFab Inc. (Plano, TX, USA).

Droplets were generated at room temperature using a fixed frequency of 200 Hz. The substrates were placed onto a platen that can move in the x and y directions. A stroboscopic video camera was used to optimize the droplet formation.

The printing settings were varied to in order to achieve a stable droplet. Typical settings for the inks using ethyl acetate solvent involved a dwell voltage of 43-55 V and a pulse width of 35 μs as illustrated by the waveform shown in figure 4.3 which produced droplets of *c.a.* 100 μm.

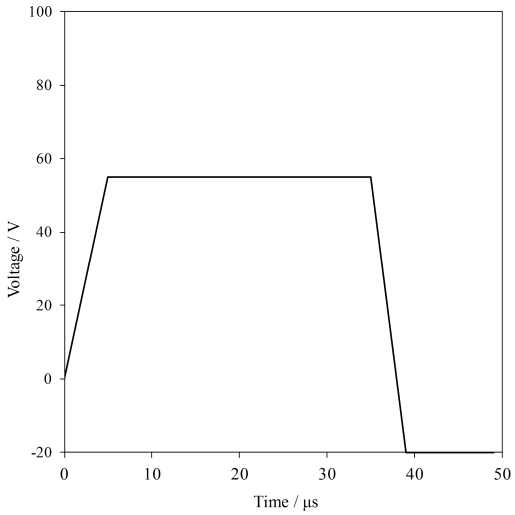

Figure 4.3: A typical waveform used to print the monomer inks. This waveform represents the conditions used to form the stable droplets of Monomer 400 5% (w/v) in ethyl acetate.

A hexagonal pattern of dots was printed with spacings dx= 0.4 μm dy = 0.2 μm as shown in Figure 4.4. This pattern can be varied but was kept constant for this work in order to maintain consistency with the patterning reported in the recent literature [29].

Two substrates were used for the printing:

1. Borosilicate microscope slides with dimensions 26 x 76 x 1 cm^3 used to test printing patterns and cure the monomer droplets on the glass slides. The glass slides were supplied by Fisher Scientific, Loughborough, UK.

2. A commercial aerospace grade toughened unidirectional epoxy-carbon prepreg system Cycom 977-2 supplied by Cytec Industries Inc, Östringen, Germany. The prepreg was less than two years old, stored sealed at -18 °C with an out-life less than the maximum number recommended by the manufacturer (40 days). The prepreg was allowed to warm to room temperature in its sealed packet for a minimum of 24 hours before use. The prepreg was cut into 150 x 150 mm^2 squares and a 140 x 90 mm^2 section was printed (as depicted in figure 4.4) which will form the test area in the subsequent double cantilever beam tests (DCB) that will feature in the following chapter. After printing the prepreg was returned to the freezer.

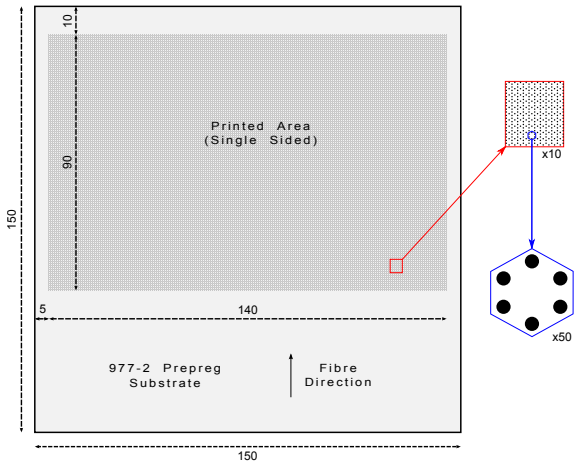

Figure 4.4: A schematic diagram showing the printed area and pattern on the 977-2 prepreg substrate which was later used to fabricate double cantilever beam (DCB) specimens. All dimensions are in mm.

4.2.3 Optical Microscopy of the Monomer Pattern

The glass slides printed with the Monomer 401 print pattern were photographed using an optical microscope, Zeiss, Jena, DE . In order to properly view the droplets which were transparent on a transparent substrate a combination of incident and transmission lighting was used.

4.2.4 Thermal Cure of the Monomer Pattern

The glass slides with Monomer 401 print pattern were placed onto a heated plate and the plate temperature was set to 130 °C; this corresponded to approximately 120 °C on the surface of the glass as measured using an infra-red non-contact thermometer. The heat was maintained for 2 hours after which the heated plate was turned off and the plate and the substrate were allowed to cool to room temperature at a natural rate.

4.2.5 Hot-Stage Optical Microscopy of the Monomer Pattern

A 2 x 2 cm^2 section of a glass slide previously printed with a Monomer 401 print pattern was placed onto a microscope hot stage and heated to 180 °C for 3 hours. A representative printed dot was chosen and photographs were taken before heating, after heating and every subsequent hour.

4.2.6 Cure Rheometry

An AR-2000 rheometer with a Peltier plate heater supplied by T.A. instruments, New Castle, Delaware, USA was used for rheometry tests. A 40 mm 2° steel cone was used to keep the rate of strain constant with a truncation gap of 52 μm. The sample was loaded onto the preheated (120 °C) Peltier plate, when the material was fully melted the head was lowered to the truncation gap and excess polymer was wiped off using a cloth. The head was run in oscillation mode at 3 frequencies (0.1, 1, and 10 Hz) with a displacement of 0.001 radians for 12 hours.

4.2.7 DMA Testing and Specimen Fabrication

DMA testing was undertaken on a Perkin Elmer DMA 8000 instrument equipped with a liquid nitrogen cooling system. Two types of specimens were produced: samples in material pockets and thin rectangular polymer specimens.

4.2.7.1 Material Pockets

Material pockets are stainless steel envelopes designed to hold small sample quantities or to allow DMA analysis when specimens are not self-supporting. The material pockets were supplied by Perkin Elmer specifically for the DMA 8000 instrument that is used in this work. The dimensions of the closed material pockets were 30 x 6 x 1 mm^3 Approximately 50 mg of monomer or ground polymer was added to the material pocket which was then closed and crimped using pliers (see figure 4.5).

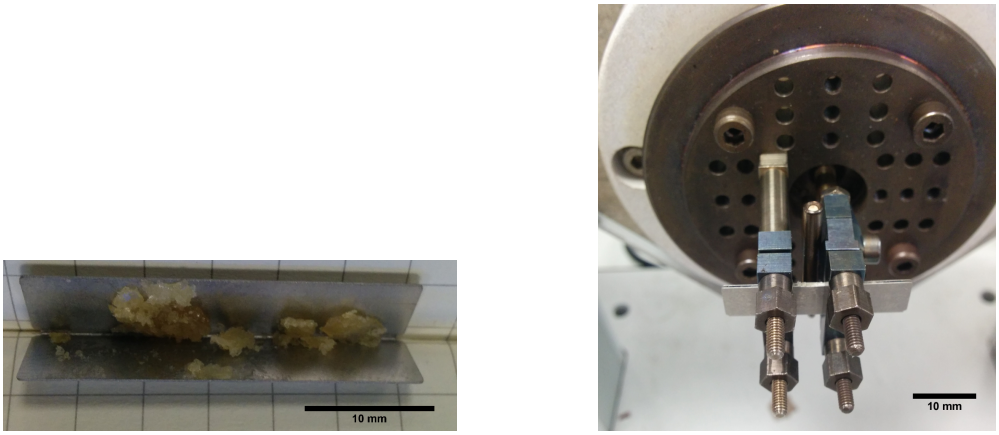

(a) Filling the material pocket **(b)** Dual-cantilever test.

Figure 4.5: A photographs of the material pocket setup.

The specimens were clamped in the single-cantilever bending geometry with a free length of 5 mm and displacement control fixed at 0.05 mm (1% strain) and three simultaneous frequencies (0.1 Hz, 1 Hz and 10 Hz). The specimens were subjected to a temperature scan, the range of which varied by experiment, but was generally -50 to 150 °C with a heating rate of 2 °C min^{-1}. In addition an experiment with a blank material pocket was undertaken to highlight any possible contribution to the results.

4.2.7.2 Polymer Specimen

An open female mould was produced from built-up layers of PTFE coated adhesive fibreglass mounted on a glass microscope slide. The mould cavity was approximately 20 mm x 5 mm by 3 mm deep. Finely ground monomer was added to the cavity as shown in figure 4.6. The Monomer 401 was cured under full vacuum, in a vacuum oven, at 120 °C for 12 hours, Monomer 400 was cured for the same length of time but at 150 °C.

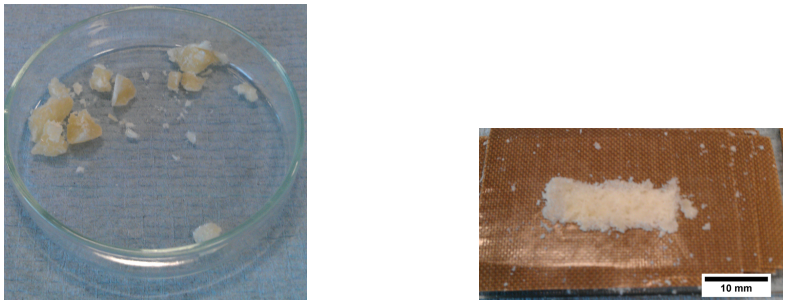

(a) Monomer 401 pieces

(b) Ground into the PTFE mould

Figure 4.6: The polymer specimen fabrication process (Monomer 401).

After the powder had initially melted additional monomer material was added to the mould to bring the level approximately up to the top of the mould. After the 12 hours had elapsed the power to the oven was cut and the door was left closed to allow gradual cooling overnight back to room temperature. The cured specimens were released by gently peeling away the layers of PTFE fabric from around the specimen.

The specimen was clamped in the single-cantilever bending geometry (free length 5 mm) with a displacement control fixed at 0.01 mm (0.2% strain) and three simultaneous frequencies (0.1 Hz, 1 Hz and 10 Hz). The specimen was subjected to a temperature scan, the range of which was -50 to 250 °C with a heating rate of 2 $^{\circ}\mathrm{C}\,\mathrm{min}^{-1}$.

4.3 Results and Discussion

In this section observations and results will be presented and discussed related to ink formulation and inkjet printing. In addition dynamic, mechanical and thermal test results will also be presented and discussed.

4.3.1 Inkjet Printing

In order to inkjet print monomers onto prepreg there were several prerequisite experiments that needed to be performed. These were:

- Printable inks first needed to be formulated with sufficient monomer solubility or suspension stability, low enough viscosity and suitable volatility.
- The printing parameters needed to be optimised in order to produce stable droplets;
- The inks needed to be tested by printing onto a suitable substrate such as a glass slide in order to view the patterns with optical microscopy and perform thermal stability experiments.

4.3.1.1 Ink Formulation and Droplet Stability

Initially chloroform was chosen as a solvent; the reason for this was it was known to be a good solvent for the monomers from the synthetic work undertaken in Chapter 3. Prior to the optimisation there were many satellite droplets or undesirable droplet elongations. The formation of the satellite droplets was not ideal as it has an effect on printing quality; however in this case it was not deemed to be a critical problem for this application as the printing is being used as a method of regular material deposition (sandwiched between prepreg plies) rather than for the production of features. After optimisation of the printing parameters, the monomer solutions in chloroform formed relatively stable droplets (see Figure 4.7) .

It was found that attempts to print monomers with a higher concentration than 1% w/v in chloroform led to blocked printheads after only one or two minutes of printing.

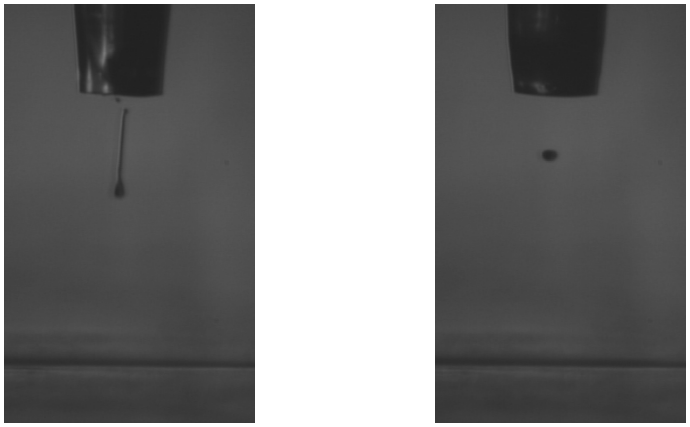

(a) Before optimisation an elongated tail was visible

(b) After optimisation

Figure 4.7: Images from the stroboscopic camera showing the droplets of the monomer inks (in chloroform).

This nozzle clogging behavior was attributed to the high volatility of chloroform (vapour pressure 21 kPa [30]) leading to solvent evaporation in the print-head. In an attempt to cure this behaviour 10% acetophenone (vapour pressure 0.05 kPa [31]) was added to the 5% w/v inks but there did not appear to be any noticeable improvement as the printheads were still getting blocked. In order to deposit larger concentrations of monomer an alternative solvent had to be found.

The second thing that needs to be considered is whether a particular solvent ink is likely to be printable. In order to select an alternative solvent first the solubility was considered by returning to the Hansen solubility parameters of the monomers previously calculated in Chapter 3, Section 3.3.1.5 on page 121. These solubility parameters are presented in Table 4.1 along with the distance, R_a, in Hansen space between them and a selection of common laboratory solvents. R_a was calculated using equation 3.11 which is presented in Chapter 3, Section 3.3.1.3 on page 120.

It can be seen from Table 4.1 that the solvents with the best potential solubility for the monomers are Acetone, Tetrahydrofuran, Dichloromethane, Chloroform, Toluene, Ethyl Acetate and Dimethylformamide.

The monomers that are being dissolved are relatively low molecular weight concentrations therefore it is sufficient to consider the properties of the solvents alone.

Table 4.1: A Summary of the Modelled Solubility Parameters for the Monomers Showing the Distance, R_a, in Hansen Space Between Monomers and Selection of Common Laboratory Solvents

Substance Name	**Hansen Solubility Parameter**			**Distance in Hansen Space, R_a**	
	δ_d	δ_p	δ_h	**From M400**	**From M401**
Monomer 400	16.0[a]	10.2[a]	0.00[a]	0.0	0.8
Monomer 401	16.0[a]	11.0[a]	0.00[a]	0.8	0.0
Acetone	15.6[b]	11.7[b]	4.1[b]	4.4	4.3
Tetrahydrofuran	16.8[b]	6.8[b]	7.2[b]	8.1	8.4
Dichloromethane	18.2[b]	6.1[b]	6.3[b]	8.8	9.1
Chloroform	17.8[b]	3.1[b]	5.7[b]	9.8	10.3
Toluene	18[b]	1.4[b]	2[b]	9.9	10.5
Ethyl Acetate	15.1[b]	5.3[b]	9.2[b]	10.6	11.0
Dimethylformamide	17.4[b]	13.7[b]	11.3[b]	12.2	12.0
Isopropanol	15.3[b]	6.1[b]	17.[b]2	17.7	17.9
Methanol	15.1	11.3	22.9	23.0	23.0
Water	15.5[b]	16.0[b]	42.3[b]	42.7	42.6

δ values in units of $J^{\frac{1}{2}}$ $cm^{-\frac{3}{2}}$.

[a] values calculated using the method outlined in Chapter 3, Section 3.2.1 on page 105

[b] data from Ullmann's Encyclopedia of Industrial Chemistry [30]

The physical properties and calculated Z numbers of the same common laboratory solvents are presented in Table 4.2. The Z number calculation has been introduced previously in Section 4.1.1.

From Table 4.2 it is possible to exclude dichloromethane and acetone on the basis of their high volatility (their vapour pressure is even higher than that of chloroform) and very large Z numbers from the list potential solvents. Tetrahydrofuran has been suspected, anecdotally, from previous experiments within the group to cause some problems due to incompatibility with materials within the printer and is also quite volatile and so will also be excluded from the list. After these exclusions the remaining potential solvents are dimethyl formamide, toluene and ethyl acetate.

From this list, ethyl acetate was chosen because it was available within the laboratory at the time and has low toxicity.

Table 4.2: A Summary of Physical Properties and Z-Numbers for Each Fluid[a]

Solvent	**Density**[b] ($Kg\,m^{-3}$)	**Vapour Pressure**[b] (kPa)	**Viscosity**[b] (mPa s)	**Surface tension**[b] ($mN\,m^{-1}$)	**Inverse (Z) of Ohnesorge number**[c]
Isopropanol	786	4.2	2.2	21.7	14.5
Dimethyl Formamide	949	0.6	0.92	36.8	49.7
Methanol	791	12.8	0.61	22.6	53.7
Tetrahydrofuran	888	17.3	0.61	26.4	61.5
Toluene	867	2.9	0.599	28.5	64.3
Water	1000	3.2	1	72.0	65.7
Ethyl Acetate	900	10.3	0.45	23.9	79.8
Chloroform	1488	21	0.58	27.2	84.9
Acetone	791	24.1	0.33	23.7	101.6
Dichloromethane	1326	47.5	0.44	29.0	109.2

[a] droplet diameter assumed to be the nozzle diameter, 50 μm

[b] data from Ullmann's Encyclopedia of Industrial Chemistry [30]

[c] Calculated using equation 4.1 on page 160

The inks prepared using ethyl acetate as a solvent proved to be highly successful for printing higher concentrations (5% w/v) without any print-heads clogging. Toluene or dimethylformamide (if the solubility is sufficient) are also likely to be suitable solvents but as a successful system was identified further trials were not necessity.

4.3.1.2 Glass Slide Substrate

In order to test that the monomers were being successfully deposited by the printing process, Monomer 401 was printed onto a glass microscope slide. Optical microscopy of the pattern obtained can be seen in Figure 4.8. The pattern produced was regular and repeatable with few misplaced droplets. The diameters of the printed dots varied between about 100 and 120 μm.

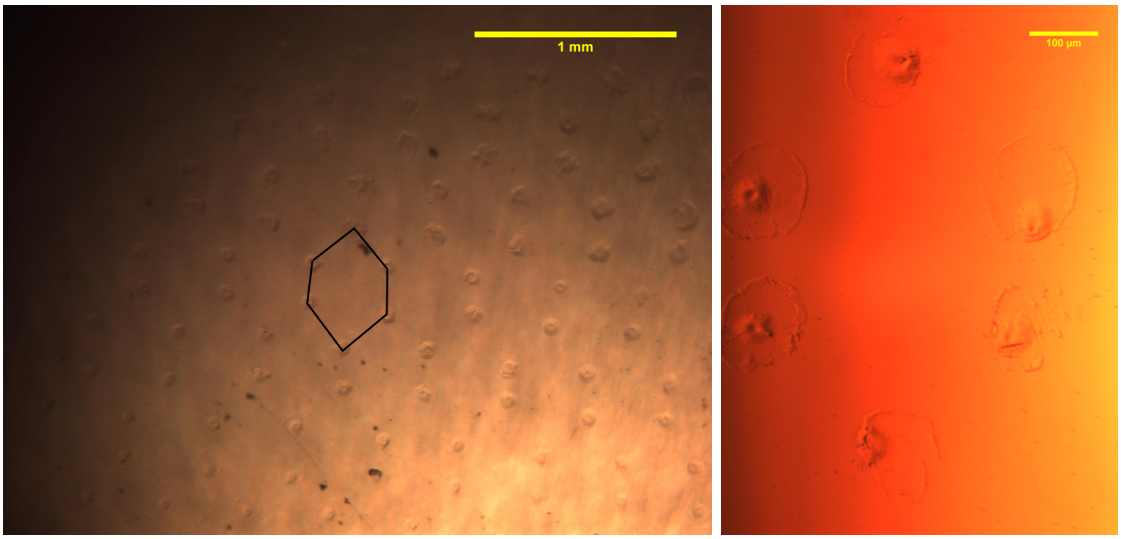

(a) **(b)**

Figure 4.8: Optical microscopy of Monomer 401 printed onto a glass microscope slide substrate in the standard hexagonal shape.

The dots, as-printed, could be smeared across the surface by a soft cloth but after cure at 120 °C for 2 hours the pattern had hardened (presumably through cure of the monomer) and adhered strongly to the glass substrate as they could not be dislodged even with a needle tip.

The Monomer 401 pattern was also analysed by hot-stage optical microscopy in which the dot was heated to 180 °C (to simulate the cure conditions of the epoxy pre-preg). A single dot before and after the thermal treatment is shown in Figure 4.9. These images show the dot is still in position after the thermal treatment and that there has been no significant spreading ($\sim$100 μm before, $\sim$100 μ m after) or coalescence prior to complete cure.

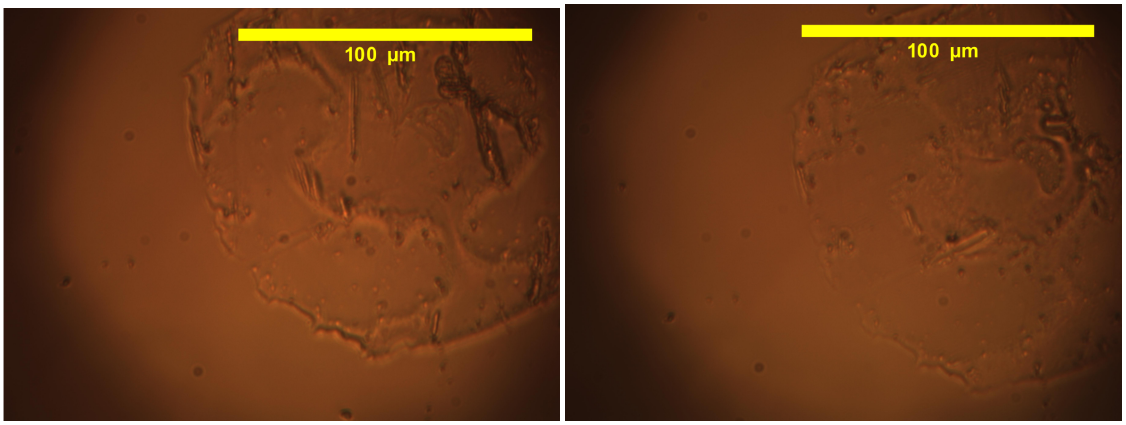

(a) Before heating **(b)** After 3 hours at 180 °C

Figure 4.9: Optical microscopy of Monomer 401 printed onto a glass microscope slide substrate.

4.3.1.3 Prepreg Substrate

The monomer inks were successfully printed onto carbon fibre-epoxy prepreg. The details of the manufacture and testing of specimens made from this prepreg are given in Chapter 5. It was not possible to obtain similar hot stage images on the prepreg substrate but the surface roughness is likely to lead to decreased spreading. The printed pattern on the surface of the prepreg is visible with the naked eye but it has not been possible to show this with a photograph. The glass substrate is more suitable for printing characterisation because they are very smooth, chemically inert and optically transparent so the printed droplets can be observed.

As discussed previously in Section 4.1, there was not sufficient material available to study the behaviour of these specific monomers on the prepreg. It is very difficult to see patterning on prepreg with optical microscopy, however this has been studied for printed thermoplastics on an identical prepreg substrate after adding fluorescent dye. In this study the printed material was shown to remain on the prepreg after a thermal treatment although there was some preferential flow along the fibre direction [29].

4.3.2 Volume fraction of additive printed

Using the same assumptions made by Zhang *et al.* [32] it is possible to estimate the volume fraction of printed additive within the composite. The assumptions are that

the droplets are perfect spheres and that the diameter of the droplet is the same as the diameter of the printhead orifice.

Therefore a 60 μm printhead (30 μm radius) produces droplets with a volume (V) of:

$V = \frac{4}{3}\pi 30^3 = 113097\,\mu\text{m}^3 = 1.13 \times 10^{-13}\,\text{m}^3$

Dual Cantilever Beam Specimens Chapter 5 reports on the results from dual cantilever beam (DCB) testing. The DCB specimens were printed on a single ply with either 5% w/v or 1% w/v concentration ink.

- For the 5% w/v inks approximately 5% of this volume (assuming negligible difference in density) is material that is deposited and the other 95% is solvent that is evaporated. Therefore the volume of material deposited per droplet is $1.13 \times 10^{-13} \times 0.05 = 5.65 \times 10^{-15}\,\text{m}^3$.
- For a single DCB specimen the printed area is nominally 90 mm x 25 mm with a dot spacing of 0.4 mm across the width and 0.2 mm along the length. This requires $(^{90}/_{0.2}) \times (^{20}/_{0.4}) = 22500$ droplets.
- The total volume of printed material can be calculated as $5.65 \times 10^{-15} \times 22500 = 1.27 \times 10^{-10}\,\text{m}^3$
- Considering the section thickness is approximately 3 mm, the volume fraction can be calculated as $\frac{1.27 \times 10^{-10}}{0.003 \times 0.020 \times 0.090} = 2.36 \times 10^{-5}$or 0.0024 %
- For the 1% inks the volume fraction can be calculated as 0.00047 % using the same method.

Short Beam Shear Specimens Chapter 5 also reports on the results from short beam shear (SBS) testing. The SBS specimens were either printed with 1% w/v ink on all eight plies or with 5% w/v ink on four out of eight plies. The short beam shear specimens had nominal dimensions of 20 mm x 10 mm x 2 mm.

Using the same approach the volume fraction of printed material in the short beam shear specimens can be calculated as:

- 0.014% for the 5% w/v inks printed on 4 out of 8 plies.
- 0.0057% for the 1% w/v inks printed on 8 out of 8 plies.

4.3.3 Monomer & Polymer 401

Details of the synthesis of Monomer 401 are given in Chapter 3, Section 3.3.2.4 on page 127. This synthesis produced the most material and as such enabled the most in depth study.

4.3.3.1 Isothermal Rheometry of Monomer 401

In order to obtain the optimum cure time Monomer 401 was analysed using a rheometer in oscillation mode set with an isothermal temperature program at 120 °C. The results of this are shown in Figure 4.10.

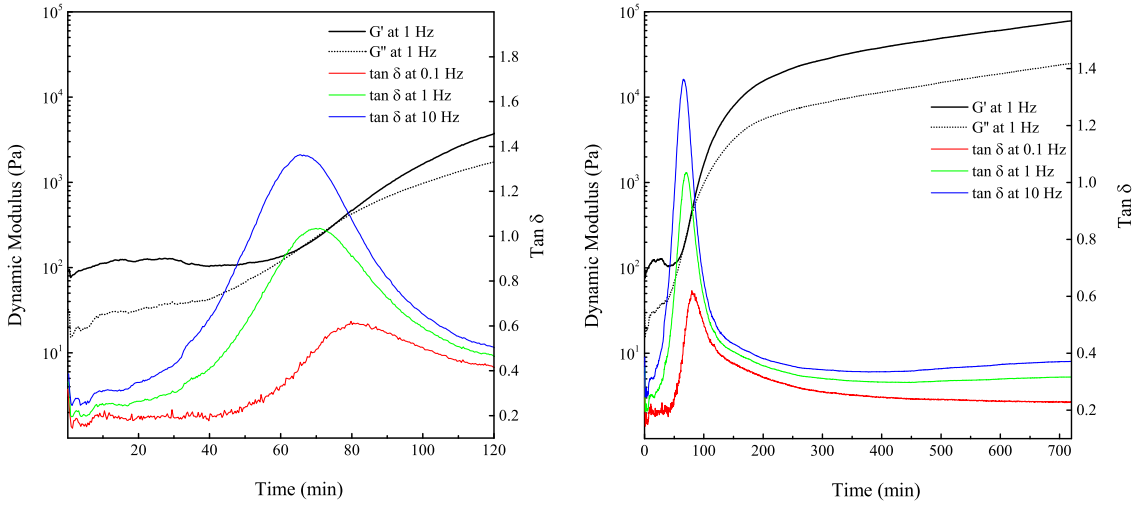

(a) Initial 2 hours expanded **(b)** Full plot

Figure 4.10: Isothermal rheometry on Monomer 401 at 120 °C for 12 hours (Y scale shown is logarithmic).

For clarity, Figure 4.10a shows an expanded view of the start of the rheometry experiment. The interesting features of this region are the fact that the shear storage modulus (G') is initially higher than the shear loss modulus (G''); this indicates that Monomer 401, in the melt shows viscoelastic behaviour immediately. A viscous liquid would generally have an initial G'' several orders of magnitude larger than G'. G' itself may be initially 0 or negligible and after an initial heat-up phase the crossover of G' with G'' is typically used as an estimation of gelation in a resin [33,

34]. A better estimate of gelation is thought to be the point at which tan delta is frequency independent [35].

These features do not appear in the Monomer 401 sample. G' does however initially reduce and briefly cross the G'' trace at t = 65.5 min and remain slightly lower before crossing again at t = 75 min. This area also corresponds to the point just before a rapid increase in both G' and G''; therefore 75 min can be used as a rough estimation of the gel time.

The experiment time was set to 12 hours and run overnight, as can be seen in Figure 4.10b the G' andG'' does not reach a steady plateau in this time period and was still increasing at the point that the experiment was stopped. The length of the time scale required was not anticipated because the conditions previously reported for curing this material were *c.a* 10 hours [36]. In some thermosets the modulus increases almost indefinitely with cure at the expense of toughness and elongation; this is more commonly encountered in elastomer systems and is known as a 'marching modulus'. It is possible that Monomer/Polymer 401 could be displaying this kind of cure behaviour because of the reversible nature of the Diels-Alder bonds that are forming and reforming into a progressively more ordered structure.

It was not possible to re-run this experiment for a longer period to see if a plateau could be obtained because of the amount of material consumed. It was the possibility of this marching modulus that lead to the decision to cure the specimens for 12 hours despite the fact that this may leave possibility for additional cure as the behaviour over longer time periods was an unknown.

4.3.3.2 DSC of Monomer 401

A DSC heating and cooling scan on Monomer 401 is shown in Figure 4.11.

Unfortunately the facility to run DSC from sub-ambient temperatures was not available and the machine itself was prone to shifts in baseline and artefacts even after prolonged attempts to get heat flow to stabilise. A typical trace ia shown in Figure 4.11. The melting endotherm visible at *c.a.* 40 °C was not integrated due to the lack of a proceeding baseline caused by the lack of cooling facility and the influence of the immediately preceding exothermic peak which is likely to be due to cold crystallisation. The small irregular peaks and jumps in baseline at *c.a.* 175 °C

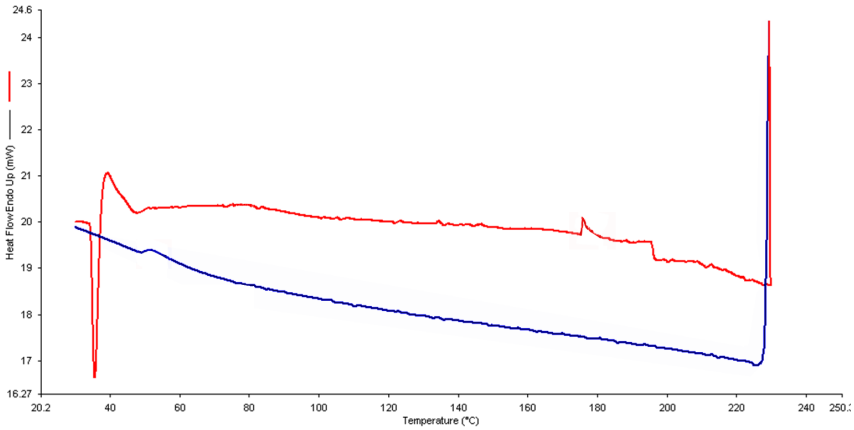

Figure 4.11: Monomer 401 DSC trace. The red line is heating and the blue line is cooling Heating and cooling rate 10 °C min^{-1}..

and 185 °C appear to be artefacts from the machine as they were not present on the other runs.

Upon cooling there were no exothermic crystallisation peaks observed; this suggests that either a reaction has taken place (such as crosslinking) which will inhibit the crystallisation but it could also be due to the lack of low temperature information as the crystallisation may occur at sub-ambient temperatures. The fact that nothing was observed even in the region where the cold crystallisation occurred during heating suggests the former explanation but more useful information was obtained by the DMA testing of this material.

4.3.3.3 Blank Material Pocket Run

In order to demonstrate that the aluminium material pocket has minimal contribution to the transitions observed in this experiment a blank run was performed using an unloaded material pocket. The result of this run is shown in Figure 4.12.

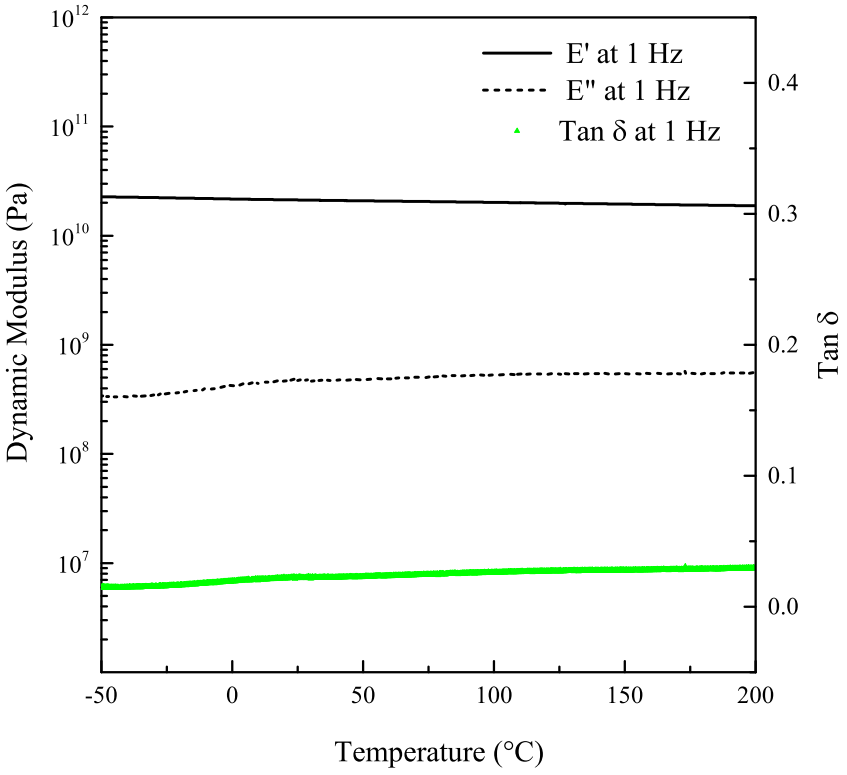

Figure 4.12: DMA plot for an empty material pocket (note the logarithmic left y axis scale).

As would be expected there are no significant transitions observed; consequently it can be concluded that any transitions that are later observed in material pockets are as a direct result of transitions in the material of interest.

4.3.3.4 DMA of Monomer 401 in a Material Pocket (First Run)

Figure 4.13 shows the results from the temperature scan on Monomer 401 in a material pocket.

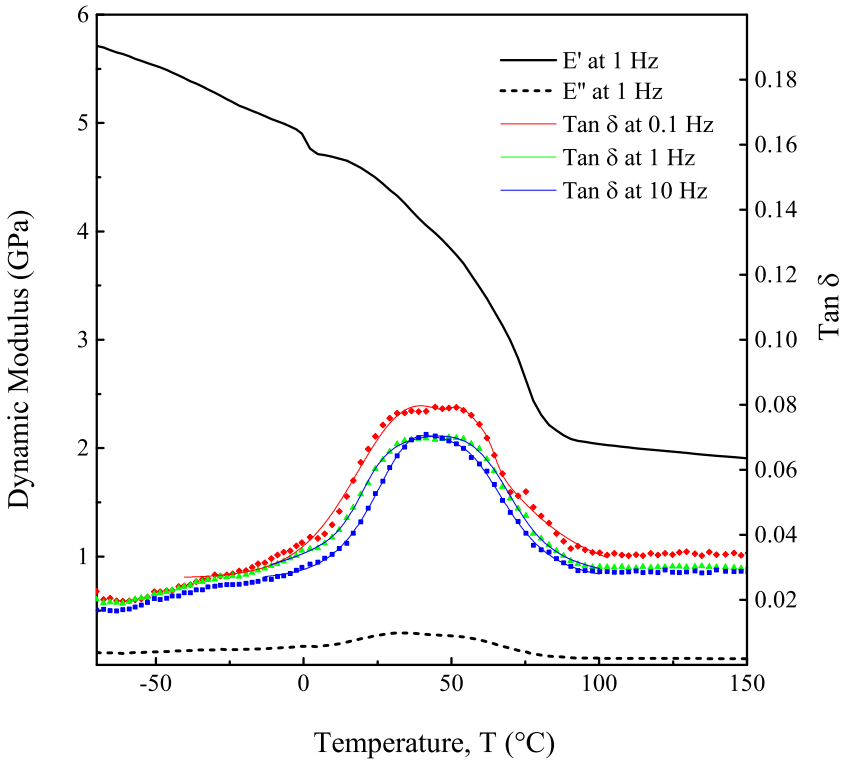

Figure 4.13: DMA plot of Monomer 401 in a material pocket (1% strain).

In order to preserve clarity in the plots only a single frequency has been shown for the storage and loss modulus points due to a large amount of overlap from the points at different frequencies. To show the frequency dependence the loss factor has been plotted at 3 frequencies as it has been possible to do so without rendering the plots illegible.

The storage modulus (E', solid black line in Figure 4.13) starts at about 5.7 GPa at -70 °C. The magnitude of the storage modulus is not a direct measure of a monomer stiffness, rather it is but the combination of the steel material pocket and the monomer. It is for this reason the actual dynamic moduli values on the Y axis should not be taken as an explicit measure of the material (even comparatively between samples) because it is highly sensitive to the amount of monomer within

the actual test area of the material pocket which is not controlled. The relevant information that can be obtained from this specimen type are the temperatures and frequencies at which transitions take place.

There is a small step in the storage modulus at approximately 1 °C after which the slope increases steadily until it reaches a maxima at at around 75 °C (this can be seen more clearly on the derivative curve in Figure 4.14a). The step appeared in all 3 frequencies and its onset was calculated (as illustrated in Figure 4.14a) by determining the intersection of a tangent line (green dotted line) centred at the local slope maxima and a linear baseline (dotted red line). These three onset points are presented in Table 4.3 but do not appear to show any clear frequency dependence. It has not been possible to calculate onset points of the subsequent modulus drop as the step prevents a linear baseline being drawn before the onset point position.

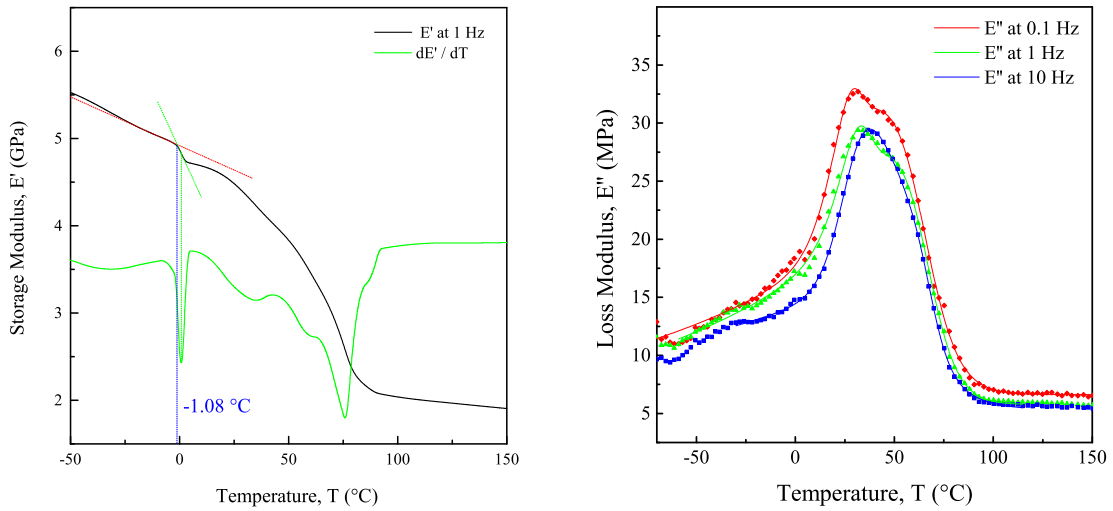

(a) Onset of E' drop at 1 Hz. **(b)** Fitting of E'' curves.

Figure 4.14: Monomer 401 material pocket DMA analysis graphs.

The frequency dependence (or lack of), however, has been illustrated by the loss factor (tan δ) trace which has been presented for 3 frequencies. The loss factor shows wide flat peaks that seem to be fairly frequency independent; a frequency independent transition such as this would normally be attributed to melting. Interestingly, it may be of note that the peak onset of the loss factor transition shows

some frequency dependence; at lower frequency it occurs at lower temperature.

This observation lead to the hypothesis that the observed peak may be a combination of a frequency dependent glass transition at lower temperature and a dominating frequency independent melting transition at higher temperature. In support of this hypothesis there is visual evidence of a double peak that can be seen in the low frequency (0.1 Hz) trace but it is less pronounced at higher frequency (10 Hz). The hypothesis that there is a proportion of amorphous (*i.e.* partially polymerised) material present would also be supported by the cure rheometry previously discussed in Section 4.3.3.1 in which initial viscoelastic behaviour was observed in the melt. An attempt has been made to fit two multiple peaks to the loss factor points (on Figure 4.13) and a reasonable fit has been achieved. There does not, however, appear to be a clear pattern as to the individual peak maxima .

The loss modulus (E'', dotted black line in Figure 4.13) has been plotted for the three separate frequencies in Figure 4.14b and was given a similar dual peak fitting treatment as the loss factor with a similar result. The fit appears convincing but it could easily be an example of how several hundred computational iterations can over-fit data. In addition none of the individual peaks show a clear frequency dependence. Therefore it is likely that the influence of the glass transition, if it is present, is minor.

Table 4.3: Monomer 401, Material Pocket, DMA summary of transitions (1% strain).

Value	f **(Hz)**	**Type**	**Temp. (°C)**
E_0'	0.1	Mixed Onset	0.93227
E_0'	1	Mixed Onset	-1.0753
E_0'	10	Mixed Onset	-0.90519

f: frequency of the applied sinusoidal deformation, E_0': the onset of the drop in storage modulus as calculated in Section 4.3.3.4, E''_{max}: the maximum of the loss modulus peak (fitted curve), $\tan\delta_{max}$: the maximum of the tan delta peak (fitted curve).

4.3.3.5 DMA of Monomer 401 in a Material Pocket (Second Run)

In order to gain insight into the strange DMA results highlighted in the previous selection an experiment was designed in order to remove the influence of the melting transition. A material pocket was loaded with Monomer 401 as before and was heated to 150 °C in the DMA without any significant clamping force before immediately quenching to cryogenic temperatures using liquid nitrogen. The aim was to not allow the sample time to crystallise. The clamping force was reapplied while the sample was below -100 °C and then the DMA experiment was started. The results of this second DMA experiment on Monomer 401 are shown in figures 4.15 and 4.16.

After the thermal treatment and subsequent quench a frequency dependent transition is clearly visible in the area of 15 °C which is almost certainly a glass transition. Both the loss factor peaks (in Figure 4.15) and the loss modulus peaks (in Figure 4.16b) have been fitted with asymmetric double sigmoidal peaks using non-linear regression. The fit was used to more accurately determine the temperatures at maximum loss factor ($\tan\delta_{max}$) and loss modulus (E''_{max}) that are presented in Table 4.4.

The onset of the drop in storage modulus has also been calculated, this is shown for one frequency (1 Hz) in Figure 4.16a and the results for all frequencies are shown in Table 4.4. The step in the storage modulus which is most easily visible as a local maxima in the first derivative graph is most likely due to limited cold crystallisation or partial reorganisation of the polymer side-groups which partially reduces the rate of decrease in stiffness caused by the temperature increase.

There are also peaks present in the loss factor and loss modulus centred around 75 and 85 °C respectively; at this point the storage modulus has already reached the lower plateau indicating that there are no further melting transitions. These peaks can therefore be attributed to changes in the Diels-Alder linkages. These changes are likely to relate to the curing of the monomer which are not mirrored with an increase in storage modulus due to the fact that the rate of cure is slow (of the order of hours) and therefore unable to overcome the reduction in stiffness due to the increase in temperature.

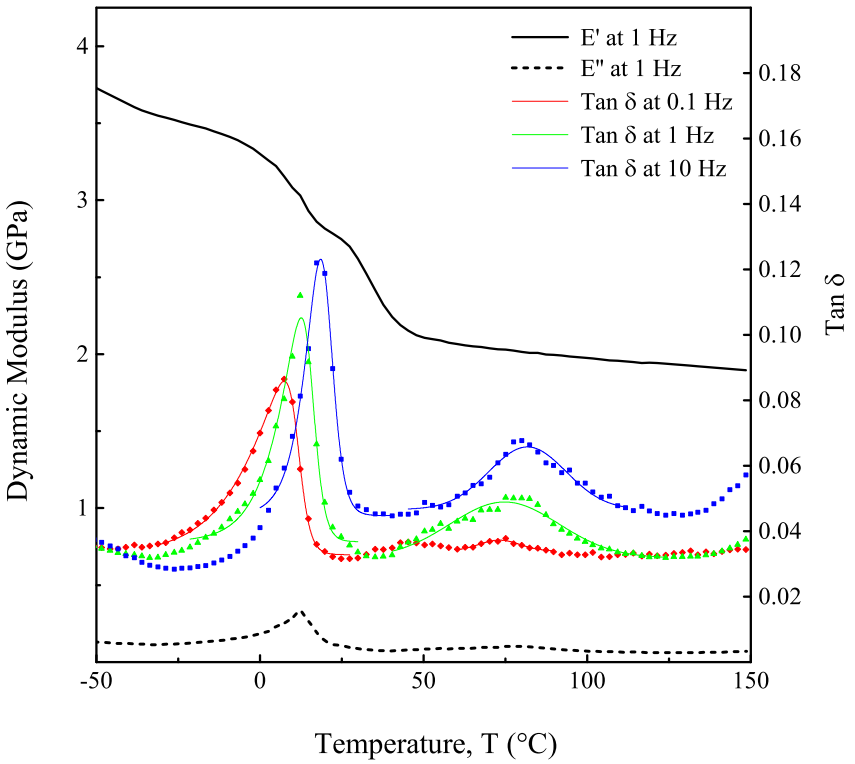

Figure 4.15: DMA plot of Monomer 401 in a material pocket (after melting and quenching), 1% strain.

Table 4.4: Monomer 401 (after melting and quenching), DMA summary of transitions (1% strain).

Value	**Type**	$\overline{R}^2$	**Temp. (°C), f = 0.1 Hz**	**Temp. (°C), f = 1 Hz**	**Temp. (°C), f = 10 Hz**
$E_0^{'}$	T_g Onset	N.A.	-1.242	1.407	5.091
$\tan\delta_{max}$	T_g Peak 1	<0.98	7.37	12.59	18.52
$E_{max}^{''}$	T_g Peak 1	<0.98	7.21	12.50	18.42
$\tan\delta_{max}$	Cure Peak 2	<0.91	73.15	74.75	81.75
$E_{max}^{''}$	Cure Peak 2	<0.84	73.68	78.68	80.58

f: frequency of the applied sinusoidal deformation, $\overline{R}^2$: Coefficient of determination adjusted to prevent additional degrees of freedom artificially inflating the value, $E_0^{'}$: the onset of the drop in storage modulus as calculated in Section 4.3.3.4, $E_{max}^{''}$: the maximum of the loss modulus peak (fitted curve), $\tan\delta_{max}$: the maximum of the tan delta peak (fitted curve), N.A.: Not applicable.

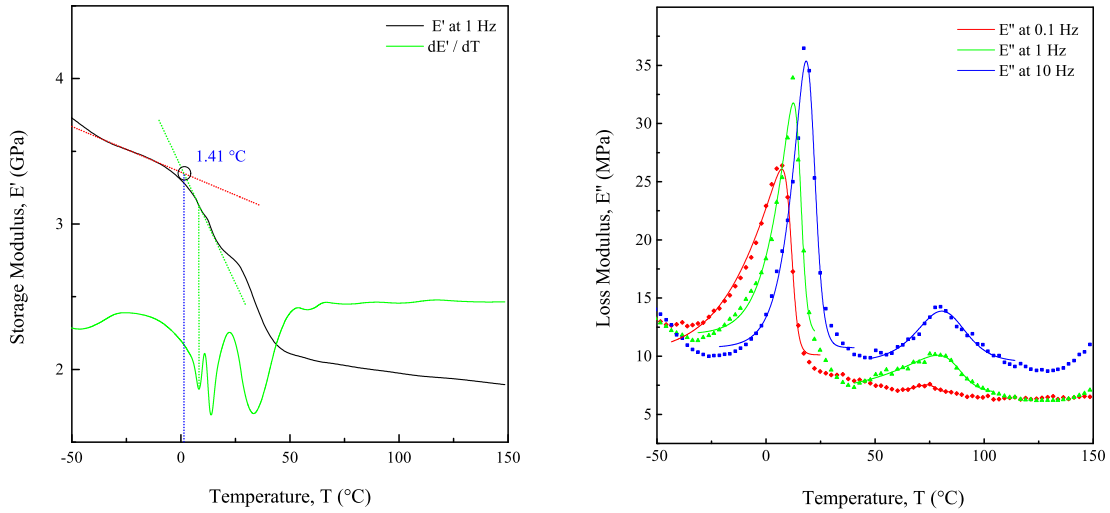

(a) Onset of E' drop at 1 Hz. **(b)** Fitting of E'' curves.

Figure 4.16: Monomer 401 in a material pocket (after melting and quenching) DMA analysis graphs.

This second experiment, therefore, shows that even in early stages of cure there is a glass transition developing between -1 and 19 °C depending on the method of determination. This temperature of this transition would have increased slightly due to the thermal treatment but from these results it is perfectly feasible to conclude that the partial frequency dependence observed in Section 4.3.3.4 is indeed due to the presence of both amorphous and crystalline material with overlapping transitions.

4.3.3.6 DMA of a Polymer 401 Specimen

Polymer 4-0-1 specimens were fabricated using the method outlined in Section 4.2.7.2 on page 172. Two attempts were made at polymer fabrication. The first attempt resulted in significant void content and fractured easily while demoulding. The second specimen was cured under vacuum and therefore much more void-free; it was, however, extremely brittle and the first attempt to mount it in the DMA resulted in a fracture during the application of the clamping force (see Figure 4.17a on the next page). After the break there was enough free length remaining on the second specimen to mount a second time in the DMA using a 5 mm free length single cantilever geometry as shown in Figure 4.17b on the following page. In order to prevent damage the full clamping force was not applied.

Figure 4.18 on page 193 shows the results of the DMA temperature scan on the polymer specimen. For clarity, due to the magnitude of the transitions, the left y-axis (on which the dynamic moduli have been plotted) has been presented as a $\log_{10}$ scale. The loss factor ($\tan \delta$) peak magnitudes are also significantly higher compared to the response from material pocket specimens; this is due to the higher relative quantity of material.

As done in the previous section the loss factor peaks were deconvoluted by fitting asymmetric double sigmoidal curves; the fit can be seen in Figure 4.18 and the peak temperatures and their adjusted fit coefficients are reported in Table 4.5.

The onset of the drop in storage modulus (E') was calculated using the method previously reported. This is shown for a single frequency (1 Hz) in Figure 4.19a but reported for all 3 frequencies in Table 4.5 on the following page. The rise in both dynamic moduli at high temperature was surprising because it implies that there may be a form post-cure happening at these temperatures.

The loss modulus (E'') peaks were again also fitted with asymmetric double sigmoidal curves in and the results of which are also reported in Table 4.5.

From this experiment it is possible to conclude that the glass transition temperature of Polymer 401 from DMA is between 53 and 78 °C depending on which transition is used to measure it (and the applied frequency) although it is possible that this could rise with further cure as there does appear to be further stiffening occurring at around 180 °C.

(a) Broken Polymer 401 pieces

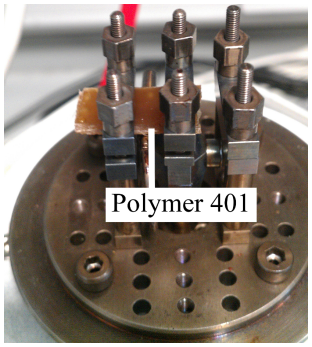

(b) Polymer 401 specimen mounted in the DMA single cantilever geometry (after testing). Note: the fixed clamp shown on the right is not being used.

Figure 4.17: Photos from the DMA testing of the polymer specimens.

Table 4.5: Polymer 401, DMA summary of transitions (0.2% strain).

Value	**Type**	$\overline{R}^2$	**Temp. (°C), f = 0.1 Hz**	**Temp. (°C), f = 1 Hz**	**Temp. (°C), f = 10 Hz**
$E_0^{'}$	T_g Onset	N.A.	53.58	55.09	55.68
$\tan\delta_{max}$	T_g Peak	<0.99	69.15	72.96	78.30
$E_{max}^{''}$	T_g Peak	<0.98	59.92	63.43	69.04

f **:** frequency of the applied sinusoidal deformation, $\overline{R}^2$ **:** Coefficient of determination adjusted to prevent additional degrees of freedom artificially inflating the value, $E_0^{'}$: the onset of the drop in storage modulus as calculated in Section 4.3.3.4, $E_{max}^{''}$: the maximum of the loss modulus peak (fitted curve), $\tan\delta_{max}$: the maximum of the tan delta peak (fitted curve), N.A.: Not applicable.

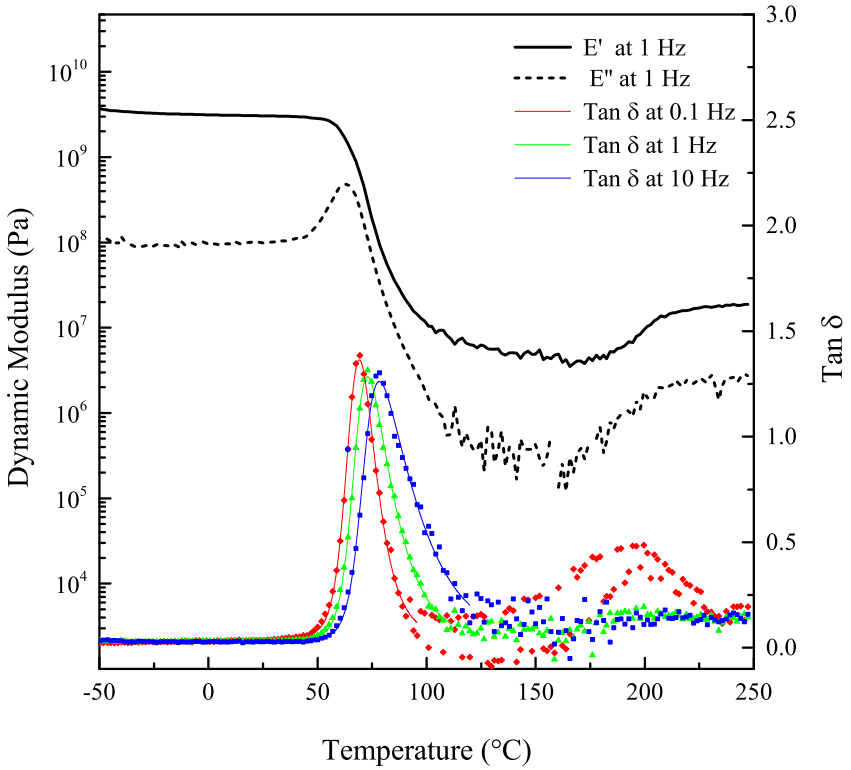

Figure 4.18: Polymer 401 specimen DMA plot (0.2% strain).

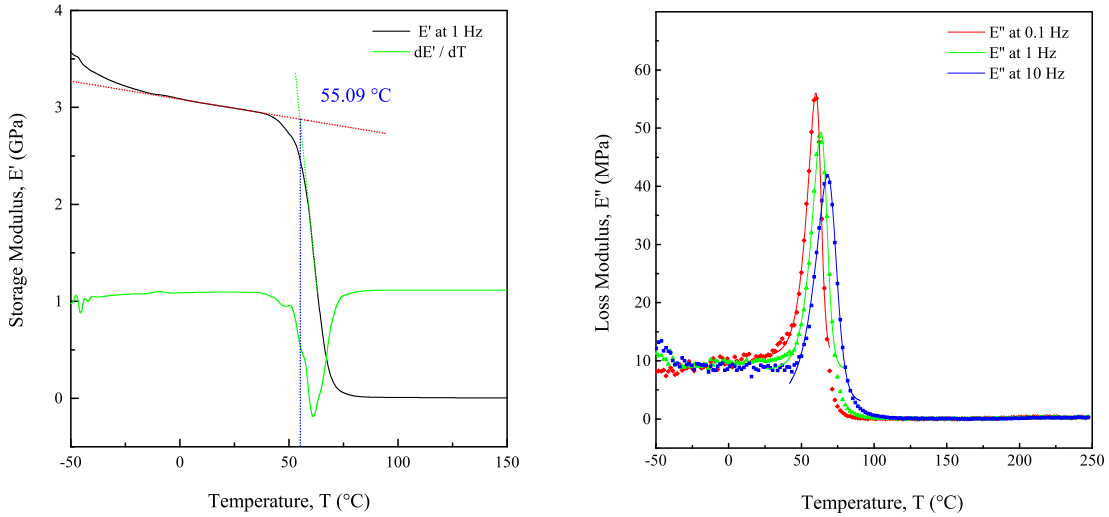

(a) Onset of E' drop at 1 Hz. **(b)** Fitting of E'' curves.

Figure 4.19: Polymer 401 specimen DMA analysis graphs.

4.3.4 Monomer & Polymer 400

Details of the synthesis of Monomer 401 are given in Chapter 3, Section 3.3.2.3 on page 125. This synthesis produced a reasonable amount of product; due to the amount of material the cure rheometry consumes the decision was taken not to run the rheometry experiment. This meant more material was available for the other characterisation techniques.

4.3.4.1 DSC of Monomer 400

The DSC trance of Monomer 400 is shown in Figure 4.20

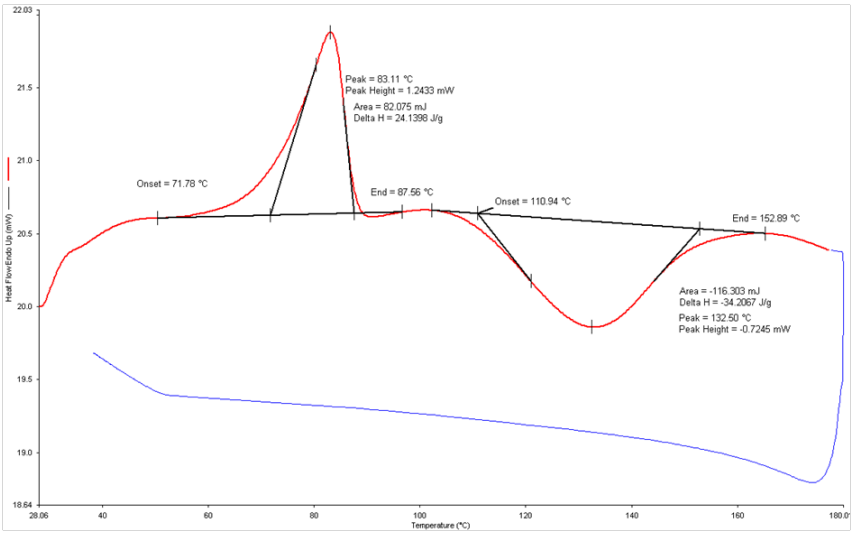

Figure 4.20: Monomer 400 DSC. The response during heating is shown in red and during cooling is shown in blue. Heating and cooling rate 10 °C min^{-1}.

Upon heating, with an onset at *c.a.* 72 °C and a peak temperature at *c.a.* 83 °C an endotherm is clearly visible that can be attributed to the melting of the monomer. At higher temperature, with an onset at *c.a.* 111 °C and a peak temperature at at *c.a.* 133 °C there is an exothermic peak which is due to a chemical reaction (*i.e.* the Diels-Alder crosslinking reaction). Upon cooling the trace is relatively free of transitions which suggests that the material is now not capable of crystallising and is amorphous and presumably at least partially cured which is good. Upon second heating the polymerisation exotherm was not present.

4.3.4.2 DSC of Polymer 400

The DSC of Polymer 400 is shown in Figure 4.21.

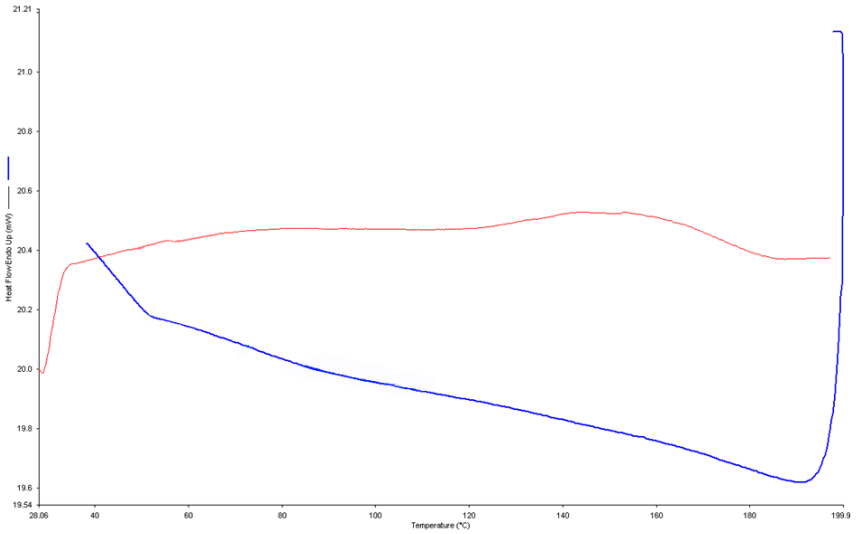

Figure 4.21: Polymer 400 DSC, (cured at 150 °C, see Page 172) the response during heating is shown in red and during cooling is shown in blue Heating and cooling rate 10 °C min^{-1}.

There is surprisingly little by way of transitions, there is a very wide and very slight broad endothermic peak at *c.a.* 150 °C that could be attributed to bond reorganisation (*i.e.* formation or breaking of Diels-Alder bonds*)*.

The results from the DSC are promising as they show clear exothermic transitions after melting endotherms (if present) which show that chemical reactions are taking place.

4.3.4.3 DMA of Monomer 400 in a Material Pocket

The DMA plot of Monomer 400 in a material pocket is shown in Figure 4.22 with further analysis shown in Figure 4.23 and the transitions summarised in tabular form for all 3 frequencies in Table 4.6. For this experiment the range of the temperature scan was extended to -100 to 250 °C.

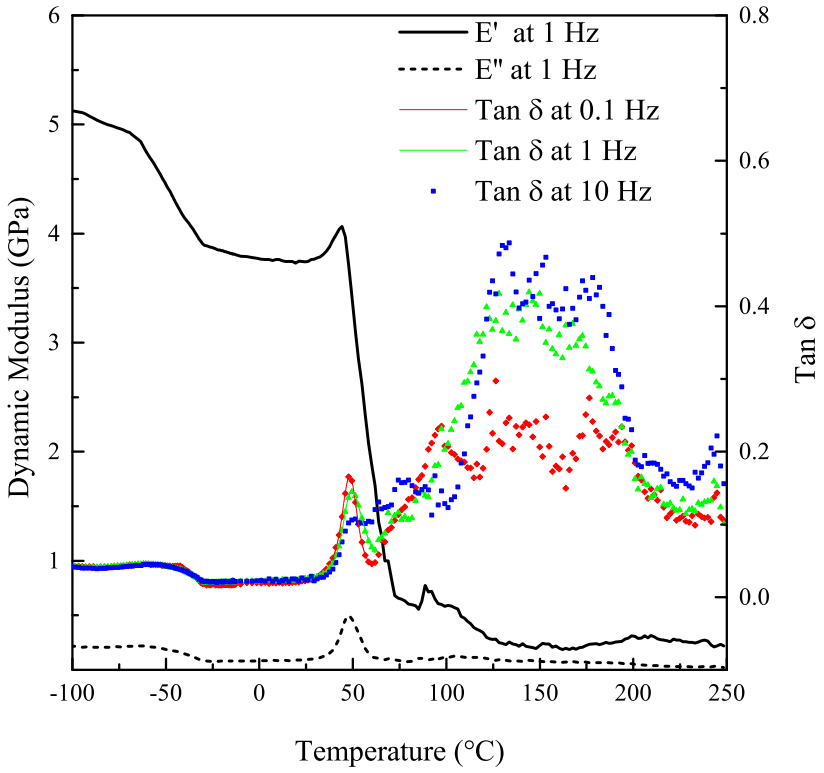

Figure 4.22: DMA plot of monomer 400 in a material pocket (after melting and quenching), 1% strain.

Figure 4.22 has many interesting features. The storage modulus (E') shows a cold transition between -75 and -25 °C that shows little frequency dependence in the loss factor graph. Since there is no clear frequency dependence this could not be considered to be a glass transition but it could be attributed to a pre-melting $T_\alpha*$ transition such as a crystal slip.

There is what appears to be a melting transition at about 48 °C which is relatively frequency independent. The summary of transitions table (Table 4.6) shows that

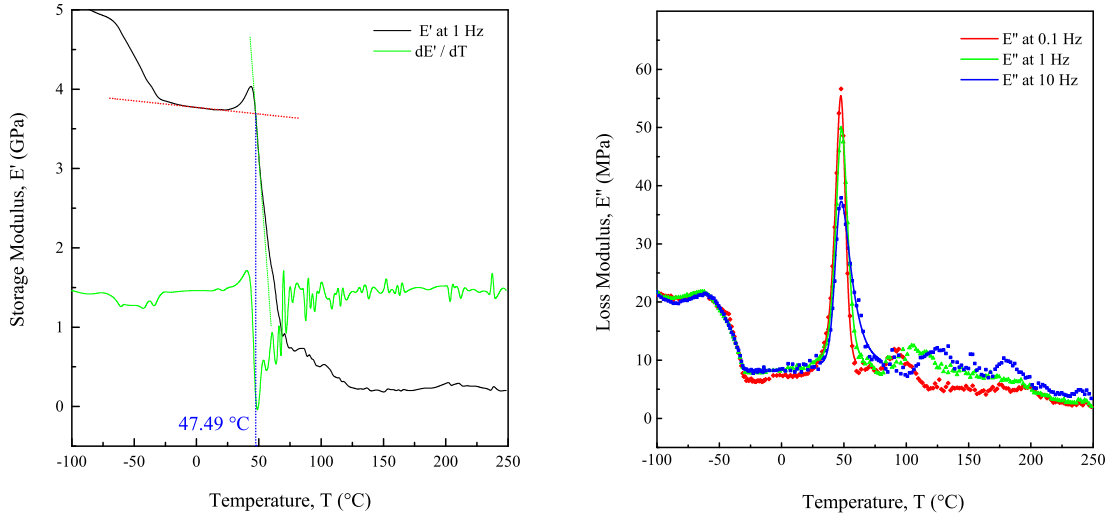

(a) Onset of E' drop at 1 Hz. **(b)** Fitting of E'' curves.

Figure 4.23: Monomer 400 material pocket DMA analysis graphs.

the transitions do not vary by much more than 1 °C across all the frequencies. Immediately preceding the melting point is a slight rise in storage modulus; this is commonly found in DMA and relates to the material having the energy to reorganise and release some locked-in stresses and this causes a short-lived stiffening before a main transition [19]. For onset calculations (*i.e.* Figure 4.23a) this effect does not influence the onset value because a tangent is drawn on the area prior to the rise.

After the melting point the DMA instrument has some difficulty obtaining clear loss modulus and loss factor values; normally a specimen would not be measured past melting but due to the material pocket this is possible in this case. What is clear, however hard they might be to resolve, is that there is certainly peaks in the loss factor that are most likely due to the curing from about 100 °C. There are also two slight increases in storage modulus after melting (at *c.a.* 90 °C and *c.a.* 180 °C) which can be attributed to the curing reaction.

It is worth noting that there is a discrepancy on melting point between this DMA measurement and that seen in the DSC in Section 4.3.4.1 on page 195. Possible explanations for this are that the measurements were taken on the same batch, but several weeks apart (the DSC measurement on the monomer was done later on a

Table 4.6: Monomer 400 (First Material Pocket), DMA summary of transitions (1% strain).

Value	**Type**	$\overline{R}^2$	**Temp. (°C), f = 0.1 Hz**	**Temp. (°C), f = 1 Hz**	**Temp. (°C), f = 10 Hz**
$E_0^{'}$	T_m Onset	N.A.	46.63	47.49	47.97
$\tan\delta_{max}$	T_m Peak	1.00	48.26	49.49	N.R
$E_{max}^{''}$	T_m Peak	<0.99	47.48	48.22	47.78

f: frequency of the applied sinusoidal deformation, $\overline{R}^2$: Coefficient of determination adjusted to prevent additional degrees of freedom artificially inflating the value, $E_0^{'}$: the onset of the drop in storage modulus as calculated in Section 4.3.3.4, $E_{max}^{''}$: the maximum of the loss modulus peak (fitted curve), $\tan\delta_{max}$: the maximum of the tan delta peak (fitted curve), N.A.: Not applicable, N.R: No result (due to poor baseline, insufficient resolution or high scatter).

small monomer sample that was retained). It could be possible that the monomer started to polymerise in storage; this would be expected, however, to instead show a glass transition which would be a second order DSC transition.

Another fundamental difference between the DSC and DMA experiments that can affect transition temperatures was the heating rate. The DSC used a heating rate of 10 °C min^{-1}as this was the calibration that was available. The DMA used a significantly slower heating rate of 2 °C min^{-1}in order to maximise the number of data points. This could be expected to contribute to the discrepancy but not to the extent that has been observed in this case.

Another possible explanation is that there is a mixture of crystalline and partially polymerised amorphous material present in the sample as was also suggested for Monomer 401 (see 4.3.3.4 on page 185). It may be that the start of the transition is actually a glass transition that is distorted by a broad melting transition with some overlap.

4.3.4.4 DMA of Polymer 400 in a Material Pocket (2 Further Runs)

The material pocket that was used in the previous Section (4.3.4.3) was retested 2 more times to get an indication of whether cure can be completed by shorter, higher temperature, treatment. It was noted immediately that material was now polymeric. These two DMA results are shown in Figure 4.24, with further analysis in figures 4.25 and 4.26. The transitions are summarised in Tables 4.7 and 4.8.

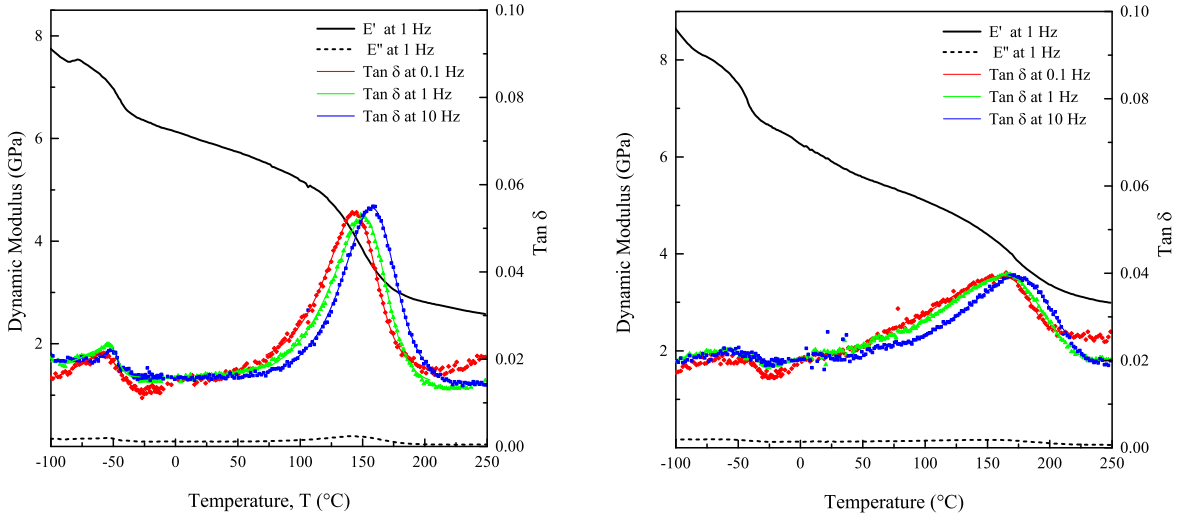

(a) 2nd Run (1% strain) **(b)** 3rd Run (1% strain)

Figure 4.24: DMA plot of polymer 400 in a material pocket (2nd and 3rd runs).

The storage modulus (E') trace in Figure 4.25 shows a low temperature beta (T_β) transition at *c.a.* -48 °C in both runs in addition to the glass transition which occurs at higher temperature. It is unlikely that the lower transition is another glass transition (as exhibited by polyurethanes with hard and soft segments) because the 'tether' link between the stiff norbornene-like segments is only four carbon atoms long.

Due to the lack of a linear baseline immediately prior to the transition it has only been possible to calculate this T_β onset temperature for the second run at 1 Hz (Figure 4.25a), the storage moduli at the other frequencies do not exhibit the necessary linear region above the transition needed to calculate the onset. The onset has been measured for the 3rd run as the upper baseline is clearer; the transition

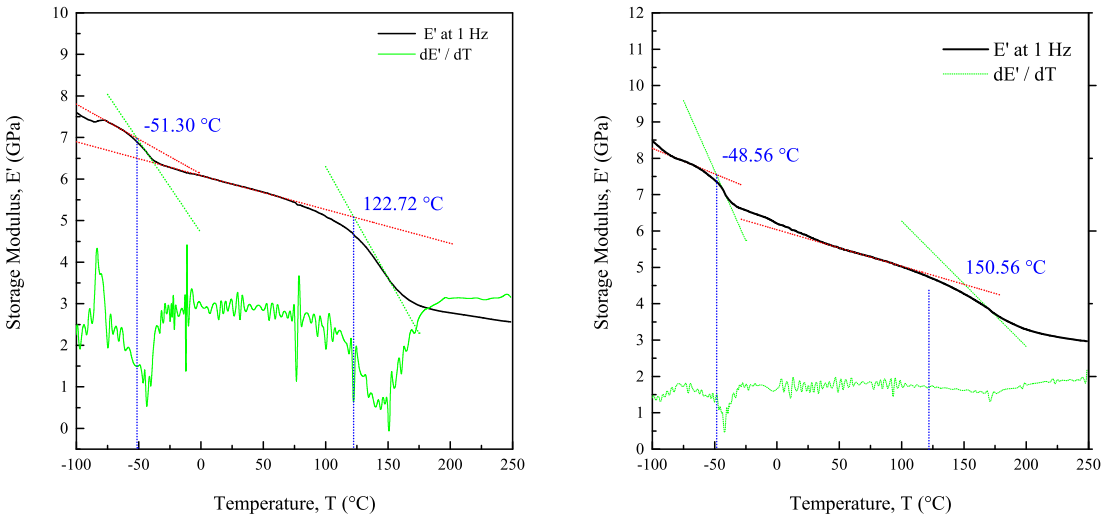

(a) 2nd Run **(b)** 3rd Run.

Figure 4.25: Polymer 400 Run 2 and 3, Onset of $E^{'}$ drop at 1 Hz.

shows frequency dependence. In run 2 it was possible to fit curves and therefore find the peak temperatures of the T_β in thetan δ and $E^{''}$curves but this was not possible in the 3rd run due to the signal to noise ratio.

The onset of the frequency dependent glass transition temperature rises from 119-128 °C in the second run up to 148-156 °C in the third run which shows that considerable crosslinking took place during the second scan.

This upward trend is mirrored in the loss factor and loss modulus peak values as can be seen in the differences between the temperatures reported in Table 4.7 and Table 4.8.

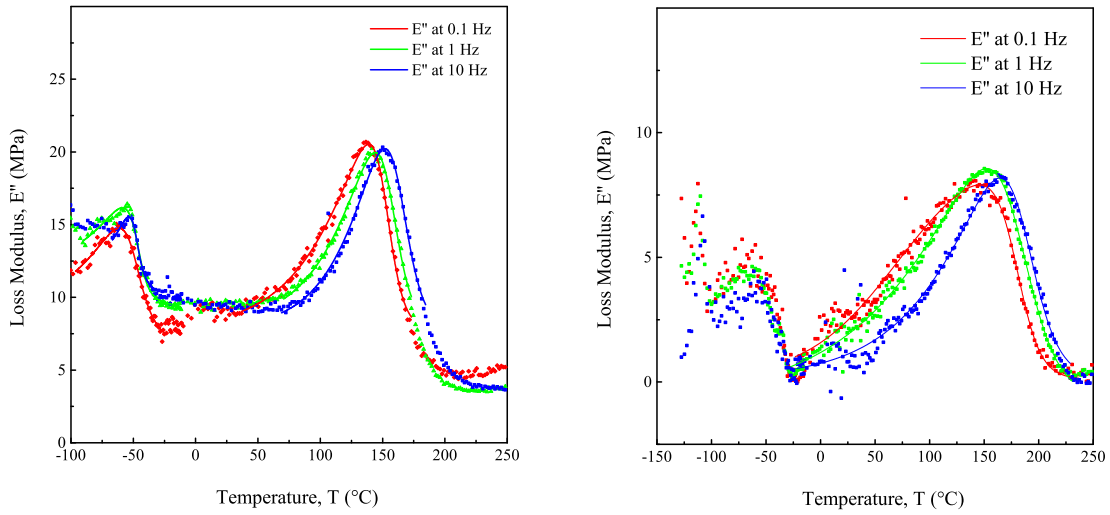

(a) 2nd Run **(b)** 3rd Run.

Figure 4.26: Polymer 400, Run 2 and 3, Fitting of E'' curves

Table 4.7: Monomer/Polymer 400 (material pocket run 2), DMA summary of transitions (1% strain).

Value	**Type**	$\overline{R}^2$	**Temp. (°C), f = 0.1 Hz**	**Temp. (°C), f = 1 Hz**	**Temp. (°C), f = 10 Hz**
$\tan\delta_{\max}$	T_β peak	<0.94	-59.17	-54.89	-50.81
$E''_{\max}$	T_β peak	<0.96	-64.44	-58.79	-53.60
E'_0	T_β onset	N.A.	N.R.	-51.30	N.R.
E'_0	T_g onset	N.A	118.73	122.72	127.81
$\tan\delta_{\max}$	T_g Peak	<0.99	143.78	150.66	157.52
$E''_{\max}$	T_g Peak	<0.98	138.80	144.43	151.78

f: frequency of the applied sinusoidal deformation, $\overline{R}^2$: Coefficient of determination adjusted to prevent additional degrees of freedom artificially inflating the value, E'_0: the onset of the drop in storage modulus as calculated in Section 4.3.3.4, $E''_{\max}$: the maximum of the loss modulus peak (fitted curve), $\tan\delta_{\max}$: the maximum of the tan delta peak (fitted curve), N.A.: Not applicable, N.R: No result (due to poor baseline, insufficient resolution or high scatter).

Table 4.8: Monomer/Polymer 400 (material pocket Run 3), DMA summary of transitions (1% strain).

Value	**Type**	$\overline{R}^2$	**Temp. (°C), f = 0.1 Hz**	**Temp. (°C), f = 1 Hz**	**Temp. (°C), f = 10 Hz**
$\tan\delta_{\max}$	T_β peak	N.R.	N.R.	N.R.	N.R.
$E''_{\max}$	T_β peak	N.R.	N.R.	N.R.	N.R.
E'_0	T_β onset	N.A.	-49.04	-48.56	-47.75
E'_0	T_g onset	N.A.	147.80	150.58	155.65
$\tan\delta_{\max}$	T_g Peak	<0.98	160.72	163.59	173.11
$E''_{\max}$	T_g Peak	<0.96	145.38	152.39	164.71

f: frequency of the applied sinusoidal deformation, $\overline{R}^2$: Coefficient of determination adjusted to prevent additional degrees of freedom artificially inflating the value, E'_0: the onset of the drop in storage modulus as calculated in Section 4.3.3.4, $E''_{\max}$: the maximum of the loss modulus peak (fitted curve), $\tan\delta_{\max}$: the maximum of the tan delta peak (fitted curve), N.A.: Not applicable, N.R: No result (due to poor baseline, insufficient resolution or high scatter).

4.3.4.5 DMA of a Polymer 400 Specimen

Polymer 400 specimens were fabricated using the method outlined in Section 4.2.7.2 on page 172. The resultant polymer specimens were noticeably less brittle and could be loaded into the DMA with normal clamping force applied via the small torque socket (see Figure 4.27).

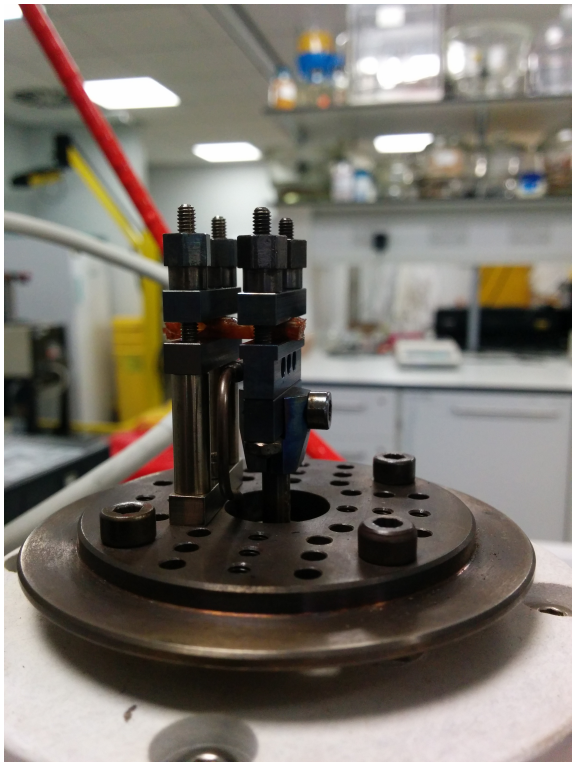

Figure 4.27: Polymer 400 specimen loaded in the DMA single cantilever mode.

The DMA plot of the Polymer 400 specimen is presented in Figure 4.28 with further analysis shown in Figure 4.29 and the transitions summarised in tabular form for all 3 frequencies in Table 4.9.

A clear frequency dependent glass transition can be seen on all of the plots between 93 and 140 °C dependent on which frequency and feature is used to calculate it; these values are summarised in Table 4.9. The fact that these transitions occur at lower temperature compared to the 3rd material pocket run is surprising considering this specimen was given a 12 hour cure schedule at 150 °C. The material pocket specimen had encountered much higher temperatures in the DMA scan

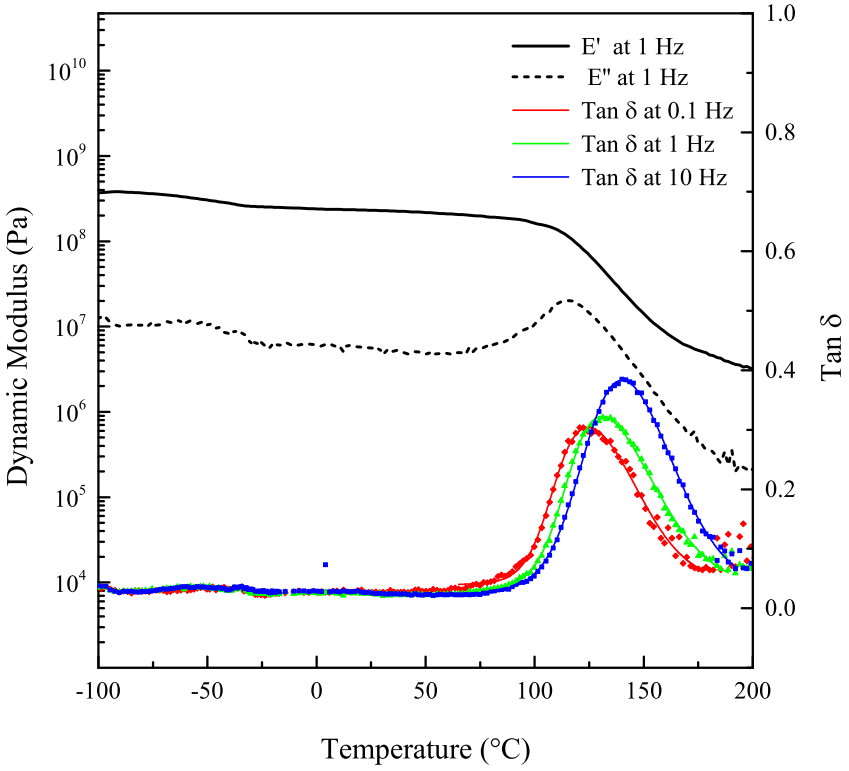

Figure 4.28: DMA plot of Polymer 400 specimen (0.2% strain).

compared to the actual cured specimen so the lower glass transition temperature can be explained by the hypothesis that the full cure of the polymer specimen was hindered by vitrification.

It is not obvious in 4.28 due to the logarithmic y-axis but there is the same beta transition present that was seen in the material pocket tests. This beta transition can be in the onset calculation plot (Figure 4.29a) as a drop in E' prior to the glass transition calculation that is marked but the lack of a linear section before the transition meant that the onset could not be calculated.

In order to better investigate the frequency dependence of the glass transition peak and to calculate the activation energy the Polymer 400 specimen was subjected to a temperature scan with a greater number of frequencies. In order to generate enough data points for this experiment it was required to slow the heating rate down to 0.2 °C. This is because a data point is generated for a minimum of one whole

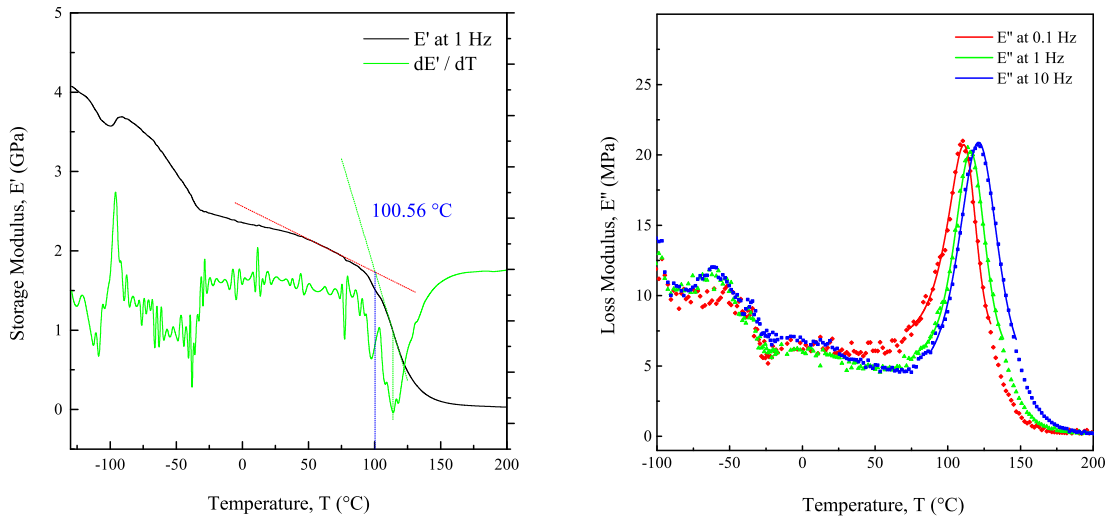

(a) Onset of E' drop at 1 Hz. **(b)** Fitting of E'' curves.

Figure 4.29: Polymer 400 specimen DMA analysis graphs.

frequency cycle; so at 0.05 Hz a full cycle corresponds to $1/0.05 = 20$ s between data points which would lead to poor resolution with 8 frequencies at the normal heating rate used ($2\ ^{\circ}\mathrm{C\,min^{-1}}$.

Table 4.9: Polymer 400, DMA summary of transitions (0.2% strain).

Value	**Type**	$\overline{R}^2$	**Temp. (°C), f = 0.1 Hz**	**Temp. (°C), f = 1 Hz**	**Temp. (°C), f = 10 Hz**
$E_0^{'}$	T_g Onset	N/A	93.82	100.56	103.08
$\tan\delta_{max}$	T_g Peak	<0.99	124.46	130.99	140.20
$E_{max}^{''}$	T_g Peak	<0.99	110.98	115.56	121.15

f : frequency of the applied sinusoidal deformation, $\overline{R}^2$:- Coefficient of determination adjusted to prevent additional degrees of freedom artificially inflating the value, $E_0^{'}$: the onset of the drop in storage modulus as calculated in Section 4.3.3.4, $E_{max}^{''}$: the maximum of the loss modulus peak (fitted curve), $\tan\delta_{max}$: the maximum of the tan delta peak (fitted curve), N.A.: Not applicable.

The DMA plot containing 8 different frequencies is presented in Figure 4.30.

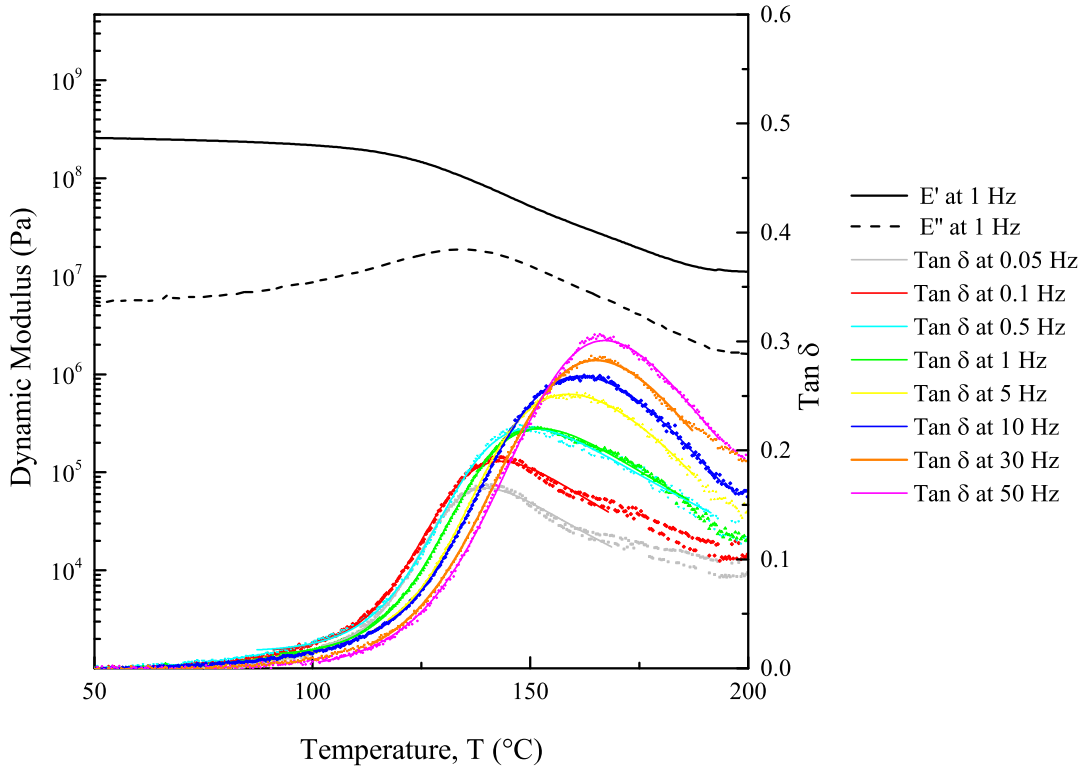

Figure 4.30: Polymer 400 specimen DMA plot, 8 frequency (0.2% strain).

The loss factor peaks are summarised in Table 4.10. These peak temperatures can be used to calculate the activation energy of the transition as discussed in Section 4.1.2.

A plot of the natural log of the oscillation frequency against the reciprocal temperature is shown in Figure 4.31 on page 210. Using linear regression a line has been fitted through the points yielding an excellent adjusted co-efficient of determination $\overline{R}^2$. According to equation 4.9 (which was first presented on page 164) the slope of the line, (-46593.77 K^{-1}) is equal to $^{-E_a}/_R$.

$$\ln(f) = \ln(A) - \frac{E_a}{RT} \tag{4.9}$$

Therefore the activation energy is :

Table 4.10: Polymer 400, DMA Summary of the $\tan\delta_{\max}$ transitions for 8 frequencies (0.2% strain).

Value	f **(Hz)**	**Type**	$\overline{R}^2$	**Temp. (°C)**
$\tan\delta_{\max}$	0.05	T_g Peak	1.00	139.84
$\tan\delta_{\max}$	0.1	T_g Peak	1.00	143.25
$\tan\delta_{\max}$	0.5	T_g Peak	1.00	150.05
$\tan\delta_{\max}$	1	T_g Peak	1.00	152.29
$\tan\delta_{\max}$	5	T_g Peak	1.00	158.75
$\tan\delta_{\max}$	10	T_g Peak	1.00	161.47
$\tan\delta_{\max}$	30	T_g Peak	1.00	165.09
$\tan\delta_{\max}$	50	T_g Peak	1.00	166.98

f **:** frequency of the applied sinusoidal deformation, $\overline{R}^2$ **:** Coefficient of determination adjusted to prevent additional degrees of freedom artificially inflating the value, $E_0^{'}$: the onset of the drop in storage modulus as calculated in Section 4.3.3.4, $E_{\max}^{''}$: the maximum of the loss modulus peak (fitted curve), $\tan\delta_{\max}$: the maximum of the tan delta peak (fitted curve).

$-46593.77 \times 8.3144621 = 387402\ \mathrm{J\,mol^{-1}} = 387\ \mathrm{kJ\,mol^{-1}}$

As expected, this activation energy is consistent with a glass transition [23, 25, 37–40].

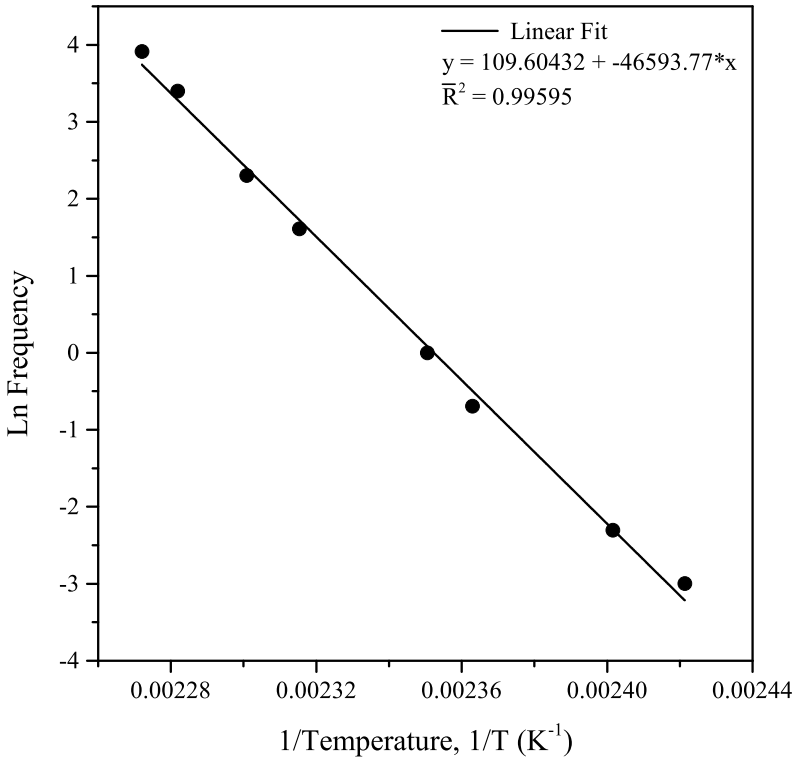

Figure 4.31: Polymer 400 specimen Arrhenius plot

4.3.5 Monomer & Polymer Mixture from Poly(Tetrahydrofuran)

The monomer mixture based upon the reaction of Thiele's acid chloride and Poly(THF) has been reported previously in the previous Chapter in Section 3.3.2.5 on page 128. It was discovered that this reaction produces a mixture of monomers 400, 801 and 12-0-2 and it was anticipated that these would be able to cure concurrently as they contain the same Diels-Alder groups.

4.3.5.1 DSC of the Monomer Mixture from PolyTHF

A sample of the monomer mixture (400, 801 & 12-0-2) was analysed using DSC; the trace is shown in Figure 4.32.

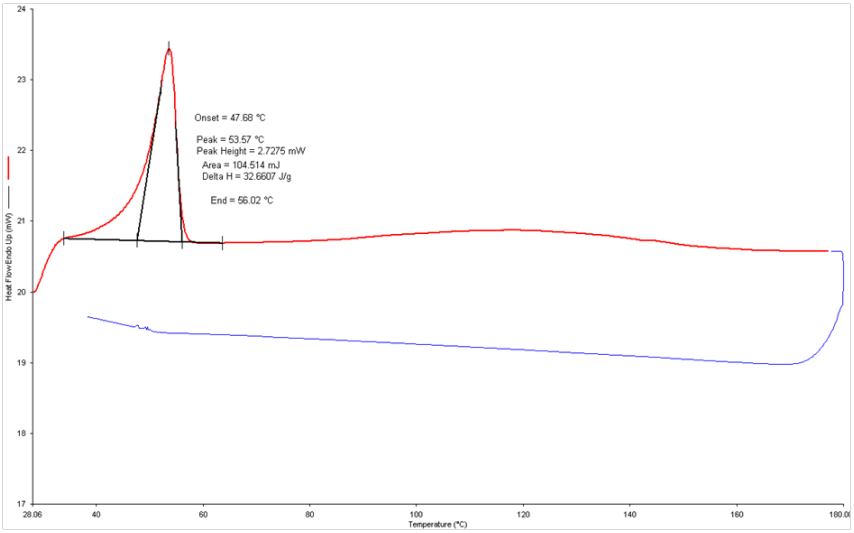

Figure 4.32: DSC of the monomer mixture based on poly(THF), heating and cooling rate 10 °C min^{-1}.

The sample shows a clear single melting endotherm with a peak temperature of 53.57 °C but there is no obvious polymerisation exotherm present. There is possibly a very slight and extremely broad peak from about 80 °C which is minor. There does, however, not appear to be any recystallisation on cooling which suggests that a transformation has occurred. As a qualitative test of curing some of the material was put onto a piece of PTFE and heated up to 150 °C for 12 hours. After cooling the sample did not appear to have cross-linked as it appeared to be a viscous liquid. It would appear that this mixture is not capable of curing under these conditions

but a material pocket would be used first to see if any transitions are visible on the DMA.

4.3.5.2 DMA of the Monomer Mixture from Poly(THF) in a Material Pocket

The DMA trace of the monomer mixture (400, 801 & 12-0-2) from poly(THF) is shown in Figure 4.33

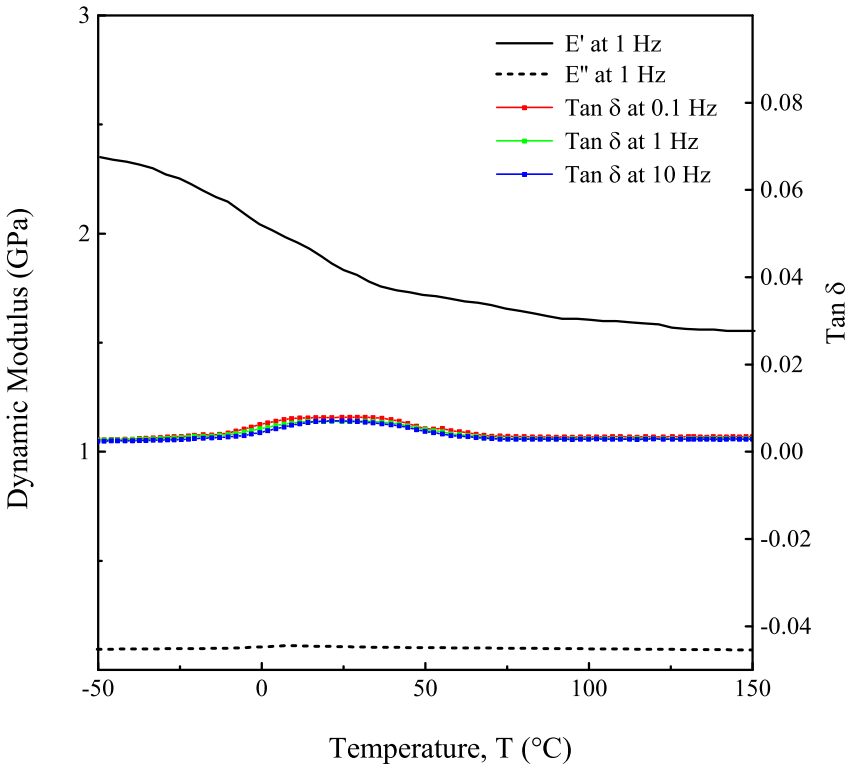

Figure 4.33: DMA plot of the monomer mixture from poly(THF) in a material pocket (1% strain).

The DMA of the monomer mixture appeared to show the same melting behaviour that was observed in the DSC but it is very weak with barely any loss factor response. No further transitions were visible but when the specimen was removed it appeared to have ejected from around the edges of the material pocket which would explain why nothing else is measured after the melting point. Again, however, there was no

sign of any cure behaviour; so the decision was made to stop producing and testing the monomer mixture and focus on applications of Monomer 400 and Monomer 401 in the next chapter.

One possible reason for the lack of cure is that the monomer mixture is very crude and there are almost certainly higher oligomers and impurities present. It is possible to separate the monomers from the mixture using flash column chromatography but if this was to be done there would be no advantage to using the poly(THF) starting material. The different length tether units could also potentially prevent any potential closely cross-linked network from forming by disrupting the morphology.

4.4 Summary and Conclusions

It was the main aim of this chapter to develop an inkjet printing method for the monomers that are synthesised as described in Chapter 3. Inkjet printing is an extremely well suited method for the application of small amounts of additive to prepreg interlayers and is thus perfect for this application given the relatively small quantities of monomer produced. The formulation of the inks has been successful and Ethyl Acetate has been found to be a suitable solvent for concentrations of up to 5% w/v of monomer monomers. The inks have been inkjet printed onto both glass and carbon-epoxy prepreg substrates with an excellent level of precision.

The monomer print pattern has been shown, on a glass substrate, after curing, to be robust and capable of withstanding sustained temperatures of 180 °C such as the temperatures that would be encountered when curing the prepreg substrate with the printed patterns. The monomers printed onto the prepreg substrate can be just about seen with the naked eye and have been printed in exactly the right position for fabricating samples for testing with double cantilever beam and short beam shear in the next chapter.

Another aim of this chapter was to characterise the resultant polymers. Material shortages limited some of the analysis that could be done on the synthesised materials, however, a lot was still achieved. DSC analysis of the monomers show peaks that are promising for self-healing.

Monomer 401 has been shown to cure quite slowly at 120 °C and most likely has some latent cure after 12 hours. The resultant polymer was brittle and showed a fairly low glass transition, T_{g0}= 55.09 °C, at $\tan\delta_{max}$= 72.96 °C and a E''_{max}= 63.43 °C all at 1 Hz. This polymer was also calculated to be more compatible with the epoxy matrix than Polymer 400 and so has potential to be a good healing agent for small interlaminar defects at relatively low temperatures.

Polymer 400 was significantly stronger and tougher compared to Polymer 401. The cure rheology of Monomer 400 was not required however it was shown to be possible to achieve a high glass transition temperature after a shorter treatment at a much higher temperature (*i.e.* the DMA increasing the temperature to 250 °C) at a rate of 2 °C min^{-1}).

There was a discrepancy in melting temperature between that measured by DSC and that measured by DMA. A difference in heating rate can partially explain this but it is most likely that there is a proportion of amorphous oligomers present in the sample that cause perceived lower melting point on the DMA that is actually a glass transition overlaid with a melting transition.

The glass transition of Polymer 400 (after cure at 150 °C for 12 hours) was found to be much higher than Polymer 401 with T_{g0}= 100.53 °C, $\tan\delta_{max}$= 130.99 °C and a E''_{max}= 115.56 °C all at 1 Hz. The activation energy of the glass transition was calculated using Arrhenius relationships to be 387 kJ mol^{-1}.

The glass transition temperatures after repeated DMA cycles up to 250 °C were T_{g0}= 150.58 °C, $\tan\delta_{max}$= 163.59 °C and E''_{max}= 152.39 °C all at 1 Hz. The implication of this is that vitrification caused the cure to halt when the glass transition temperature rose above the curing temperature. Therefore the 180 °C cure temperature that the printed interlayers will experience during the epoxy prepreg cure should also be sufficient to cure the pattern however healing temperatures may need to be quite high in order to soften this polymer for self-healing of the prepreg.

Given the small amount of material produced inkjet printing is a useful approach for the application of these monomers within composite materials.

The following chapter is concerned with the production of carbon-fibre epoxy specimens with the monomers printed as interlaminar additives. The printed specimens are benchmarked against unprinted controls and testing is done to discover whether self-healing behaviour can be observed.

4.5 References

(1) A. Nollet and M. Watson, "Extract of a Letter from the Abbe Nollet, F.R.S. &c. to Charles Duke of Richmond, F. R. S. Accompanying an Examination of Certain Phaenomena in Electricity, Published in Italy, by the Same, and Translated from the French by Mr. Watson, F. R. S.", *Philos. Trans. R. Soc. London*, 1749, **46**, 368–397.
(Cit. on p. 157.).

(2) G.-L. de Buffon, *Mémoires de l'académie Royale des Sciences, Reflexions sur la loi d'attraction*, Compagnie des Libraires, Paris, 1745, pp. 119–133.
(Cit. on p. 157.).

(3) Q. Dumont and R. B. Cole, "Jean-Antoine Nollet: The father of experimental electrospray", *Mass Spectrom. Rev.*, 2013, 1098–2787.
(Cit. on p. 157.).

(4) F. Savart, "Mémoires sur la constitution des veines liquides. lancées par des orifices circulaires en mince paroi", *Ann. Chim.*, 1833, **53-54**, 337.
(Cit. on p. 158.).

(5) J. Plateau, *Acad. Sci. Bruxelles Mém.*, 1849, **XXIII**.
(Cit. on p. 158.).

(6) J. Eggers, *Nonsmooth Mechanics and Analysis: Theoretical and Numerical Advances*, *A Brief History of Drop Formation*, ed. P. Alart, O. Maisonneuve, and R. Rockafellar, Springer, 2006.
(Cit. on p. 158.).

(7) L. Rayleigh, *Proc. London Math. Soc.*, 1879, **10**.
(Cit. on p. 158.).

(8) R. Elmqvist, Sweden Patent 2566443, 1951.
(Cit. on p. 158.).

(9) R. G. Sweet, "High Frequency Recording with Electrostatically Deflected Ink Jets", *Rev. Sci. Instrum.*, 1965, **36**, 131–136.
(Cit. on p. 158.).

(10) H. Kobayashi, N. Koumura, and S. Ohno, US Patent 4243994 A, 1981.
(Cit. on p. 158.).

(11) F. L. Cloutier, D. K. Donald, J. D. Meyer, C. A. Tacklind, H. H. Taub, and J. L. Vaught, US Patent 4490728 A, 1984.
(Cit. on p. 158.).

(12) J. Brunahl and A. M. Grishin, "Piezoelectric shear mode drop-on-demand inkjet actuator", *Sens. Actuators, A*, 2002, 371–382.
(Cit. on p. 159.).

(13) J. T. Delaney Jr., PhD Thesis, Eindhoven University of Technology, 2010.
(Cit. on p. 160.).

(14) D. Jang, D. Kim, and J. Moon, "Influence of Fluid Physical Properties on Ink-Jet Printability", *Langmuir*, 2009, **25**, 2629–2635.
(Cit. on p. 160.).

(15) J. E. Fromm, "Numerical-calculation of the fluid-dynamics of drop- on-demand jets", *IBM J. Res. Dev*, 1984, **28**, 322–333.
(Cit. on p. 160.).

(16) N. Reis and B. Derby, "Ink Jet Deposition of Ceramic Suspensions: Modeling and Experiments of Droplet Formation", *MRS Proceedings*, Jan. 2000, **625**.
(Cit. on p. 160.).

(17) D. B. van Dam and C. L. Clerc, "Experimental study of the impact of an ink-jet printed droplet on a solid substrate", *Phys. Fluids.*, 2004, **16**, 3403.
(Cit. on p. 161.).

(18) J. Perelaer, P. J. Smith, E. van den Bosch, S. S. van Grootel, P. H. Ketelaars, and U. S. Schubert, "The Spreading of Inkjet-Printed Droplets with Varying Polymer Molar Mass on a Dry Solid Substrate", *Macromol. Chem. Phys.*, 2009, **210**, 495–502.
(Cit. on p. 161.).

(19) K. Menard, *Dynamic Mechanical Analysis: A Practical Introduction, Second Edition*, Taylor & Francis, Boca Raton, FL, USA, 2008.
(Cit. on pp. 162, 198.).

(20) G. W. Ehrenstein, G. Riedel, and P. Trawiel, Dynamic Mechanical Analysis (DMA), in *Thermal Analysis of Plastics*, Carl Hanser Verlag GmbH & Co. KG, München, DE, 2004, pp. 236–299.
(Cit. on pp. 163, 165.).

(21) Perkin Elmer, *Dynamic Mechanical Analysis Basics: Part 2 Thermoplastic Transitions and Properties*, Published Online (Accessed 15th December 2013), 2007, `http://www.perkinelmer.co.uk/CMSResources/Images/44-74305app_thermaldynmechanalybasicspart2.pdf`.
(Cit. on p. 164.).

(22) J. Menczel and R. Prime, *Thermal Analysis of Polymers, Fundamentals and Applications*, Wiley, Hoboken, NJ, USA, 2009.
(Cit. on p. 164.).

(23) Perkin Elmer, *Alpha and Beta Relaxations of PMMA and Calculation of the Activation Energy*, Published Online (Accessed 15th December 2013), 2007, `http://www.perkinelmer.co.uk/CMSResources/Images/44-74239APP_PMMAAlphaBetaRelaxations.pdf`.
(Cit. on pp. 164, 209.).

(24) G. Li, P. Lee-Sullivan, and R. Thring, "Determination of Activation Energy for Glass Transition of an Epoxy Adhesive Using Dynamic Mechanical Analysis", English, *J. Therm. Anal. Calorim.*, 2000, **60**, 377–390.
(Cit. on p. 164.).

(25) R. Seyler, *Assignment of the Glass Transition*, ASTM, 1994.
(Cit. on pp. 165, 209.).

(26) International Organization for Standardization, Plastics - Differential scanning calorimetry (DSC) - Part 1: General principles, in *ISO 11357-1*, 2009.
(Cit. on p. 165.).

(27) International Organization for Standardization, Plastics - Determination of dynamic mechanical properties, Part 11: Glass transition temperature, in *BS ISO 6721-11*, 2012.
(Cit. on p. 165.).

(28) ASTM International, Standard Practice for Plastics: Dynamic Mechanical Properties: Determination and Report of Procedures, in *ASTM D4065*, 2012.
(Cit. on p. 165.).

(29) Y. Zhang, J. Stringer, R. Grainger, P. J. Smith, and A. Hodzic, "Improvements in carbon fibre reinforced composites by inkjet printing of thermoplastic polymer patterns", *Phys. Status. Solidi RRL*, 2014, 56–60.
(Cit. on pp. 169, 178.).

(30) D. Stoye, Solvents, in *Ullmann's Encyclopedia of Industrial Chemistry, Electronic Release*, Wiley-VCH, Weinheim, DE, 2012.
(Cit. on pp. 174–176.).

(31) T. Daubert and R. Danner, *Physical and Thermodynamic Properties of Pure Chemicals Data Compilation.* Taylor and Francis, Washington D.C. USA, 1989.
(Cit. on p. 174.).

(32) Y. Zhang, J. Stringer, R. Grainger, P. J. Smith, and A. Hodzic, "Fabrication of patterned thermoplastic microphases between composite plies by inkjet printing", *J. Compos. Mater.*, 2014, DOI: `10.1177/0021998314533715`.
(Cit. on p. 178.).

(33) H. A. Barnes, *A Handbook of Elementary Rheology*, University of Wales, Institute of Non-Newtonian Fluid Mechanics, Aberwystwyth, Wales, 2000.
(Cit. on p. 181.).

(34) C. Y. M. Tung and P. J. Dynes, "Relationship between Viscoelastic Properties and Gelation in Thermosetting Systems", *J. Appl. Polym. Sci.*, 1982, **27**, 569.
(Cit. on p. 181.).

(35) H. H. Winter, "Can the Gel Point of a Cross-Linking Polymer Be Detected by the G' - G" Crossover?", *Polymer Engineering and Science*, 1987, **27**.
(Cit. on p. 182.).

(36) E. B. Murphy, E. Bolanos, C. Schaffner-Hamann, F. Wudl, S. R. Nutt, and M. L. Auad, "Synthesis and Characterization of a Single-Component Thermally Remendable Polymer Network: Staudinger and Stille Revisited", *Macromolecules*, 2008, **41**, 5203–5209.
(Cit. on p. 182.).

(37) J. Bicerano, *Computational Modeling of Polymers*, Taylor & Francis, 1992.
(Cit. on p. 209.).

(38) N. M. Alves, J. F. Mano, and J. L. Gomez-Ribelles, "Molecular mobility in a thermoset as seen by TSR and DMA near Tg", *Mater. Res. Innov.*, 2001, **4**, 170–178.
(Cit. on p. 209.).

(39) C. Komalan, K. George, P. Kumar, K. Varughese, and S. Thomas, "Dynamic mechanical analysis of binary and ternary polymer blends based on nylon copolymer/EPDM rubber and EPM grafted maleic anhydride compatibilizer", *Express. Polym. Lett.*, 2007, **1**, 641–653.
(Cit. on p. 209.).

(40) Thermal Analysis & Surface Science GmbH, *Applicatio Note AN44: Advantages of frequency multiplexing DMA experiments*, Published Online (3rd March 2014), `http://www.thass.org/DOWN/applications/App_SIINT/An%2044.pdf`.
(Cit. on p. 209.).

Chapter 5

Composite Fabrication and Testing

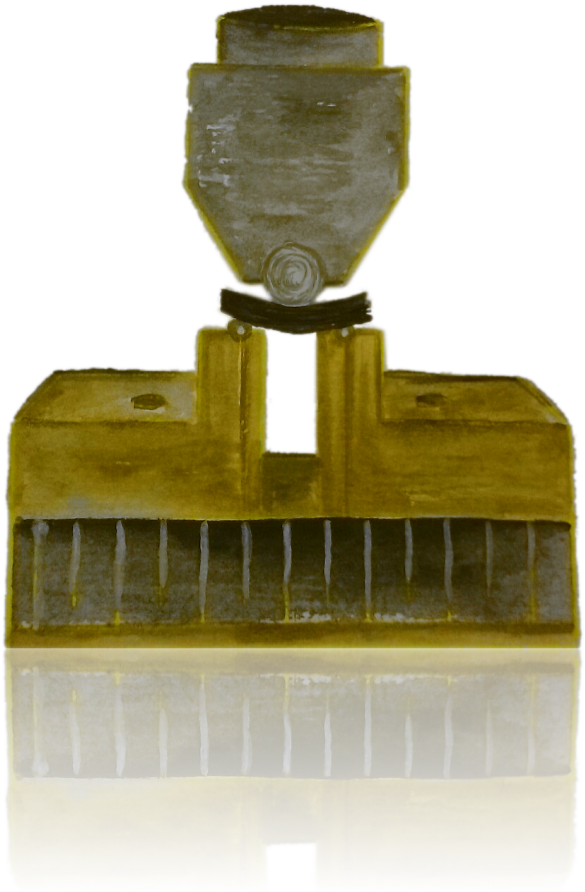

5.1 Introduction

Composite materials are well known for their high strength, fatigue resistance and low density but many are susceptible to delamination in which the bonding between plies is compromised which leads to a large decrease in properties. Delamination is said to represent the weakest failure mode in composite materials [1]; therefore interlaminar toughening or lifetime enhancement by self-healing is of great interest.

This chapter is concerned with testing the interlaminar properties of composites containing plies printed as detailed in Chapter 4 with materials synthesised in Chapters 2 and 3. The printed materials are compared with unprinted controls to examine any differences in interlaminar properties. The materials are then subjected to a thermal healing treatment and re-tested in order to observe any restoration in properties.

Several tests exist that are used to examine the interlaminar properties of composites including the short beam shear test, the double cantilever beam test, the edge-determination test, the end-notched flexure test, the single/double cracked-lap shear test and the off-axis centre notch tensile test. The first two of these tests (short beam shear and double cantilever beam) will be used in this chapter and consequently relevant background information on these tests is given in the following sections.

5.1.1 Short Beam Shear Testing

The short beam shear (SBS) test is the most commonly used interlaminar test commonly employed in materials characterisation due to its relative simplicity compared to the other methods. It resembles a 3-point bending flexural test except with a span-to-thickness ratio chosen so that the failure occurs predominantly in interlaminar shear rather than the more common flexural failure modes (compression on the upper face and tension on the bottom face). A diagram showing the test arrangement is presented in Figure 5.1.

The short beam method measures the 'apparent interlaminar shear strength' (aILSS) and is only applicable if the specimens can be induced to fail in the correct mode [1]. In addition the test can be geometry and layup dependent so while it is of limited use for design purposes it can be used as a comparative test between

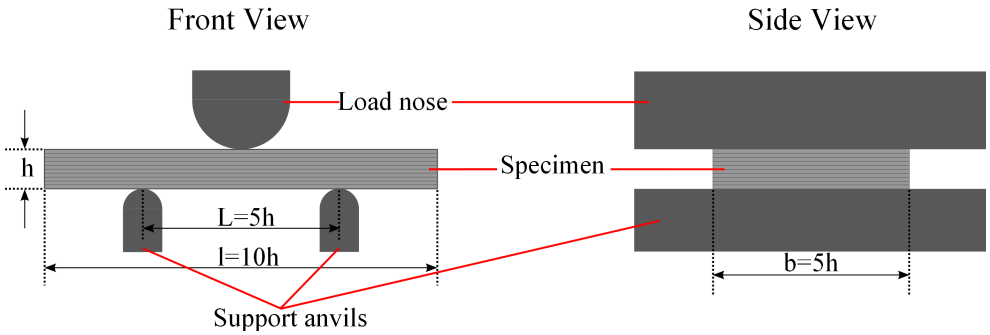

Figure 5.1: The short beam shear loading arrangement with dimensions shown relative to the thickness according to BS EN ISO 14130 [2] .

materials on the condition that they are not dissimilar enough to require a completely different specimen geometry to achieve the correct failure mode.

Classical beam theory states that the maximum normal stress ($\sigma_{\max}$) and maximum shear stress ($\tau_{\max}$) can be described by equations 5.1 and 5.2 [3].

$$\sigma_{\max} = \frac{3P_{\max}L}{2ht^2} = \frac{3}{2ht}\left(\frac{L}{h}\right) \tag{5.1}$$

$$\tau_{\max} = \frac{3P_{\max}}{4bh} \tag{5.2}$$

Where:

$P_{\max}$ is the maximum force

L is the span length

b is the width

h is the thickness.

Considered together, equations 5.1 and 5.2 show that the maximum normal stress on the beam decreases with decreasing span-to-thickness ratio (L/t) but the maximum shear stress is not affected by the reduction in span as it lies on the neutral axis. The consequence of this is that reducing the span will often incite an interlaminar shear failure with interlaminar shear strength given by Equation 5.2. This relationship forms the basis of the short beam shear test in BS EN ISO 14130 [2].

5.1.2 Interlaminar Fracture Toughness and Double Cantilever Beam Testing

The science behind the interlaminar fracture toughness tests has, like many aspects of composite science, developed from work initially related to metals. Linear elastic fracture mechanics are not usually directly applicable to composites as through-thickness cracks do not develop. For delamination damage, however, these concepts can be applied [1].

In 1921 A. A. Griffith proposed that solid materials are similar to liquids in that they possess a surface energy that must be overcome in order to propagate a crack [4]. The increase in energy can be compensated for by internally released or externally added energy. Griffith's theory hinged upon the assumption that the behaviour of the material at the crack tip was purely elastic; this assumption was later independently disputed by G. R. Irwin and E. Orowan in 1948 [5, 6] who determined that the plastic deformation around the crack tip should be taken into account.

Irwin, however, later observed that the plastic zone around the crack tip is very small which lead to the acceptance of Griffith's original assumption [7, 8] and the adoption of a purely elastic solution to the problem:

The critical energy release rate of a material stems from energy based fracture mechanics which was proposed Irwin in 1956 [7]. In this approach the crack is assumed to propagate at the point that the energy release rate overcomes the fracture toughness of a material. This means when the strain energy release rate (G) is greater than a critical level (G_{C}) the crack will propagate.

$$G = -\frac{dE_p}{da} = \frac{d(W - U_\varepsilon)}{da} \tag{5.3}$$

Where:

G is the strain energy release rate

E_p is the potential energy.

W is the work done by external forces.

U_ε is the internal energy stored as strain.

a is the crack length.

d is denoting a differential

When a material is loaded in a static fashion (such as a tensile crack opening) under displacement control it is assumed that no external work is applied (*i.e.* no significant energy converted to heat within the body) and therefore the change in potential energy is equal to the change in internal energy stored as strain and Equation 5.3 simplifies to Equation 5.4.

$$G = \frac{dU_\epsilon}{da} \tag{5.4}$$

This approach can also be applied to the interlaminar region of composite materials. The initiation of a delamination in a composite material can be caused by stresses that overcome the through-thickness strength; for example at stress concentrations caused by bolted joints, ply drops or joints. It can also be initiated by impacts or fatigue. The propensity of a delamination in a laminate to propagate is controlled by the interlaminar fracture toughness of the composite material [9].

The interlaminar fracture toughness is measured in terms of the critical energy release rate discussed previously (G_C) measured in Joules per square meter. The critical energy release rate can be measured in three basic modes: mode I (opening), mode II (shear) and mode III (tearing) [9] shown in Figure 5.2.

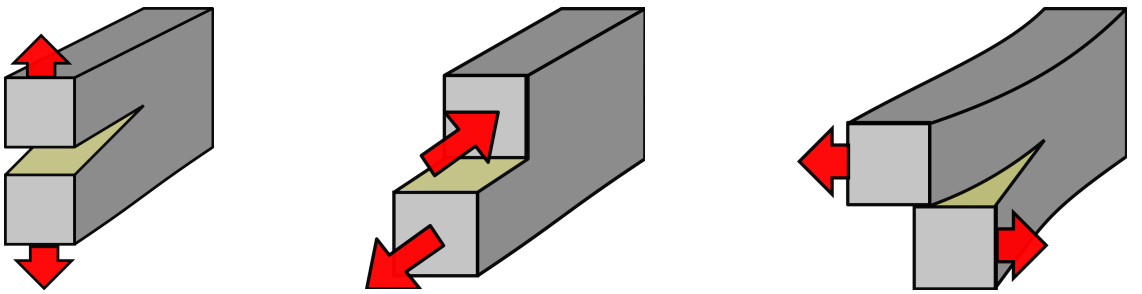

(a) Mode I (tension/opening)

(b) Mode II (in plane shear/sliding)

(c) Mode III (out of plane shear/tearing)

Figure 5.2: Crack opening modes

The mode that will be investigated in this chapter by double cantilever beam (DCB) testing is mode I and therefore the Mode I critical energy release rate is

termed G_{IC}. The reason for this is that the methodology is the best established and mode I is one of the main damage mechanisms contributing to delaminations in carbon-epoxy composites [10].

There are two main international standards covering the DCB test which contain similar test setups and identical data reduction schemes [11, 12]. The principle of the DCB test is that a delamination is introduced into a laminate by the inclusion of a thin starter film such as released polyimide film or PTFE. The film is placed in the mid plane of a unidirectional laminate which is cut into test specimens of 20 mm width. The film ends of the specimen are adhesively bonded to load blocks or piano hinges which can be opened by a tensile testing machine while still allowing free rotation at the loading points. A diagram of a DCB specimen showing the main dimensions is shown in Figure 5.3.

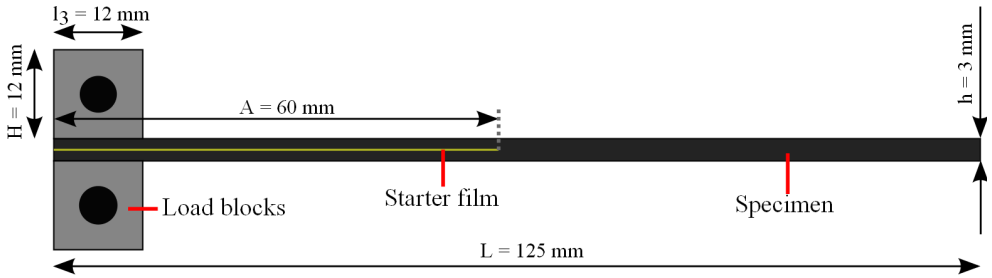

Figure 5.3: A double cantilever beam specimen using load blocks with the main dimensions shown as in BS ISO 15024:2001 [11] .

The standard BS ISO 15024 [11] on which the tests in this chapter are based also stipulates a pre-crack condition followed deloading and reloading which allows better measurement of initiation values where the crack tip is not adjacent to a starter film which is often resin-rich [9].

There are three initiation G_{IC} values obtained as an output from the DCB test and these are described as follows:

NL POINT The NL point is the initiation determined by the deviation from linearity; *i.e.* the G_{IC} value at the point where the load-extension curve ceases to be linear (see Figure 5.4).

VIS Point The VIS point is the visually observed initiation point. It corresponds to the value of G_{IC}at the point where the delamination is first seem to move from the starter position.

C5% Max Point The C5% Max Point is determined by the intersection with the load-extension curve of a line drawn with a slope equal to the linear fit used to determine the NL point but with 5% additional compliance. In the case that the maximum load occurs first this point is used instead (see Figure 5.4).

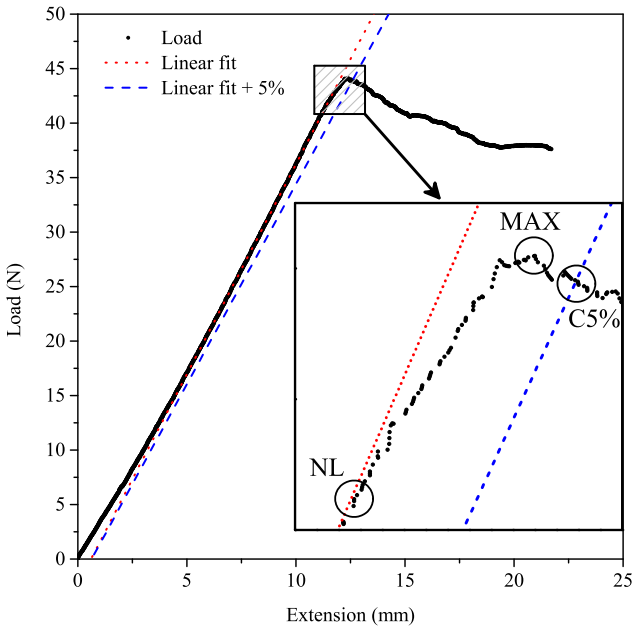

Figure 5.4: An expanded load-displacement plot highlighting the NL, C5% and MAX Point. This VIS point is usually between the NL point and the C5% or Max point.

It is also possible to calculate the above values from the pre-crack loading, (i.e. the crack initiated by the starter film). The starter film values are generally higher than the values of initiation from the pre-crack because the thickness of the starter film leads to a resin rich region in the vicinity of the starter film tip which leads to artificially inflated G_{IC} values. As the purpose of this research is not to investigate the effects of different starter films on crack initiation these starter film values will not be discussed further in this thesis.

Propagation G_{IC} points can be obtained at periodic intervals throughout the remainder of the test. In some cases the G_{IC} may increase due to fibre bridging but it may also stay constant or in rare cases decrease. In order to obtain a mean propagation value for comparison between the printed and the unprinted specimens the median point is taken from each specimen. The median value is appropriate

because the BS ISO 15024 [11] method requires a set of data points from symmetrical positions throughout the crack growth (*i.e.* a tight grouping of data points around the initiation values are compensated for by an equally tight grouping of data points near the end of the test. Therefore the mean-median propagation point will be used for comparison.

5.1.2.1 DCB Data Reduction

The G_{IC} value can be obtained by two different data reduction strategies. Modified beam theory (MBT) or modified compliance calibration (MCC); this chapter will use MBT but both methods produce equivalent results and are equally valid.

Simple beam theory can calculate the energy release rate for a specimen with two arms that are considered to be clamped at the delamination front (Equation 5.5).

$$G_{\mathrm{I}} = \frac{3Ps}{2ba} \tag{5.5}$$

Where:

G_{I} is the mode I energy release rate in $\mathrm{kJ\,mol^{-1}}$

P is the load in N

s is the displacement in mm

b is the specimen width

a is the crack length.

In order to account for rotation at the delamination front and distortion of the end region, an end-factor (Δ) is added to the crack length in order to obtain a more accurate 'true' crack length. The end-factor is calculated by making a plot of the cube root compliance ($\sqrt[3]{C}$) against the crack length (a) and determining the intercept. This works according to Equation 5.6 [13].

$$C = \frac{8(a + \triangle)^3}{Ebh_{0.5}^3} \tag{5.6}$$

Where:

C is compliance, equal to $\frac{s}{P}$

E is the elastic modulus.

$h_{0.5}$ is the half thickness of the laminate.

The inclusion of the end-factor yields the so-called modified beam theory equation (Equation 5.7).

$$G_I = \frac{3Ps}{2b(a+\Delta)} \tag{5.7}$$

The end blocks which are used for the attachment of the specimens to the tensile head of the tensometer create a need for a correction due to their stiffening of the end portions of the specimen as the blocks are able to freely rotate. This free rotation reduces the displacement for a given load by shorterning the lever arm to the delamination front as the test proceeds [9].

The displacement can be corrected by dividing the measured displacement (s) by a load block correction factor N which is given by Equation 5.8. N can then also be used to correct the compliance (C) value used in Equation 5.6 [14].

$$N = 1 - (\frac{l_2}{a})^3 - \frac{9sl_1}{8a^2}\left\{1 - (\frac{l_2}{a})^2\right\} - \frac{9}{35}(\frac{s}{a})^2 \tag{5.8}$$

Where:

l_1 is the distance from the centre of the loading pin to the mid plane of the specimen beam

l_2 is the distance from the loading-pin centre to the edge of the end block.

In Equation 5.8 the term $(\frac{l_2}{a})^3$ corrects for the rigidity of the load blocks, the term $\frac{9sl_1}{8a^2}\left\{1 - (\frac{l_2}{a})^2\right\}$ corrects for the change in lever length caused by the rotation of the load block and the final term $(\frac{9}{35}(\frac{s}{a})^2)$ corrects for the change in lever arm caused by large displacements.

The final correction also comes about from the use of the load-blocks on the end of the specimens. The previous equations assume that the load is applied at the mid-plane of the specimens but the reality is that the load is significantly removed

from this point. In order to correct for these effects at large displacements the measured crack length needs further correction using the large displacement factor F_{L} which is given in Equation 5.9 [14].

$$F_{\mathrm{L}} = 1 - \frac{3}{10}(\frac{s}{a})^2 - \frac{3}{2}(\frac{sl_1}{a^2}) \tag{5.9}$$

The combination of the modified beam theory Equation (5.7) with the load block correction (Equation 5.8) and the large displacement correction (Equation 5.9) yields Equation 5.10 which is published in BS ISO 15024 [11].

$$G_{\mathrm{IC}} = \frac{3Ps}{2b(a + |\Delta|)} \times \frac{F}{N} \tag{5.10}$$

5.2 Experimental

5.2.1 Inkjet Printing onto Prepreg

The details of the inkjet printing of the monomer solutions onto prepreg are given in Chapter 4, Section 4.2.2 on page 168.

5.2.2 Laminate Manufacture

The prepreg was a commercial aerospace grade toughened unidirectional epoxy-carbon prepreg system Cycom 977-2 supplied by Cytec Industries Inc, Östringen, Germany. The prepreg was less than two years old, stored sealed at -18 °C with an out-life less than the maximum number recommended by the manufacturer (40 days). The prepreg was allowed to warm to room temperature in its sealed packet for a minimum of 24 hours before use.

All laminates were unidirectional, flipped in a symmetric fashion at the mirror plane to reduce strains arising from distortions caused by storage on the prepreg roll. The laminates were consolidated by hand using a blunt plastic tool and the application of gentle heat from a domestic hair-dryer. There were no separate vacuum debulking stages.

The laminates were envelope bagged on a PTFE covered steel tool with perforated PTFE and breather cloth above as shown in Figure 5.5 which shows a schematic diagram of the envelope vacuum bagging technique.

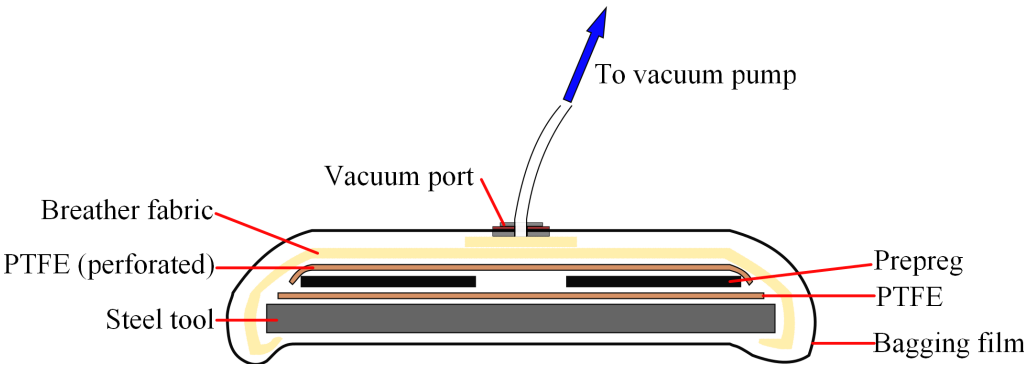

Figure 5.5: Envelope vacuum bagging technique used for oven curing of the laminates

The laminates were oven-cured under vacuum due to a long period of autoclave downtime. The following cure schedule was used:

1. Ramp 20 °C → 120 °C at 1 °C min^{-1}
2. Hold at 120 °C for 30 min
3. Ramp 120 °C → 150 °C at 1 °C min^{-1}
4. Hold at 150 °C for 30 min
5. Ramp 150 °C → 180 °C at 1 °C min^{-1}
6. Hold at 180 °C for 195 min
7. Ramp 180 °C → 20 °C at 1 °C min^{-1}

The ramp rate was slowed down and additional holds were added compared to the manufacturers' recommended cure schedule. This was because the 3 mm thickness laminates were thicker than the maximum suggested thickness from the manufacturer (2 mm) and to allow good consolidation despite the lack of autoclave pressure.

5.2.3 Specimen Fabrication

The following specimens were fabricated for the testing in this chapter.

5.2.3.1 Short Beam Shear

Eight plies of prepreg were used for the short beam shear panels. These were 60 mm x 75 mm with the fibres orientated in the long direction. After cure this produced panels with a thickness of approximately 2 mm. The panels were cut into fifteen 20 mm x 10 mm specimens (fibre direction in the long dimension) using an abrasive diamond cutter saw with water cooling (1.5 mm blade).

Batch 12 was a control; batches 13 and 15 were printed with 5% M501 and M400 respectively on the middle four plies and batch 14 was printed with 1% M400 on all eight plies. The specimens were washed and conditioned in a vacuum oven at 50 °C for at least 24 hours prior to testing.

5.2.3.2 Double Cantilever Beam

12 plies of prepreg with dimensions 150 mm x 150 mm were used for the double cantilever beam specimens with a layer of PTFE film (60 μm, Tygavac, Oldham, UK) included between the middle plies 75 mm from the edge (60 mm after final trimming) as shown in Figure 5.6. The printed area was on the 6th ply from the tool surface facing towards the middle of the laminate and were printed in the test area of interest between the PTFE and the end of the specimen as previously shown in Section 4, Figure 4.4 on page 169.

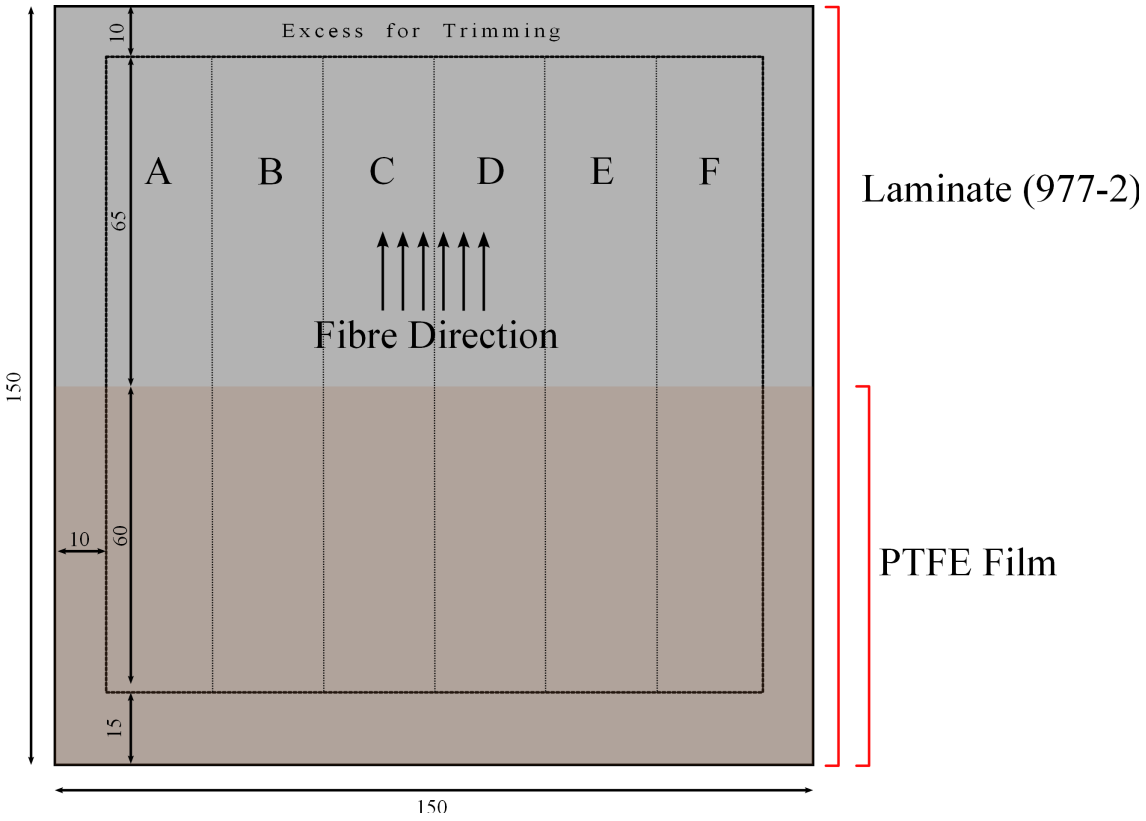

Figure 5.6: DCB specimen position on each laminate panel with dimensions in mm. All specimens are 20 mm wide incorporating a margin for the material removed by the saw.

Six specimens were cut to 125 mm x 20 mm x 3 mm along the fibre direction using an abrasive diamond cutter saw with water cooling (1.5 mm blade). The specimens were washed and then dried in a vacuum oven at 50 °C for around 2 hours. 12 mm x 12 mm centre-drilled aluminium blocks were bonded (Araldite standard, Huntsman),

to the PTFE-containing specimen ends after light preparation with 240 grit wet and dry paper (used dry). The edges of the specimens were painted with corrector fluid (Tipp-ex) to allow better contrast.

5.2.4 DMA Testing and Specimen Fabrication

DMA testing was undertaken on a Perkin Elmer DMA 8000 instrument equipped with a liquid nitrogen cooling system. The specimen dimensions were approximately 8 mm x 25 mm x 0.5 mm with a free length of 2 x 10 mm in the dual cantilever geometry. The temperature was increased from 0 to 250 °C and the dynamic mechanical properties were measured at 1 Hz and 10 Hz with a displacement of 50 μm.

5.2.5 Mechanical Testing

Mechanical testing was done on a Lloyd LS1 materials testing machine (Lloyd Materials Testing, Bognor Regis).

5.2.5.1 Short Beam Shear

Short beam shear testing was carried out following BS EN ISO 14130:1998 [2] using the preferred specimen and a crosshead speed of 1 mm min^{-1} using a pre-load of 2N and the displacement taken from the crosshead. In order to prevent complete destruction of the specimens the test was stopped at the point that the load dropped to 5% of the maximum.

The apparent interlaminar shear strength was calculated using Equation 5.2 on page 224 for the specimens that appeared to fail in single or multiple shear. Specimens that failed in tension or compression or mixed modes were discarded.

The specimens that successfully failed in an acceptable shear mode were retained for a thermal healing treatment (see Section 5.2.6 for details). After healing they were re-tested in the same orientation as they were tested initially.

5.2.5.2 Double Cantilever Beam

Double cantilever beam testing was carried out following BS ISO 15024:2001 [11]. The precrack was introduced using mode I opening at 5 mm min^{-1} until the crack

had propagated 3 to 5 mm before unloading at 25 mm min^{-1} and reloading at 5 1 mm min^{-1}.

The crack growth was recorded using an HD video camcorder (Panasonic HC-X900) manually focussed on the edge of the specimen recorded at 1080p and 60 fps.

The machine time and the camera time was synchronized to the nearest frame by tapping the sample gently during the initial opening. The time was correct by subtracting the difference between the frame featuring the tap and the corresponding blip on the load-time plot.

Crack growth was measured by taking first thresholding the image at a fixed level determined on a specimen by specimen basis. This was done in order to remove experimenter bias from the crack position determination. The crack length was then measured in pixels and converted to mm by multiplying by the resolution. The resolution was obtained by holding up a ruler next to the specimen during the start of each run. A clear frame featuring the ruler was used to measure a known distance e.g. 200 mm in pixels using freeware graphics software (GIMP) to give a resolution in px mm^{-1}.

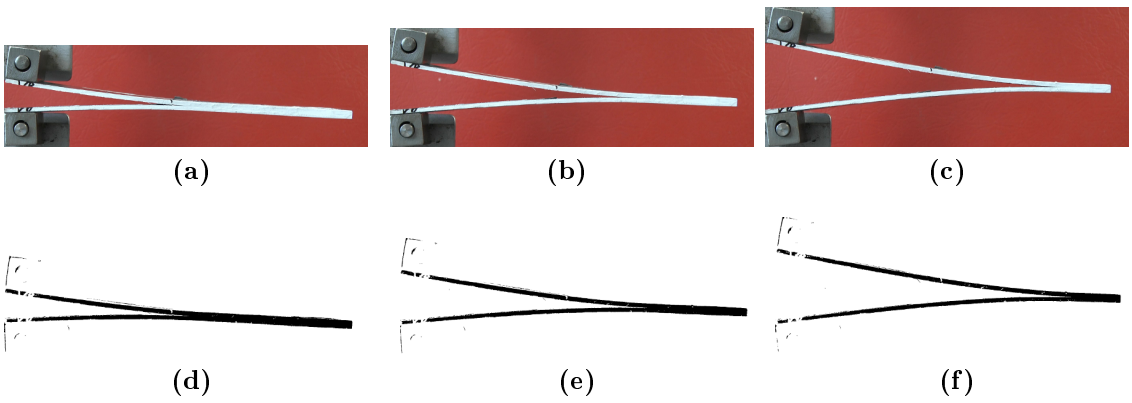

Figure 5.7: DCB Stills from Panel 5, Specimen A. (a-c: as recorded, d-f: with threshold).

In order to produce reproducible results the calculation of the NL point was automated and was done as follows:

A straight line was fitted to the linear portion of the load-extension plot using a linear regression least squares method. The equation of the line was then used to generate y values for every x value recorded in the region within 40% of the maximum

y value. Each measured y value was subtracted from the y value produced by the linear equation with a 3 point moving average. The NL point was identified as the point at which the deviation from linearity (within a 3 point average) is greater than 0.3 N.

An worked example G_{IC} calculation is given in Appendix B on page 289 for one of the initiation NL points. The same process was undertaken for all the initiation points and propagation points that were measured; this was automated using an Excel spreadsheet template.

After testing some of the batches were subjected to a heating cycle (see the next section for details). After the healing cycle the specimens were re-tested using the same conditions as the virgin specimens other than the absence of a pre-cracking load-unload cycle.

5.2.6 Thermal healing cycle

5.2.6.1 SBS Specimens

After testing the short beam shear specimens were place in an aluminium tray and heated in a preheated oven at 180 °C for 6 hours. After 6 hours the oven was turned off without opening the door to allow a slow (although not controlled) cool down to room temperature over approximately 2 hours.

5.2.6.2 DCB Specimens

After testing and the load was removed the double cantilever beam specimens were taped shut using high temperature tape. The specimens were then enclosed in a vacuum bag and heated at 180 °C for 6 hours with a heating and cooling rate of 2 °C min^{-1} under the pressure exerted by the atmospheric pressure on the vacuum bag.

After the healing cycle it was necessary to re-bond the end blocks because the high temperature had degraded the adhesive bond. The high temperature tape was left in place until the specimens were re-mounted in the testing machine in order to prevent premature damage before testing. When the specimens were mounted the tape was cut using a scalpel blade.

5.3 Results and Discussion

The following sections will present and discuss the results of of the double cantilever beam (DCB), short beam shear (SBS) and dynamic mechanical analysis (DMA) tests on the printed and unprinted panels before and after healing cycles. For the sake of clarity. Table 5.1 gives a summary of all the panels produced for all the experiments discussed in this chapter.

Table 5.1: Summary of the composite panels referred to in this chapter

Panel Number	**Production Date**	**Type**	**For Test**	**No. Plies [printed]**	**Lay-up***
1	18/06/2013	Control	DCB	12	$[(0)_{12}]_T$
2	18/06/2013	Control	DCB	12	$[(0)_{12}]_T$
3	18/06/2013	Printed 1% M401	DCB	12 [1]	$[(0)_5/0_p/(0)_6]_T$
4	18/06/2013	Printed 1% M401	DCB	12 [1]	$[(0)_5/0_p/(0)_6]_T$
5	05/07/2013	Control	DCB	12	$[(0)_{12}]_T$
6	05/07/2013	Printed 1% M401	DCB	12 [1]	$[(0)_5/0_p/(0)_6]_T$
7	05/07/2013	Control	DMA	2	$[(0)_2]_T$
8	05/07/2013	Printed 1% M401	DMA	2 [2]	$[(0_p)_2]_T$
9	09/01/2014	Control	DCB	12	$[(0)_{12}]_T$
10	09/01/2014	Printed 5% M401	DCB	12 [1]	$[(0)_5/0_p/(0)_6]_T$
11	09/01/2014	Printed 5% M400	DCB	12 [1]	$[(0)_5/0_p/(0)_6]_T$
12	10/01/2014	Control	SBS	8	$[(0)_8]_T$
13	10/01/2014	Printed 5% M401	SBS	8 [4]	$[(0)_2/(0_p)_4/(0)_2]_T$
14	10/01/2014	Printed 1% M400	SBS	8 [8]	$[(0_p)_8]_T$
15	10/01/2014	Printed 5% M400	SBS	8 [4]	$[(0)_2/(0_p)_4/(0)_2]_T$

* Viewed from the tool surface, subscript numbers refer to repeated plies, $_p$ refers to printed plies, $_T$ confirms that the total layup is shown (to remove ambiguity).

5.3.1 DMA

Dynamic mechanical analysis was performed in order to investigate whether any polymer transitions from the printed layers were visible. DMA is a highly sensitive tool for investigating thin films even on thick substrates; it is possible, for example, to measure transitions of coatings on metal substrates. Therefore it is possible that it might be possible to detect the printed polymers within the laminate.

In order to get good quality DMA results thin panels were required (2 plies) which gave a thickness of *c.a.* 0.5 mm. DMA tests were undertaken using an unprinted control (Panel 7) and 1% M401 (Panel 8), (See Table 5.1 on the preceding page for layup and print details). Two typical DMA plots are given in Figure 5.8.

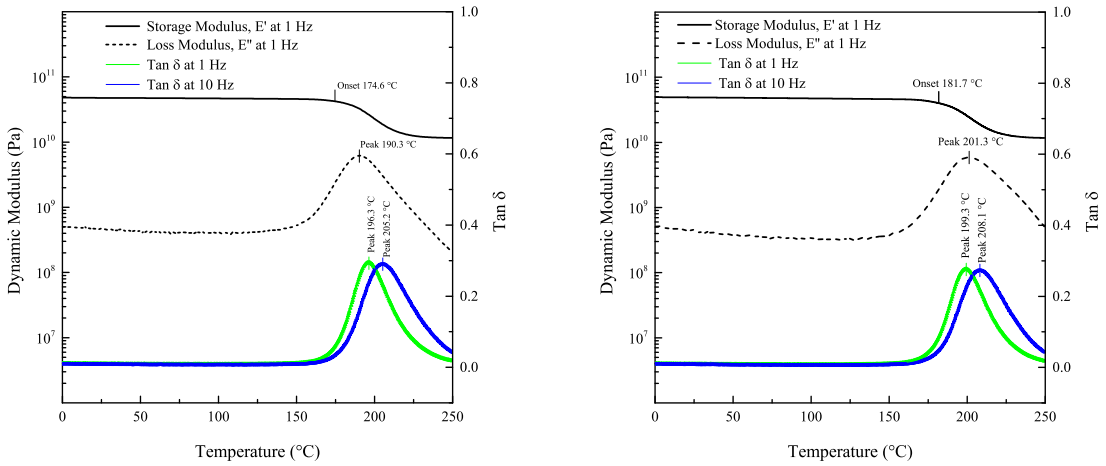

(a) Unprinted **(b)** Printed 1% M401 both plies

Figure 5.8: DMA results for laminates made from printed and unprinted prepreg.

The DMA plots show there are no transitions, such as printed polymer glass transitions, between 0 and 250 °C other than the glass transition of the epoxy resin. Therefore the printed polymer transitions are not visible on the DMA; this may be due to the very low concentration of the ink. No further laminates, for example with higher monomer concentrations, were made for DMA purposes due to time and material constraints.

The glass transition of the printed specimens appear to be higher by between 5 to 10 °C; this is interesting but it is very unlikely to be due to the printing. The biggest influence on the glass transition of epoxy resin, other than its formulation, is its cure temperature. A higher cure temperature will delay vitrification from occurring until a higher temperature which leads to a higher glass transition. A higher temperature could occur due to being in a different oven position or local exotherms.

5.3.2 Double Cantilever Beam

As described in Table 5.1 on page 241, four DCB unprinted control panels were produced at different times (Panels 1, 2, 5 and 9) for two reasons.

Firstly this was to account for differences between panels cured under slightly different conditions and secondly it was to to provide a clear baseline for the properties of the unmodified material. Panels produced could have systematic variations for many reasons that are difficult to control such as:

Cure temperature, dependent on reproducibility of the temperature program and uniformity of temperature across the oven.

Prepreg age, prepreg that has aged would be expected to perform worse in terms of interlaminar properties; this effect, however, should be minimal as freezer out-life was minimised and relatively consistent across different panels.

Consolidation pressure, this is dependent on vacuum pump performance, quality of vacuum bag and atmospheric pressure.

Operator variation, with all hand layups there can be significant variation between operators as the process of panel manufacture is not automated. In order to minimise this source of variation all the panels under consideration were produced by myself and I took particular care to keep the process consistent.

Other sources of error should be random and consistent across all panels.

5.3.2.1 The Control Panels

Typical results from the DCB tests for the unprinted samples are given in Figure 5.9. Figure 5.9a is a load-extension curve with the total delamination length (a) also plotted on the secondary axis. The linear fit (C_0) is shown which was used to determine the NL point and a second line at 5% compliance ($C_{5\%}$) which is used to calculate the C5% point is drawn through the same intercept. Figure 5.9b shows the plot of cube root compliance (load block corrected) against total delamination length (a); this is used to determine the Δ correction which is used in the G_{IC} calculation. Figure 5.9c shows the critical energy release rate (G_{IC}) against total delamination length which for the unprinted samples was mostly constant.

A column chart showing 95% confidence intervals (CI) of the mean factors is given in Figure 5.10a from which, taking the error bars into consideration, it appears that the different groups are equivalent. This was checked formally using analysis of variance (ANOVA) which is a suitable way of comparing multiple groups.

In order to investigate whether the four control sample means describe the same population mean it is prudent to set up the null hypothesis that the control samples all represent the same population mean (*i.e.*H_0: $\mu_1 = \mu_2 = \mu_3 = \mu_4$) . This null hypothesis was tested using a one-way ANOVA. The four control samples were compared in order to see if there is a non-negligible influence from the possible systematic errors mentioned in the previous section. The ANOVA nomenclature and equations (adapted from several sources[15–17]) are given in Appendix B on page 289.

The result, for each value, yields an F-statistic notated $F(df_{\text{between}}, df_{\text{within}})$ which when used to evaluate a F probability distribution function yields a probability (p value). If the p value is greater than the significance level (in this case 0.05) this outcome directs the acceptance of the null hypothesis (H_0).

There was no significant difference between the NL points of the groups at the p<0.05 level for the four groups [$F(3, 18) = 1.28$, $p = 0.31$]. The differences between the group means can be represented graphically (as shown in Figure 5.10b) using the output of the Tukey range test (also known as the Tukey-Kramer method or the honest significant different test). If a group mean was to be further from another group mean by the distance represented by the range bars this would be considered a significant deviation at the 0.05 significance level.

A similar result was found for the VIS points [F(3, 18) = 1.97, $p = 0.15$], the Max/C5% points [F(3, 18) = 1.54, $p = 0.24$] and the mean of the median propagation points [F(3, 18) = 0.52, $p = 0.68$].

The results of the ANOVA confirm that the control groups are equivalent and will, therefore, be combined.

It can also be be concluded that any significant differences between the printed samples and the controls can be attributed to to the printing as opposed to panel to panel variations.

The critical energy release rate (GIC) for the unprinted composites can therefore be presented as a mean of 22 specimens:

NL Point 329 $\mathrm{J\,m^{-2}} \pm$ [SD = 15.5 $\mathrm{J\,m^{-2}}$, 95% CI = 6.89 $\mathrm{J\,m^{-2}}$]

VIS Point 336 $\mathrm{J\,m^{-2}} \pm$ [SD = 14.9 $\mathrm{J\,m^{-2}}$, 95% CI = 6.59 $\mathrm{J\,m^{-2}}$]

MAX / C5% Point 338 $\mathrm{J\,m^{-2}} \pm$ [SD = 13.3 $\mathrm{J\,m^{-2}}$, 95% CI = 5.91 $\mathrm{J\,m^{-2}}$]

Median Prop Point 331 $\mathrm{J\,m^{-2}} \pm$ [SD = 11.6 $\mathrm{J\,m^{-2}}$, 95% CI = 5.15 $\mathrm{J\,m^{-2}}$]

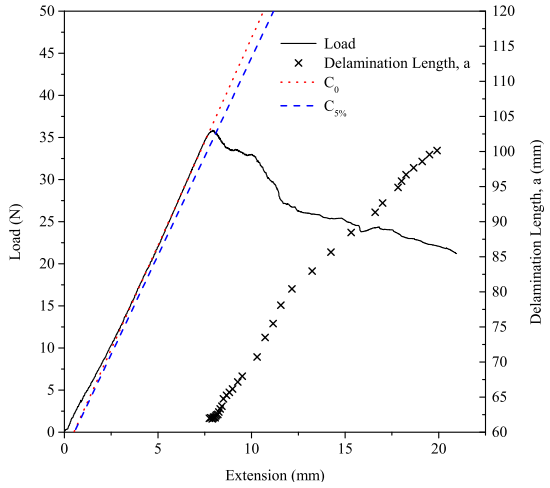

(a) Load and total delamination length against crosshead extension

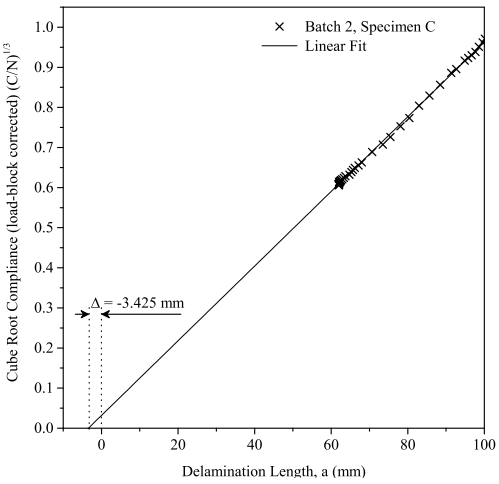

(b) Linear fit used to determine Δ correction

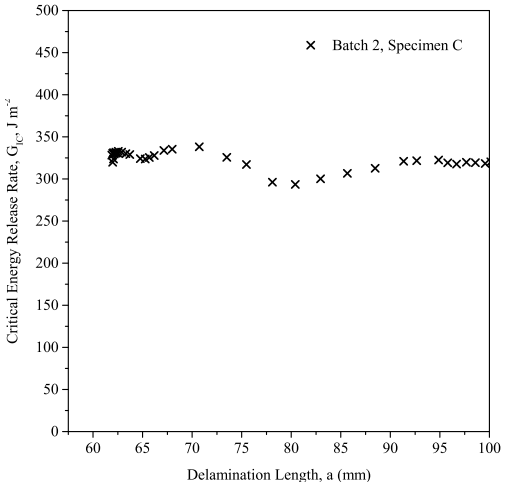

(c) Resistance curve: critical energy release rate (G_{IC}) against delamination length.

Figure 5.9: Typical Control DCB Results (Panel 2, Specimen C)

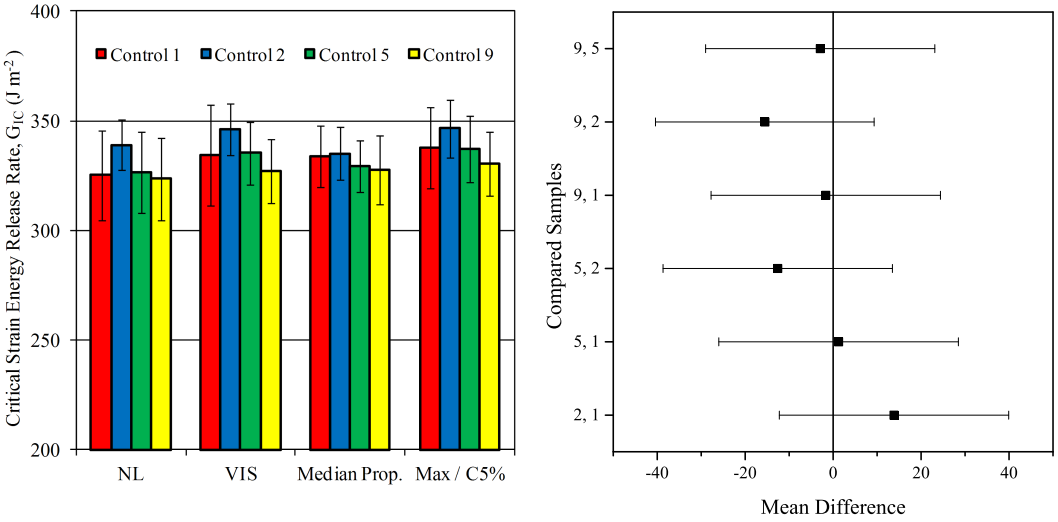

(a) Column chart (error bars are 95% confidence intervals, CI)

(b) Differences between the Mean NL Points from the four groups using Tukey range test

Figure 5.10: Comparison of the mean interlaminar fracture toughness, G_{IC}, values for the different control groups.

5.3.2.2 Panels 4 and 6 Printed with 1% M401

Typical results from Panel 6, which were printed with 1% M401, are given in Figure 5.11. Figure 5.11a shows a typical load extension curve along with the measured delamination length, Figure 5.11b shows the Δ correction plot and Figure 5.11c shows the critical energy release rate (G_{IC}) which does not significantly vary with the delamination length for these panels.

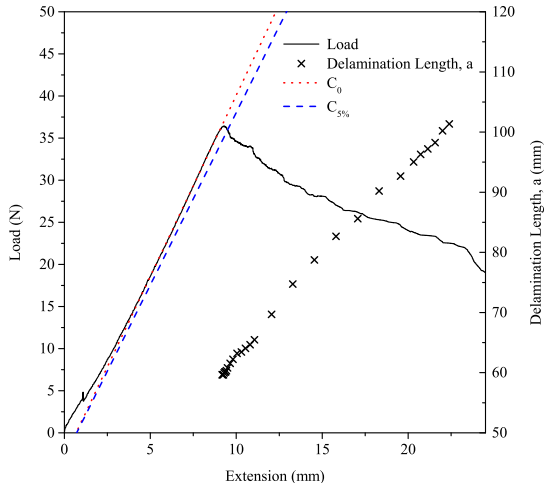

(a) Load and total delamination length against crosshead extension

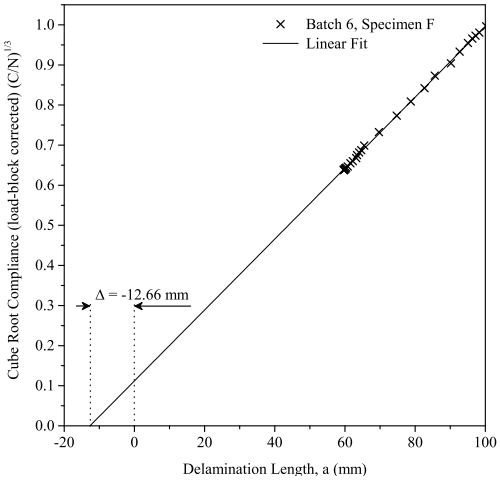

(b) Linear fit used to determine Δ correction

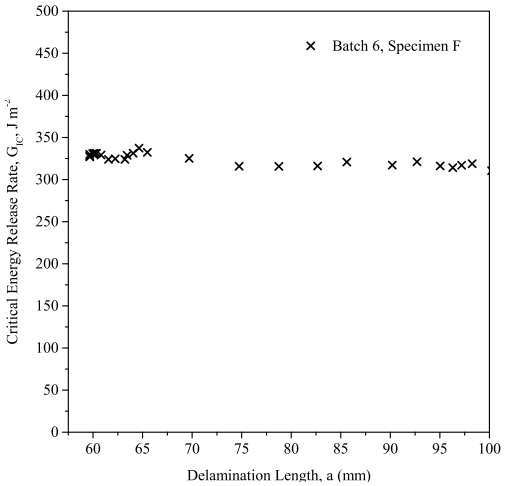

(c) Resistance curve: critical energy release rate (G_{IC}) against delamination length.

Figure 5.11: Typical DCB results for panels printed with 1% M401 (Panel 6, Specimen F)

The DCB results of the two panels printed with 1% M401 are summarised in in Table 5.2.

Table 5.2: DCB Results, Panels Printed with 1% M401

Panel #	NL Point			VIS Point			C5%/Max Point			Median Prop Point		
	Mean	SD	95% CI	Mean	SD	95% CI	Mean	SD	95% CI	Mean	SD	95% CI
4 (1% M401)	321	15.4	16.2	332	18.3	19.2	333	20.8	21.8	328	13.6	14.3
6 (1% M401)	329	17.3	18.1	337	19.0	20.0	338	13.0	13.7	328	19.1	38.2

All units are $\mathrm{J\,m^{-2}}$

The two panels were produced in the same manner but on different days. Panel 4 was produced at the same time as controls 1 and 2. Panel 6 was produced along with control 5. The previous section concluded that there is no significant difference between control samples produced on different days; therefore panels 4 and 6 should also be equivalent. This is very likely because for each parameter the mean is within 1 standard deviation of the other. As there are only two panels to compare, this sample equivalence can be confirmed formally by using 2-sample unpaired t-tests instead of using ANOVA.

The results of the t-tests are as follows for each parameter: NL Point [t(10) = 0.79, p = 0.45]; VIS Point [t(10) = 0.45, p = 0.67]; MAX / C5% Point [t(10) = 0.45, p = 0.66] and Median Prop Point [t(10) = 0.09, p = 0.93].

The t-tests show formally that panels 4 and 6 have no significant differences between the means of all 4 measured parameters. Panels 4 and 6 will therefore be combined and the critical energy release rate (G_{IC}) for the composites printed with 1% of M401 can be presented as a mean of 12 specimens:

NL Point 325 $\mathrm{J\,m^{-2}}$ ± [SD = 16.1 $\mathrm{J\,m^{-2}}$, 95% CI = 10.2 $\mathrm{J\,m^{-2}}$]

VIS Point 334 $\mathrm{J\,m^{-2}}$ ± [SD = 18.0 $\mathrm{J\,m^{-2}}$, 95% CI = 11.4 $\mathrm{J\,m^{-2}}$]

MAX / C5% Point 335 $\mathrm{J\,m^{-2}}$ ± [SD = 17.4 $\mathrm{J\,m^{-2}}$, 95% CI = 11.1 $\mathrm{J\,m^{-2}}$]

Median Prop Point 328 $\mathrm{J\,m^{-2}}$ ± [SD = 15.8 $\mathrm{J\,m^{-2}}$, 95% CI = 10.0 $\mathrm{J\,m^{-2}}$]

5.3.2.3 Panel 10 printed with 5% M401 and Panel 11 printed with 5% M400

Typical DCB results from Panel 10, which was printed with 5% M401, are given in Figure 5.12. Figure 5.12a shows a typical load extension curve along with the measured delamination length, Figure 5.12b shows the Δ correction plot and Figure 5.12c shows the critical energy release rate (G_{IC}) which increases slightly with delamination length in Panel 10.

Typical results from the DCB test of Panel 11, which was printed with 5% M400, are in Figure 5.13. Figure 5.13a shows a typical load extension curve along with the measured delamination length, Figure 5.13b shows the Δ correction plot and Figure 5.13c shows the critical energy release rate (G_{IC}) which increases significantly with delamination length.

Only one panel was made printed with 5% M401 and 5% M400 respectively therefore the results can be immediately presented in Table 5.3 in the following section.

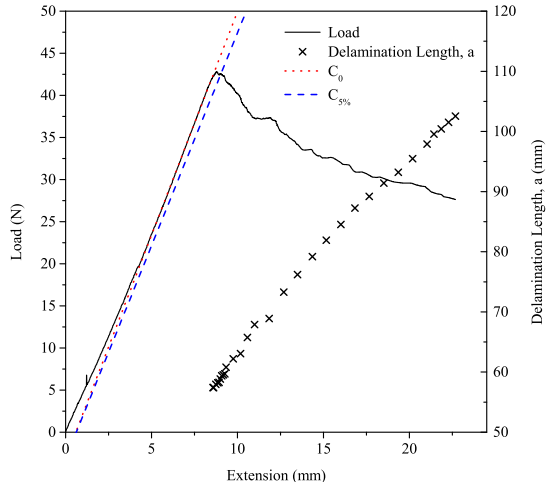

(a) Load and total delamination length against crosshead extension

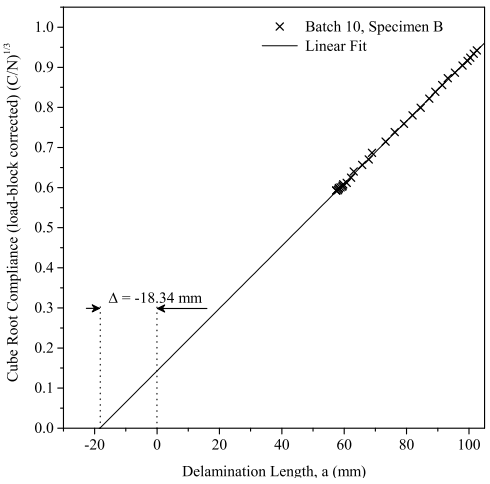

(b) Linear fit used to determine Δ correction

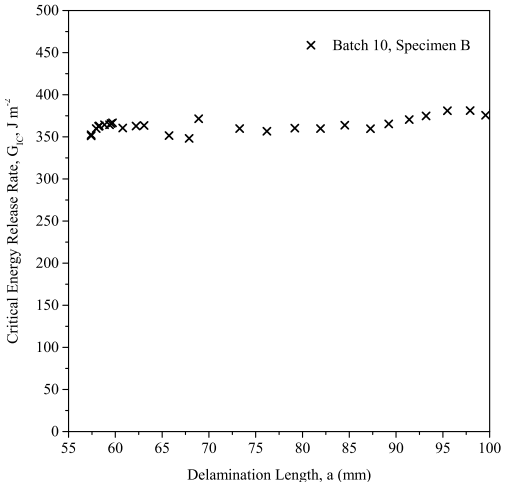

(c) Resistance curve: critical energy release rate (G_{IC}) against delamination length.

Figure 5.12: Typical DCB results for panels printed with 5% M401 (Panel 10, Specimen B)

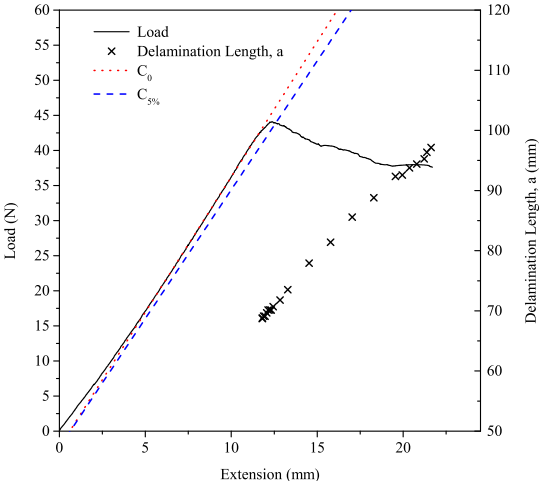

(a) Load and total delamination length against crosshead extension

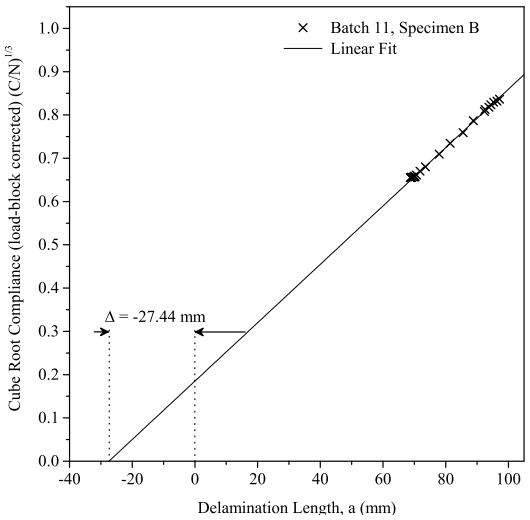

(b) Linear fit used to determine Δ correction

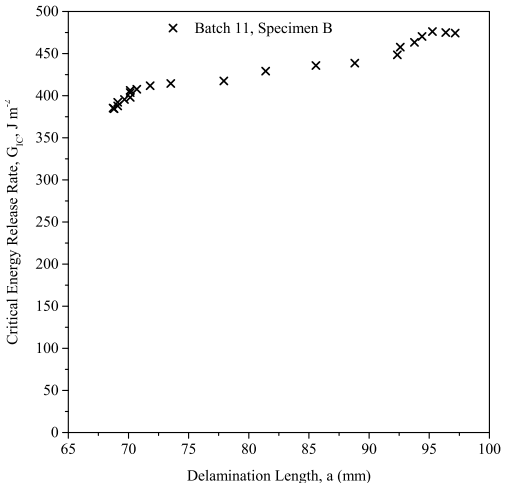

(c) Resistance curve: critical energy release rate (G_{IC}) against delamination length.

Figure 5.13: Typical DCB results for panels printed with 5% M400 (Panel 11, Specimen B)

5.3.2.4 Comparison of Printed to Unprinted DCB Samples

A column chart summarising all the DCB results from the four different groups is shown in Figure 5.14

Table 5.3: Combined DCB Results

Panel #		NL Point			VIS Point			C5%/Max Point			Median Prop Point		
	n	Mean	SD	95% CI	Mean	SD	95% CI	Mean	SD	95% CI	Mean	SD	95% CI
Control													
1, 2, 5, 9	22	329	15.5	6.89	336	14.9	6.59	338	13.3	5.91	331	11.6	5.15
4, 6 (1% M401)	12	325	16.1	10.2	334	18.0	11.4	335	17.4	11.1	328	15.8	10.0
10 (5% M401)	5	354	21.8	27.1	360	11.4	14.2	363	20.0	24.9	377	20.6	25.6
11 (5% M400)	6	360	21.4	22.5	370	19.3	20.3	380	17.7	18.6	420	27.6	29.0

All units are $\mathrm{J\,m^{-2}}$

From the chart several aspects are striking: firstly that both 5% printed laminates show higher G_{IC} values and secondly that the 1% concentration print doesn't appear to have significantly affected the interlaminar properties. The increase in G_{IC} is most apparent from the mean-median propagation points; this can be attributed towards the fact that these samples appear to show a rising trend in G_{IC} with delamination length that is not present in the control samples. Such a rising trend is normally attributed to the influence of fibre bridges near the crack tip which increase the rate of critical energy release required to propagate the crack.

It is likely that the presence of the patterned polymers at the interface increases $G_{\mathrm{IC}}$by interrupting the process of microcrack coalescence by forcing alternative paths which also produces a fibre bridging effect.

Using the same method previously used in Section 5.3.2.1 on page 243, the statistical difference in means between the different groups was also tested using ANOVA. The means of the NL points [F(3, 41) = 8.09, $p = 2.39\times10^{-4}$] ; VIS points [F(3, 41) = 9.26, $p = 8.45\times10^{-5}$]; Max/C5% points [F(3, 41) = 14.82, $p = 1.10\times10^{-5}$] and the mean of the median propagation points [F(3, 41) = 56.70, $p = 1.21\times10^{-14}$] are statistically shown not to be equivalent as the p values are much lower than the significance level 0.05. In order to determine exactly which means are significantly different the Tukey range test can be applied, the results of this are shown in Figure 5.15.

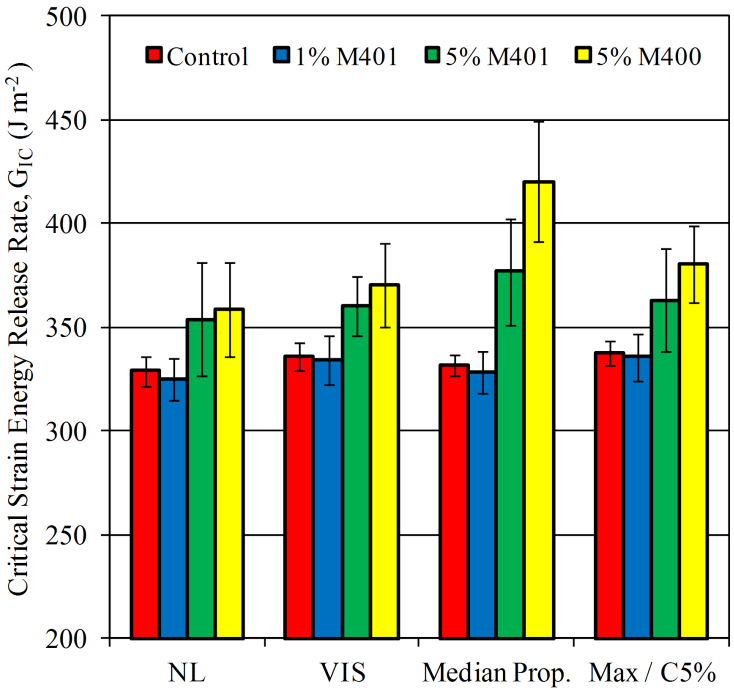

Figure 5.14: Column chart comparing DCB means (error bars are 95% confidence intervals, CI)

What Figure 5.15 confirms is:

- The 1% M401 samples do not differ from the unprinted controls significantly for any of the four parameters.
- Both of the 5% printed laminates perform significantly better for all four parameters compared to the control (and the 1%).
- There is no significant difference between the 5% printed laminates with M400 and M401 in terms of NL point, VIS point and MAX/C5% point but in terms of propagation points M400 performs significantly better.

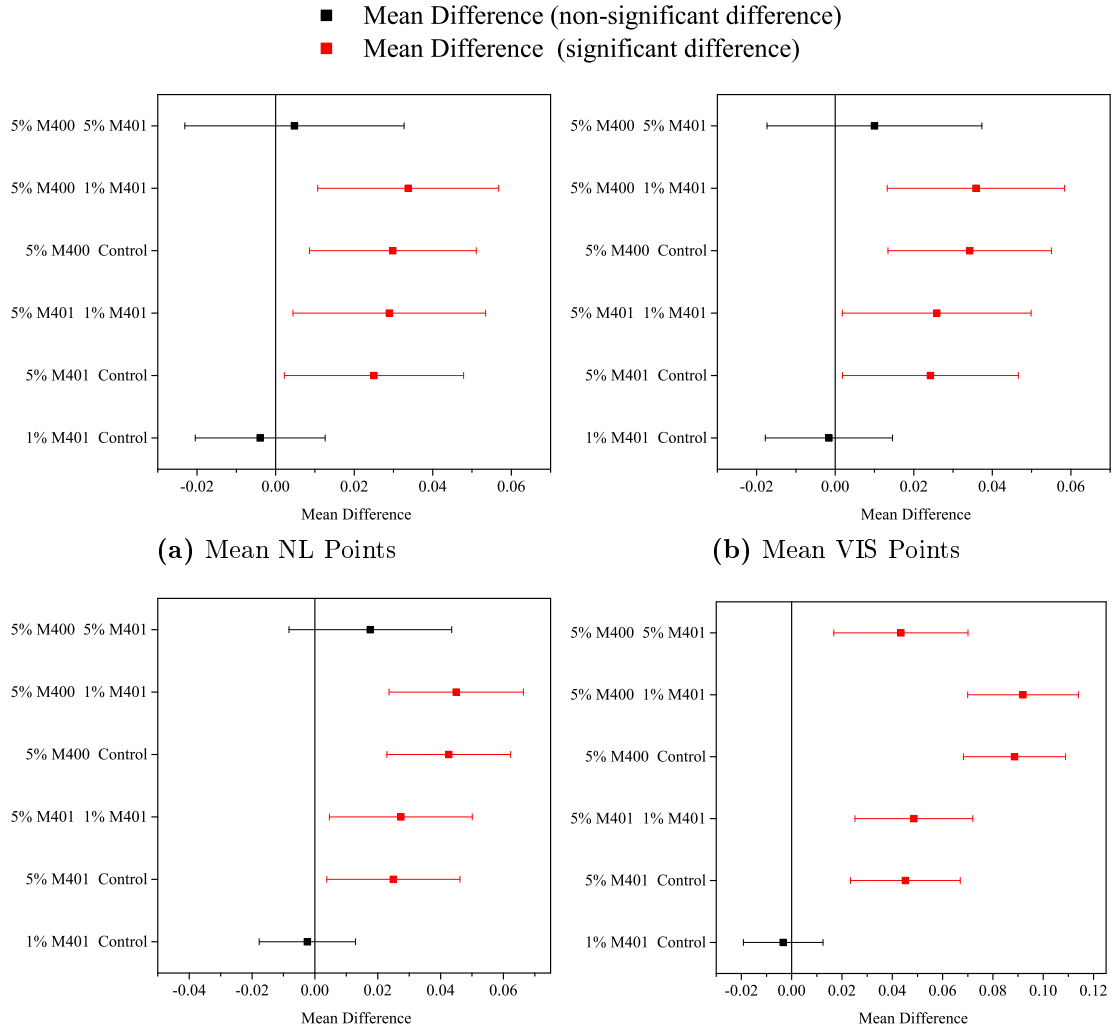

(a) Mean NL Points

(b) Mean VIS Points

(c) Mean MAX / C5% Points

(d) Mean median PROP points

Figure 5.15: Means comparisons between all four groups using Tukey Range Test

5.3.2.5 DCB tests after healing cycle

Panel 9 (control), 10 (5% M401) and 11 (5% M400) were subjected to a thermal healing cycle after testing as outlined in Section 5.2.6. The DCB tests were repeated for the thermally cycled specimens. The aim of the test was to see if there was any rebonding of the previously delaminated specimen faces. Healing, however, was not observed as there was no noticeable resistance to delamination up until the point where the test had previously been stopped ($\sim$ 5 mm from the end of the specimen). There was also not enough remaining specimen length to get the required data points need to produce G_{IC} values for the re-initiation of the crack.

By comparing the load-extension curves for the same specimens (Figure 5.17) before and after healing it is clear that after reloading the crack propagation appears to continue along the same path with a similar level of load before and after healing; this occurs for the printed specimens and the controls. In Figure 5.17 a single typical specimen is shown from each panel for clarity but a similar observation was made for all specimens. The differences in slope in the initial loading lines of both initial and healed lines are not relevant as these are due to the differences in initial crack length and therefore lever action.

The fact that healing was not observed is disappointing but not entirely surprising given the small quantity of material printed between the plies (*c.a.* 0.0024 % volume fraction for the 5% ink, see Section 4.3.2 on page 178). The test is quite severe as the plies are completely peeled away from each other (see Figure 5.16) and there is no guarantee that perfect contact is re-established during the healing cycle. In order to see any healing at this level much more material is likely to be required.

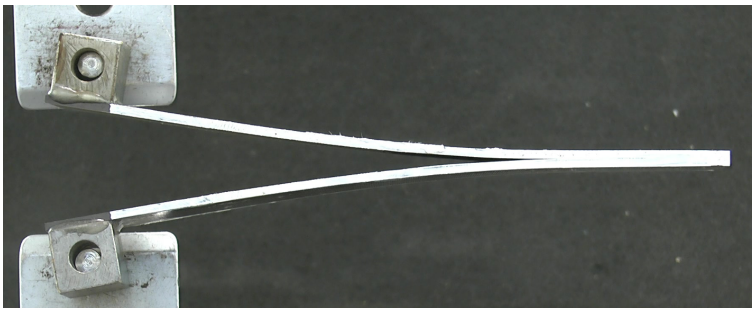

Figure 5.16: A photo showing the typical damage to which a specimen is subjected during a DCB test.

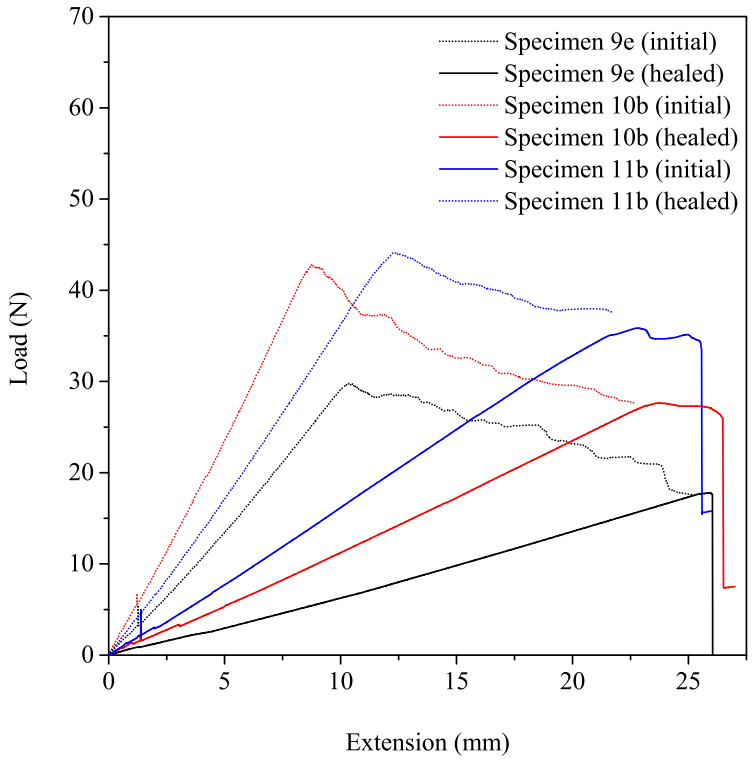

Figure 5.17: Load extension graphs for 3 typical specimens from each panel from the tests carried out before and after the thermal healing cycle. The dotted lines represent the initial propagation and the solid lines represent the reloading after healing.

5.3.3 Short Beam Shear

Short beam shear testing was performed on four samples. Panel 12 was an unprinted control, Panel 13 was printed with 5% M401, Panel 14 was printed with 1% M400 and Panel 15 was printed with 5% M400. Out of the eight plies present in the laminate panels 13 and 15 were printed on the four inner plies whereas Panel 14 was printed on all eight plies. The number of specimens produced from each panel was 14; however the specimens that failed obviously in compression or tension were discarded leaving between 7 and 10 specimens from each sample that appeared to fail in single or multiple shear.

Typical plots of the apparent interlaminar shear stress against extension are shown for all four samples in Figure 5.18 with the particular specimens chosen because they were close to the mean and therefore good representations of the sample.

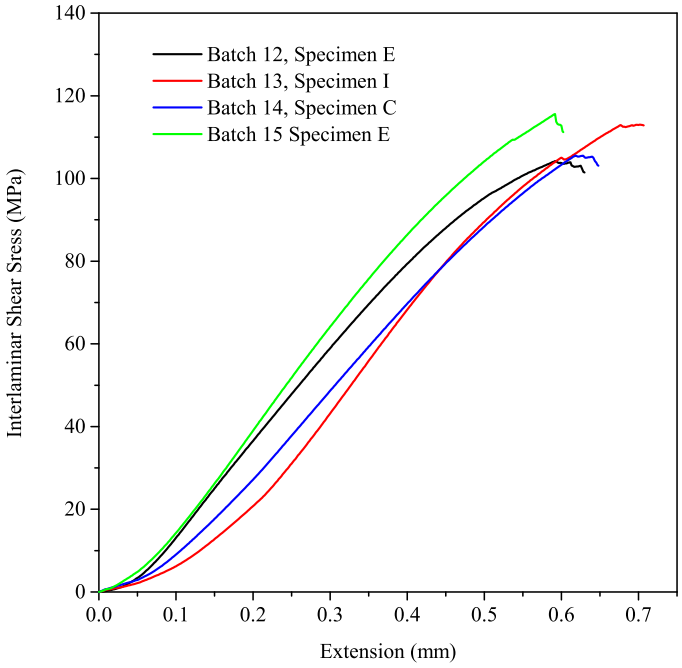

Figure 5.18: Typical Short Beam Shear plots for Unprinted and Printed Specimens

The mean results are tabulated in Table 5.4 and shown in a column chart in Figure 5.19a. A one-way ANOVA [F(3, 30) = 17.86, $p = 7.70 \times 10^{-7}$] shows that the means are significantly different at the 0.05 level. Post-hoc analysis with the Tukey range test reveals that the significant differences only involve the 5% printed

samples (panels 13 and 15, Figure 5.19b) despite the fact that the 1% M400 printed sample (Panel 14) contained double the amount of printed plies.

Table 5.4: SBS Results

Panel #	**Apparent interlaminar shear strength (MPa)**			
	Mean	n	**SD**	**95% CI**
12 (unprinted)	105	7	2.26	2.09
13 (5% M401)	115	9	3.28	2.52
14 (1% M400)	106	8	4.00	3.34
15 (5% M400)	116	10	3.44	2.46

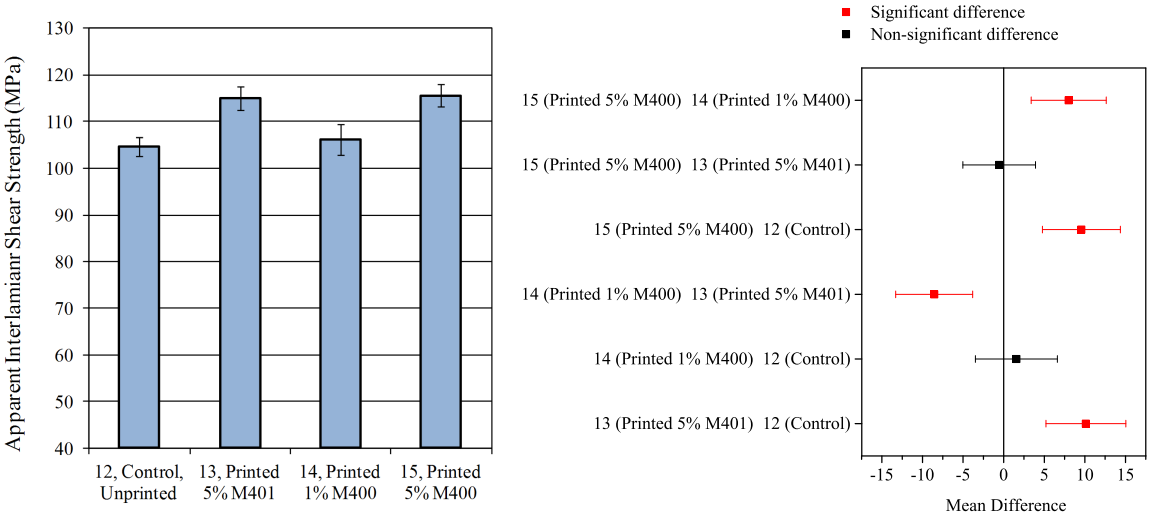

(a) Column chart of mean values. Error bars are 95% CI

(b) Means comparisons using Tukey range test

Figure 5.19: Short Beam Shear results for printed and unprinted samples

These results compare favourably with those from the DCB tests. Printed M400 and M401 at the 5% level clearly has a beneficial effect on interlaminar properties. Printing at the 1% concentration clearly deposits an amount of material that is too small to have any effect on the properties.

5.3.3.1 SBS after a thermal healing cycle

After testing the SBS specimens were subjected to a thermal healing cycle detailed in Section 5.2.6 on page 239 and then retested. The results are shown in Table 5.5 and represented graphically in Figure 5.20a. Figure 5.20b shows the average percentage reduction in apparent interlaminar shear strength after being tested and healed on a specimen-by-specimen basis.

Table 5.5: SBS Results for Healed Specimens

Panel #	Apparent interlaminar shear strength (MPa)			
	Mean	n	SD	95% CI
12 (unprinted)	75.8	7	9.20	8.81
13 (5% M401)	98.3	8	5.51	4.60
14 (1% M400)	82.0	8	8.25	6.90
15 (5% M400)	101	9	3.58	2.75

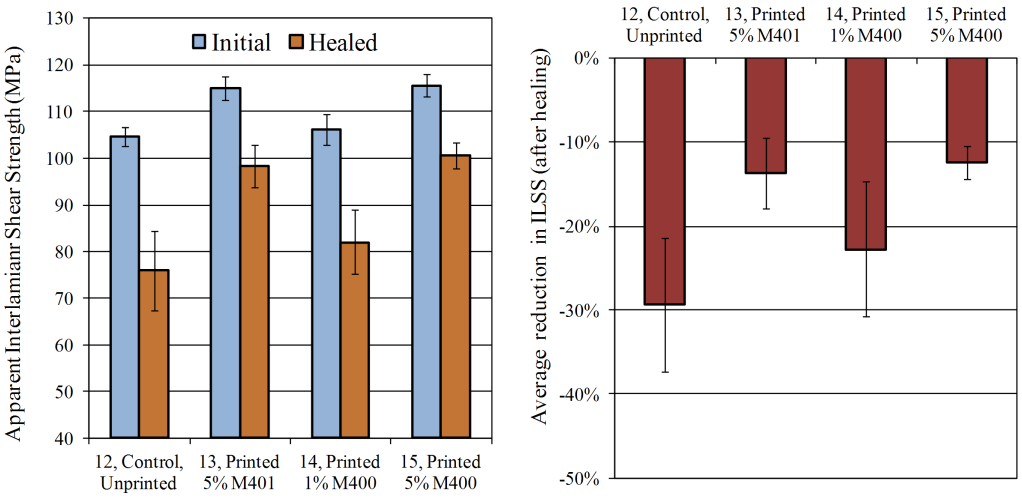

(a) Column chart of mean aILSS values.

(b) Mean average reduction in aILSS values as a percentage of the original

Figure 5.20: Short Beam Shear results for virgin and healed samples. Error bars are 95% CI.

The results show that the aILSS of the unprinted sample reduces by approximately 30% after the first round of testing and healing. This reduction should include any regain in properties by any latent cure present in the epoxy matrix. Using this sample as the control prevents this factor from affecting the results.

The aILSS of the printed specimens also reduced, but to a lesser extent than the unprinted control. This difference can be attributed to thermal rebonding at the interface by the additive. With reference to Figure 5.20b it is clear that the aILSS results for Panel 13 and Panel 15 show a significantly smaller reduction compared to the unprinted control. These panels contained a higher percentage of healing agent (See Table 5.1 on page 241 for layup and print details).

Panel 14, however, is a much more borderline case and as the scatter is quite large it is difficult to state confidently that the difference is significant compared to the control. A 2-sample unpaired t-test [t(13) = 1.70, p = 0.056] shows that under the conditions tested the difference is not significant at the 0.05 level as p is $>$ 0.05. It must be noted, however, that Sample 14 is very close to being significantly different from the control despite the 1% concentration of the material printed.

For all specimens the level of healing is not straight forward to quantify in this case. Many authors generate a 'healing efficiency' percentage for their system but the normal approaches are not suitable for use with this test. The most common methods for calculating healing efficiency are based upon specimens tested to destruction such as compact tension or width tapered double cantilever beam sample and is expressed as a percentage of the healed properties compared to the virgin material (Equation 5.11) as proposed by Wool and Connor in 1981 [18].

$$\text{Healing efficiency } \% = \frac{\text{Healed Property}}{\text{Virgin Property}} \times 100 \tag{5.11}$$

In this case this equation is not appropriate because the specimens were not tested to destruction (the system cannot be expected to heal macroscopic fibre fracture). Consequently this equation would lead to a misleadingly high value of healing efficiency. A more appropriate test of healing efficiency would be based upon the difference in properties rather than the absolute values.

Such a measure of healing efficiency for the short beam shear test is proposed as follows:

- Take the percentage difference in aILSS properties for the **unprinted control** between the virgin (τ_{Mv}) and healed (τ_{Mh}) specimens as a baseline (q) that is used as a constant for all the samples

$$q = \frac{\left(\tau_{\text{Mv(control)}} - \tau_{\text{Mh(control)}}\right)}{\tau_{\text{Mv(control)}}} = 0.2750 \tag{5.12}$$

- For each sample remove the baseline % from the average aILSS of the virgin **printed** samples to obtain an approximation (τ_{Ma}) of the expected properties without the effect of the healing interlayer

$$\tau_{\text{Ma}} = \tau_{\text{Mv}} - (q\tau_{\text{Mv}}) \tag{5.13}$$

- Calculate the difference between the measured properties of the **printed-healed** specimens and the approximate unmodified properties previously calculated $\tau_{\text{Mh}} - \tau_{\text{Ma}}$

- Express this difference as a percentage of the difference between the measured virgin properties and the measured healed properties

$$\text{Healing Efficiency} = \frac{\tau_{\text{Mh}} - \tau_{\text{Ma}}}{\tau_{\text{Mv}} - \tau_{\text{Mh}}} \times 100 \tag{5.14}$$

This gives an estimated % recovery in properties or healing efficiency that is not effected by the role of latent cure.

Using Equations 5.12 to 5.14, the healing efficiency for the printed samples 13, 14 and 15 is calculated to be the following:

- **Panel 13, (5% M401):** 47.4%
- **Panel 14, (1% M400)**: 17.2%
- **Panel 15, (5% M400):** 52.8%

The control sample returns 0% healing efficiency as this was used as the baseline level of 100% damage.

5.4 Summary and Conclusions

The main aim of this chapter was to investigate the influence of inkjet printed monomer interlayers within carbon-epoxy composites that were polymerised *in situ* during the curing.

Some of the printed laminates were analysed using DMA; a thin laminate was printed with 1% M401 and compared to an unprinted control. Despite the sensitivity of the DMA to small components there were no detected transitions from the polymer; it is likely that the concentration (and therefore the coverage) of M401 was too low to detect. This is not surprising given the small amount of material deposited and the fact that this concentration of monomer did not lead to any differences in any of the other material properties measured.

Laminates for DMA made from prepreg printed with higher concentrations of monomer were not done. The reason for this is that after the first results (with the 1% concentration) the technique was not deemed to be sensitive enough and tests such as the DCB and SBS were given higher priority for the limited material available. Since the higher concentrations of monomer did have a significant effect on the DCB and SBS results there is a possibility that the polymers would be detectable using DMA. The additional DMA tests would be a good starting point for further work in this area.

Many double cantilever beam tests were performed including four control panels that were produced on different days. An ANOVA analysis showed that the batch to batch variation was not unreasonable which means that it is valid to compare all the results.

The mean initiation (NL point) mode I critical energy release rate (G_{IC}) was found to be 329 $\mathrm{J\,m^{-2}} \pm 6.89\ \mathrm{J\,m^{-2}}$ and for propagation it was found to be 331 $\mathrm{J\,m^{-2}} \pm 5.15\ \mathrm{J\,m^{-2}}$. The addition of 1% M401 to the mid plane of the DCB specimen produced no statistically significant difference to the G_{IC} values; presumably the concentration of this monomer was too low.

The addition of patterned layers by inkjet printing with 5% monomer concentrations produced statistically significant effects at the 0.05 significance level in the case of both M400 and M401. The printed M401 at 5% gave rise to an increase in

G_{IC} initiation (NL point) to 354 $J\,m^{-2} \pm 27.1\ J\,m^{-2}$ (8% increase) and propagation to 377 $J\,m^{-2} \pm 25.6\ J\,m^{-2}$ (14% increase).

The printed M400 at 5% gave rise to a further increase in G_{IC} initiation (NL point) to 360 $J\,m^{-2} \pm 22.5\ J\,m^{-2}$ and propagation to 420 $J\,m^{-2} \pm 29.0\ J\,m^{-2}$ representing a 9% and 27% increase respectively.

After thermal treatment of the tested DCB samples, healing was not observed. It is possible that the level of additive is insufficient to produce significant rebonding between the plies.

The results from the short beam shear testing showed a similar trend. The apparent interlaminar fracture toughness was shown to be 105 MPa ± 2.09 MPa for the unprinted prepreg. No significant change in this property was observed for a sample of specimens containing 8 printed plies with 1% M401 but statistically significant increases were observed for samples with 5% M401 (115 MPa ± 2.52 MPa) and 5% M400 (116 MPa ± 2.46 MPa) printed within the middle four layers. These increases represent a 10% and an 11% increase respectively.

Thermal treatment of the SBS specimens did lead to the observation of what is taken to be self-healing in all 3 printed samples. The printed specimens showed a significantly smaller decrease in properties on retesting compared to the unprinted controls. A method of quantifying the healing efficiency from the SBS test was proposed which which gave results of 47.4%, 17.2% and 52.8% for 5% M401, 1% M400 and 5% M400 respectively although the difference for the 1% sample did not pass the statistical significance test. The healing efficiency calculation could be improved by also including a group of samples that are tested twice without the thermal cycle (with and without printing) in order to better quantify the baseline damage introduced by the initial testing.

The approximate volume fraction of printed material was calculated in Chapter 4, Section 4.3.2 on page 178; there it can be seen that the SBS specimens printed with the most material contained approximately six times as much additive as the DCB specimens. The DCB specimens, however, contained material printed in the region where the delamination was created and is therefore a more efficient use of processing time and material. It is possible however, for the DCB specimens that the amount of additive was simply too low for any self-healing to be observed.

In conclusion, such an increase in interlaminar properties is surprising with such a small addition of material but it is not extraordinary, as patterning by inkjet printing has recently been shown to be capable of producing such changes[19]. The self-healing behaviour stemming from the inkjet printed interlaminar patterns that were observed in the short beam shear samples have not been reported before and is, therefore, highly novel.

5.5 References

(1) J. M. Whitney, Experimental Characterization of Delamination Fracture, in, *Interlaminar Response of Composite Materials*, ed. N. Pagano, Elsevier Science, Amsterdam, NL, 2012.
(Cit. on pp. 223, 225.).

(2) British Standards International, Fibre-reinforced plastic composites - Determination of apparent interlaminar shear strength by short-beam method. In *BS EN ISO 14130*, 1998.
(Cit. on pp. 224, 236.).

(3) P. Mallick, *Fiber-Reinforced Composites: Materials, Manufacturing, and Design, Second Edition*, Taylor & Francis, New York, NY, USA, 1993.
(Cit. on p. 224.).

(4) A. A. Griffith, "The Phenomena of Rupture and Flow in Solids", *Philos. Trans. R. Soc., A*, 1921, **221**, 163–198.
(Cit. on p. 225.).

(5) G. R. Irwin, Fracturing of Metals, in, *Fracture Dynamics*, ed. F. Jonassen, W. P. Roop, and G. R. Bayless, ASM, Cleveland, OH, USA, 1948.
(Cit. on p. 225.).

(6) E. Orowan, "Fracture and strength of solids", *Rep. Prog. Phys.*, 1949, **12**, 185.
(Cit. on p. 225.).

(7) G. R. Irwin, *Onset of fast crack propagation in high strength steeel and aluminium alloys.* NRL Report 4763, Naval Research Laboratory, Washington D.C., USA, 1956.
(Cit. on p. 225.).

(8) F. Erdogan, "Fracture mechanics", *Int. J. Solids Struct.*, 2000, **37**, 171 –183.
(Cit. on p. 225.).

(9) J. Hodgkinson, *Mechanical Testing of Advanced Fibre Composites*, Woodhead Publishing, Cambridge, UK, 2000.
(Cit. on pp. 226, 227, 230.).

(10) W. Ninienda, A. S. D. Wang, Y. Zhong, and E. S. Reddy, A Criterion for Mixed-Mode Matrix Cracking in Graphite-Epoxy Composites, in, *Composite Materials: Testing and Design*, ed. S. P. Garbo, ASTM International, Ann Arbor, MI, USA, 9th edn., 1990.
(Cit. on p. 227.).

(11) British Standards International, Fibre-reinforced plastic composites - determination of mode I interlaminar fracture toughness, HIC for unidirectionally reinforced materials, in *BS ISO 15024*, 2001.
(Cit. on pp. 227, 229, 231, 236.).

(12) ASTM International, Standard Test Method for Mode I Interlaminar Fracture Toughness of Unidirectional Fiber-Reinforced Polymer Matrix Composites, in *ASTM D5528 - 13*, 2013.
(Cit. on p. 227.).

(13) S. Hashemi, A. Kinloch, and J. Williams, "Corrections needed in double-cantilever beam tests for assessing the interlaminar failure of fibre-composites", English, *Journal of Materials Science Letters*, 1989, **8**, 125–129.
(Cit. on p. 229.).

(14) J. G. Williams, "The fracture mechanics of delamination tests", *J. Strain Anal. Eng. Des.*, 1989, **24**, 207–214.
(Cit. on pp. 230, 231.).

(15) H. J. Seltman, *Experimental Design and Analysis*, Published Online, 2013, `http://www.stat.cmu.edu/\~hseltman/309/Book/`.
(Cit. on p. 244.).

(16) S. Dean and B. Illowsky, *F Distribution and ANOVA: The F Distribution and the F Ratio*, Available Online (Accessed 23rd February 2014), `http://www.saylor.org/site/wp-content/uploads/2011/06/MA121-6.3.2-s3.pdf`.
(Cit. on p. 244.).

(17) J. Gosling, *Introductory Statistics*, Pascal Press, Glebe, NSW, AU, 1995.
(Cit. on p. 244.).

(18) R. P. Wool and K. M. O'Connor, "A theory crack healing in polymers", *Journal of Applied Physics*, 1981, **52**, 5953–5963.
(Cit. on p. 261.).

(19) Y. Zhang, J. Stringer, R. Grainger, P. J. Smith, and A. Hodzic, "Improvements in carbon fibre reinforced composites by inkjet printing of thermoplastic polymer patterns", *Phys. Status. Solidi RRL*, 2014, 56–60.
(Cit. on p. 265.).

Chapter 6

Conclusions and Future Work

6.1 Conclusions

Over the last few decades polymer composite materials have become increasingly important across multiple industries. The driving force behind this mass adoption can be attributed in part to the rising costs of fuel which drives the development of light weight composite replacements. In the construction industry there is a developing trend for prefabricated sections that can be transported to the site and assembled; composites are ideal for this. In the case of aerospace, automotive and mass transport a reduction in weight for equivalent performance leads to a direct fuel saving which has clear financial and environmental benefits over the lifetime of the vehicle. In most cases a lifetime of at least 40 years is expected and the structural components need to be capable of performing for this time period.

Carbon-fibre composite materials are experiencing widespread use in the primary airframes of both civilian and military aircraft. However, there are concerns over the development of barely visible internal damage and delaminations within these composites that may occur over their lifetime and are difficult to detect using conventional non-destructive testing techniques [1]. Delaminations are the most common mode of failure in carbon-fibre composites. Interfacial cracks, which are initially small and negligible, can grow until the mechanical performance of a part is severely impaired [2, 3]. These problems are currently addressed by the use of toughened resins and large safety factors [4, 5] which lead to the use of additional material and therefore more weight than would be necessary for a system that was not sus-

ceptible to this kind of damage. The work presented in this thesis aims to address this problem by providing a mechanism in which these micro delaminations can be repaired using a thermal treatment.

The proposed solution involves inkjet printing of self-healing or toughening polymers between layers on parts (manufactured from prepreg) that are the most susceptible to delamination damage. The main advantage to using inkjet printing is that small concentrations of materials can be applied accurately and consistently using high levels of automation to the areas that need it. The application of small amounts of material to strategically designed locations has the potential to improve properties and safety with a negligible weight gain. The patterns and inks can also be varied to suit the requirements of the part which gives design engineers a good deal of flexibility and control.

The organic synthesis of monomers that, upon polymerisation, form thermally reversible polymer networks was undertaken in order to provide the specialised material for incorporation into composites. For the purpose of this work two of these monomers were selected for printing but there is wide scope for the use of other materials.

Chapter 1 gave an introduction to polymer composite materials and the current approaches to damage detection and damage repair currently used in composite materials. The recent literature related to self-healing of composites was then reviewed in order to set this work in context with other approaches.

Chapter 2 described the development of the organic synthesis of Thiele's Acid which is the common precursor for all the monomer systems tested. After a lengthy period of development Thiele's Acid was synthesised with high purity and an excellent yield (64%). The high yield produced plenty of material for the subsequent synthetic steps. The identity of the material was confirmed by use of NMR and the good match of the melting point to the literature. In addition a derivatization approach was employed in which the methyl ester of Thiele's acid was produced and confirmed with NMR and melting point.

Chapter 3 detailed a monomer selection process in which several candidate monomers were chosen with potential for self-healing initially as a bulk additive to epoxy matrices. The development of the synthetic procedure for production of

the selected monomers was then given. The synthesis of the monomers proved extremely difficult to optimise; large improvements were made to the synthesis but the yields were limited to a maximum of approximately 18% at the gram scale. The identity of the produced monomers was demonstrated using proton and carbon NMR which were clearly assigned.

Chapter 4 reported two pieces of work that were undertaken in parallel:

The first piece of work reported in Chapter 4 was the development of monomer inks that are suitable for inkjet printing; this was done by comparison of monomer modelled solubility parameters with reference solvent values. This prevented the loss of time and material by conducting physical solubility tests. The list of suitable solvents was refined further by calculating the inverse of the Ohnesorge number (Z) which can give an indication for the printability of the inks. A suitable solvent (Ethyl Acetate) was selected which was used to successfully print monomer concentrations of up to 5% onto both prepreg and glass slide substrates. The printed patterns were shown to successfully cure upon thermal treatment without significant spreading.

The second piece of work reported in Chapter 4 was the study of the monomer polymerisations. This was studied using DSC, DMA, and rheometry. Monomer 401 was shown by DMA in a material pocket to cure from about 71 °C and rheometry showed that although there was still some cure present after a 12 hour test the sharpest rise was completed after 3 hours at 120 °C. Monomer 400 was shown to cure at higher temperature; there was some DMA evidence showing some cure starting at 90 °C but mostly proceeding from 125 °C upwards. The DSC also showed a curing exotherm for Monomer 400 with an onset, peak and endset of 111 °C, 133 °C and 153 °C respectively. Cured Polymer 401 and Polymer 400 were shown to have glass transitions of 54 °C to 78°C and 123 °C to 165 °C depending on the DMA transition and frequency applied. The dynamic storage moduli (E') for M401 and M400 (at room temperature and 1Hz) was shown to be *c.a.* 3 GPa and *c.a.* 2.5 GPa respectively which is approximately similar to that shown for epoxy resin systems[6].

Chapter 5 presented the properties of carbon-fibre composites with printed monomer patterns at their interface. Printing 5% solutions of M400 and M401 on a single ply at the mid-plane of double cantilever beam specimens was shown to increase the initiation (by NL Point) of the interlaminar fracture toughness by 8% and 9%

respectively. The interlaminar fracture toughness with regards to median crack propagation was increased further by 14% and 27% respectively. An application of thermal treatment (under pressure) did not show any evidence of re-bonding the fracture surfaces.

Printing of 5% M400 and 5% M400 on the four middle plies of 8-ply samples produced statistically significant increases in apparent interlaminar shear strength (10% and 11% respectively). After a thermal treatment specimens were retested and it was found that the printed specimens had significantly smaller decreases in properties. The healing efficiency based upon the percentage regain in properties was calculated to be 48% and 53% for 5% M401 and 5% M400 .

In conclusion, monomers have been synthesised from base chemicals and successfully integrated into aerospace grade composites using the novel technique of inkjet printing. The printing has been shown to have a positive effect on both interlaminar fracture toughness and apparent interlaminar shear strength. In addition there is evidence of self-healing behaviour after retesting of thermally treated short beam shear specimens compared to the control. This is an excellent result which warrants further development. In addition several avenues for future work were highlighted over the course of this research which will be introduced in the next and final section.

6.2 Future Work

1. The tests chosen to demonstrate the self-healing behaviour of the printed patterns are fairly extreme and represent a case of damage far greater than that at which they would be employed to combat. Now that the concept has been proven it would be ideal to show if the healing behaviour can be demonstrated as a lifetime extension in fatigue testing (with periodic thermal treatments). It is highly probable that the self-healing mechanism would be even more effective to slow down the fatigue damage build-up by re-bonding micro delaminations.

2. More material could be used in order to investigate the extent of the property increases or self-healing that can be achieved. More material could be included by printing on more plies, using higher ink concentrations or by making multiple printing passes.

3. The printed pattern could be varied easily by modifying the printing program. It is likely that the composite properties could be enhanced further by optimising the printing pattern.

4. Almost any polymer system could be feasibly printed onto the prepreg and therefore included in the composite. The only other materials that are known to have been printed onto prepreg in this way are poly(ethylene glycol) and poly(methyl-methacrylate) [7]. The only requirement would be that a printable ink could be formulated; it is not necessary for polymers or monomers to be soluble, if a dispersion of micro-particles can be obtained it can also be possible to print. In addition multiple inks can be printed which allows the possibility of reactive inkjet printing [8].

5. Taking a different approach the thermally reversible Diels-Alder bonds could be integrated into an epoxy curing agent or epoxy resin itself which would allow a proportion of crosslinks to disconnect and reform. The performance, however, is likely to be influenced negatively by this approach.

6.3 References

(1) P. Kumar and B. Rai, "Delaminations of barely visible impact damage in CFRP laminates", *Compos. Struct.*, 1993, 313–318.
(Cit. on p. 269.).

(2) A. C. Garg, "Delamination - a damage mode in composite structures", *Eng. Fract. Mech.*, 1988, 557–584.
(Cit. on p. 269.).

(3) A. Arguelles, J. Viña, A. F. Canteli and J. Bonhomme, "Fatigue delamination, initiation, and growth, under mode I and II of fracture in a carbon-fiber epoxy composite", *Polym. Composites*, 2009, 700–706.
(Cit. on p. 269.).

(4) NASA Preferred Reliability Practices, *GD-ED-2205, Design and manufacturing guidence for aerospace composites*, Available online (accessed 22nd March 2014), `http://oce.jpl.nasa.gov/practices/2205.pdf`.
(Cit. on p. 269.).

(5) I. Kroo and J. Alonso, *Aircraft Design: Synthesis and Analysis*, Available Online (accessed 22nd March 2014), `http://adg.stanford.edu/aa241/`.
(Cit. on p. 269.).

(6) M. Naebe, J. Wang, A. Amini, H. Khayyam, N. Hameed, L. H. Li, Y. Chen and B. Fox, "Mechanical Property and Structure of Covalent Functionalised Graphene/Epoxy Nanocomposites", *Sci. Rep.*, 2014, **4**, 4375.
(Cit. on p. 271.).

(7) Y. Zhang, J. Stringer, R. Grainger, P. J. Smith and A. Hodzic, "Improvements in carbon fibre reinforced composites by inkjet printing of thermoplastic polymer patterns", *Phys. Status. Solidi RRL*, 2014, 56–60.
(Cit. on p. 273.).

(8) P. J. Smith and A. Morrin, "Reactive inkjet printing", *J. Mater. Chem.*, 2012, **22**, 10965–10970.
(Cit. on p. 273.).

Appendix A

NMR Spectra

Appendix A.1: Proton NMR of Thiele's Acid

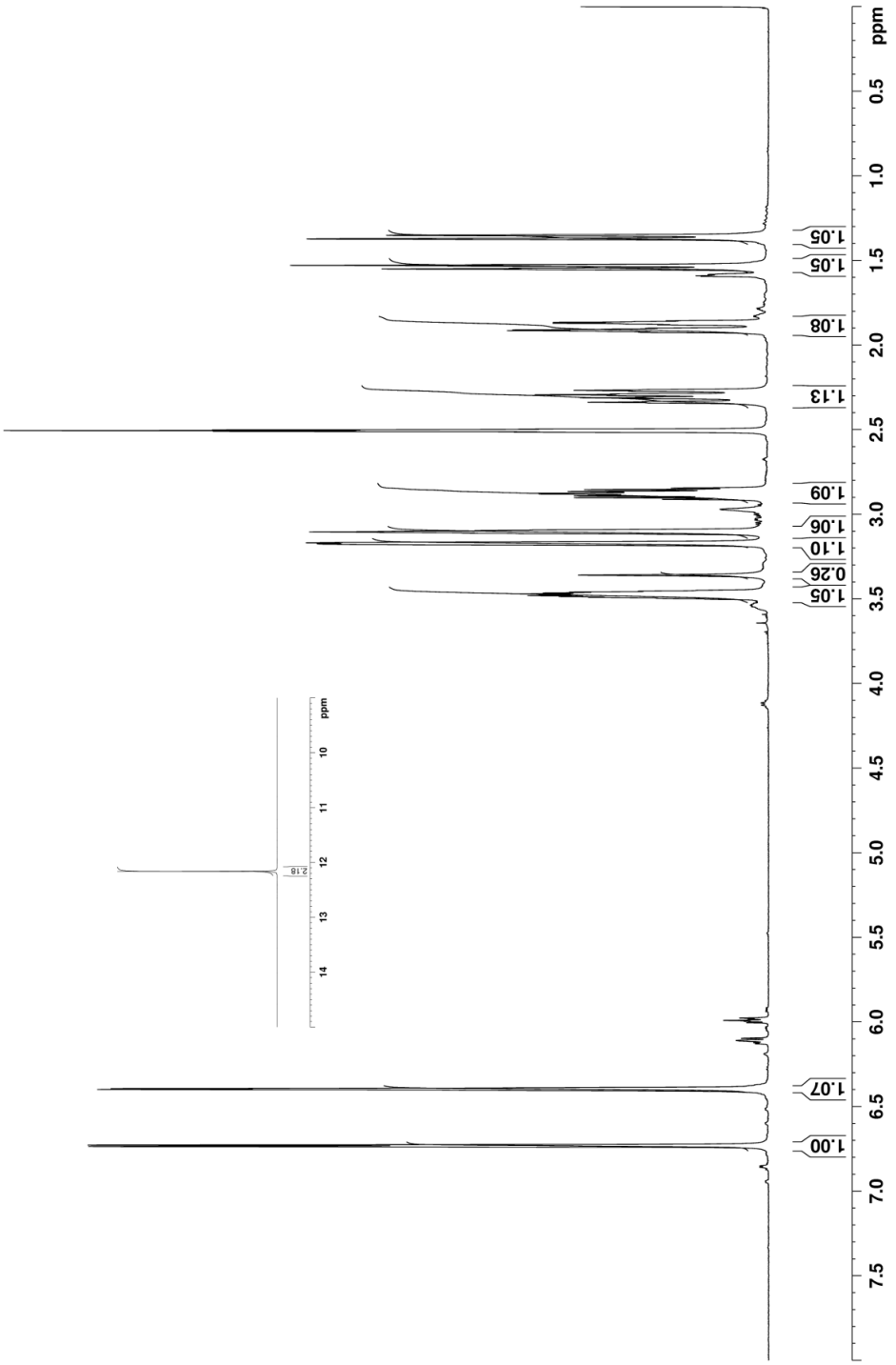

Appendix A.2: Carbon 13 NMR Spectrum of Thiele's Acid

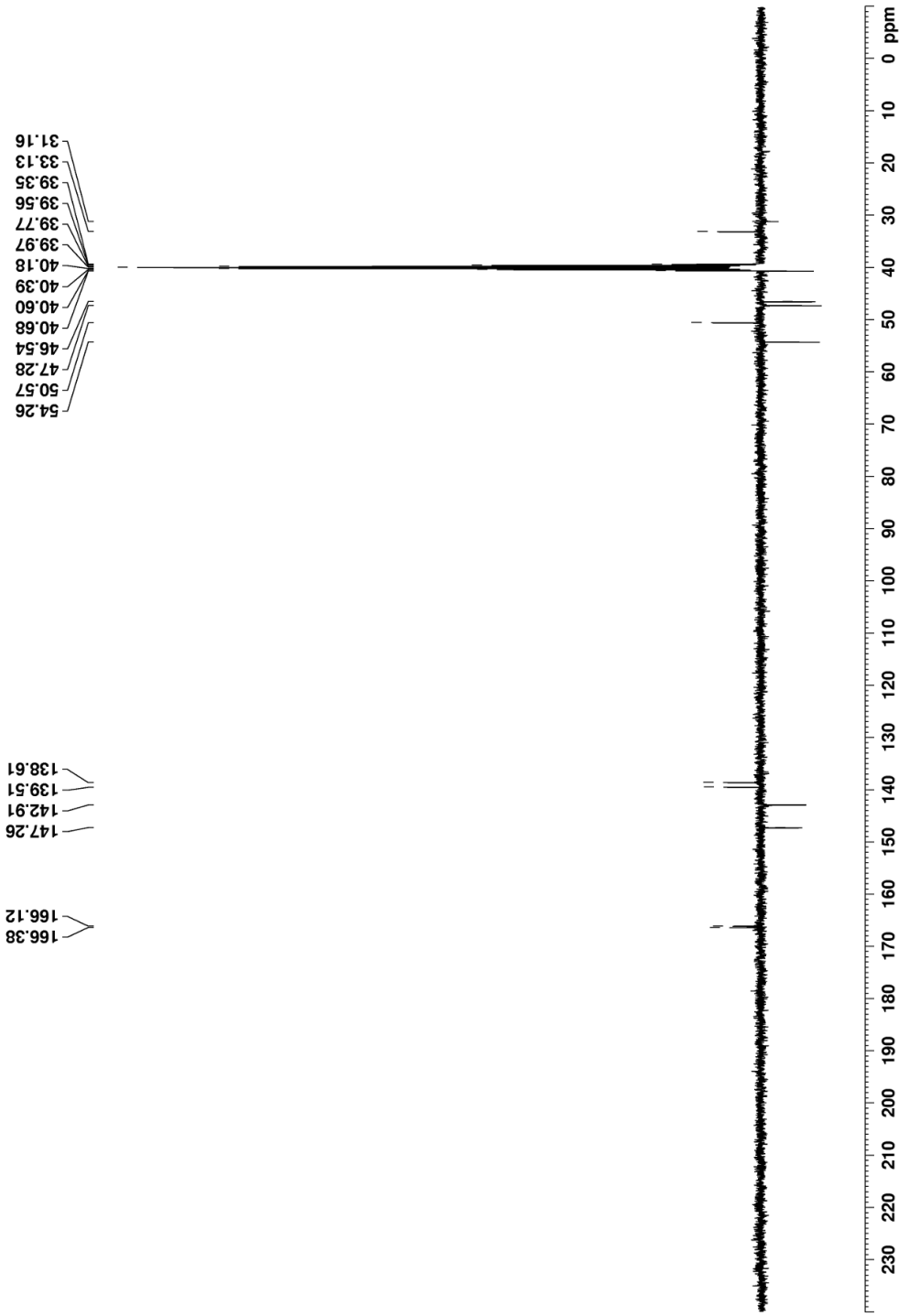

Appendix A.3: Proton NMR of Thiele's Ester (Produced using the acid catalysed direct route)

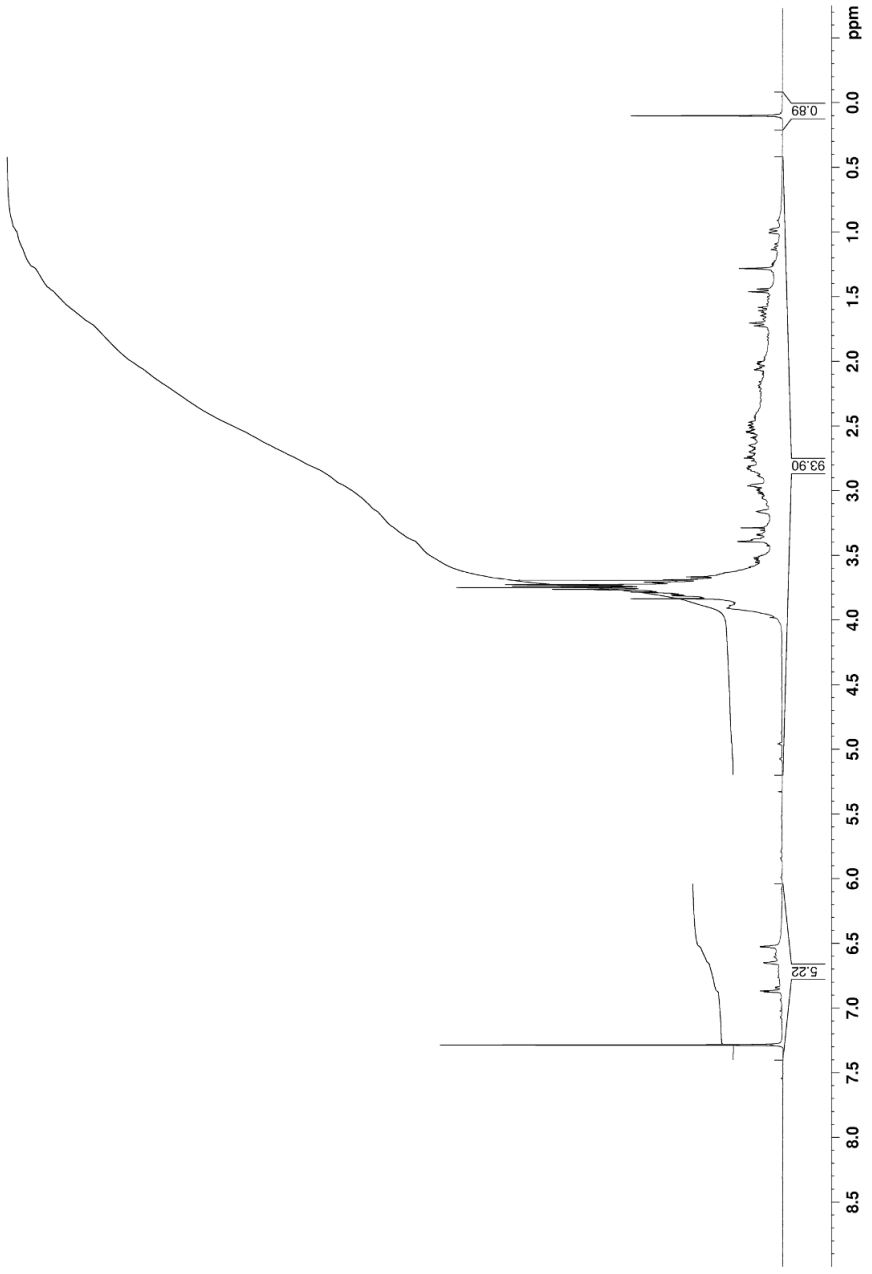

Appendix A.4: Proton NMR of Crude Thiele's Acid

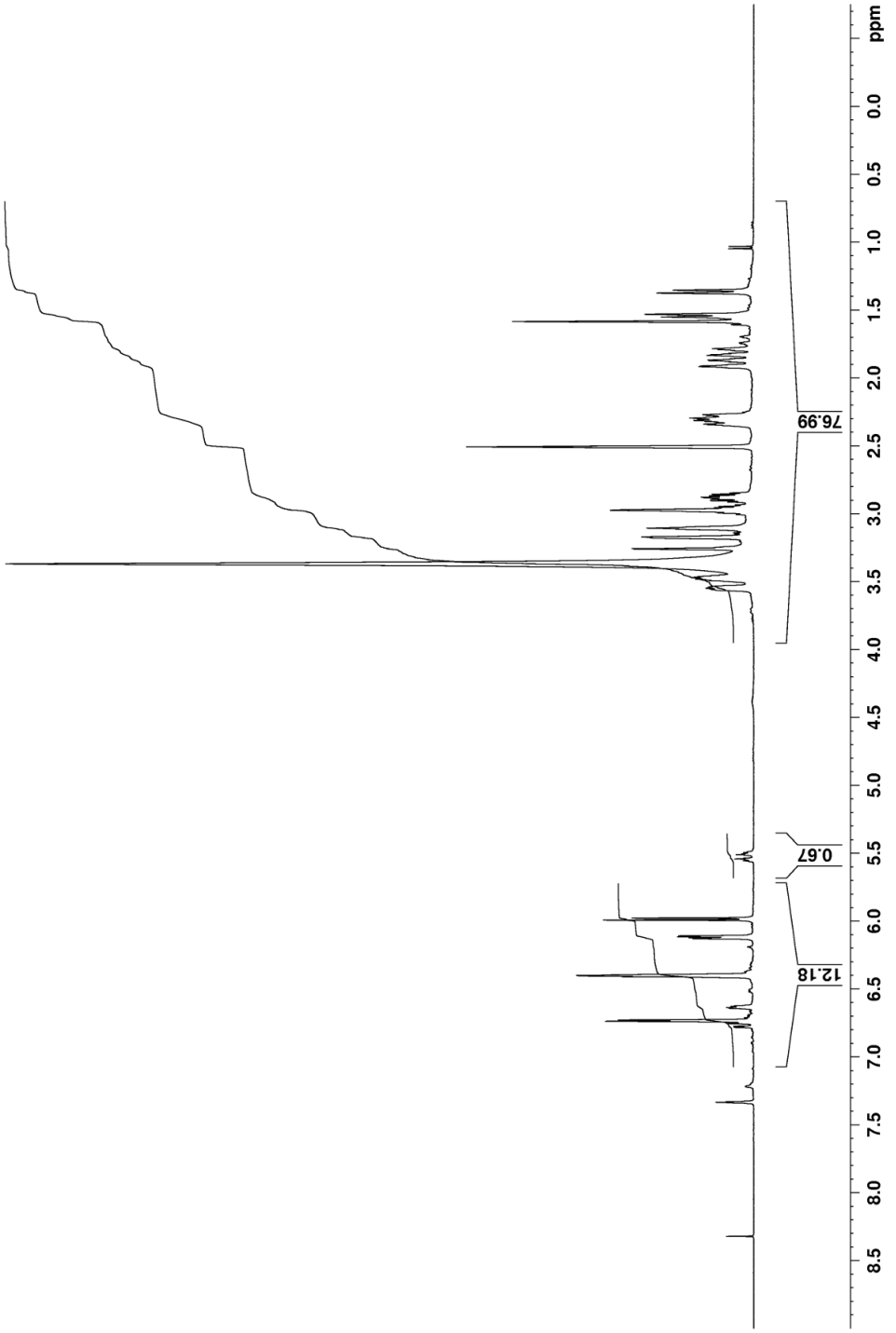

Appendix A.5: Proton NMR of Monomer 15-0-0

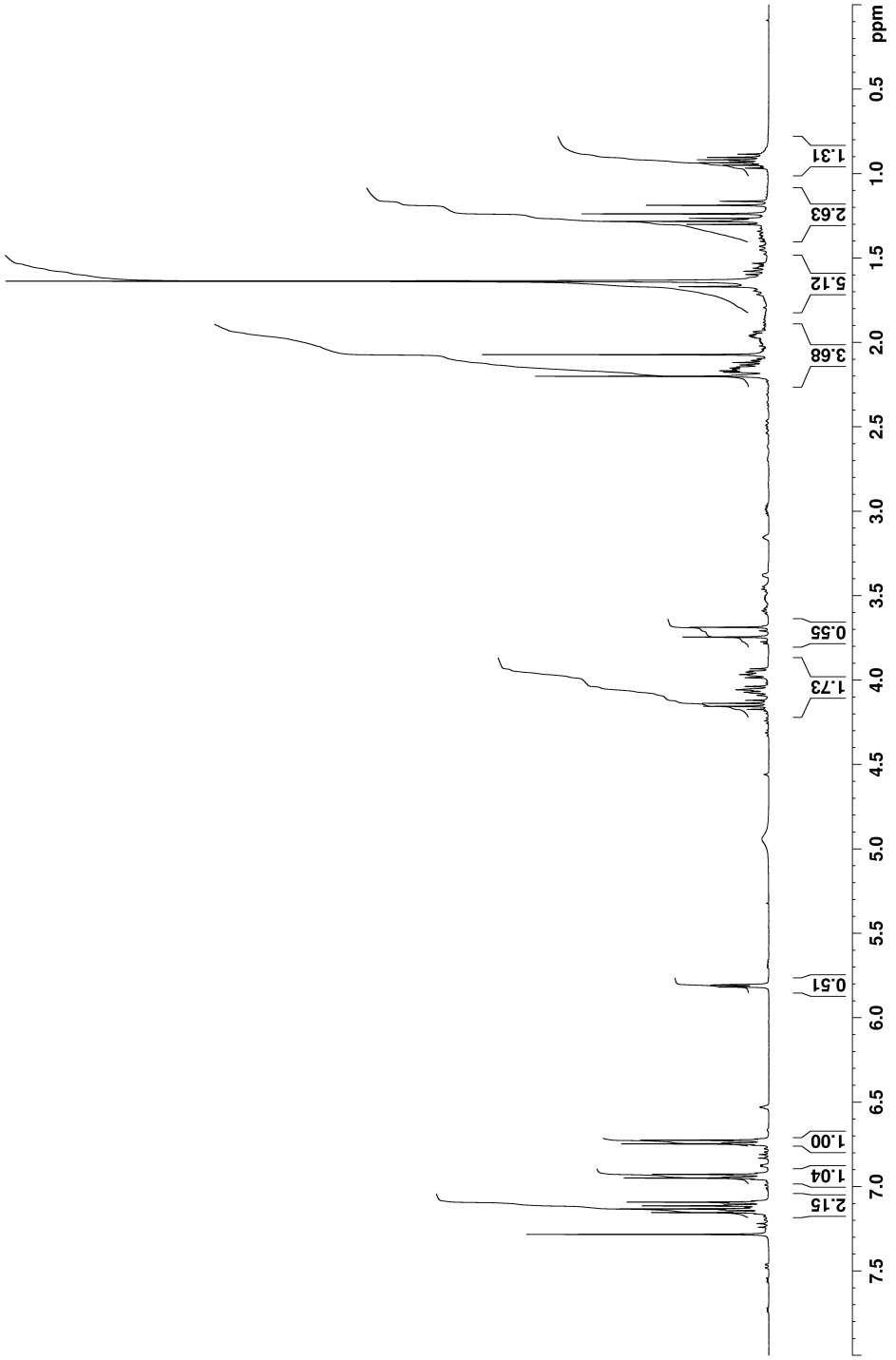

Appendix A.6: Proton NMR of Monomer 400

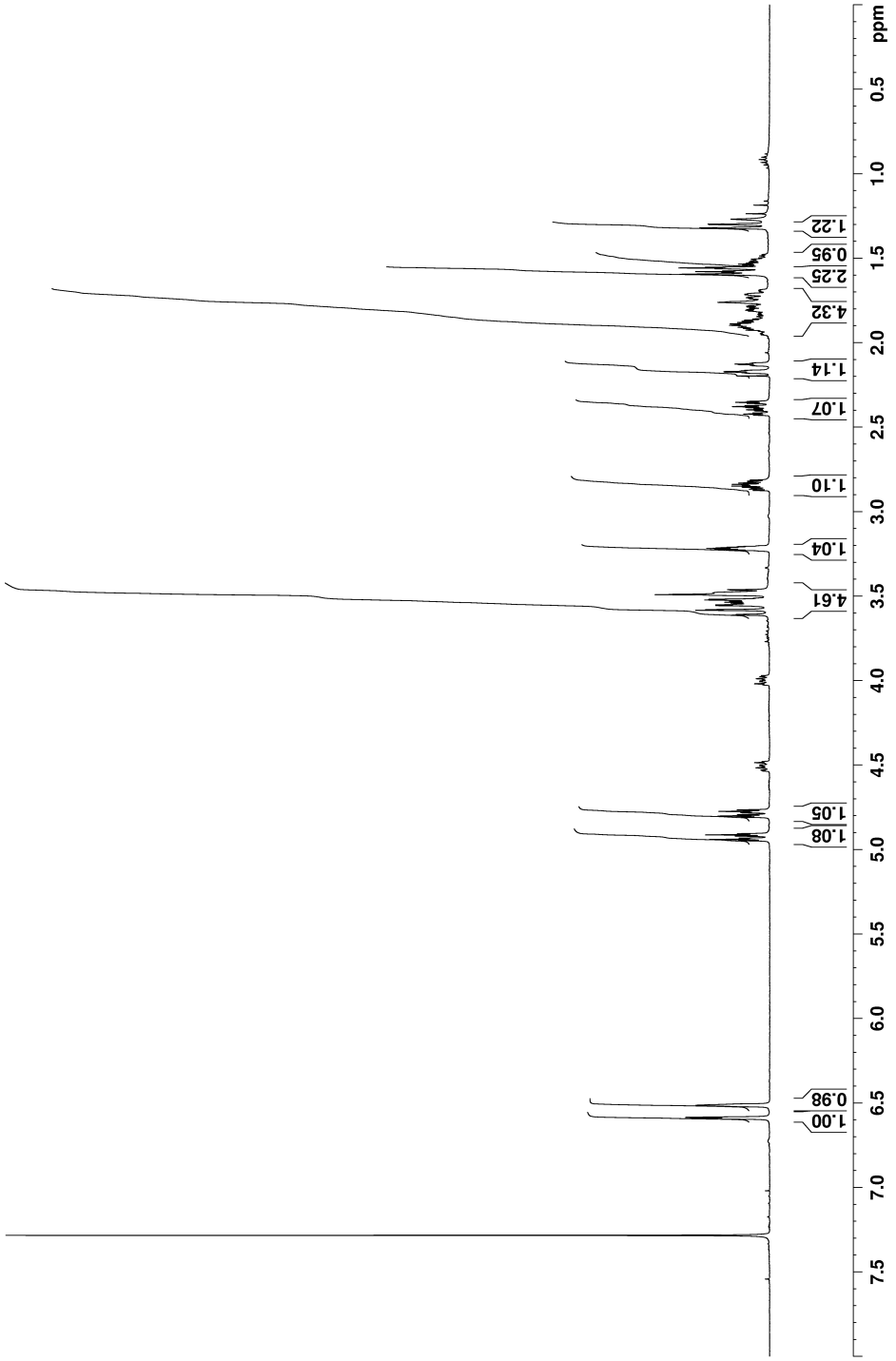

Appendix A.7: Carbon 13 NMR of Monomer 400

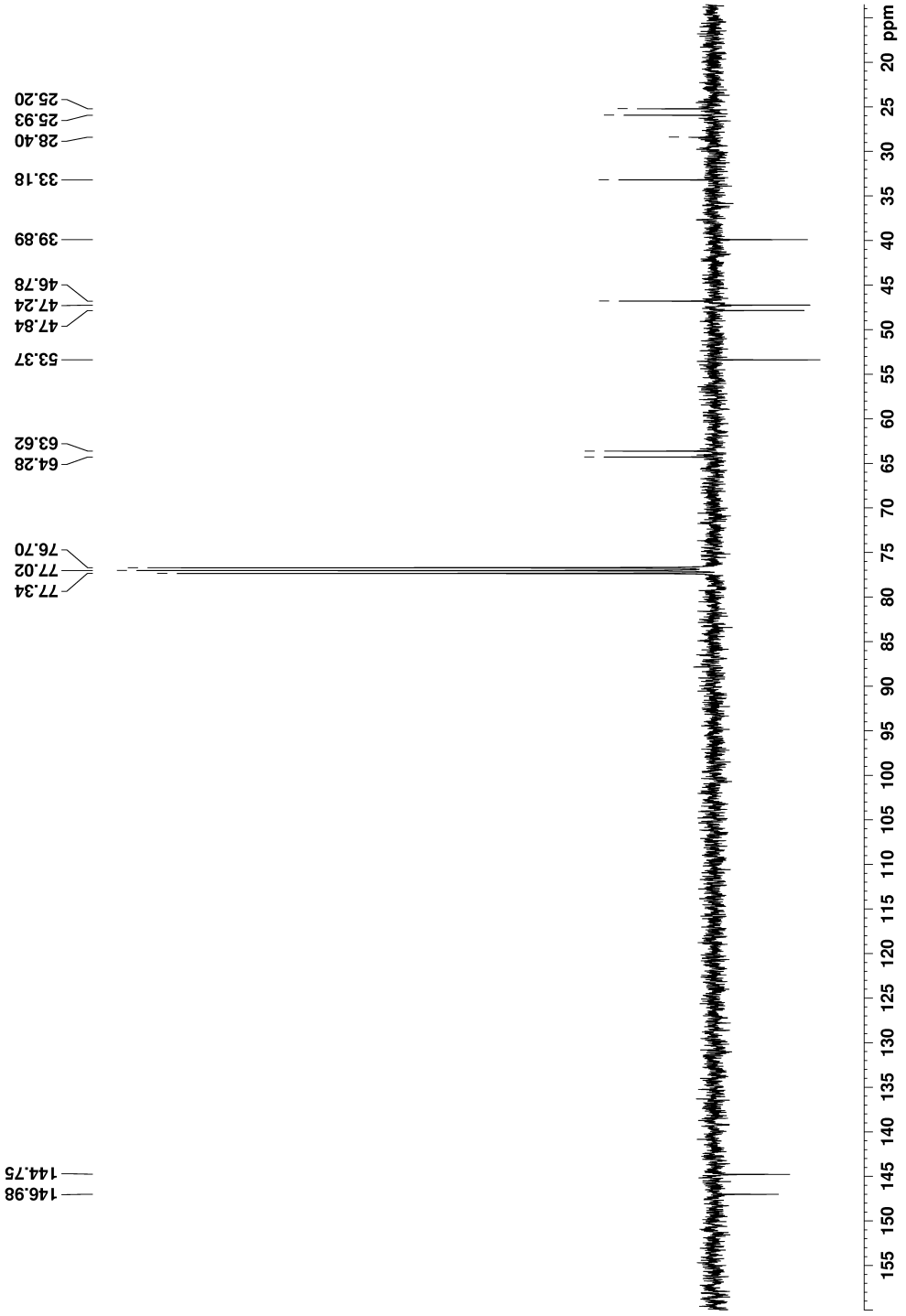

Appendix A.8: Proton NMR of Monomer 401

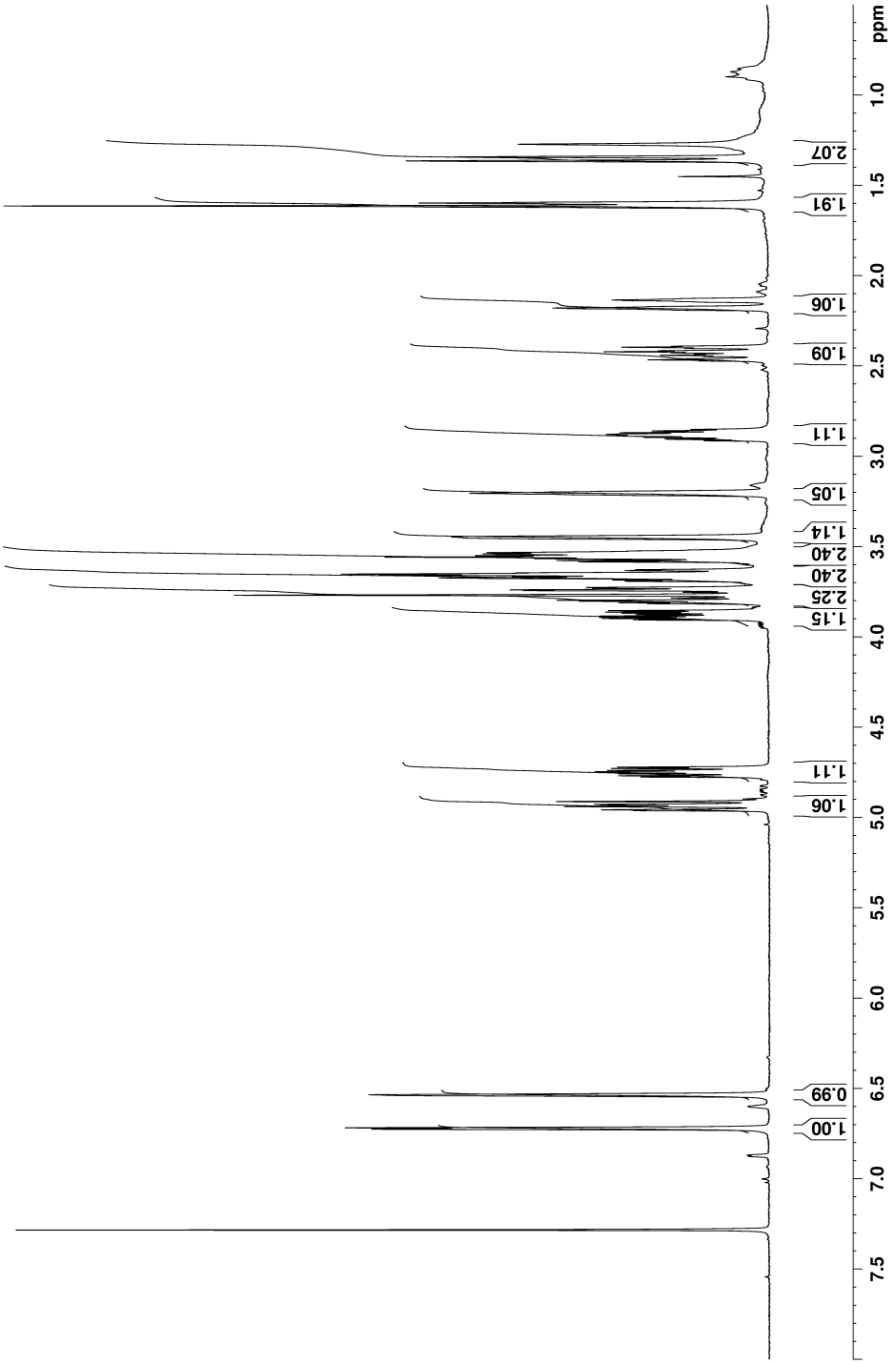

Appendix A.9: Carbon 13 NMR of Monomer 401

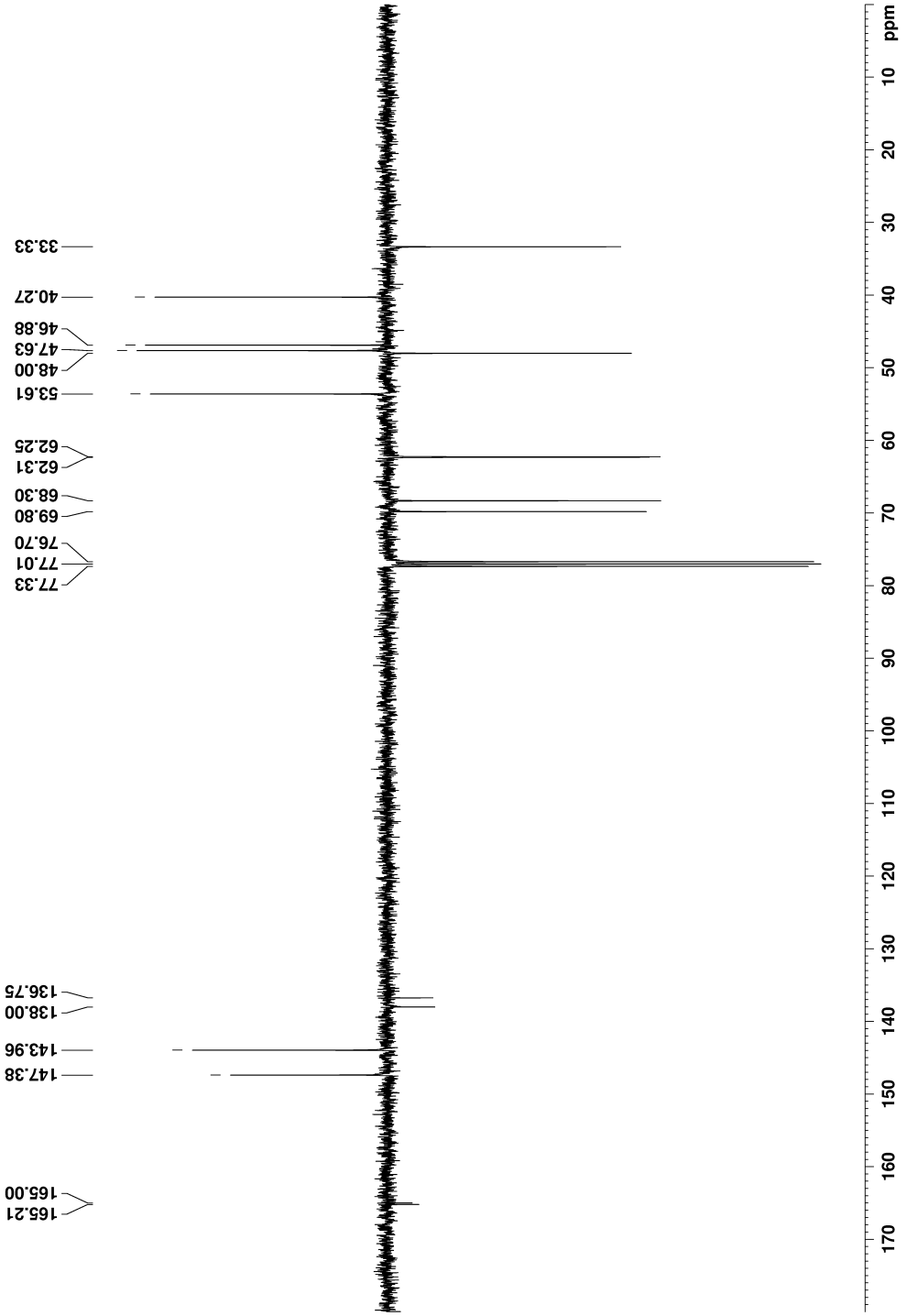

Appendix A.10: Proton NMR of Compound B3 (Monomer 801)

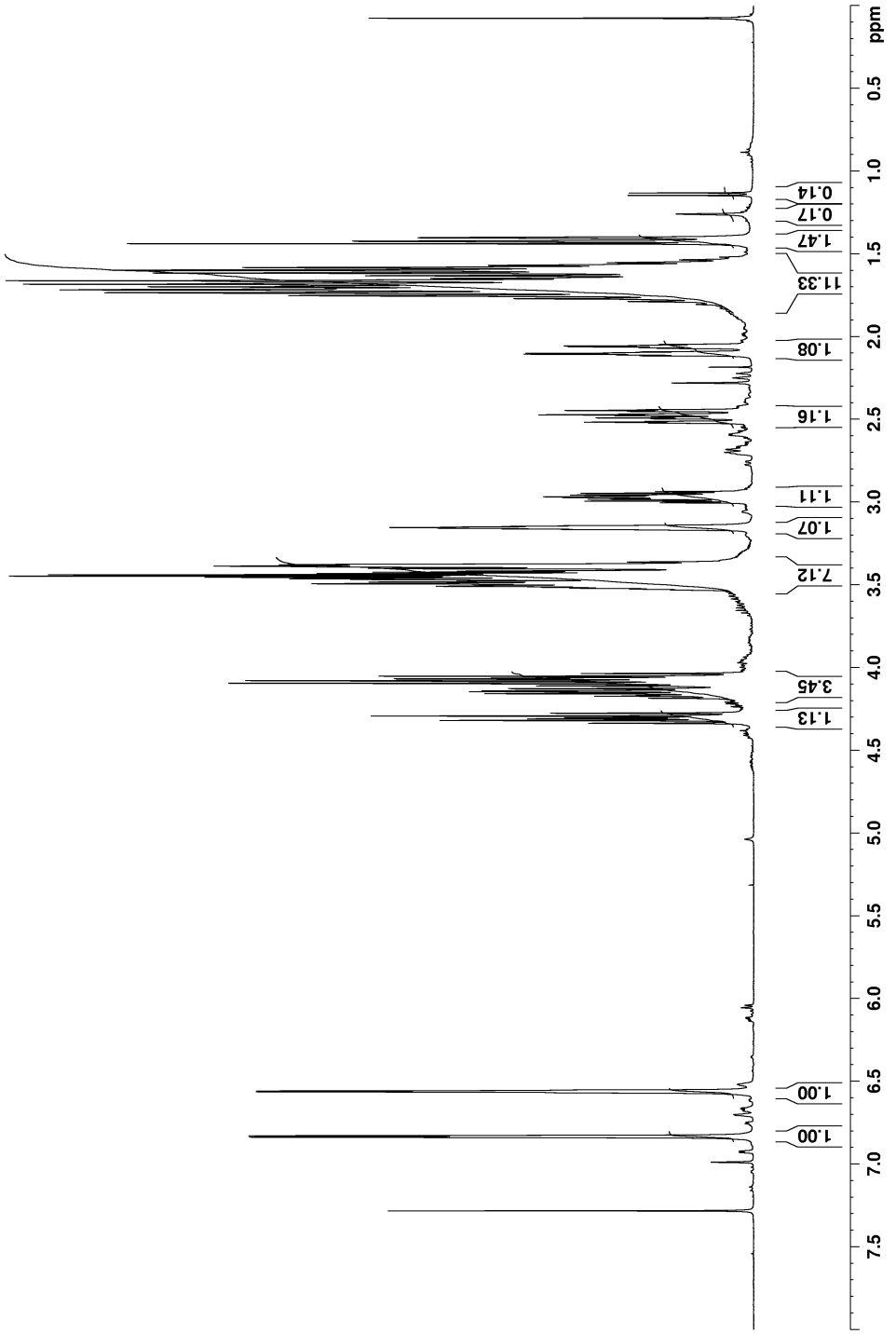

Appendix A.11: Carbon 13 NMR Spectrum of Compound B3 (Monomer 8-0-1)

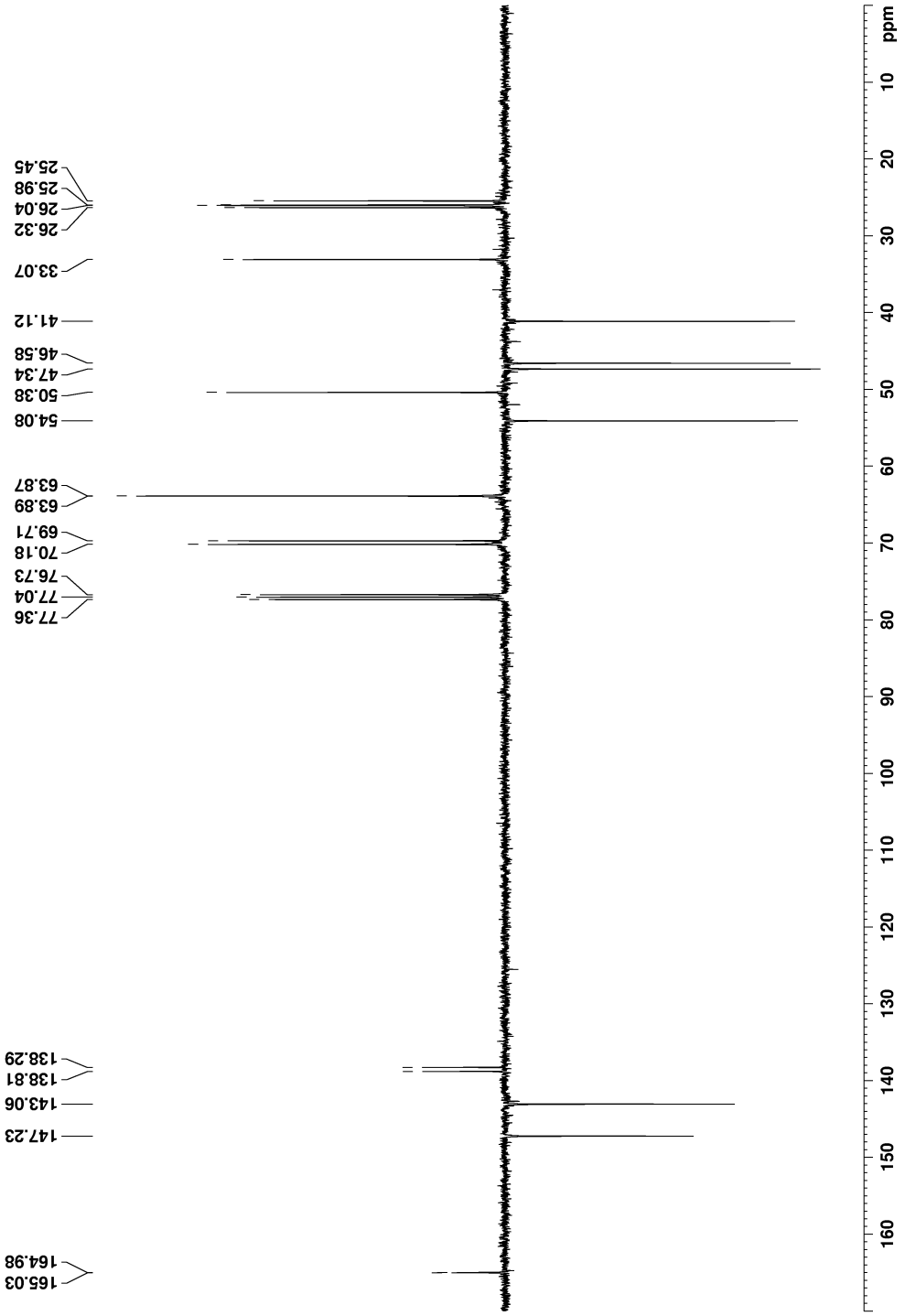

Appendix A.12: Proton NMR of Compound B4 (Monomer 12-0-2)

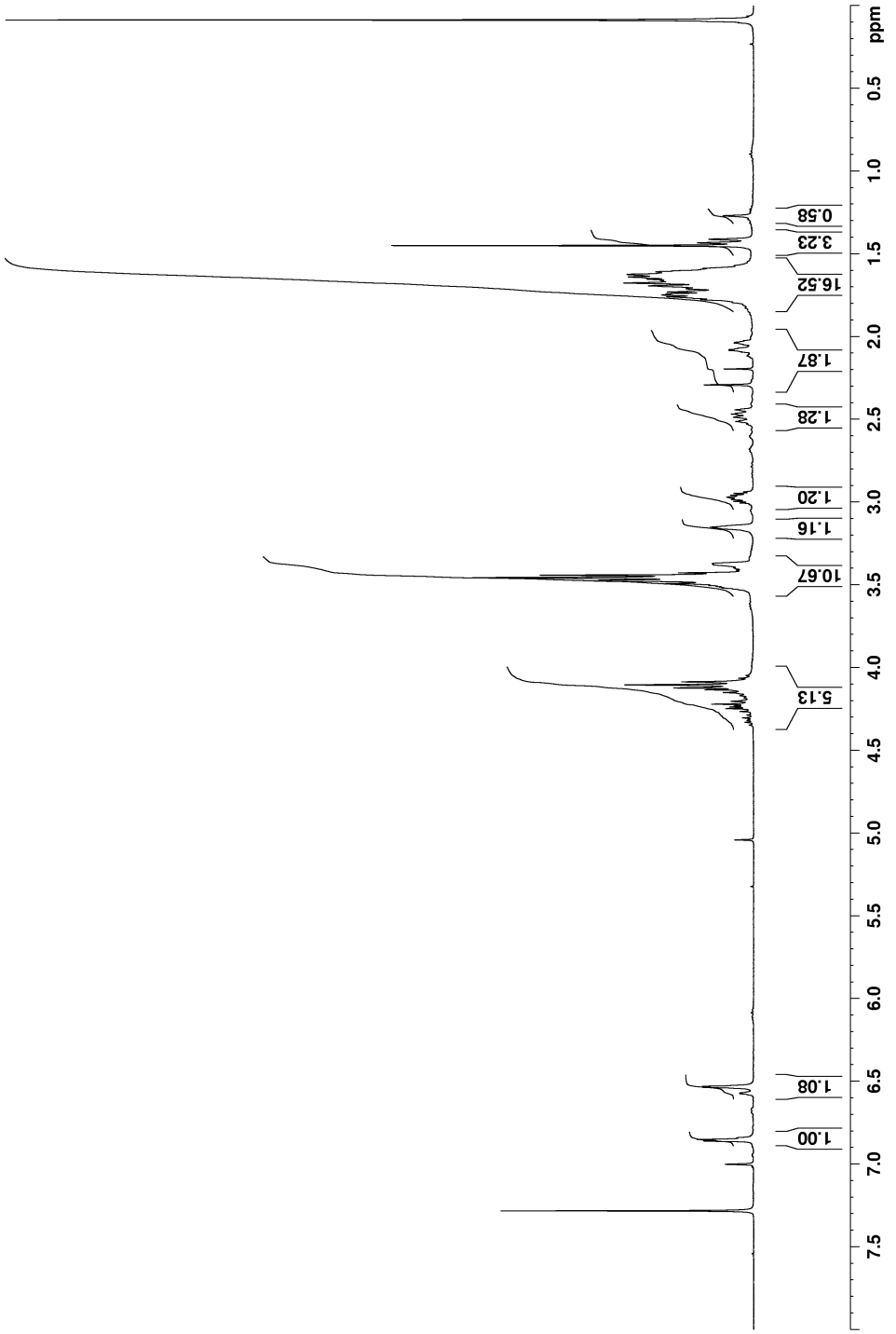

Appendix A.13: Carbon 13 NMR Spectrum of Compound B4 (Monomer 12-0-2)

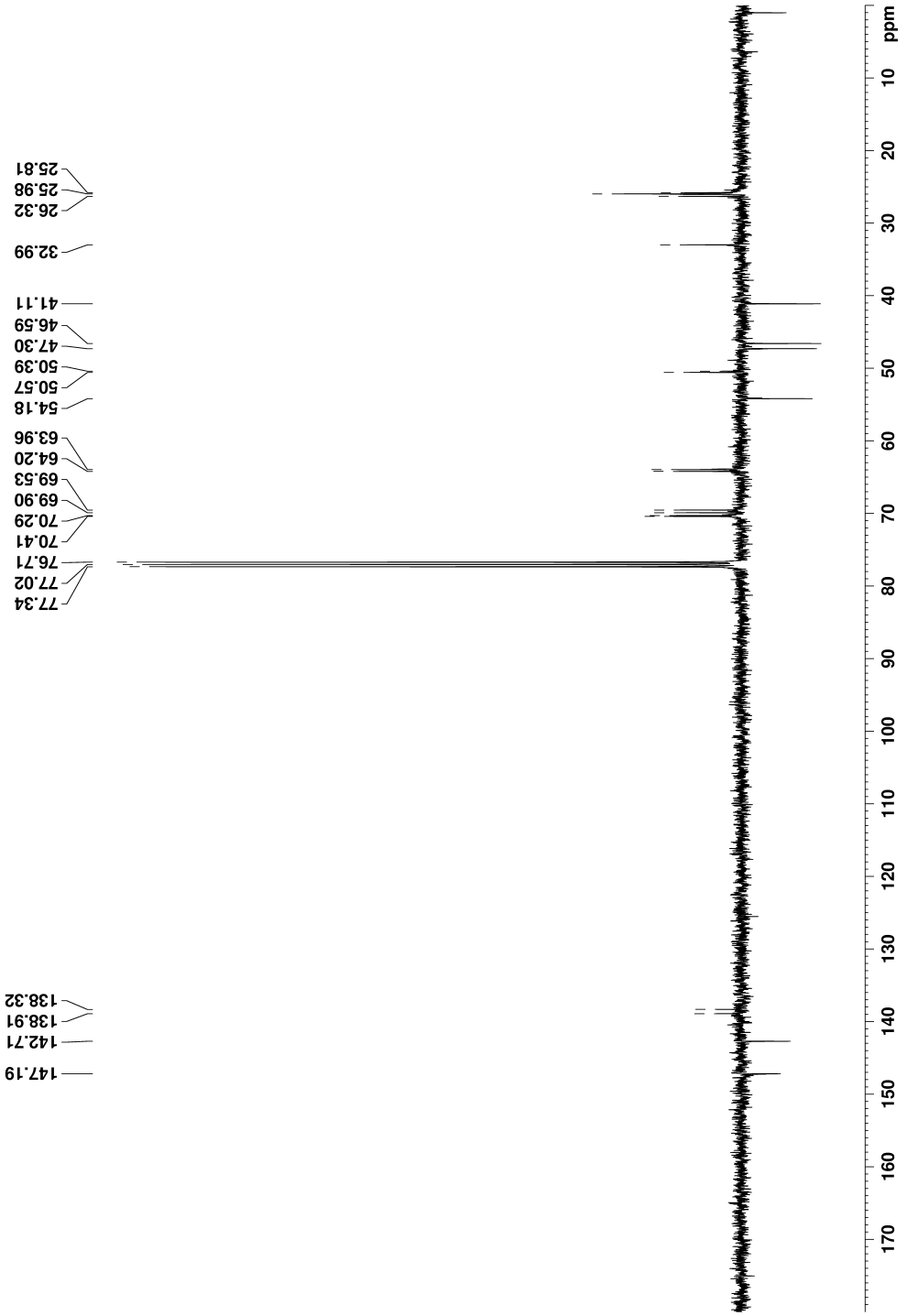

Appendix B

Worked Example G_{IC} Calculation

Panel 2, Specimen D

Specimen Measurements

- Image resolution: 12.18 px mm^{-1}
- Thickness, $\boldsymbol{h}$, 3.22 mm
- Width, $\boldsymbol{b}$, 19.26 mm
- Insert length: 64 mm
- Specimen length, $\boldsymbol{l}$ = 121.32 mm
- Centre of loading pin to midplane of specimen, $\boldsymbol{l_1}$ = 7.21 mm
- Distance of from the centre of the loading pin to the edge, $\boldsymbol{l_2}$ = 5.92 mm
- Block Length, $\mathbf{l_3}$ = 11.84 mm

Calculating the load-block correction (N)

The load-block correction is calculated using equation 5.8 on page 230 (repeated below) for each point.

$$N = 1 - (\frac{l_2}{a})^3 - \frac{9sl_1}{8a^2}\left\{1 - (\frac{l_2}{a})^2\right\} - \frac{9}{35}(\frac{s}{a})^2$$

Where:

$\boldsymbol{a}$ is the total delamination length in mm at the point of interest.

$\boldsymbol{s}$ is the displacement in mm at the point of interest.

Calculating the large displacement correction (F_{L})

The large displacement correction is calculated using equation 5.9 on page 231 (repeated below) for each point.

$$F_{\mathrm{L}} = 1 - \frac{3}{10}(\frac{s}{a})^2 - \frac{3}{2}(\frac{sl_1}{a^2})$$

Calculating the End-Factor (Δ)

The end factor is calculated by taking the x-intercept of a plot of $(\frac{C}{N})^{\frac{1}{3}}$against total delamination length (a).

Where:

$\boldsymbol{C}$ is compliance, equal to $\frac{s}{P}$

NL Point data

The NL point (the point at which the load-extension plot deviates from linearity) was calculated computationally as the point where:

- Extension, $\boldsymbol{s}$ = 8.28 mm
- Load, $\boldsymbol{P}$ = 34.819 N
- Time, $\boldsymbol{t}$ = 101 s

The distance from the end of the specimen was measured from the video frame at 101 s (figure B.1).

- Distance from end of specimen to the crack tip = 719.9 px; 59.114 mm

The total delamination length is calculated by subtracting this distance from the overall length.

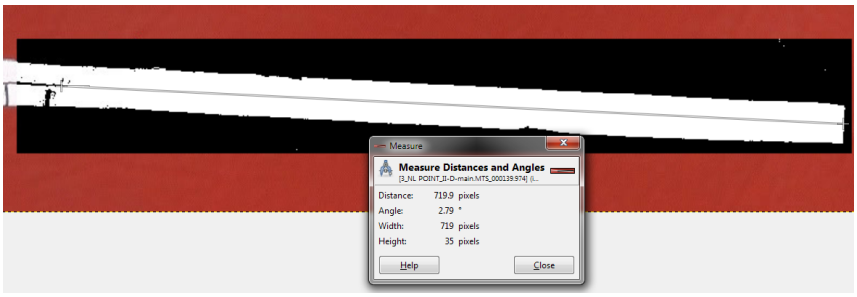

Figure B.1: Measuring distance from the end of the specimen to the crack tip in pixels.

- Total delamination length, **a** = 121.32 - 59.114 = 62.206 mm

The corrections were calculated as described on page 289.

- Load-block correction, $\boldsymbol{N}$ = 0.982
- Large displacement correction, F_{L} = 0.984
- End factor correction, · = -5.2 mm

Calculating the Mode I critical energy strain release rate (G_{IC}) at the initiation NL point.

The Mode I critical energy strain release rate (G_{IC}) is calculated using equation 5.10 on page 231 (repeated below with substituted values).

$$G_{\mathrm{IC}} = \frac{3Ps}{2b(a+|\Delta|)} \times \frac{F_{\mathrm{L}}}{N} = \frac{3 \times 34.819 \times 8.28}{2 \times 19.26(62.202+5.2)} \times \frac{0.984}{0.982} = 0.334 \text{ kJ m}^{-2} = 334 \text{ J m}^{-2}$$

Appendix C

Analysis of Variance (ANOVA) Equations

An example presentation of a result of an ANOVA is presented as follows ([$F(3, 18) = 1.28$, $p = 0.31$]). The first value is the F statistic at 3 degrees of freedom between groups and 18 degrees of freedom within groups. The second value is the probability (p value). If the p value is greater than the significance level (in this case 0.05) this outcome directs the acceptance of the null hypothesis (H_0). The p value is calculated computationally by evaluating an F distribution function with the given degrees of freedom. This can be done, for example, using the excel function FDIST.

Calculating the F-Statistic

Nomenclature

The following nomenclature is used in this section.

$df_{between}$ is the degrees of freedom between groups $(k - 1)$

df_{within} is the degrees of freedom within groups $(N - k)$.

k is the number of different groups.

n_j is the number of items in the j_{th} group.

N is the total sample size $= \sum_{j=1}^{k} n_j$

$\overline{x}_j$ is the mean of the j_{th} group

x_{ij} is the i_{th} value of the j_{th} group

$\overline{\overline{x}}$ is the grand mean (mean of all the values regardless of group).

MS_{between} is the mean squares between groups (equation C.2)

MS_{within} is the mean squares within the groups (equation C.3)

SS_{between} is the the sum of squares between groups (equation C.5)

SS_{within} is the sum of squares within the groups (equations C.4)

Equations

The F-statistic is sometimes known as the the F-ratio due to the fact that it is the ratio of the mean squares between and within the different groups (equation C.1).

$$F = \frac{MS_{\text{between}}}{MS_{\text{within}}} \tag{C.1}$$

The mean squares between and within are calculated by dividing the sum of squares by the respective degrees of freedom (equations C.2 and C.3)

$$MS_{\text{between}} = \frac{SS_{\text{between}}}{df_{\text{between}}} \tag{C.2}$$

$$MS_{\text{within}} = \frac{SS_{\text{within}}}{df_{\text{within}}} \tag{C.3}$$

The sum of squares between groups is obtained by calculating the sum (over the different groups, from j=1 to j=k) of the squared differences between the group mean and the grand mean.

$$SS_{\text{between}} = \sum_{j=1}^{k} (\overline{x_j} - \overline{\overline{x}})^2 \tag{C.4}$$

The sum of squares within groups is calculated by summation (over all values, over all groups) of the squared differences between each individual value and the respective group's mean.

$$SS_{\text{within}} = \sum_{j=1}^{k} \sum_{i=1}^{n_j} (x_{ij} - \overline{x_j})^2 \tag{C.5}$$